Inaugural dissertation

for

obtaining the doctoral degree

of the

Combined Faculty of Mathematics, Engineering and Natural Sciences

of the

Ruprecht - Karls - University

Heidelberg

Presented by

Simay Çelikyürekli, M.Sc.

Born in Ankara, Türkiye

Oral Examination: 24.10.2024

Specific Combination Therapy for H3K27M Pediatric Diffuse Midline Glioma

Referees: Prof. Dr. Lazaro Centanin
Apl.-Prof. Dr. Ina Oehme

Aileme.

Hayatta en hakiki mürşit ilimdir, fendir.

Mustafa Kemal ATATÜRK

Declaration

I hereby declare that I have written this dissertation myself, using only the cited literature and sources.

I hereby declare that I have not applied to be examined at any other institution, nor have I used the dissertation in this or any other form at any other institution as an examination paper, nor submitted it to any other faculty as a dissertation.

Heidelberg,

Simay Çelikyürekli

Acknowledgements

This project could not have been accomplished without the outstanding dedication and expertise of my colleagues, as well as the support of my family and friends. I would like to express my gratitude to each person who played a pivotal role during this project:

Apl.-Prof. Dr. Ina Oehme and Dr. Heike Peterziel, for being my supervisors. It was truly inspiring to work alongside such excellent female scientists. I am more than grateful for your guidance and support throughout this journey. Ina, thank you for giving me the chance to work in your group and believing in me during every phase of this project. You always made sure that I was on the right path, motivated me for better and helped me grow as a scientist. You made this very challenging part of my life a less challenging one with your constant support and understanding in and outside the lab. Heike, thank you for your continuous support through all the ups and downs, having always an open door for yet another question and for all our scientific and non-scientific chats. Your blend of humor and insight has not only enriched our discussions but also made them something I look forward to. You made this PhD much simpler for me.

Prof. Dr. Olaf Witt, for providing the most motivating and collaborative environment I could ever wish for. Thank you, Olaf for pushing this project further, your invaluable scientific inputs and last but not least for your efforts and resources to carry this project to clinical trials.

Prof. Dr. Lazaro Centanin, for his invaluable scientific feedback and contributions to the project as my TAC member. Thanks a lot for taking the time to teach me blastula injections and being in my defense committee, Lazaro.

Dr. David Jones, for his expertise in HGGs, providing resources and helping shape this project as one of my brilliant TAC members.

Apl.-Prof. Dr. Martin Müller and Prof. Dr. Christiane Opitz for agreeing to take part in my defense committee as my examiners.

All the collaborators, who always carried this project one step ahead: Prof. Dr. Marlon Veldwijk for radiosensitization analyses and fun and educational meetings. Dr. Tim Holland-Letz and Dr. Silvia Calderazzo for providing their help and expertise in bioinformatic and statistical analyses. Prof. Dr. Oliver Krämer and Andreas Mieland for DNA damage studies. Dr. Angela Schulz and the entire NGS Core Facility team for assistance on RNAseq experimental design and smooth running of my samples. Dr. Dominic Helm and Martin Schneider for their exceptional assistance and critical feedback in my proteomic analysis from the design to MS run and data analyses. Manuela Brom, Gaby Blaser, Dr. Damir Krunic and Dr. Felix Bestvater for their technical and scientific assistance in microscopy and histology. Lastly, all collaborators in UNITE consortium and KiTZ for their feedback in my project.

My dear B310 members, for making my time in the department an enjoyable experience. I sincerely thank you all for supporting me and making me feel home 2,500 km away from my home: Lisa, Sonja H., Marta, Anna L., Kyriaki, Olga, Charlotte, Till S., Coco, Annsophie, Alex, Aileen, Marko, Anette, Ina S., Eugene, Sonja B., Lea, Till M., Romain, Anna K., Daniela, Flo, Jonas, Isabel, Carina, Yvonne, Pauline,

Leo, Raquel, Natja, Elisabeth and Nicola. Alex, for your impeccable assistance when I got deeply stuck. Natja, for all sort of administrative help. You are an amazing project manager. My PhD friends, whom I was lucky to work with: Lisa, for showing my way around in the lab and being there for me whenever I needed mental or scientific support. A special thanks to Sonja H., who not only escorted me to the hospital after my unexpected audition for 'Break a Leg', but also mastered the arts of culinary delights and bath-time logistics during my recovery. Your support was my crutch, literally and figuratively, through every step of this journey! Marta, for being the Pollyanna of our group, always positive, helpful and caring. Your magic hands always bring the best out of any experiment and dish (especially Paella) you touch! Special thanks to Anna L., who always lends a listening ear to me and offers unwavering support and understanding. Your empathy and kindness have been pillars of strength for me since you joined our group! Big thanks to Kyriaki, whose spirited personality is as bright and unique as her hair. Thanks for all the moments we shared. My officemates: Daniela and Romain, for all the scientific discussions we had. You are an amazing duo and will continue rock in your new group in Jena! Anna K., for our lovely moments in Happy Hours and brainstorming sessions about mitotic catastrophe. Pauline, for giving the biggest smile every morning and cheerful conversations.

My PhD council family: Francisco, Aga, Shiv, Noor and Nina. Thank you from the bottom of my heart. Together, we have organized wonderful events and faced our fair share of challenges, but it is the laughter and support we shared that I will cherish the most. You have made this journey more than just academic, thanks for the memories. To the one who may be older by age but is forever young at heart—thank you for being the 'little brother' I never knew I needed, Francisco. I am grateful for every moment of laughter we shared. Thanks for being the amazing friend you are that I can always count on.

My Good Boys: Aga, Anna, Cansu, Flavio, Paul and Yunhee. You all made navigating the twists and turns of PhD life not just bearable, but genuinely fun. We have not shared our research, but we supported each other during the toughest times, laughed together in the midst of chaos, and threw the best parties! Thank you for being the highlight of my days and being the family I found along the way, always ready to drink yet another cocktail. Here is to all the future memories we have yet to create! Love, Petra.

All my friends in Turkey, Heidelberg and across the globe. Thank you for being my unwavering support system, no matter the distance. Your belief in me has been a beacon during my darkest hours, lifting me when I have felt the lowest and guiding me through tough days. Your constant encouragement and care have made my journey brighter and my burdens lighter. I am endlessly grateful for every call, message, and moment of comfort you have shared. Here is to more laughter, growth, and adventures together, no matter where we find ourselves in the world.

Canım ailem, çocukluğumdan beri bana inandığınız, hayallerimin peşinden koşmamı her daim desteklediğiniz ve her kararımda arkamda durduğunuz için size teşekkür ederim. Bu başarı sadece benim değil, sizin de başarınız. İyi ki varsınız, iyi ki ailemsiniz. Canım teyzem, hep yanımdasın, hep yanındayım. Sizinle gurur duyuyorum ve sizi çok seviyorum.

My husband, Engin. I could never have imagined finding you along the way. I could not have finished this journey without you by my side. Your strive for growth inspires my own. Thank you for being my partner, my rock, and my biggest cheerleader. I love you.

Summary

Pediatric high-grade gliomas (pHGGs) are the leading cause of cancer related death in children and among the most aggressive and devastating brain tumors, characterized by rapid progression and poor prognosis. Within this group, H3K27M diffuse midline gliomas (DMGs) stand out as particularly aggressive, due to a defining mutation in the histone H3 genes. This mutation results in the substitution of lysine 27 with methionine (K27M), which impairs the function of the polycomb repressive complex 2 (PRC2), leading to a global reduction in histone H3 lysine 27 di- and trimethylation (H3K27me2/3) and subsequent increase in H3K27 acetylation (H3K27ac). These epigenetic changes affect gene regulation, promoting oncogenic processes that drive tumor growth and resistance to conventional therapies. Despite extensive research, there are currently no effective treatment strategies that specifically target the unique pathology of H3K27M DMGs, underscoring a critical need for the development of novel therapeutic approaches. In this thesis, I focused on developing a targeted combination therapy for H3K27M DMGs. To contextualize the unique therapeutic responses associated with H3K27M DMGs, this work also compared the H3K27M DMGs with other pHGGs harboring different histone H3 statuses, such as H3 wild-type (H3 WT) and H3 glycine 34 mutants (H3G34R/V). Each of these tumor types exhibits distinct molecular signatures and clinical outcomes, highlighting the necessity of tailored therapeutic approaches.

Epigenetic drug library screens of nine H3K27M, two H3G34R/V and three H3 WT pHGG cell models along with three non-malignant cell lines identified atuveciclib, mivebresib and alisertib as hits with H3K27M DMG-selective potency. These hits targeted cyclin-dependent kinase 9 (CDK9), bromodomain and extra-terminal domain motif containing protein (BET) and aurora kinase (AURK), respectively. These top hits were further subjected to combination screens to discover optimal compound combinations. The most potent combination partners were identified to be CDK9 inhibitor (CDK9i) atuveciclib and BET inhibitor (BETi) BMS-986158, the interaction of which was confirmed to be synergistic for H3K27M DMG models. Two different compound combinations were investigated: combo high (one to one combination of the two drugs at their 50% inhibitory concentration) and combo low (combination of the two drugs reaching to 50% inhibition), the latter emphasized the synergistic interaction between the compounds.

High content microscopy (HCM) revealed that single-agent treatments with atuveciclib (CDK9i) and BMS-986158 (BETi) demonstrated cytostatic effect. The outcome of the combo low treatment was similar to monotherapies stressing that same effect size could be achieved with the combination of the two compounds at much lower doses compared to using higher doses of the individual compounds, increasing the therapeutic window and potentially reducing the risk of side effects. On the other hand, combo high elicited apoptotic cell death, which was specifically and significantly more pronounced for H3K27M DMG models. This was further validated *in vivo* using a zebrafish xenograft model. In line with these results, combo high prevented colony formation of an H3K27M DMG model in soft-agar colony formation assay. The effect of the combination treatment was also examined in conjunction with radiotherapy (RT), which is the standard of care for H3K27M DMGs. Observed synergism or additivity for H3K27M DMG models in the RT screens with compound treatments suggested that this combination therapy is compatible with RT.

Multi-omics analyses revealed that DNA replication and cell cycle-related genes were downregulated by atuveciclib (CDK9i), BMS-986158 (BETi) and combo low. Different DNA damage response (DDR) pathways were suppressed by these treatments, indicating a synergistic effect on inhibiting DNA repair. Moreover, DNA damage accumulation was observed under combo high treatment, leading to the hypothesis that both CDK9 and BET inhibitors induce DNA damage primarily through R-loop formation, caused by collisions of the replication machinery with stalled RNA polymerase II (RNAPII), which remains unresolved due to downregulation of spliceosome by the presence of both inhibitors. This damage accumulates over time due to reduced DNA damage repair activity. Cells are unable to halt progression through the cell cycle due to underlying mutations in *TP53* or *PPM1D* or due to the impact of inhibitors on cell cycle checkpoints, proceed through mitosis with accumulating DNA damage, eventually leading to apoptosis via mitotic catastrophe.

In summary, compound and synergy screens discovered the synergistic combination of CDK9 and BET inhibitors, which was validated to be specific and more cytotoxic for H3K27M DMG models *in vitro* and *in vivo* in zebrafish embryo xenografts. The combinatorial inhibition of CDK9 and BET capitalizes on the transcriptional vulnerabilities of H3K27M DMGs, characterized by decreased H3K27me2/3 and increased H3K27ac, a result of PRC2 dysfunction. These inhibitors together trigger apoptosis, by most likely synergistically inducing DNA damage, which remains unrepaired due to the downregulation of DDR pathways. Future *in vivo* studies in mice are planned to further assess the clinical viability of the CDK9 and BET inhibitor combination.

Zusammenfassung

Die hochgradigen pädiatrischen Gliome (engl: pHGG) sind die häufigste Ursache für krebsbedingte Todesfälle bei Kindern und gehören zu den aggressivsten und bösartigen Hirntumoren, die sich durch schnelles Wachstum und schlechte Prognosen auszeichnen. In dieser Gruppe zeichnen sich die diffusen Mittellinengliome (DMG) durch eine H3K27M-Mutation in den Histon-H3-Genen als besonders aggressiv aus. Durch diese Mutation wird Lysin 27 durch Methionin (K27M) ersetzt, was die Funktion des Polycomb Repressive Complex 2 (PRC2) hemmt und zu einer globalen Verringerung der Di- und Trimethylierung von Histon H3-Lysin 27 (H3K27me2/3) und einer anschließenden Zunahme der H3K27-Acetylierung (H3K27ac) führt. Diese epigenetischen Veränderungen wirken sich auf die Genregulation aus und fördern onkogene Prozesse, die das Tumorwachstum und die Resistenz gegen herkömmliche Therapien verstärken. Trotz umfangreicher Forschung gibt es derzeit keine wirksamen Behandlungsstrategien, die gezielt auf die einzigartige Pathologie von H3K27M-DMGs gerichtet sind, weshalb ein dringender Bedarf an der Entwicklung neuer therapeutischer Ansätze besteht. In dieser Arbeit habe ich mich auf die Entwicklung einer gezielten Kombinationstherapie für H3K27M DMGs konzentriert. Um die einzigartigen therapeutischen Antworten von H3K27M-DMGs zu validieren, wurden sie in dieser Arbeit auch mit anderen pHGGs mit verschiedenen Histon-H3-Status verglichen, nämlich mit H3-Wildtyp (H3 WT) und H3-Glycin-34-Mutanten (H3G34R/V). Jeder dieser Tumorarten weist individuelle molekulare Signaturen und klinische Ergebnisse auf, was die Notwendigkeit von gezielten therapeutischen Ansätzen unterstreicht.

In einem Screening von epigenetischen Wirkstoffen in neun H3K27M-, zwei H3G34R/V- und drei H3 WT pHGG-Zellmodellen sowie drei nicht malignen Zelllinien konnten Atuveciclib, Mivebresib und Alisertib als Kandidaten mit H3K27M-DMG-selektiver Wirksamkeit identifiziert werden. Die identifizierten Wirkstoffe inhibieren die Cyclin Dependent Kinase 9 (CDK9), das Bromodomain and Extra-Terminal Domain Motif Containing Protein (BET) beziehungsweise die Aurora-Kinase (AURK). Im Anschluss wurde ein Kombinations-Screening durchgeführt, um die optimalen Wirkstoffkombinationen zu ermitteln. Die Kombination von dem CDK9-Inhibitor (CDK9i) Atuveciclib und dem BET-Inhibitor (BETi) BMS-986158 erwies sich als synergistisch in H3K27M-DMG-Modellen. Zwei unterschiedliche Wirkstoffkombinationen wurden untersucht: Combo High (Kombination der beiden Wirkstoffe bei ihrer jeweiligen mittleren inhibitorischen Konzentration) und Combo Low (Kombination der beiden Wirkstoffe bis zu einer gemeinsamen mittleren inhibitorischen Konzentration). Letztere zeigte die synergistische Interaktion zwischen den Wirkstoffen besonders deutlich.

High-Content-Mikroskopie (HCM) wies nach, dass Einzelbehandlungen mit Atuveciclib (CDK9i) und BMS-986158 (BETi) eine zytostatische Wirkung zeigten. Die Ergebnisse der Combo-Low-Behandlung waren mit denen der Monotherapien vergleichbar, was darauf hindeutet, dass mit der Kombination der beiden Wirkstoffe bei deutlich niedrigeren Dosen die gleiche Wirksamkeit erzielt werden kann. Somit wird die therapeutische Breite vergrößert und das Risiko von Nebenwirkungen verringert. Im Gegensatz dazu löste Combo High Apoptose aus, die bei H3K27M-DMG-Modellen spezifisch und deutlich stärker war. Diese Ergebnisse wurden anschließend anhand eines Zebrabärbling-Xenotransplantationsmodells *in vivo* weiter validiert. In Übereinstimmung mit diesen Ergebnissen verhinderte Combo High die Koloniebildung eines H3K27M-DMG-Modells im Softagar-Koloniebildungstest. Darüber hinaus wurde die Wirkung der Kombinationstherapie zusammen mit der Strahlentherapie (engl.

RT) untersucht, welche bei H3K27M-DMGs den aktuellen Behandlungsstandard darstellt. Die beobachteten synergistischen oder additiven Wirkungen auf H3K27M-DMG-Modelle in RT-Screens mit Kombinationsbehandlungen deuten darauf hin, dass die Kombinationstherapie mit RT kompatibel ist.

Multiomics-Analysen zeigten, dass DNA-Replikation und Zellzyklus-regulierende Gene durch Atuveciclib (CDK9i), BMS-986158 (BETi) und Combo Low herunterreguliert wurden. Diese Wirkstoffe inhibierten verschiedene Signalwege der DNA-Schadensantwort (engl. DDR), was auf einen synergistischen Effekt bei der Inhibierung der DNA-Reparatur hinweist. Darüber hinaus konnte unter der Behandlung mit Combo High eine Akkumulation von DNA-Schäden beobachtet werden, was die Hypothese aufstellt, dass sowohl CDK9- als auch BET-Inhibitoren DNA-Schäden hauptsächlich durch die Bildung von R-Loops induzieren. Diese werden durch Kollisionen des DNA-Polymerasenkomplexes mit der RNA-Polymerase II (RNAPII) verursacht, welche aufgrund der Herunterregulierung des Spliceosoms durch beide Inhibitoren blockiert bleibt. Im Verlauf der Zeit kommt es zu einer Akkumulation der DNA-Schäden, da die Aktivität der DNA-Schadensantwort reduziert ist. Zellen, die aufgrund von Mutationen in TP53, PPM1D oder durch die Inhibitoren selbst unfähig sind, den Zellzyklus zu unterbrechen, durchlaufen die Mitose mit einer Akkumulation von DNA-Schäden, was zu einer mitotischen Katastrophe und letztlich zur Apoptose führt.

Insgesamt konnte durch Wirkstoff- und Synergie-Screenings eine synergistische Kombination von CDK9- und BET-Inhibitoren identifiziert werden, die sich sowohl *in vitro* als auch *in vivo* als spezifisch und zytotoxisch für H3K27M-DMG-Modelle erwies. Die gemeinsame Inhibition von CDK9 und BET macht sich die transkriptionellen Anfälligkeiten von H3K27M-DMGs zunutze, die als Folge der Dysfunktionalität von PRC2 durch eine Verringerung von H3K27me2/3 und eine Erhöhung von H3K27ac gekennzeichnet sind. Die Kombination der Inhibitoren löst die Apoptose aus, indem höchstwahrscheinlich eine synergistische Induktion von DNA-Schäden erfolgt, welche aufgrund der Herunterregulierung der DDR-Signalwege nicht repariert werden können. Künftige in-vivo-Studien an Mäusen sind geplant, um die klinische Wirksamkeit der Kombination aus CDK9- und BET-Inhibitoren weiter zu untersuchen.

Abbreviations

7SK	7SK small nuclear RNA
ACKR4	Atypical chemokine receptor 4
ACTB	Beta actin
aHGG	Adult high grade glioma
AKT	Protein kinase B
AKTi	AKT inhibitor
amp	Amplification
AP-1	Activator protein 1
APS	Ammonium persulfate
ATP	Adenosine triphosphate
ATR	Ataxia Telangiectasia and Rad3-related protein
AUC	Area under the curve
BCA	Bicinchoninic acid
BCOR	BCL6 Corepressor
BET	Bromodomain and extra-terminal domain containing protein
BETi	BET inhibitor
BRAF	V-Raf murine sarcoma viral oncogene homolog B
BRD2	Bromodomain containing protein 2
BRD3	Bromodomain containing protein 3
BRD4	Bromodomain containing protein 4
BRDT	Testis specific bromodomain containing protein
BRG1 (SMARCA4)	SWI/SNF-related, matrix-associated, actin-dependent regulator of chromatin, subfamily A, member 1
BSA	Bovine serum albumin
BztCl	Benzethonium chloride
c-Fos	Fos proto-oncogene
c-Jun	Jun proto-oncogene
CCCTC-binding	CCCTC-binding factor
CCND2	Cyclin D2
CDK	Cyclin-dependent kinase
CDK9	Cyclin-dependent kinase 9
CDK9i	CDK9 inhibitor
CDK12	Cyclin-dependent kinase 12
CDK13	Cyclin-dependent kinase 13
CDKN2A/B	Cyclin dependent kinase inhibitor 2A/B
cDNA	Coding desoxyribonucleic acid
CLIP2	CAP-Gly domain-containing linker protein 2
C_{max}	Maximum plasma concentration
CNS	Central nervous system
CO_2	Carbon dioxide
CycK	Cyclin K
CycT	Cyclin T

DAPI	4’,6-Diamidin-2-phenylindol
DAXX	Death-domain associated protein
ddH2O	Double-distilled water
del	Deletion
DHG	Diffuse hemispheric glioma
DIPG	Diffuse intrinsic pontine glioma
DMG	Diffuse midline glioma
DMSO	Dimethyl sulfoxide
DNA	Deoxyribonucleic acid
DRB	5,6-Dichloro-1-beta-D-ribofuranosylbenzimidazole
DSB	DNA double-strand breaks
DSS_{asym}	Asymmetric drug sensitivity score
DSS_{asym}_combo	Asymmetric drug sensitivity score for combination treatments
DSS_{asym}_mono	Asymmetric drug sensitivity score for monotherapy
DTT	Dithiothreitol
E2F	Early region 2 binding factor
ECL	Enhanced chemiluminescent
EDTA	Ethylenediaminetetraacetic acid
EGF	Epidermal growth factor
EGFR	Epidermal growth factor receptor
ERBB	Erythroblastic leukemia viral oncogene homologue
ERK	Extracellular regulated kinase
ET	Extra-terminal
EtOH	Ethanol
FCS	Fetal calf serum
FDA	Food and Drug Administration
FDR	False discovery rate
FGFR	Fibroblast growth factor receptor
FOS	Fos proto-oncogene
FosB	FBJ murine osteosarcoma viral oncogene homolog B
G34R	Glycine to arginine substitution at position 34
G34V	Glycine to valine substitution at position 34
GDP	Guanosine diphosphate
GFP	Green fluorescent protein
GO	Gene ontology
GPCR	G-protein coupled receptor
GRCh37	Genome reference consortium human build 37
GTP	Guanosine triphosphate
H2A	Histone H2A
H2B	Histone H2B
H_2O	Water
H3G34	Histone H3 glycine 34
H3K27	Histone H3 lysine 27

HCl	Hydrogen chloride
HDAC	Histone deacetylase
HEXIM1	Hexamethylene bis-acetamide inducible 1
HGG	High-grade glioma
HMT	Histone methyltransferase
HPLC	High-performance liquid chromatography
HRP	Horseradish peroxidase
HTS	High-throughput screening
HU	Hydroxyurea
IC	Inhibitory concentration
IC50	50% inhibitory concentration
IC75	75% inhibitory concentration
IDH	Isocitrate dehydrogenase
IgG	Immunoglobulin G
ii	Interaction index
INFORM	Individualized Therapy for Relapsed Malignancies in Childhood
IP	Immunoprecipitation
iTReX	Interactive therapy response exploration
JAK	Janus kinase
JNK	C-Jun N-terminal kinase
JUN	Jun proto-oncogene
K27M	Lysine to methionine substitution at position 27
KEGG	Kyoto Encyclopedia of Genes and Genomes
KDM6B	Lysine demethylase 6B
LC	Liquid chromatography
LC-MS/MS	Liquid chromatography–mass spectrometry/mass spectrometry
LD	Lethal dose
Log2FC	Log2-transformed fold-change
MAPK	Mitogen-activated protein kinase
MAPKi	MAPK inhibitor
MCL1	Myeloid cell leukemia 1
MEK	Mitogen-activated protein kinase kinase
MEKi	MEK inhibitor
MePCE	Methyl phosphate capping enzyme
MET	Hepatocyte growth factor receptor
METi	MET inhibitor
MPNSTs	Malignant peripheral nerve sheath tumors
mRNA	Messenger ribonucleic acid
MS	Mass spectrometry
mTOR	Mammalian target of rapamycin
mTORi	mTOR inhibitor
MTT	3-(4,5-Dimethylthiazol-2-yl)-2,5-Diphenyltetrazolium Bromide
mut	Mutation

MYB	Avian myeloblastosis viral oncogene homolog
MYC	Myelocytomatosis oncogene
MYBL1	MYB proto-oncogene like 1
NA	Not applicable
NaCl	Sodium chloride
NaOH	Sodium hydroxide
NEAA	Non-essential amino acids
NELF	Negative elongation factor
NF-kB	Nuclear factor kappa-light-chain-enhancer of activated B cells
NF1	Neurofibromin 1
NGS	Next-generation sequencing
NHEJ	Non-homologous end joining
ns	Not significant
O/N	Overnight
OLIG2	Oligodendrocyte transcription factor 2
OPCs	Oligodendroglial progenitor cells
OS	Overall survival
OTP	One-touch pipeline
P-TEFb	Positive transcription elongation factor b
PAK1	p21 activated kinase 1
PARP	Poly (ADP-ribose) polymerase
PARP1	Poly (ADP-ribose) polymerase 1
PBS	Phosphate-buffered saline
PC	Principal component
PC1	Principal component 1
PC2	Principal component 2
PCA	Principal component analysis
PD	Progressive disease
PDGFRA	Platelet-derived growth factor receptor alpha
PE	Phycoerythrin
PEP	Phosphoenolpyruvate
PFA	Paraformaldehyde
PFS	Progression-free survival
pHGG	Pediatric high-grade glioma
PI	Propidium iodine
PI3K	Phosphoinositide 3-kinases
PI3Ki	PI3K inhibitor
PID	P-TEFb Interacting Domain
PIK3CA	Phosphatidylinositol-4,5-bisphosphate 3-kinase catalytic subunit alpha
PIM	Proto-oncogene serine/threonine-protein kinase
PK	Pharmacokinetics
PKC	Protein kinase C
pHGG	Pediatric high-grade glioma

pLGG	Pediatric low-grade glioma
PP1	Protein phosphatase 1
PPM1D	Protein phosphatase, Mg2+/Mn2+ dependent, 1d
PR	Partial response
pRb	Retinoblastoma protein
PRC2	Polycomb repressive complex 2
PROTAC	Proteolysis targeting chimera
PTEN	Phosphatase and tensin homolog
PTM	Post-translational modification
PTU	Propylthiouracil
PVDF	Polyvinylidene fluoride
QC	Quality control
RAD51	Resection and DNA repair protein RAD51 homolog 1
RAF	Proto-oncogene serine/threonine-protein kinase
RECIST	Response Evaluation Criteria in Solid Tumors
RIN	RNA integrity number
RIPA Buffer	Radio-immunoprecipitation assay buffer
RLU	Relative light unit
RNA	Ribonucleic acid
RNAi	RNA interference
RNAPII	RNA polymerase II
RNAseq	RNA sequencing
ROCK	Rho kinase
RT	Radiotherapy
RTK	Receptor tyrosine kinase
S6K1	Ribosomal protein S6 kinase beta-1
SDC	Sodium deoxycholate
SDC4	Syndecan-4
SDS	Sodium dodecyl sulfate
SDS-PAGE	SDS polyacrylamide gel electrophoresis
$sDSS_{asym}$	Selective asymmetric drug sensitivity score
SEC	Super enhancer complex
SEs	Super enhancers
SF	Surviving fraction
SF100	Surviving fraction 100%
SF50	Surviving fraction 50%
SF75	Surviving fraction 75%
SMAD2/3	Mothers against decapentaplegic homolog 2/3
SOC	Standard-of-care
SOX10	Sex-determining region y-box transcription factor 10
SOX8	Sex-determining region y-box transcription factor 8
SPRY	Sprouty
SRY	Sex-determining region y

STAT	Signal transducer and activator of transcription
STS	Staurosporine
SV40-TAg	Simian Vacuolating Virus 40 large T antigen
TBP	TATA-binding protein
TBS	Tris-buffered saline
TBS-T	Tris-buffered saline with tween
TDSU	Translational drug screening unit
TEMED	Tetramethyl ethylenediamine
TFA	Trifluoroacetic acid
TICRR	TOPBP1 interacting checkpoint and replication regulator
TME	Tumor microenvironment
TMRE	Tetramethyl rhodamine ethyl ester
TOPBP1	DNA topoisomerase II binding protein 1
TP53	Tumor protein p53
TPM	Transcript per million
Tris-SDS	Trisodium dodecyl sulfate
tRNA	Transfer RNA
trunc	Truncation
TSM	Tumor stem medium
UMAP	Uniform Manifold Approximation and Projection
UPLC	Ultra-performance liquid chromatography
VPA	Valproic acid
WB	Western Blot
WHO	World Health Organization
WNT	Wingless-type MMTV integration site family
WT	Wild-type

Table of Contents

Summary ..... *I*

Zusammenfassung ..... *III*

Abbreviations ..... *V*

List of Figures ..... *XV*

List of Tables ..... *XVI*

List of Supplementary Figures ..... *XVIII*

List of Appendix Figures ..... *XIX*

1 Introduction *1*

1.1 Pediatric high-grade glioma **1**

1.1.1 World Health Organization classification of pediatric high-grade gliomas 1

1.1.2 Histone H3 2

1.1.2.1 H3 mutations in pediatric high-grade gliomas 2

1.1.2.1.1 H3K27M diffuse midline glioma 3

1.1.2.1.2 H3G34R/V diffuse hemispheric glioma 4

1.1.3 Current treatment strategies for H3K27M diffuse midline glioma 5

1.2 Cyclin-dependent kinases **6**

1.2.1 CDK9 and P-TEFb 7

1.2.1.1 Transcription elongation and termination control by P-TEFb 7

1.2.1.2 P-TEFb role in cell cycle 9

1.2.1.3 P-TEFb role in DNA repair 9

1.2.1.4 Utilizing CDK9 inhibitors in cancer treatment 9

1.3 Bromodomain and extra-terminal domain containing proteins **10**

1.3.1 The role of BET proteins in RNAPII release and transcriptional elongation 11

1.3.2 Organization of chromatin structure by BET proteins 12

1.3.3 The impact of BET proteins on super enhancers 12

1.3.4 BET protein function on replication-transcription modulation 12

1.3.5 BET inhibitors in cancer treatment 13

1.4 Functional precision oncology and drug sensitivity profiling **14**

2 Aim *15*

3 Materials & Methods *17*

3.1 Materials **17**

3.1.1 Cell models and cell culture 17

3.1.2 Inhibitors 20

3.1.3 Antibodies 27

3.1.4 Biochemical reagents 28

3.1.5 Buffers and Solutions 29

3.1.6 Fluorescent dyes 31

3.1.7 Consumables 32

3.1.8 Kits 33

3.1.9 Instruments and devices 34
3.1.10 Software 35
3.1.11 Databases and online tools 35
3.2 Methods 36
3.2.1 Cell culture 36
3.2.1.1. Propagation of cells 36
3.2.1.2. Freezing and thawing cells 37
3.2.1.3 Authentication and contamination testing of cell lines 38
3.2.1.4. Routine mycoplasma check 38
3.2.2 Epigenetic drug library printing and screening 38
3.2.2.1 Epigenetic drug library printing 38
3.2.2.2 Metabolic activity assay 39
3.2.2.2.1 Seeding density optimization 39
3.2.2.3 Assessing drug sensitivity 39
3.2.3 TDSU drug library printing and combination screens 40
3.2.3.1 TDSU drug library printing 40
3.2.3.2 Printing of the combination partner 40
3.2.3.3 Examining compound combination sensitivity 41
3.2.3 Synergy screens 41
3.2.3.1 Synergy screen with multiple-ray design 41
3.2.3.2 Synergy screen with matrix design 42
3.2.4 Western Blot 42
3.2.4.1 Cell lysate preparation 42
3.2.4.2 Measurement of protein concentration 43
3.2.4.3 Gel electrophoresis and immunoblotting 44
3.2.5 Caspase-3/7 activity assay 44
3.2.6 Soft-agar colony formation assay (Soft-agar CFA) 45
3.2.7 High content microscopy imaging 45
3.2.8 RNA sequencing 46
3.2.8.1 Sample generation 46
3.2.8.2 RNA sequencing 46
3.2.8.3 Data analysis 46
3.2.9 LC-MS/MS proteomics 47
3.2.9.1 Sample generation 47
3.2.9.2 Sample processing 47
3.2.10 Radiosensitization analysis 48
3.2.10.1 Plating efficiency test 48
3.2.10.2 Radiosensitivity assessment via colony formation assay 48
3.2.10.3 Metabolic activity analysis of combo low in conjunction with radiotherapy 48
3.2.10.4 Radiosensitization exploration via colony formation assay 48
3.2.11 Exploration of DNA damage induction in H3K27M DMG cell model under treatment 49
3.2.11.1 DNA damage investigation with WB 49
3.2.11.2 DNA damage investigation with flow cytometry 49
3.2.12 Toxicity assay, xenotransplantation and drug treatment in zebrafish embryo 50
3.2.12.1 Zebrafish embryo toxicity assay 50
3.2.12.2 Zebrafish embryo xenotransplantation 51
3.2.12.3 Zebrafish embryo xenograft imaging and treatment 51
3.2.13 Statistical analyses 51
3.2.14 The use of artificial intelligence 52

4 Results *53*

4.1 Establishment of the epigenetic drug library to target H3K27M DMGs **53**

4.2 Epigenetic drug screen identified CDK9i, BETi and AURKi as top hits for H3K27M DMG models **54**

4.2.1 All models passed quality control 54

4.2.2 Metabolic activity assay found mivebresib, atuveciclib and alisertib as lead compounds specifically targeting H3K27M DMGs 55

4.3 Identification of CDK9i plus BETi as optimal drug combination **58**

4.3.1 Synergy screens with multiple-ray design approach demonstrated that atuveciclib and BMS-986158 synergize for H3K27M DMG 60

4.4 Combination treatment with atuveciclib and BMS-986158 specifically targets H3K27M DMG *in vitro* **61**

4.4.1 Atuveciclib and BMS-986158 displayed on-target activity in H3K27M DMG cell models 61

4.4.2 High content microscopy analysis revealed that the combination treatment led to complete remission in H3K27M DMG cell models 63

4.4.3 Combinatorial treatment induced apoptosis in H3K27M DMG cell models 65

4.4.4 Combinatorial treatment prevented colony formation of H3K27M DMG in soft agar colony formation assay 65

4.5 The combination of atuveciclib and BMS-986158 sensitized the H3K27M DMG cells to radiotherapy **66**

4.6 Multi-omics analysis identified the MoA of atuveciclib, BMS-986158 and their combination for H3K27M DMG cell models **68**

4.6.1 The samples passed quality control pre- and post-omics analyses 69

4.6.2 Gene expression analysis identified that DNA damage response pathways were negatively regulated by atuveciclib and BMS-986158 69

4.6.3 Proteomics analysis confirmed gene expression findings 73

4.7 DNA damage exploration displayed increased γH2A.X level under combo high treatment **75**

4.8 Compound combination was potent *in vivo* in zebrafish embryo xenograft model **76**

4.9 Blood brain barrier penetrability of atuveciclib and BMS-986158 was calculated to be moderate **77**

4.10 The effect of blood brain barrier penetrant CDK9i, KB-0742, on H3K27M DMG was found to be similar to atuveciclib **78**

5 Discussion *79*

5.1 Compound screens **79**

5.2 Molecular characterization of atuveciclib, BMS-986158 and their combination **80**

5.2.1 Mode of cell death 81

5.2.2 Mode of action 83

5.2.2.1 Mode of action of BET inhibition 83

5.2.2.2 Mode of action of CDK9 inhibition 84

5.2.2.3 The effect of the inhibitors on cell cycle 85

5.2.2.4 The effect of the inhibitors on DNA damage 85

5.2.3 Specificity of combinatorial treatment with CDK9i and BETi towards H3K27M DMG 86

5.2.4 Sensitization to radiotherapy 87

6 Conclusion & Outlook 89

Supplementary Figures 91

Appendix 103

References 127

List of Figures

Figure 1. Co-alterations, age distribution and survival time observed for pHGGs 3
Figure 2. The role of CDK9 on transcription elongation and termination 8
Figure 3. Overview of the various functions of BET proteins 12
Figure 4. Epigenetic drug library 53
Figure 5. H3K27M DMG models are clustered by PCA 55
Figure 6. The compound effect on pHGG models visualized by unsupervised hierarchical clustering heatmap 56
Figure 7. Analysis on the upper arm of the hierarchical clustering heatmap 58
Figure 8. Composition of the TDSU drug library 58
Figure 9. Dose-response curves of the epigenetic hits for four H3K27M DMG cell models selected for the combination screens 59
Figure 10. Compound combination screen with epigenetic hits and TDSU drug library 60
Figure 11. Synergism between atuveciclib (CDK9i) and BMS-986158 (BETi) for four H3K27M DMG cell models at 50% inhibition 61
Figure 12. On-target analysis of the effects of atuveciclib (CDK9i), BMS-986158 (BETi) and combination treatments in WB 62
Figure 13. Representative HCM images of SU-DIPG-17 (H3K27M) spheroids treated with different conditions for 72h 63
Figure 14. HCM imaging analysis depicting spheroid area change from baseline and cell death 64
Figure 15. Caspase-3/7 activity analysis of H3K27M DMG cell models upon treatment 65
Figure 16. Soft-agar colony formation assay 66
Figure 17. Radiosensitivity and radiosensitization analyses 67
Figure 18. Pathway analysis of the pooled RNAseq data of downregulated genes upon atuveciclib (CDK9i) treatment 70
Figure 19. Pathway analysis of the pooled RNAseq data of differentially expressed genes upon BMS-986158 (BETi) treatment 71
Figure 20. Pathway analysis of the pooled RNAseq data of differentially expressed genes following combo low treatment 71
Figure 21. Hierarchical clustering heatmap of KEGG cell cycle pathway genes for all four H3K27M DMG cell models under combo low and DMSO treatments 72
Figure 22. *MYC* expression in four H3K27M DMG cell models under different treatments 73
Figure 23. Downregulated pathways under atuveciclib (CDK9i) treatment in H3K27M and H3 WT models 74
Figure 24. Downregulated pathways under BMS-986158 (BETi) treatment in H3K27M and H3 WT models 74
Figure 25. Downregulated pathways under combo low treatment in H3K27M and H3 WT models 75
Figure 26. DNA damage and apoptosis induction by combo high 75
Figure 27. Waterfall plot demonstrating the change in tumor volume (%) from baseline for each individual zebrafish embryo xenograft 77
Figure 28. Dose-response curves of KB-0742 (CDK9i) for four H3K27M DMG cell models 78
Figure 29. Graphical explanation of CDK9i and BETi combination effect on H3K27M DMG 90

List of Tables

Table 1. Ongoing clinical trials for pHGG....6
Table 2. CDK9 inhibitors that have advanced to clinical trials 10
Table 3. BET inhibitors that have advanced to clinical trials....13
Table 4. Cell models 17
Table 5. Cell culture solutions 18
Table 6. Cell culture media....19
Table 7. Epigenetic drug library compounds....20
Table 8. TDSU drug library compounds 23
Table 9. Additional epigenetic compounds added to TDSU drug library 26
Table 10. Dead control compounds 27
Table 11. Primary antibodies 27
Table 12. Secondary antibodies 27
Table 13. Biochemical reagents 28
Table 14. 20% SDS 29
Table 15. 1M Tris-HCl 29
Table 16. 1M NaCl 29
Table 17. RIPA buffer for cell lysis 29
Table 18. Cell lysis buffer for proteomic sample preparation....30
Table 19. 4x Laemmli buffer for protein loading....30
Table 20. 10X TBS 30
Table 21. 1X TBS-T....30
Table 22. Coomassie Brilliant Blue staining for SDS gels....30
Table 23. Ponceau staining for membranes....30
Table 24. 5% milk in TBS-T as blocking solution 31
Table 25. 5% BSA in TBS-T as blocking solution 31
Table 26. 50X E3 zebrafish embryo buffer....31
Table 27. 1X E3 buffer 31
Table 28. Fluorescent dyes....31
Table 29. Consumables 32
Table 30. Kits 33
Table 31. Instruments and devices 34
Table 32. Software 35
Table 33. Databases and online tools 35
Table 34. Cell culture conditions....36
Table 35. Seeding densities for metabolic activity assays....40
Table 36. Cell models analyzed in combination screens and the combination partners 40
Table 37. Seeding densities in all experiments 42
Table 38. Concentrations used in *in vitro* assays 43
Table 39. Treatment conditions used in omics analyses....46
Table 40. Compound doses used in radiosensitization assay 49
Table 41. Compound combination concentrations used in zebrafish embryo toxicity analysis 50
Table 42. Calculated SF50 and SF75 values for H3K27M DMG cell models 67

Table 43. BBB scores of atuveciclib (CDK9i) and BMS-986158 (BETi) 77

List of Supplementary Figures

Figure S1. Cell titer and drug dispensing volume controls 91
Figure S2. HCM image analysis depicting spheroid area change from baseline and cell death.....91
Figure S3. Radiosensitization assessment of combo low on HSJD-DIPG-007 (H3K27M) cells conducted using a metabolic activity assay 92
Figure S4. Radiosensitization assessment of combo low on SU-DIPG-17 (H3K27M) cells conducted using a metabolic activity assay 92
Figure S5. Quality check of bulk RNAseq and LC-MS/MS proteomic data 93
Figure S6. Hierarchical clustering heatmap using Z-score based on MSigDB HALLMARK MYC Targets version 1 (V1) and 2 (V2) for four H3K27M DMG cell models.....95
Figure S7. GO term analysis for biological processes displaying downregulated ontologies in H3K27M DMG and H3 WT pHGG models under atuveciclib (CDK9i) treatment.....96
Figure S8. GO term analysis for biological processes showing negatively regulated ontologies in H3K27M DMG and H3 WT pHGG models, and upregulated ontologies under BMS-986158 (BETi) treatment 97
Figure S9. GO term analysis for biological processes demonstrating downregulated ontologies in H3K27M DMG and H3 WT pHGG models under combo low treatment 97
Figure S10. Toxicity analysis of atuveciclib (CDK9i) and BMS-986158 (BETi) on zebrafish embryos ...99
Figure S11. Toxicity analysis of six different combination treatments with atuveciclib (CDK9i) and BMS-986158 (BETi) on zebrafish embryos.....100
Figure S12. Box-dot plots of zebrafish xenograft data for HSJD-DIPG-007 (H3K27M) and KNS42 (H3G34V) 101
Figure S13. Synergy screen with KB-0742 (CDK9i) and BETis using a matrix design 101

List of Appendix Figures

Appendix Figure 1. QC data of all cell models screened with epigenetic drug library 108
Appendix Figure 2. Dose response curves of non-H3K27M pHGG cell models for atuveciclib (CDK9i), mivebresib (BETi) and alisertib (AURKi).....109
Appendix Figure 3. Separate synergy plots for four H3K27M DMG models tested in synergy screens with 7-ray approach 111
Appendix Figure 4. HCM analysis of KNS42 (H3G34V) cells with the treatment conditions of SU-DIPG-17 (H3K27M) 112
Appendix Figure 5. HCM analysis of HMC3 (microglia) cells under the treatment conditions of SU-DIPG-17 (H3K27M) 113
Appendix Figure 6. HCM analysis of HSJD-DIPG-007 (H3K27M) cells under different treatments ...114
Appendix Figure 7. HCM analysis of KNS42 (H3G34V) model under the treatment conditions of HSJD-DIPG-007 (H3K27M) 115
Appendix Figure 8. HCM analysis of HMC3 (microglia) under the treatment conditions of HSJD-DIPG-007 (H3K27M) 116
Appendix Figure 9. Radiosensitization experiments conducted on SU-DIPG-19 (H3K27M).....117
Appendix Figure 10. Bioanalyzer QC check of RNA samples submitted for RNAseq 121
Appendix Figure 11. Identified and quantified proteins in LC-MS/MS 121
Appendix Figure 12. UMAP clusters of 128 proteomic samples.....125
Appendix Figure 13. Representative images of a zebrafish early larvae engrafted with HSJD-DIPG-007 (H3K27M) cells in the yolk sac.....125
Appendix Figure 14. Representative images of a zebrafish early larvae engrafted with KNS42 (H3G34V) cells in the yolk sac 126

1 Introduction

1.1 Pediatric high-grade glioma

Annually, around 420,000 children aged 0-14 are diagnosed with cancer globally[1]. Over the past decades, there has been an increase in the childhood cancer incidence, with the highest rates observed in high-income countries, likely due to improved diagnostic methods, changes in how childhood cancers are classified, and possible environmental and genetic influences[1,2]. While many childhood cancers have good survival rates with five-year overall survival (OS) of approximately 80% post-diagnosis, owing to the advancements in treatment, the prognosis for some, especially inoperable or recurrent cancers, is still grim[1,3]. Central nervous system (CNS) tumors in children are varied, ranging from benign to malignant[4,5], and make up 21% of all pediatric cancers[6], being second after leukemia[7,8]. CNS tumors account for the primary cause of solid tumor morbidity in this age group[7,8]. In Europe, the incidence of primary CNS tumors in children under 15 is approximately 2.99 per 100,000 annually[9]. Gliomas are the most common CNS tumors, accounting for half of these cases[10,11]. While pediatric low-grade gliomas (pLGGs) are more commonly observed[12–14], the incidence rate of pediatric high-grade gliomas (pHGGs) remains low (1.1 – 1.78 cases in 100,000 children). Despite the low prevalence, pHGGs are responsible for over 40% of cancer-related deaths in children due to their aggressive nature and treatment resistance[15]. pHGGs originate in the supratentorial cerebral cortex and spine, the majority arises in the midline structures, particularly pons, thalamus and brainstem (diffuse intrinsic pontine glioma (DIPG)), making the tumors typically inoperable[15,16].

1.1.1 World Health Organization classification of pediatric high-grade gliomas

Current treatment strategies for pHGGs are based on the studies conducted on adult HGGs (aHGGs), which employ surgical resection when possible with subsequent radiation therapy and chemotherapy[17]. However, large-scale genomic sequencing analyses have debated initial assumptions about the biological resemblance between pediatric and adult HGGs, uncovering notable molecular differences within these malignancies[18,19]. As a matter of fact, pHGGs were separated from aHGGs in the 2021 World Health Organization (WHO) Classification of Tumors of the CNS (WHO CNS 5)[20] acknowledging their biological disparities. One of the prominent distinctions between pediatric and adult HGGs lies in the elevated occurrence of mutations in genes, proteins of which are associated with chromatin regulation in pediatric tumors. In particular, point mutations in the gene encoding histone-H3 (will hereafter be denoted as H3) proteins have been officially renowned as diagnostic subcategories within pHGGs[7]. According to WHO CNS 5, the pHGG comprises four types that feature diffuse growth[20]:

- Diffuse midline glioma (DMG), H3 lysine 27-altered (H3K27-altered)
- Diffuse hemispheric glioma (DHG), H3 glycine 34-mutant (H3G34-mutant)
- Diffuse pediatric-type HGG, H3-wild-type (H3 WT) and isocitrate dehydrogenase-wild-type (IDH WT)
- Infant-type hemispheric glioma

Approximately 85% of DMGs harbor a point mutation leading to amino acid change from lysine (K) to methionine (M) at position 27 of H3 amino (N) terminal tail (referred as H3K27M herein unless specified for different H3 proteins), which arise in midline structures of the brain and spine. The H3K27M DMGs are predominantly observed in children aged five to 10 years with median OS of 11 months, representing the most aggressive tumor type among all pHGGs[21]. The question of whether the onset

of H3K27M DMGs occurs during embryonic development or in early childhood continues to be a subject of discussion. Current research results indicate that oligodendroglial progenitor-like cells (OPCs) may be the origin cells for these tumors[22,23]. Moreover, the identification of OPC-related super-enhancers, found in the promoters of e.g. sex-determining region Y (SRY)-box 8 (*SOX8*) and SRY-box 10 (*SOX10*) in H3K27M DMGs underscores the OPC lineage of these tumors[24].

1.1.2 Histone H3

The genetic information of the eukaryotic cells is contained in the deoxyribonucleic acid (DNA) for over one meter length that is packed in the nucleus, which is approximately $2x10^5$ times smaller in length[25]. The histones are the proteins which condense DNA into a smaller volume to form a chromatin complex in the nucleus. Sections of DNA wrap around histone octamers to form nucleosomes, which are the repeating functional unit of chromatin[26,27]. A histone octamer consists of four core histone dimers: H2A, H2B, H3 and H4, which wrap around 146 base pairs (bp) of DNA. The linker histone H1 further stabilizes the global chromatin structure by associating with the nucleosomes[28].

The predominant composition of nucleosomes includes canonical histones, notably histone H3.1/H3.2, which are encoded by 13 genes within the human genome. The synthesis of these histones are restricted to the S-phase of the cell cycle and are swiftly congregated near the site of DNA replication[29]. Conversely, the histone variant H3.3 is characterized by its replication-independent expression[30], indicating that it is expressed across all stages of the cell cycle and is substituted for canonical histones that are dislodged from their positions outside the S-phase[31].

Two genes, *H3F3A* and *H3F3B*, encode histone H3.3 in the human genome. It exhibits alterations from the canonical H3.1/H3.2 at residues 31, 87, 89, and 90, along with an additional variation at position 96 when compared to H3.1. The distinct sequence at positions 87, 89, and 90 is crucial for facilitating interactions with chaperone assembly complexes[32]. This unique combination of replication-independent production and specialized chaperones grants H3.3 a specific pattern of genome localization and function that sets it apart from the canonical H3.1/H3.2. Whereas H3.1/H3.2 histones, which are associated with DNA replication, are evenly dispersed throughout the genome following DNA polymerase activity. H3.3 predominantly marks the promoters of actively transcribing genes, stepping in to replace histones dislodged by RNA polymerase activity[31,33]. Furthermore, H3.3 is linked to distinctive chromatin contexts, including telomeres[32,34], endogenous retrovirus repeats[35] and the V_H locus involved in V(D)J recombination[36]. Consequently, H3.3 is implicated in a variety of roles involving embryonic development, the maintenance of stem cell conditions, and the activation of differentiation programs[37]. The precise reasons for the critical role of H3.3 in either maintaining or modifying chromatin states remain elusive, yet it is clear that it is functionally divergent from the canonical H3.1/H3.2 despite its close sequence similarity[18].

1.1.2.1 H3 mutations in pediatric high-grade gliomas

The revelation of oncogenic mutations in H3.3 has notably distinguished the critical role of H3.3 further. It has been identified that heterozygous substitution mutations, leading to K27M and G34R/V, found solely in *H3F3A* of H3.3, along with a less common substitution in *HIST1H3B* or *HIST1H3C* of

H3.1, and *HIST2H3C* of H3.2 leading to K27M [38,39]. Over the last decade, research has shown that gliomas with the mutation resulting in H3K27M are clinically and molecularly distinct from H3K27 WT and H3G34R/V gliomas. Moreover, the H3 mutation status is associated with differences in gene and protein expression profiles and DNA methylation patterns, along with distinct epigenetic features and three dimensional (3D) chromatin structures[40].

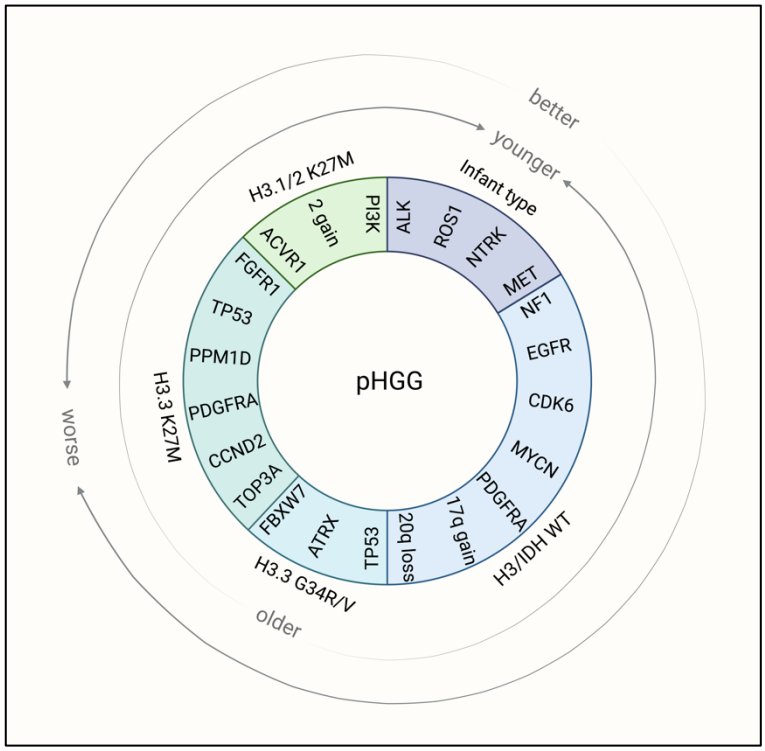

Figure 1. Co-alterations, age distribution and survival time observed for pHGGs. Adapted from Mackay et al. 2017[15].

1.1.2.1.1 H3K27M diffuse midline glioma

H3K27M mutation was documented for DMGs for the first time in 2012 through two studies[38,41]. This somatic missense mutation causes a lysine (Lys, K) to methionine (Met, M) replacement at the 27th position on the N-terminal tail of H3. The H3K27 site is pivotal for the regulation of the cellular epigenome, typically undergoing acetylation (ac) or trimethylation (me3), which are linked to transcriptional activation and silencing, respectively.

The mechanism of action (MoA) of H3K27M is unclear. Despite representing only a minor proportion of the total H3 pool (3–17%), H3K27M exerts a dominant effect by significantly diminishing the overall levels of the repressive H3K27me3 mark within cells. Several studies demonstrated that the mutant H3K27M histone acts by blocking the function of polycomb repressive complex 2 (PRC2), a multiprotein complex that is responsible for adding trimethyl groups to the H3K27 sites via its catalytic subunit enhancer of zeste 2 (EZH2)[42–46]. Sequestration of PRC2 by H3K27M oncohistones leads to a global reduction of H3K27me3 throughout epigenome[42–46]. Besides, it was demonstrated that the residual PRC2 activity is still detected *in vitro*[47–49] and increased H3K27me3 was observed at loci of tumor suppressor genes, suppression of which is essential for DMG proliferation and survival[50]. However, *in vivo* PRC2 inhibition remains to be elusive[47]. Moreover, H3K27M DMGs harbor elevated levels of H3K27ac, a transcriptional activating mark, in addition to global loss of H3K27me3[51]. The enrichment of the genome with H3K27ac enhances chromatin accessibility to transcriptional machinery, involving ribonucleic acid (RNA) polymerase II (RNAPII), through the creation of H3K27M-K27ac heterotypic nucleosomes. These structures recruit histone acetyl group reader proteins, specifically bromodomain-containing proteins 2 and 4 (BRD2/4)[43,47,52]. Furthermore, H3K27M and BRD2/4 tend to co-localize within super-enhancer and promoter regions, enabling transcription[47]. An example of a promoter activated by H3K27M is AFF4 (transcription factor II A alpha/beta-like factor (ALF) transcription elongation factor 4), a core component of the super-en-

hancer complex (SEC), which engages cyclin-dependent kinase 9 (CDK9) to facilitate the phosphorylation of RNAPII[53]. This action rescues RNAPII from its initial pausing at promoter-proximal sites, thereby enhancing the transcription of various oncogenes, including myelocytomatosis oncogene (*MYC*) and myeloid cell leukemia-1 (*MCL-1*)[54].

DMGs with H3.3K27M are uniquely different from H3.1/H3.2K27M, linked with distinct secondary mutations, variations in age distribution and survival time, as well as differences in gene expression patterns[15] as depicted in **Figure 1**. In several studies involving systematic review and meta-analysis, it was revealed that the mutation H3.3K27M appears in more than 70% of DMG cases in children six to nine years of age, resulting in median OS of 11 months[15,55–57,58]. Mutations in H3.1/H3.2 are linked to the earlier development of gliomas. In contrast to H3.3 mutations, which are specific to gliomas, mutations in H3.1 have been detected in acute myeloid leukemia (AML) and melanomas, too. This variance implies that the H3.1/H3.2 and H3.3 oncohistones differ in their tumorigenic potential[15,59–61]. H3.1/H3.2 K27M DMGs are linked to a comparatively longer OS with median of 15 months and exhibit a decreased likelihood of metastatic dissemination[15,55–57,58]. Mutations in the *TP53* and platelet derived growth factor alpha (*PDGFRA*) gene amplifications are more frequently found in DMGs with the H3.3K27M mutation. These aberrations facilitate tumor growth and advancement by impairing the function of the p53 protein[62]. Conversely, DMGs with the H3.1K27M often segregate with mutations in the activin captor type-1 (*ACVR1*) gene, which are linked to increased activity of the bone morphogenic protein (BMP) signaling pathway, contributing to tumor proliferation[63]. Moreover, H3.1K27M is commonly associated with alterations in phosphatidylinositol 3-kinase (PI3K)-signaling pathway associated genes[64,65]. The genome-wide distribution of these H3 mutations varies, with H3.3K27M found in nucleosomes at active chromatin sites and gene bodies, whereas H3.1K27M is more uniformly distributed across the genome, mirroring the patterns of their WT counterparts[66]. These differences extend to the profiles of active enhancers and promoters, affecting treatment responses. Tumors with H3.3K27M show enhancer activity linked to noncanonical wingless/integrated (WNT) signaling and cytoskeletal remodeling genes, while H3.1K27M tumors have enhancers influencing PI3K and p38 mitogen activated protein kinase (MAPK) signaling pathways. These variations suggest distinct impacts on PRC2 complex targets by the two histone variants. Additionally, the DNA methylation profiles of cells expressing H3.1K27M and H3.3K27M histone variants also show notable differences, further distinguishing these two forms of histone mutations[39,64,66,67].

1.1.2.1.2 H3G34R/V diffuse hemispheric glioma

Mutations affecting H3G34, leading to diffuse hemispheric gliomas (DHGs), specifically target the H3.3 histone variant of the *H3F3A* gene, with a predominance of glycine to arginine (G34R, ~95%) over glycine to valine (G34V, ~5%) replacements, which are mutually exclusive with the H3K27M variant[15]. Although H3G34 itself is not subject to post-translational modifications (PTMs) that regulate the epigenome, such as methylation, it is located near K36, trimethylation of which (H3K36me3) is indicative of transcriptionally active chromatin[68]. A cohesive model that explains the fundamental abnormalities and subsequent impacts of the H3G34 variant remains elusive. Present findings indicate that G34 mutations might simultaneously influence various chromatin-related pathways. The exclusive occurrence of G34 substitutions on histone H3.3 suggests that the oncogenic process is specific for this histone variant[69]. DHGs with H3G34R/V often harbor *ATRX/DAXX* and *TP53* mutations[38] and observed in children with a median age of 15 years and median OS of 18 months[15,70].

1.1.3 Current treatment strategies for H3K27M diffuse midline glioma

Traditionally, DMGs were identified solely through radiographic means, as their distinct magnetic resonance imaging (MRI) characteristics and the comparative risks associated with surgical biopsies for histological examination were well recognized[71]. This approach resulted in a limited availability of tumor samples for molecular investigation, hindering advancements in comprehending the pathology of the disease and in the development of effective treatments. Consequently, DMGs remain the leading cause of cancer associated death in children with almost all patients succumb within two years post-diagnosis[56,72]. The conventional treatment for pHGGs involves surgical removal of the tumor and radiation therapy (RT). However, the inherent location and invasive characteristics of H3K27M DMGs frequently render complete removal unachievable[40,69]. To date, chemotherapy has not shown effectiveness against pHGGs. Although temozolomide is used as an adjuvant therapy with radiation in some centers, it is not effective in treating DMGs harboring the H3K27M mutation. The resistance against temozolomide is partly explained by elevated level of O6-methylguanine DNA methyltransferase (MGMT) in H3K27M DMGs [73–75]. Hence, the radiation therapy treatment remains to be the standard of care temporarily alleviating the symptoms for two to four months but does not extend patient survival[40,69]. Besides the general challenges of efficacy, selectivity, and tolerable side effects, successful medications must also have the ability to penetrate the blood-brain barrier (BBB), which consists of endothelial cells, basement membranes and capillaries impeding most anticancer drugs from entering the brain[76–78]. Various potential therapeutic agents are under investigation, but definitive frontrunners are still to be established[69]. Understanding the mutations and underlying molecular dynamics helps optimizing targeted therapeutic interventions. Recent progress in neurosurgical methods, particularly the adoption of image-guided stereotactic biopsy, has improved the acquisition of tumor samples for molecular studies. Current techniques enable biopsy of thalamic and brainstem lesions with a risk of transient neurological deficits under 5%, and less than a 1% chance of permanent impairment[42,79]. Successful biopsy acquisition facilitates exploration of targeted therapies against H3K27M, several of which have been translated into clinical trials (**Table 1**). Trials are ongoing to test the inhibition of EZH2 with tazemetostat and the polycomb ring finger protein B cell specific Moloney murine leukemia virus integration site 1 (BMI1) with PTC596 inhibitor. Both of the strategies posed limited efficacy by introducing DNA damage[80]. Various drugs that impact chromatin, modify epigenetic markers, or cause DNA damage are commonly incorporated into chemotherapy regimens for diverse cancer types. However, their efficacy as standalone treatments for pHGGs has not been established[84]. Consequently, current research mainly focuses on evaluating these treatments in combination with other therapeutic agents. Among the most frequently utilized drugs in this category are histone deacetylase inhibitors (HDACis), such as panobinostat, a nanoparticle formulation MTX110, fimepinostat, and vorinostat[84]. Agents targeting the genome involve nucleoside analogs such as gemcitabine, topoisomerase inhibitors such as etoposide, irinotecan, and topotecan, and alkylating agents such as temozolomide, lomustine, and carboplatin[84]. Furthermore, there is ongoing research into the use of poly ADP-ribose polymerase (PARP) inhibitors, which are believed to enhance the effects of DNA alkylation by interrupting the break-excision repair pathway, several of which are currently under clinical investigation[69,80].

Table 1. Ongoing clinical trials for pHGG. Adapted from Damodharan et al., 2022[80].

Clinical Trial (NCT Number)	Compound Investigated
NCT02717455, NCT04341311	Panobinostat (HDAC inhibitor)
NCT03566199, NCT04264143	MTX110 (HDAC inhibitor nanoparticle formulation)
NCT02909777, NCT03893487	Fimepinostat (HDAC inhibitor)
NCT02420613, NCT01189266	Vorinostat (HDAC inhibitor)
NCT02992015	Gemcitabine (Nucleoside analog)
NCT04049669	Etoposide (Topoisomerase inhibitor)
NCT01837862	Irinotecan (Topoisomerase inhibitor)
NCT03709680	Topotecan, Temozolomide (Topoisomerase inhibitor, alkylating agent)
NCT03243461	Temozolomide (Alkylating agent)
NCT04049669	Lomustine (Alkylating agent)
NCT01837862	Carboplatin (Alkylating agent)
NCT04749641	Neoantigen peptide (Peptide vaccine)
NCT02960230	Peptide vaccine combined with nivolumab (PD-1 inhibitor)
NCT03155620	Tazemetostat (EZH2 inhibitor)
NCT03605550	PTC596 (BMI1 inhibitor)

Overall, while radiotherapy remains the primary treatment for H3K27M DMGs, the distinct molecular characteristics of these tumors, such as reduction of H3K27me3, elevation of H3K27ac, alterations in chromatin and aberrant transcription, present opportunities for innovative epigenetic and transcriptional interventions[15,38,69].

1.2 Cyclin-dependent kinases

Cyclin-dependent kinases (CDKs) are serine/threonine kinases that play essential roles in conjunction with their cyclin partners in various cellular processes, particularly in cell division and transcription, with their malfunctions often linked to cancer development. The human genome contains 20 CDKs, numbered from 1 to 20, which are part of the CDK and CDK-like branch within the CMGC subfamily of human kinases (cyclin-dependent, mitogen-activated, glycogen synthase, and CDC-like kinases). CDKs feature a two-lobed structure where the active site is placed between an N-terminal lobe, predominantly formed of β-sheets, and a C-terminal lobe composed of α-helices. The activity of CDKs is modulated through the binding of cyclin subunits and by the phosphorylation of conserved residues within the T-loop and glycine-rich loop structures of the CDK[81]. CDKs can be categorized into two principal groups, according to their evolutionary lineage and primary functional roles: those involved in cell cycle regulation, involving CDKs 1-7, 14-18 and those involved in transcription regulation, encompassing CDKs 7-13, 18-20[82]. While the contribution of cell cycle CDKs to cancer is well recognized, the significance of transcriptional CDKs, such as CDK9, has gained acknowledgment more recently. Many cancers depend on transcriptional CDKs to continuously produce short-lived gene products essential

for their survival. Consequently, the dysregulation of the CDK9 pathway is noted in a range of hematological and solid tumors, positioning it as a promising target for cancer therapy. The exploration of CDK9 inhibitors has advanced, with some candidates progressing to human clinical trials[83].

1.2.1 CDK9 and P-TEFb

The CDK9 gene produces two isoforms, the short CDK9-S (42-kDa) and the long CDK9-L (55-kDa), transcribed from two distinct promoters over 500-bp apart. CDK9-L contains an extra 117 amino acids at the N-terminus. In cells, the short isoform is more prevalent. CDK9-S is primarily distributed throughout the nucleoplasm and to a lesser extent in the cytoplasm, whereas CDK9-L is mainly found in the nucleolus[84]. CDK9-L is associated with apoptosis and DNA repair regulation, while CDK9-S is extensively studied for its role in global transcriptional control. However, these insights are based on studies using ectopically expressed epitope-tagged constructs, leaving the normal subcellular localization, expression patterns across different cell types and tissues, and the exact functions, particularly of the long isoform, less understood[85,86].

In their enzymatically active form, CDKs pair up with cyclin proteins to create heterodimers[87]. CDK9 follows this pattern by forming a heterodimer with either Cyclin T1 or Cyclin T2, collectively referred to as CycT, to establish the positive transcription elongation factor complex (P-TEFb)[88,89]. Beyond regulating kinase activity, CycT is believed to be essential for the assembly of CDK9 with its substrates at active transcription sites within the nucleus[90,91]. Notably, the CDK9-CycT complex is crucial for the localization of both CDK9 and RNAPII to centers of active transcription[90,92]. The precise control of CDK9 kinase activity is crucial for cells to maintain transcriptional balance. One deactivating mechanism involves the integration of CDK9 into the 7SK small nuclear ribonucleoprotein (snRNP) complex[93,94]. Within this complex, two CycT/CDK9 molecules engage with hexamethylene bis-acetamide-inducible protein 1/2 (HEXIM) in a manner dependent on 7SK RNA, facilitating the formation of dimers that act as a scaffold for snRNP organization[95]. Besides the interaction of CycT/CDK9 with HEXIM, the la-related protein 7 (LARP7) and the 7SK snRNA methylphosphate capping enzyme (MePCE) are also stabilizing 7SK RNA and the overall structural integrity of the snRNP complex[96,97]. The detailed molecular process by which P-TEFb is released from the 7SK snRNP complex under various cellular or stress stimuli is still under investigation. This release might be associated with post-translational modifications of 7SK snRNP components or their direct engagement with specific regulators, such as bromodomain-containing protein 4 (BRD4). Various modifications targeting HEXIM1, CDK9, and CycT facilitate the P-TEFb release[83,98].

1.2.1.1 Transcription elongation and termination control by P-TEFb

Cell growth and development are critically dependent on the accurate regulation of gene expression. This process is centered around the interactions of various cellular proteins with the C-terminal domain (CTD) of RNAPII, which contains tandem heptapeptide repeats (52 in mammals) with the consensus sequence Tyrosine-Serine-Proline-Threonine-Serine-Proline-Serine (YSPTSPS)[99,100]. These interactions are crucial for directing RNAPII to transcription sites, initiating and elongating transcription, and linking the transcription of messenger RNA (mRNA) with its processing, which involves capping, splicing, and polyadenylation (polyA)[100,101].

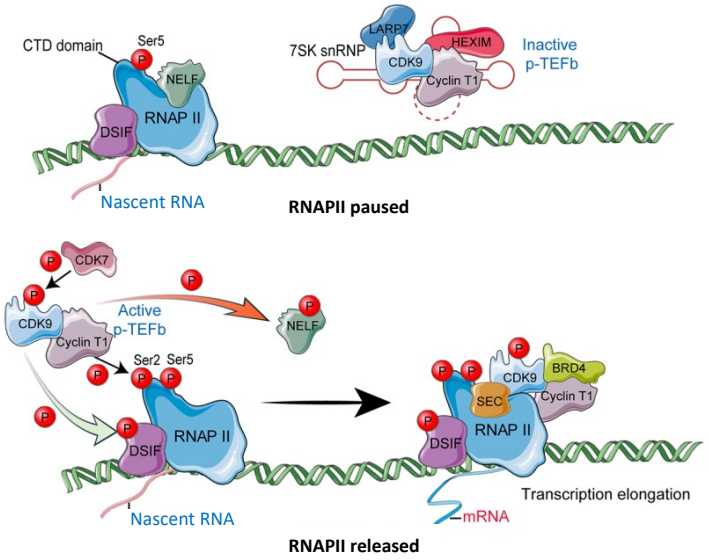

Figure 2. The role of CDK9 on transcription elongation and termination. Adapted from Bacon and D'Orso et al., 2019[92].

Previously, the regulation of transcription was thought to be primarily at the initiation stage, with less focus on the elongation phase. However, this perception has changed, recognizing elongation as a tightly regulated step[100]. Shortly after starting transcription and producing 20-50 nucleotides of RNA, the elongation process by RNAPII is hampered[102] often at the promoter-proximal regions of many genes[103]. The pausing of RNAPII has multiple functions[104]: enhancing gene accessibility[105], enabling synchronized gene activation[106], utilizing various regulatory signals[107], and serving as a checkpoint to coordinate elongation with the 5' end-capping of the nascent RNA strand[108]. The DRB sensitivity-inducing factor (DSIF) and the negative elongation factor (NELF) are key players in this pausing process[109,110].

For RNAPII to proceed with transcription elongation past the pause, it requires the kinase activity of P-TEFb, mediated by CDK9[111]. When P-TEFb is recruited to the stalled RNAPII by BRD4, it phosphorylates certain components of the NELF and DSIF complexes. These phosphorylations cause the release of NELF from RNAPII and transform DSIF into a positive elongation factor, accompanying RNAPII as it elongates[112] (**Figure 2**). Additionally, P-TEFb phosphorylates the CTD of RNAPII, mainly at the S2 residue[113], which is essential for re-activating RNAPII and connecting the elongation of transcription with the processing of pre-mRNA[114]. The phosphorylated CTD attracts various factors involved in chromatin modification, elongation, co-transcriptional splicing, and pre-mRNA 3' end processing[115,116]. Besides CDK9, other kinases such as CDK12, CDK13, and BRD4 (atypically) can also phosphorylate the S2 residue on the CTD. However, the specific effects of this phosphorylation by CDK12 and CDK13 are not yet fully elucidated[117,118].

Furthermore, P-TEFb is integral not just in progressing from pausing to elongation but also in ending transcription. A crucial elongation checkpoint dependent on P-TEFb has been identified near the terminal polyA sites, similar to the pausing at promoter-proximal sites. RNAPII, after passing the initial pause, can elongate the transcript but often terminates prematurely at polyA sites, a process linked to P-TEFb, DSIF, and specific polyA factors like SSU72 homolog, RNA polymerase II CTD phosphatase (Ssu72) and cleavage stimulation factor subunit 64 (CstF64) dissociating from RNAPII[119]. Beyond the polyA site, the role of CDK9 in transcription termination involves phosphorylation of Xrn2, a 5'-3' exoribonuclease, at Thr439, which facilitates the RNA transcript cleavage from RNAPII[120]. CDK9 further modulates the transcription by phosphorylating and inhibiting the activity of protein phosphatase 1 (PP1) on DSIF and RNAPII until the complex arrives at the transcription termination sites, where PP1 is activated, leading to DSIF dephosphorylation and transcription termination[121] (**Figure 2**).

1.2.1.2 P-TEFb role in cell cycle

The progression through the cell cycle is strictly controlled by the expression of specific cyclins (such as D, E, A, B), which influence the kinase functions of their respective CDKs in the cell cycle[82]. CDK9 and the expression and kinase activity of its associated cyclin are not modulated in a cell cycle-dependent way, suggesting that the role of P-TEFb extends beyond transcriptional regulation[122,123]. For example, CDK9 silencing can arrest Drosophila cells in the G1 phase, with BRD4 playing a crucial role in this context by "bookmarking" key genes during mitosis to maintain gene activation post-mitosis[123,124]. BRD4 collaborates with jumonji domain containing 6 (JMJD6) from mid to late anaphase to initiate the release of the promoter-proximal pause, enabling the recruitment of P-TEFb for phosphorylation of RNAPII, NELF, and DSIF, thereby promoting the activation of G1 phase genes for the transition to the S phase[129]. Inhibiting BRD4 disrupts P-TEFb chromosomal binding and the activation of key genes, leading to cell cycle arrest and potentially apoptosis[125].

1.2.1.3 P-TEFb role in DNA repair

The CDK9-CycT complex has a well-defined biological function, whereas the role of CDK9-cyclin K (CDK9-CycK) is less understood although it is known that the RNAPII CTD can be phosphorylated *in vitro* by CDK9-CycK[126] and this complex can initiate transcription only when attached to RNA but not to DNA[127]. Its specific function began to clarify when CycK was identified as a transcriptional target of p53 following DNA damage[128]. The suppression of CDK9 and CycK has been observed to disrupt the cell cycle under replication stress and DNA damage conditions. A similar association could not be identified for CycT. Hence, CDK9-CycK might directly contribute to DNA repair by engaging with elements of the ATR pathway, which is essential for DNA damage response (DDR)[129]. Moreover, the inhibition of CDK9 causes DNA double-strand breaks (DSBs) and induction of apoptosis, highlighting its potential role in DNA repair, possibly in association with Ku70, a protein crucial for nonhomologous end-joining, indicating a unique function not shared with CycT[130].

1.2.1.4 Utilizing CDK9 inhibitors in cancer treatment

The introduction of flavopiridol as the first pan-CDK inhibitor in clinical settings encouraged efforts to identify new small molecules that inhibit CDK9 more effectively and selectively, with several advancing to clinical trials (**Table 2**) **f**or various solid and hematological cancers as first-generation CDK9 inhibitors (CDK9is)[115]. These compounds act competitively at the conserved catalytic adenosine triphosphate (ATP) binding site[131], resulting in off-target activity on multiple CDKs and/or kinases, potentially reducing their therapeutic specificity. Despite this challenge, there has been progress in formulating second-generation CDK9 inhibitors with a higher selectivity for CDK9[132]. Atuveciclib (BAY1143572), a benzyl sulfoximine compound, is recognized for its high selectivity and effectiveness as a P-TEFb/CDK9 inhibitor (CDK9i) and was tested in clinical trials (**Table 2**). This compound/drug inhibited the proliferation of diverse cancer cell lines[133], including H3K27M DMGs[134], at sub-micromolar concentrations and has shown effectiveness in reducing tumor growth in xenograft models of various cancers[135]. Its mechanism of action includes inhibiting the phosphorylation of S2 on CTD of RNAPII, decreasing the expression of *MCL-1* and *MYC*, and inducing apoptosis. An RNA interference (RNAi) library screen identified AFF4 as a crucial protein for sustaining the clonogenic capacity, self-renewal, and stemness of H3K27M DMG tumors[134]. *AFF4* knockdown through short hairpin RNA (shRNA) upregulated the expression of prodifferentiation genes and diminished DMG self-renewal. Following this, the same study utilized

CDK9is, atuveciclib and AZD4573, which disrupt SEC by impairing RNAPII release from promoter-proximal pausing. Similar to *AFF4* reduction, CDK9 inhibition released the expression of prodifferentiation genes and decreased DMG cell self-renewal. Moreover, atuveciclib and AZD4573 demonstrated therapeutic promise, slowing tumor progression and enhancing survival in DMG orthotopic xenograft mouse models[134].

Table 2. CDK9 inhibitors that have advanced to clinical trials. Adapted from Ranjan et al., 2021[136].

CDK9 inhibitor	NCT ID	Phase	Trial status	Cancer type
AT7519	NCT02503709	I	Active, not recruiting	Metastatic malignant solid neoplasms
Atuveciclib/BAY-1143572	NCT01983638	I	Completed	Advanced cancers
AZD4573	NCT03263637	I	Recruiting	Hematological malignancies
BAY-1251152	NCT02635672	I	Active, not recruiting	Advanced cancers
BTX-A51	NCT02443785	I	Recruiting	Acute myeloid leukemia, myelodysplastic syndrome
CYC065/Fadraciclib	NCT03995754	I	Recruiting	Chronic lymphocytic leukemia
Dinaciclib	NCT00871663	I/II	Completed	Non-Hodgkin lymphoma
Flavopiridol	NCT03593915	I/II	Active, not recruiting	Myelodysplastic syndromes
KB-0742	NCT04781675	I	Recruiting	Solid tumors, non-Hodgkin's lymphoma
NMS-1116354	NCT01092352	I	Terminated	Solid tumors
RGB-286638	NCT01168882	I	Withdrawn	Hematological malignancies
Riviciclib/P-276-00	NCT00824343	II	Completed	Advanced head and neck cancer
Roniciclib/BAY-1000394	NCT02656849	I/II	Withdrawn	Solid tumors
Roscovitine/Seliciclib	NCT00372073	II	Terminated	Non-small cell lung cancer
SNS-032	NCT00446342	I	Completed	B-lymphoid malignancies
TP-1287	NCT03604783	I	Recruiting	Solid tumors
Voruciclib/P-1446	NCT03547115	I	Recruiting	B-cell malignancies, AML
ZK-304709	NCT00256849	I	Withdrawn	Solid tumors
Zotiraciclib/TG02	NCT01204164	I	Recruiting	Recurrent/progressive HGG

1.3 Bromodomain and extra-terminal domain containing proteins

The bromodomain and extra-terminal domain containing (BET) proteins contains two acetyl-histone recognition domains, the bromodomain (BD) and the extra-terminal (ET) domain. The BET proteins, consisting of BRD2, BRD3, BRD4, and testis-specific BRDT, function as epigenetic readers that identify acetylated histones, and as transcription factors, through their BDs, thereby recruiting transcriptional complexes[137,138]. BRD4 is the most well-known among the BET proteins, and has three isoforms: BRD4 long isoform (BRD4L), BRD4 short isoform a (BRD4Sa), and BRD4 short isoform b (BRD4Sb), each playing unique roles in gene expression[139]. BRD4L harbors a C-terminal motif (CTM), that is exclusive to

BRD4L and absent in BRD4S, and other BET proteins. Beyond the BD1 and BD2 domains, BET proteins feature additional functional motifs, such as casein kinase 2 (CK2) phosphorylation sites, and the basic residue-enriched interaction domain (BID)[140]. BD1 and BD2 contain a four-helical bundle structure that is evolutionarily conserved and are the most thoroughly studied domains in BET proteins. BD1 and BD2 identify acetylated lysines on histones, and transcription factors, serving as acetylation signal readers in gene expression[141]. Additionally, the ET domain is pivotal for transcriptional activation, facilitating the engagement with transcriptional complex[142]. Despite having common functional domains, BET proteins exhibit unique expression patterns across different tissues[143]. Studies have shown that BRD2 and BRD3 are predominantly expressed in variety of organs, such as brain, spleen, ovaries, lung, testis, kidney, liver and pancreas. While the expression of BRDT is specific to testis and ovaries, BRD4 has a ubiquitous expression profile in the body[143,144].

1.3.1 The role of BET proteins in RNAPII release and transcriptional elongation

BET proteins play an important role in releasing RNAPII from promoter-proximal pause sites by recruiting and activating P-TEFb to continue transcription, which in turn facilitates transcriptional elongation[145]. On a mechanistic level, the engagement of BD2 of BRD4 with tri-acetylated CycT and the interaction between CycT and C-terminal P-TEFb–interacting domain (PID) of BRD4 are crucial for rescuing P-TEFb from the inactive HEXIM1-7SK snRNP complex, thereby enabling P-TEFb transcriptional activation[146]. Research has demonstrated that BRD4-CDK9 interaction is essential for the global release of RNAPII from promoter-proximal pausing, and BRD2 plays a crucial role in the widespread positioning of RNAPII at enhancer regions[147].

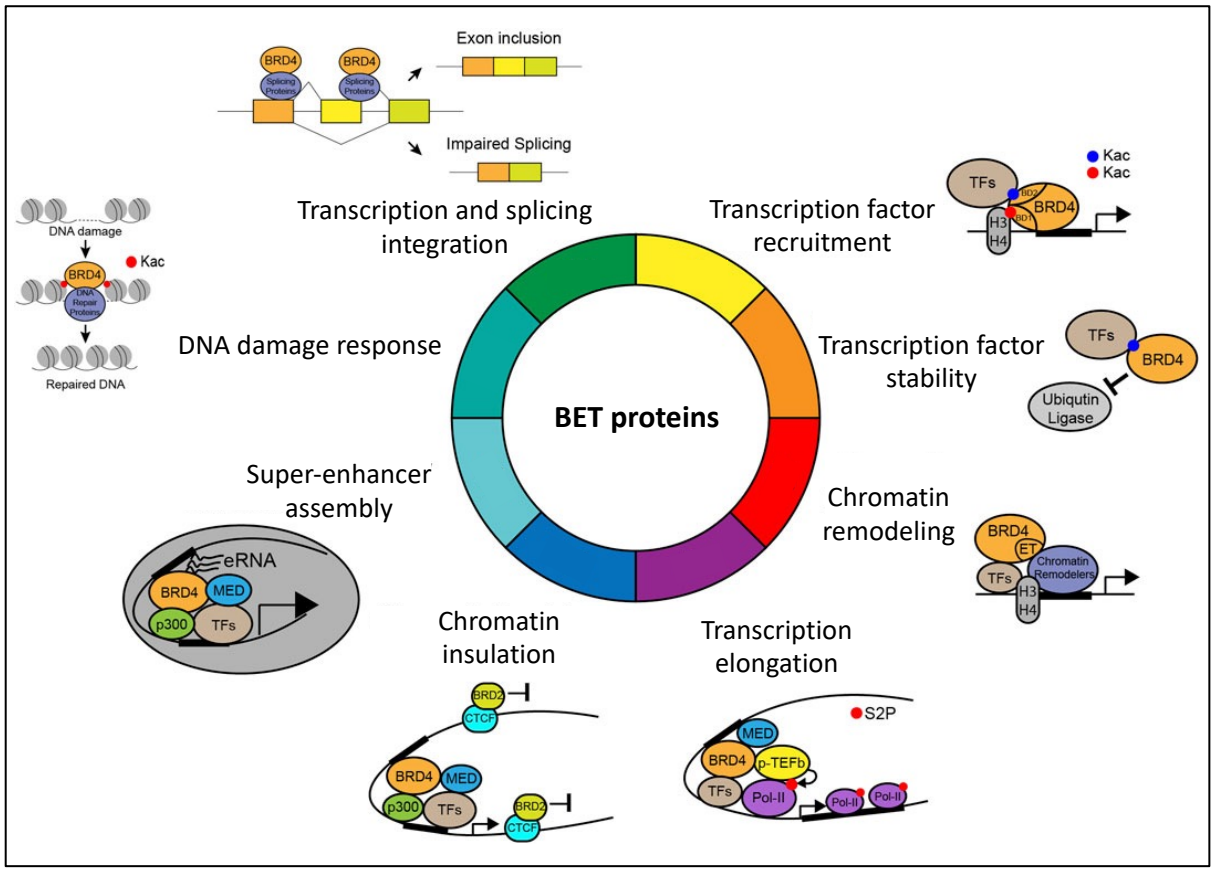

Figure 3. Overview of the various functions of BET proteins. Adapted from Cheung et al., 2021[144]. The roles of BET proteins in gene expression are multifaceted. These include: attracting transcription factors, enhancing the stability of the transcription factors, modifying chromatin structure, facilitating transcriptional elongation by phosphorylating RNAPII CTD S2, maintaining chromatin insulation, regulating SEs, participating in DDR and maintaining genomic integrity, and coordinating gene transcription and splicing.

1.3.2 Organization of chromatin structure by BET proteins

BET proteins play a key role in structuring chromatin to establish transcriptional and structural limits for gene transcription. Specifically, the CCCTC-binding factor (CTCF), which is a chromatin architectural/insulator protein engages with BRD2 (but not BRD4), and together colocalize across the genome to prevent activity from unrelated genes. This collaboration between CTCF and BRD2 sets a transcriptional boundary reliant on BRD2 function[148]. The preferential association of BRD2 with CTCF/cohesin elements underscores the distinct roles of BRD2 and BRD4, where BRD2 contributes to boundary formation along the chromatin and BRD4 is associated with enhancing transcriptional elongation[149]. Moreover, research has shown that BRD4 establishes a complex with p300/CREB-binding protein (CBP) via its BDs, augmenting histone acetyltransferase (HAT) activity of p300/CBP. In line with this, it was indicated that genomic regions containing both BRD4 and p300/CBP have increased H3K27ac and H3K56ac, which in turn influences BRG1 (SMARCA4) association with chromatin and subsequently alters chromatin structure[150].

1.3.3 The impact of BET proteins on super enhancers

Super enhancers (SEs) are identified as the large clusters of regulatory elements and marked by a significant H3K27ac buildup at the sites of crucial oncogenes in various cancers. These sites are bound and stimulated by BRD4, which results in pronounced overexpression of oncogenes, fostering malignancy, enhancing cancer cell growth, and contributing to the onset and advancement of tumors[151]. In line with this, BET inhibitors (BETis) disrupt the interaction of BDs with acetylated residues and are considered a potential therapeutic approach. These inhibitors are able to reduce BRD4 occupancy at SEs, thereby inhibiting oncogene expression, such as *MYC*[152,153].

1.3.4 BET protein function on replication-transcription modulation

BRD2 and BRD4 have pivotal roles in DNA replication. They recruit topoisomerase II beta binding protein 1 (TOPBP1) interacting checkpoint and replication regulator (TICRR), a crucial protein regulating replication initiation, S/M and G2/M checkpoints, at the origins of replication in hyperacetylated chromatin regions[154]. Furthermore, BET proteins modulate replication stress response signaling contributing to genome integrity. Upon encountering replication stress, BRD4 is known to facilitate the activation of the intra-S-phase checkpoint kinase 1 (CHK1). Consequently, inhibiting BRD4 increases the sensitivity of cancer cells to agents that induce replication stress[155]. Moreover, BRD4 is essential for the coordination of transcription and replication, helping prevent transcription-replication fork collision and DNA damage in cancerous cells[156] (**Figure 3**). Accordingly, BETis results in HEXIM1- and RAD51-dependent transcription-replication clashes, thereby replication stress due to an elevated RNA synthesis[157]. Additional studies have revealed that BRD4 plays a role in suppressing R-loop formation, which is vital for maintaining genomic integrity. It was reported for a set of cancer cells that when BRD4 is inhibited, there is an accumulation of R-loops during the S-phase resulting in cell mortality

due to collisions of transcription-replication forks and DNA DSBs[156,158,159]. Together, BETis hold potential as a cancer therapy as they drive cancer cells to cell death through mechanisms like SE clearance and associated downregulation of oncogenes, stimulation of transcription-replication conflict, accumulation of R-loop and DNA damage[144].

1.3.5 BET inhibitors in cancer treatment

There are several types of BETis, including BD1- and BD2-selective, bivalent, BRD4-selective, dual BET and tyrosine kinase inhibitors, and novel bivalent BETis with short and hydrophilic linkers. BRD4-selective inhibitors specifically inhibit BRD4. These inhibitors are particularly important for their targeted action, potentially offering a more precise approach in cancer therapy by targeting BRD4 and minimizing off-target effects on other BET family members[160]. Several BETis are tested in clinical trials (**Table 3**).

Table 3. BET inhibitors that have advanced to clinical trials. Adapted from Kenneth et al., 2023[160].

BET inhibitor	NCT ID	Phase	Trial status	Cancer type
ABBV-075 (Mivebresib)	NCT02391480	I	Completed	Various, including breast, NSCLC, AML
EP31670	NCT05488548	I	Not yet recruiting	Prostate cancer, NUT carcinoma
FT-1101	NCT02543879	I/Ib	Completed	AML, myelodysplastic syndrome
GS-5829 (Albresib)	NCT02607228	Ib/II	Completed	Prostate cancer
GSK525762 (Molibresib)	NCT01943851	I/II	Completed	Hematologic malignancies
INCBO54329	NCT02431260	I/II	Terminated	Solid tumors, hematologic malignancies
RO680810	NCT01987362	I	Completed	NUT carcinoma, solid tumors
TEN-010	NCT02308761	I	Completed	AML, myelodysplastic syndrome
ZEN003694	NCT05607108	II	Recruiting	Squamous cell lung cancer
ABBV-744	NCT02391480	I	Completed	Various, including breast, NSCLC, AML
I-BET151 (GSK2820151)	NCT02630251	I	Terminated	Solid tumors
I-BET762 (Molibresib)	NCT01943851	I/II	Completed	Hematologic malignancies
OTX-015 (Birabresib)	NCT01713582	I	Completed	AML, DLBCL, ALL, MM
BMS-986158	NCT03936465	I	Active, not recruiting	Pediatric solid tumor
CC-90010	NCT03936465	I	Active, not recruiting	Pediatric solid tumor
AZD5153	NCT03205176	I	Completed	Solid tumors, lymphomas
CPI-0610	NCT02158858	II	Active, not recruiting	Myelofibrosis, thrombocytopenia
NUV-868	NCT05252390	II	Recruiting	Solid tumors (combination therapy)
PLX51107	NCT04022785	I	Completed	Myelodysplastic syndrome, AML

1.4 Functional precision oncology and drug sensitivity profiling

The global increase in cancer diagnoses highlights the urgent need for developing antitumor drugs that are efficacious, safe, and economically feasible. Achieving clinical approval for drugs from preclinical studies to advance to phase I clinical trials is critical. At present, the success rate for anticancer drugs to receive clinical approval is significantly lower than that for medications targeting other conditions[161]. Considering the substantial expenses and time required for the clinical development of anticancer drugs, there is a pressing need to establish new, more efficient preclinical frameworks for the evaluation of antitumor agents[162,163]. Precision oncology guided by genomics aims to tailor treatments for pediatric and adolescent patients based on the molecular characteristics of their tumors to enhance survival and quality of life[164]. The adoption of various sequencing technologies has facilitated the establishment of several pediatric cancer precision medicine programs globally, such as ZERO[165] in Australia, PROFYLE[166] in Canada, and iTHER[167] in the Netherlands. However, these initiatives have identified significant limitations in relying solely on genomics for therapy, especially for cancers without actionable driver mutations and suitable treatments, a common scenario in pediatric cancers often characterized by copy number variations and gene fusions[168]. To address these challenges, recent trials like INFORM[169] have started to incorporate functional *ex vivo* drug sensitivity profiling (DSP) alongside genomic profiling to broaden therapeutic strategies for patients who do not respond to molecular analysis alone. This method, known as functional precision oncology, merges molecular profiling with direct *ex vivo* exposure of patient-derived tumor cells to clinically feasible drugs, thereby increasing treatment options for patients beyond the standard of care. Recent advancements have led to the development of *ex vivo* 3-dimensional (3D) cell culture systems employing patient-derived models, which retain many tumor features, facilitating the tailored exploration of tumor vulnerabilities[170,171]. These models effectively mimic the genomic characteristics of the original tumor, drug accessibility and the aspects of the tumor microenvironment (TME) to different degrees, emerging as a potent method for evaluating drug sensitivity[170,171]. *Ex vivo* tumor models offer a thorough screening for potential antitumor drugs, filtering out those drugs with inadequate antitumor effects before they are given to the patient. This approach facilitates a personalized treatment strategy that extends beyond merely targeting specific mutations and proves beneficial even in scenarios where no actionable targets are identified[172].

2 Aim

Pediatric H3K27M diffuse midline glioma (DMG) is an epigenetically driven cancer that currently lacks effective treatment options. Thus, the primary objective of this project was to develop a targeted combination therapy for this tumor type, which can be translated into clinical trials.

To achieve this, the first goal was to create an epigenetic drug library targeting all epigenetic components, and screen it with a panel of cell models that included pediatric high-grade gliomas (pHGG) with different H3 variants and non-cancerous cell lines. This screening was intended to identify epigenetic hit compounds that specifically target H3K27M DMGs.

As monotherapies often lead to resistance in tumors, the second goal was to find a suitable combination partner through combination screens with epigenetic hits and a library enriched for approved anti-cancer drugs. Additionally, it was aimed to identify the additive or synergistic interactions between the combination partners for the H3K27M DMG models with synergy screens.

The third goal of this project was to comprehensively evaluate specificity and effectivity of the discovered combination therapy against H3K27M DMG models *in vitro* and *in vivo* using zebrafish embryo xenograft models.

Radiotherapy (RT) is the standard of care for pediatric patients with H3K27M DMG. Therefore, the fourth goal was to evaluate the impact of the identified combination therapy in conjunction with RT, to exclude antagonizing interactions.

Finally, it was sought to unveil the underlying biological mechanism of how the drug combination synergizes on H3K27M DMGs. Thus, the fifth goal was to explore why tumors with this specific mutation responded better to the combination therapy compared to pHGGs without H3K27M mutation by performing multi-omics analysis.

3 Materials & Methods

3.1 Materials

3.1.1 Cell models and cell culture

Table 4. Cell models.

Cell model	Tumor diagnosis	Tumor location	Lab of origin	Molecular alterations	Treatment before model establishment
HSJD-DIPG-007[173] (RRID:CVCL_VU70)	DMG/DIPG	Pons	Carcaboso, Barcelona, Spain	H3.3K27M, *PPM1D* mut., *ACVR1* mut., *PIK3CA* mut., *MYC* amp.	Irinotecan, cisplatin
SU-DIPG-17[174] (RRID:CVCL_C1MW)	DMG/DIPG	Pons	Monje, Stanford, USA	H3.3K27M, *TP53* mut., *MYC* amp.	RT + avastin; panobinostat; everolimus
SU-DIPG-19[175] (RRID:CVCL_C1MV)	DMG/DIPG	Pons	Monje, Stanford, USA	H3.3K27M, *PTEN* del.	RT + chemotherapy
SU-DIPG-25[176] (RRID:CVCL_C1N0)	DMG/DIPG	Pons	Monje, Stanford, USA	H3.3K27M, *PPM1D* trunc., *PIK3CA* mut., *NF1* mut., *MYC* amp.	RT
SU-DIPG-13[177] RRID:CVCL_IT41)	DMG/DIPG	Pons	Monje, Stanford, USA	H3.3K27M, *TP53* mut., *MYCN* amp., *ATR* trunc., *KDM6B* trunc.	RT
SU-DIPG-4[174] (RRID:CVCL_IT39)	DMG/DIPG	Pons	Monje, Stanford, USA	H3.1K27M *ACVR1* mut., *PIK3CA* mut., *MDM4* amp., *BCOR* mut.	RT+ cetuximab/irinotecan
SU-DIPG-21[175] (RRID:CVCL_C1MX)	DMG/DIPG	Pons	Monje, Stanford, USA	H3.1K27M, *ACVR1* mut., *ATM* mut., *MCL1* mut., *BCOR* trunc.	RT + MK1775
SU-pSCG1[176] (RRID:CVCL_C1N9)	DMG/DIPG	Spinal cord	Monje, Stanford, USA	H3K27M, *TP53* mut.	RT; thioguanine; procarbazine; CCNU; vincristine
SJ-DIPGX9[178]	DMG/DIPG	Pons	Baker, St. Jude, USA	H3.1K27M, *ACVR1* mut., *PIK3CA* mut.	NA
KNS42[179] (RRID:CVCL_0378)	DHG	Frontoparietal lobe	Kyushu Neurosurgery, Japan	H3G34V, *TP53* mut., *PIK3CA* gain, *TERT* promoter mut.	NA
BT278	DHG	Supratentorial	INFORM, DKFZ/KiTZ, Germany	H3G34R	NA

INF_R_1073_relapse1	HGG	Cerebellum	INFORM, DKFZ/KiTZ, Germany	H3WT, *ATRX* mut., *PDGFRA* gain, *OLIG2* mut.	NA
SJ-G2[180] (RRID:CVCL_M141)	HGG	Cortical	Houghton, St. Jude, USA	H3WT, *TP53* mut., *CDKN2A/B* del., *ATRX* indel., *MYC/MYCN* amp., *CLIP2:MET*	Chemotherapy
SU-pcGBM2[181] (RRID:CVCL_IT42)	HGG	Cortex (frontal lobe)	Monje, Stanford, USA	H3WT, *TP53* mut., *MYC/MYCN* amp., *EGFR* amp., *PDGFRA* amp., *NF1* trunc.	
VH7/human juvenile fibroblasts[182]	Non-malignant	Forskin	P. Boukamp, DKFZ, Germany	NA	NA
Human fetal astrocytes (HA-1800)	Non-malignant	Brain	K. Maass, DKFZ, Germany	NA	NA
HMC3 (microglia)[183] (RRID:CVCL_II76)	SV40-TAg immortalized	Brain	ATCC (cat. No. CRL-3304)	NA	NA

Table 5. Cell culture solutions.

Solution	Catalog No.	Supplier
0.05% Trypsin-EDTA	25300054	Gibco, ThermoFisher Scientific Inc. Braunschweig, Germany
Accumax	00-4666-56	Gibco, ThermoFisher Scientific Inc. Braunschweig, Germany
B-27 supplement without vitamin A (50X)	12587-010	Gibco, ThermoFisher Scientific Inc. Braunschweig, Germany
Dulbecco's Modified Eagle's Medium (DMEM)	41965-062	Gibco, ThermoFisher Scientific Inc. Braunschweig, Germany
DMEM/F-12	11320074	Gibco, ThermoFisher Scientific Inc. Braunschweig, Germany
Dulbecco's phosphate buffered saline (DPBS)	D8537	Sigma-Aldrich, Munich, Germany
Fetal calf serum (FCS)	F7524	Sigma-Aldrich, Munich, Germany
H-PDGF-AA (10 µg/ml)	100-13A	PromoCell, Heidelberg, Germany
Heparin solution (0.2%)	H3149-10KU	Sigma-Aldrich, Munich, Germany

HEPES buffer (1 M)	15630049	Gibco, ThermoFisher Scientific Inc. Braunschweig, Germany
L-Glutamine (200 mM)	G7513	Merck, Darmstadt, Germany
MEM	31095029	ThermoFisher Scientific Inc. Braunschweig, Germany
MEM non-essential amino acids (NEAA) (100X)	11140035	Gibco, ThermoFisher Scientific Inc. Braunschweig, Germany
N-2 supplement (100X)	17502048	Gibco, ThermoFisher Scientific Inc. Braunschweig, Germany
Neurobasal A	10888-022	Gibco, ThermoFisher Scientific Inc. Braunschweig, Germany
Penicillin-streptomycin solution (P/S) (100X)	P4333	Sigma-Aldrich, Munich, Germany
Phenol red-free RPMI 1640	11835-030	Gibco, ThermoFisher Scientific Inc. Braunschweig, Germany
Recombinant human EGF (20 µg/ml)	AF-100-15B	PromoCell, Heidelberg, Germany
Recombinant human FGF basic (20 µg/ml)	AF-100-18B	PromoCell, Heidelberg, Germany
RPMI-1640	21875-091	Gibco, ThermoFisher Scientific Inc. Braunschweig, Germany
Sodium pyruvate (100 mM)	11360039	Gibco, ThermoFisher Scientific Inc. Braunschweig, Germany
Synth-a-Freeze cryopreservation medium	A1254201	ThermoFisher Scientific Inc. Braunschweig, Germany
TrypLE (1X)	12604013	Gibco, ThermoFisher Scientific Inc. Braunschweig, Germany

Table 6. Cell culture media.

Medium	Additives	Cell models	Freezing medium
TSM Base	DMEM/F-12, Neurobasal A, 1% NEAA, 1% HEPES, 1% sodium pyruvate		
TSM Complete	TSM Base, 1% B27, 1% L-glutamine, 1% P/S, 20 ng/ml EGF, 20 ng/ml FGF, 10 ng/ml PDGF, 2 µg/ml Heparin	HSJD-DIPG-007, SU-DIPG-4, SU-DIPG-13, SU-DIPG-17, SU-DIPG-19, SU-DIPG-21, SU-DIPG-25, SU-pSCG1, SU-pcGBM2, BT278, INF_R_1073_relapse1, SJ-DIPGX9	Synth-a-Freeze Cryopreservation Medium-50 mL

DMEM	10% FCS, 1% NEAA, 1% sodium pyruvate	KNS42, SJ-G2	Medium, additives, 10% DMSO
DMEM	20% FCS, 1% NEAA, 1% sodium pyruvate	VH7	Medium, additives, 10% DMSO
MEM	10% FCS, 1% NEAA, 1% sodium pyruvate	HMC3	Medium, additives, 10% DMSO
DMEM	10% FCS, 1% L-glutamine, 1% sodium pyruvate, 1% N-2 supplement	Primary human fetal Astrocytes	Medium, additives, 10% DMSO

3.1.2 Inhibitors

Table 7. Epigenetic drug library compounds. All compounds were from Selleckchem (Cologne, Germany). Compounds were screened in five different concentrations in 10-fold dilutions.

Compound	Target	Catalog No.	Stock conc.	Solvent	Conc. range (nM)
Reversine	Adenosine receptor, AURK	S7588	10 mM	DMSO	0.3-3,000
AICAR (Acadesine)	AMPK	S1802	10 mM	DMSO	3-30,000
Tozasertib (VX-680, MK-0457)	AURK	S1048	10 mM	DMSO	0.3-3,000
Alisertib (MLN8237)	AURK	S1133	10 mM	DMSO	3-30,000
Barasertib (AZD1152-HQPA)	AURK	S1147	10 mM	DMSO	0.3-3,000
TAK-901	AURK	S2718	10 mM	DMSO	3-30,000
Danusertib (PHA-739358)	AURK, BCR-ABL, c-RET, FGFR	S1107	10 mM	DMSO	3-30,000
Decitabine	DNMT	S1200	10 mM	DMSO	3-30,000
Azacitidine	DNMT	S1782	10 mM	DMSO	3-30,000
RG108	DNMT	S2821	10 mM	DMSO	3-30,000
(-)-Epigallocatechin Gallate	DNMT, HER2, telomerase, EGFR, fatty acid synthase	S2250	10 mM	DMSO	3-30,000
Procainamide HCl	DNMT, Sodium channel	S4294	10 mM	DMSO	3-30,000
GSK 5959	BET	S5916	10 mM	DMSO	3-30,000
SGC-CBP30	BET	S7256	10 mM	DMSO	3-30,000
Apabetalone (RVX-208)	BET	S7295	10 mM	DMSO	3-30,000
MS436	BET	S7305	10 mM	DMSO	3-30,000
OTX015	BET	S7360	10 mM	DMSO	3-30,000
GSK1324726A (I-BET726)	BET	S7620	10 mM	DMSO	0.3-3,000
BI-7273	BET	S8179	10 mM	DMSO	3-30,000
GSK6853	BET	S8265	10 mM	DMSO	3-30,000

Entinostat (MS-275)	HDAC	S1053	10 mM	DMSO	3-30,000
Belinostat (PXD101)	HDAC	S1085	10 mM	DMSO	3-30,000
Abexinostat (PCI-24781)	HDAC	S1090	10 mM	DMSO	3-30,000
Mocetinostat (MGCD0103)	HDAC	S1122	10 mM	DMSO	3-30,000
Pracinostat (SB939)	HDAC	S1515	10 mM	DMSO	3-30,000
PCI-34051	HDAC	S2012	10 mM	DMSO	3-30,000
Tucidinostat (Chidamide)	HDAC	S8567	10 mM	DMSO	3-30,000
TH34	HDAC	S8773	10 mM	DMSO	3-30,000
CUDC-907	HDAC, PI3K	S2759	10 mM	DMSO	0.3-3,000
BAY 87-2243	HIF	S7309	10 mM	DMSO	0.3-3,000
Daprodustat (GSK1278863)	HIF	S8171	10 mM	DMSO	3-30,000
WM-1119	HAT	S8776	10 mM	DMSO	3-30,000
Anacardic Acid	HAT	S7582	10 mM	DMSO	3-30,000
Entacapone	HMT	S3147	10 mM	DMSO	3-30,000
Tazemetostat (EPZ-6438)	HMT	S7128	2 mM	DMSO	0.6-6,000
UNC1999	EZH1/2	S7165	10 mM	DMSO	3-30,000
EPZ004777	HMT	S7353	10 mM	DMSO	0.3-3,000
BRD4770	HMT	S7591	10 mM	DMSO	3-30,000
MI-2 (Menin-MLL Inhibitor)	HMT	S7618	10 mM	DMSO	3-30,000
Tofacitinib (CP-690550,Taso-citinib)	JAK	S2789	10 mM	DMSO	3-30,000
Tranylcypromine (2-PCPA) HCl	MAO	S4246	10 mM	DMSO	3-30,000
BI-847325	MEK, AURK	S7843	10 mM	DMSO	0.3-3,000
Curcumin	NF-κB, HDAC, HAT, NRF2	S1848	10 mM	DMSO	3-30,000
Tubastatin A	HDAC	S8049	10 mM	DMSO	3-30,000
Tenovin-6	P53, Sirtuin	S4900	10 mM	DMSO	3-30,000
Olaparib (AZD2281, Ku-0059436)	PARP	S1060	10 mM	DMSO	3-30,000
Daphnetin	PKA, EGFR, PKC	S2554	10 mM	DMSO	3-30,000
Enzastaurin (LY317615)	PKC	S1055	10 mM	DMSO	3-30,000
MBQ-167	Rho	S8749	10 mM	DMSO	3-30,000
Acetyl Resvera-trol	Sirtuin	S3934	10 mM	DMSO	3-30,000
Selisistat (EX 527)	Sirtuin	S1541	10 mM	DMSO	3-30,000
CAY10602	Sirtuin	S5918	10 mM	DMSO	3-30,000
CYC116	AURK, VEGFR	S1171	10 mM	DMSO	3-30,000

Metformin HCl	Autophagy	S1950	10 mM	DMSO	3-30,000
Vorinostat (SAHA, MK0683)	Autophagy, HDAC	S1047	10 mM	DMSO	3-30,000
Atuveciclib (BAY-1143572)	CDK9	S8727	10 mM	DMSO	3-30,000
TG101209	C-RET, FLT3, JAK	S2692	10 mM	DMSO	3-30,000
dBET1	BET	S8296	10 mM	DMSO	3-30,000
INCB057643	BET	S8714	10 mM	DMSO	0.3-3,000
ABBV-744	BET	S8723	10 mM	DMSO	3-30,000
(+)-JQ1	BET	S7110	10 mM	DMSO	3-30,000
I-BET-762	BET	S7189	10 mM	DMSO	3-30,000
GSK2801	BET	S7231	10 mM	DMSO	3-30,000
Bromosporine	BET	S7233	10 mM	DMSO	3-30,000
Mivebresib (ABBV-075)	BET	S8400	10 mM	DMSO	3-30,000
EED226	BET	S8496	10 mM	DMSO	3-30,000
EBI-2511	EZH1/2	S8702	10 mM	DMSO	0.3-3,000
Pacritinib (SB1518)	FLT3, JAK	S8057	10 mM	DMSO	3-30,000
Panobinostat (LBH589)	HDAC	S1030	10 mM	DMSO	0.3-3,000
Givinostat (ITF2357)	HDAC	S2170	10 mM	DMSO	3-30,000
Resminostat	HDAC	S2693	10 mM	DMSO	3-30,000
Tacedinaline (CI994)	HDAC	S2818	10 mM	DMSO	3-30,000
Valproic acid	HDAC	S3944	1 M	Water	100-1,000,000
4SC-202	HDAC	S7555	10 mM	DMSO	3-30,000
Ricolinostat (ACY-1215)	HDAC	S8001	10 mM	DMSO	3-30,000
Citarinostat (ACY-241)	HDAC	S8464	10 mM	DMSO	3-30,000
Daminozide	HDMT	S4800	10 mM	DMSO	3-30,000
GSK J4 HCl	HDMT	S7070	10 mM	DMSO	3-30,000
GSK J1	HDMT	S7581	10 mM	DMSO	3-30,000
ORY-1001 (RG-6016) 2HCl	HDMT	S7795	10 mM	DMSO	0.3-3,000
GSK2879552 2HCl	HDMT	S7796	10 mM	DMSO	3-30,000
GSK503	HMT	S7804	10 mM	DMSO	3-30,000
Chaetocin	HMT	S8068	10 mM	DMSO	3-30,000
GSK591	HMT	S8111	10 mM	DMSO	3-30,000
CPI-1205	HMT	S8353	10 mM	DMSO	3-30,000
JQ-EZ-05 (JQEZ5)	HMT	S8607	10 mM	DMSO	3-30,000
GSK3326595 (EPZ015938)	HMT	S8664	10 mM	DMSO	3-30,000
Ruxolitinib (INCB018424)	JAK	S1378	10 mM	DMSO	3-30,000
Rucaparib (AG-014699,PF-	PARP	S1098	10 mM	DMSO	3-30,000

01367338) phosphate					
Niraparib (MK-4827)	PARP	S2741	10 mM	DMSO	0.3-3,000
Pamiparib (BGB-290)	PARP	S8592	10 mM	DMSO	3-30,000
SF2523	PI3K, DNA-PK, BET, mTOR	S8589	10 mM	DMSO	3-30,000
AZD1208	Pim	S7104	10 mM	DMSO	
SRT2104 (GSK2245840)	Sirtuin	S7792	10 mM	DMSO	3-30,000
Salermide	Sirtuin	S8460	10 mM	DMSO	3-30,000
SRT3025 HCl	Sirtuin	S8481	10 mM	DMSO	3-30,000
Quercetin	Src, Sirtuin, PKC, PI3K	S2391	10 mM	DMSO	3-30,000
Cambinol	TNF-alpha	S5913	10 mM	DMSO	3-30,000
Mitoxantrone 2HCl	Topoisomerase	S2485	10 mM	DMSO	3-30,000
Amodiaquine dihydrochloride dihydrate	Transferase, HMT	S4589	10 mM	DMSO	3-30,000
TIC10 (ONC201)	Akt/ERK	S7963	10 mM	DMSO	3-30,000
Romidepsin	HDAC	S3020	10 mM	DMSO	3-30,000

Table 8. TDSU drug library compounds. Compounds were screened in five different concentrations in 10-fold dilutions.

Compound	Target	Catalog No.	Supplier	Stock conc.	Solvent	Conc. range (nM)
A-1155463	BCL-X_L	CT-A115	ChemieTek	100 mM	DMSO	1-10,000
A-1210477	MDM2	A-9036	Active Biochem	7 mM	DMSO	5-50,000
A-1331852	BCL-XL	CT-A133	ChemieTek	10 mM	DMSO	0.1-1,000
Afatinib	EGFR, HER2, HER4	S1011	Selleckchem	10 mM	DMSO	0.1-1,000
Alectinib	ALK	CT-CH542	ChemieTek	5 mM	DMSO	0.1-1,000
Alpelisib	PI3Kα	HY-15244	Medchem Express	10 mM	DMSO	1-10,000
AMG-232	MDM2	CT-AMG232	ChemieTek	10 mM	DMSO	1-10,000
APR-246	p53	3710	Tocris Biosciences	100 mM	DMSO	1-10,000 10-100,000
Axitinib	VEGFR1, VEGFR2, VEGFR3	A-1107	LC Laboratories	50 mM	DMSO	1-10,000
Bortezomib	Proteasome	CT-BZ001	ChemieTek	10 mM	DMSO	0.1-1,000
Busulfan	DNA	B2635	Sigma-Aldrich	500 mM	DMSO	1-10,000
Cabozantinib	MET, VEGFR2	CT-XL184	ChemieTek	10 mM	DMSO	0.1-1,000

Carboplatin	DNA	Cay13112-25	Hospital pharmacy Heidelberg	24.3 mM	water	1-10,000
CCNU (Lomustine)	DNA	HY-13669	Medchem Express	10 mM	DMSO	1-10,000
Ceritinib	ALK	S7083	Selleckchem	10 mM	DMSO	0.25-2,500
Chloroquine	Autophagy, lysosome	C6628	Sigma-Aldrich	100 mM	water	10-1,000,000
Cisplatin	DNA	-	Hospital pharmacy Heidelberg	100 mM	water	10-1,000,000
Cobimetinib	MEK	HY-13064-10mM	Medchem Express	10 mM	DMSO	0.1-1,000
Copanlisib	PI3K	-		9 mM	water	0.1-1,000
Crizotinib	ALK, ROS1, MET	S1068-5	Selleckchem	50 mM	DMSO	1-10,000
Cytarabine	DNA	HY-13605	Medchem Express	100 mM	DMSO	1-10,000
Dabrafenib	BRAF	CT-DABR	ChemieTek	25 mM	DMSO	0.25-2,500
Dactinomycin	DNA	HY-17559	Medchem Express	10 mM	DMSO	0.1-1,000
Dasatinib	BCR-ABL, SRC family kinases	D-3307	LC Laboratories	10 mM	DMSO	0.1-1,000
Daunorubicin	DNA	HY-13062	Medchem Express	10 mM	DMSO	0.1-1,000
Decitabine	DNA methyltransferase	S1200	Selleckchem	100 mM	DMSO	1-10,000
Doxorubicin	DNA	D1515	Sigma-Aldrich	10 mM	DMSO	0.1-1,000
Entinostat	HDAC	CT-MS275	ChemieTek	100 mM	DMSO	1-10,000
Entrectinib	TRK, ROS1, ALK	HY-12678	Medchem Express	10 mM	DMSO	0.1-1,000
Erdafitinib	FGFR	HY-18708	Medchem Express	10 mM	DMSO	1-10,000
Erlotinib	EGFR	HY-50896	Medchem Express	100 mM	DMSO	1-10,000
Etoposide	Topoisomerase II	HY-13629	Medchem Express	100 mM	DMSO	1-10,000
Everolismus	mTOR	E-4040	LC Laboratories	10 mM	DMSO	0.01-100
Foretinib	MET, VEGFR2	S1111	Selleckchem	10 mM	DMSO	0.1-1,000
Gemcitabine	DNA	95058-81-4	Medchem Express	10 mM	DMSO	0.1-1,000
I-BET151	BET bromodomain	CT-BET151	ChemieTek	100 mM	DMSO	1-10,000
Idasanutlin	MDM2	HY-15676	Medchem Express	100 mM	DMSO	1-10,000
Imatinib	BCR-ABL, KIT, PDGFR	HY-50946	Medchem Express	100 mM	DMSO	1-10,000

Irinotecan	Topoisomerase I	I-4122	LC Laboratories	100 mM	DMSO	1-10,000
Isotretionin	Retinoid receptor	TMO-T1611	Hölzel	10 mM	DMSO	1-10,000
Lapatinib	EGFR, HER2	L-4804	LC Laboratories	10 mM	DMSO	0.1-1,000
Larotrectinib	TRK	HY-12866	Medchem Express	10 mM	DMSO	0.1-1,000
Lorlatinib	ALK, ROS1	HY-12215	Medchem Express	100 mM	DMSO	1-10,000
Melphalan	DNA	M2011	Sigma-Aldrich	100 mM	water	1-10,000
Mercaptopurine	DNA	HY-13677	Medchem Express	100 mM	DMSO	1-10,000
Merestinib	MET, AXL, MER	HY-15514A	Medchem Express	10 mM	DMSO	0.1-1,000
Methothrexate	DHFR	S1210	Selleckchem	50 mM	DMSO	0.5-5,000
Mitoxantrone	DNA	HY-13502A	Medchem Express	10 mM	DMSO	0.1-1,000
Navitoclax	BCL-2, BCL-XL	HY-10087	Medchem Express	100 mM	DMSO	1-10,000
Nilotinib	BCR-ABL	N-8207	LC Laboratories	50 mM	DMSO	1-10,000
Olaparib	PARP	O-9201	LC Laboratories	100 mM	DMSO	1-10,000
ONC201	DRD2, ClpP	Selleckchemchem	S7963	10 mM	DMSO	1-10,000
Paclitaxel	Microtubule	HY-B0015	Medchem Express	10 mM	DMSO	0.1-1,000
Palbociclib	CDK4/6	S1116-10	Selleckchem	100 mM	water	1-10,000
Panobinostat	HDAC	P-3703	LC Laboratories	10 mM	DMSO	0.1-1,000
Pazopanib	VEGFR, PDGFR, KIT	P-6706	LC Laboratories	100 mM	DMSO	1-10,000
Ponatinib	BCR-ABL, VEGFR, FGFR	S1490	Selleckchem	10 mM	DMSO	0.1-1,000
Pralsetinib	RET	TMO-TQ0277	BIOZOL		DMSO	0.1-1,000
Rapamycin	mTOR	R-5000	LC Laboratories	10 mM	DMSO	0.01-100
Ribociclib	CDK4/6	S7440	Selleckchem	20 mM	DMSO	1-10,000
Romidepsin	HDAC	HY-15149	Medchem Express	10 mM	DMSO	1-10,000
Ruxolitinib	JAK1/2	CT-INCB-2	ChemieTek	100 mM	DMSO	1-10,000
Selinexor	XPO1	S7252	Selleckchem	100 mM	DMSO	1-10,000
Selumetinib	MEK	HY-50706	Medchem Express	100 mM	DMSO	1-10,000
SN-38	Topoisomerase I (active	Hy-13704	Medchem Express	10 mM	DMSO	0.01-100

	metabolite of Irinotecan)					
Sorafenib p-Toluenesulfonate Salt	RAF, VEGFR, PDGFR	S-8502	LC Laboratories	10 mM	DMSO	0.1-1,000
Sunitinib	VEGFR, PDGFR, KIT	S-8803	LC Laboratories	10 mM	DMSO	0.1-1,000
Talazoparib	PARP	HY-16106	Medchem Express	10 mM	DMSO	0.1-1,000
Tazemetostat	EZH2	CT-EPZ438	ChemieTek	100 mM	DMSO	1-10,000
Temozolomide	DNA	S1237	Selleckchem	200 mM	DMSO	10-100,000
Temsirolimus	mTOR	T-8040	LC Laboratories	10 mM	DMSO	0.01-100
Thioguanine	DNA	HY-13765	Medchem Express	100 mM	DMSO	1-10,000
Thiotepa	DNA	T6069	Sigma-Aldrich	500 mM	DMSO	5-50,000
Topotecan	Topoisomerase I	HY-13768A	Medchem Express	100 mM	DMSO	1-10,000
Trametinib	MEK	CT-GSK112	ChemieTek	25 mM	DMSO	0.25-2,500
Valproic acid	HDAC	P4543	Sigma-Aldrich	200 mM	water	100-1,000,000
Vandetanib	VEGFR, EGFR, RET	V-9402	LC Laboratories	10 mM	DMSO	0.1-1,000
Vemurafenib	BRAF	CT-P4032-2	ChemieTek	100 mM	DMSO	1-10,000
Venetoclax	BCL-2	CT-A199-2	ChemieTek	10 mM	DMSO	0.1-1,000
Vinblastine	Microtubule	HY-13780	Medchem Express	10 mM	DMSO	0.1-1,000
Vincristine	Microtubule	S1241	Selleckchem	10 mM	DMSO	0.1-1,000
Vinorelbine	Microtubule	S4269	Selleckchem	100 mM	DMSO	1-10,000
Vismodegib	SMO	V-4050	LC Laboratories	100 mM	DMSO	1-10,000
Volasertib	PLK1	CT-BI6727	ChemieTek	10 mM	DMSO	0.1-1,000
Vorinostat	HDAC	V-8477	LC Laboratories	100 mM	DMSO	1-10,000

Table 9. Additional epigenetic compounds added to TDSU drug library. Compounds were screened in five different concentrations in 10-fold dilutions.

Compound	Target	Catalog No.	Supplier	Stock conc.	Solvent	Conc. range (nM)
AZD4573	CDK9	HY-112088	Medchem Express	10 mM	DMSO	3-30,000
Flavopiridol (L86-8275)	CDK9	S1230	Selleckchem	10 mM	DMSO	3-30,000

KB-0742 dihydrochloride	CDK9	HY-137478A	Medchem Express	10 mM	DMSO	3-30,000
Zotiraciclib (TG02; SB1317)	CDK9	HY-15166	Medchem Express	10 mM	DMSO	3-30,000
CYC065 (Fadraciclib)	CDK9	HY-101212	Medchem Express	10 mM	DMSO	3-30,000
BMS-986158	BET	HY-101567	Medchem Express	1 mM	DMSO	0.3-3,000
CC-90010	BET	HY-137573	Medchem Express	10 mM	DMSO	3-30,000
CPI-0610	BET	A16076	AdooQ Bioscience	10 mM	DMSO	3-30,000
LY3295668	AURK	HY-114258	Medchem Express	10 mM	DMSO	3-30,000

Table 10. Dead control compounds.

Compound	Target	Catalog No.	Supplier	Stock conc.	Solvent
Staurosporine (STS)	apoptosis inducer	S1421	Selelckchem	10 mM	DMSO
Benzethonium Chloride (BztCl)	detergent, cell lysis	843983	Sigma-Aldrich	100 mM	DMSO

3.1.3 Antibodies

Table 11. Primary antibodies.

Target	Type	Dilution	Catalog No.	Supplier
MYC	rabbit, monoclonal	1:2,000	ab32072	Abcam, Cambridge, UK
RNAPII CTD pSer2	mouse, monoclonal	1:5,000	MA5-23510	ThermoFisher Scientific, Braunschweig, Germany
RNAPII	mouse, polyclonal	1:5,000	05-623	ThermoFisher Scientific, Braunschweig, Germany
GAPDH	mouse, monoclonal	1:30,000	MAB374	Merck, Darmstadt, Germany
HEXIM1	rabbit, monoclonal	1:2,000	ab25388	Abcam, Cambridge, UK

Table 12. Secondary antibodies.

Target	Type	Conjugate	Dilution	Catalog No.	Supplier
Rabbit	donkey, polyclonal	Horseradish peroxidase	1:20,000	V795A	Promega, Madison, WI, USA
Mouse	goat, polyclonal	Horseradish peroxidase	1:20,000	115-035-003	Dianova, Hamburg, Germany

3.1.4 Biochemical reagents

Table 13. Biochemical reagents

Article	Catalog No.	Supplier
10x Tris/Glycine/SDS Running Buffer	1610732	Bio-Rad, Munich, Germany
Acetic acid	6755.1	Carl Roth, Karlsruhe, Germany
Acrylamide/Bis solution (40 % w/v)	10681.01	SERVA, Heidelberg, Germany
Agar	S210.3	Carl Roth, Karlsruhe, Germany
Agarose, low gelling temperature	A9414	Sigma-Aldrich, Munich, Germany
Albumin Standard (2 mg/mL)	23209	ThermoFisher Scientific Inc. Braunschweig, Germany
APS	A3678	Sigma-Aldrich, Munich, Germany
Benzonase	E1014-25KU	Sigma-Aldrich, Munich, Germany
Brilliant Blue G	27815	Sigma-Aldrich, Munich, Germany
Bromophenol Blue	A23331.0005	AppliChem, Darmstadt, Germany
BSA	A4612	Sigma-Aldrich, Munich, Germany
Citric acid	33114-1KG	Sigma-Aldrich, Munich, Germany
cOmplete(TM), Mini, EDTA-free protease inh.	4693159001	Sigma-Aldrich, Munich, Germany
DNase I	D4527-10KU	Sigma-Aldrich, Munich, Germany
EDTA	1034	GERBU Biotechnik GmbH, Heidelberg, Germany
Ethanol, absolute	20821.321	VWR chemicals, Darmstadt, Germany
Glycerol	15523	Honeywell Riedel-de-Haën, Seelze, Germany
Glycine	33226	Sigma-Aldrich, Munich, Germany
HCl	13-1683	Sigma-Aldrich, Munich, Germany
HEPES	9105.2	Carl Roth, Karlsruhe, Germany
Isopropanol	20842.330	VWR chemicals, Darmstadt, Germany
KCl	6781.1	Carl Roth, Karlsruhe, Germany
Methanol	M/4000/PC17	ThermoFisher Scientific Inc. Braunschweig, Germany
Milk powder	T145.2	Carl Roth, Karlsruhe, Germany
Na_2HPO_4	28029.292	WR chemicals, Radnor, PA, USA
NaCl	BP358-1	ThermoFisher Scientific Inc. Braunschweig, Germany
NaOH	30620	Sigma-Aldrich, Munich, Germany
Normal goat serum	5-000-121	Dianova, Hamburg, Germany
PhosSTOP	49068450001	Sigma-Aldrich, Munich, Germany
Ponceau S solution	A2935.0500	AppliChem, Darmstadt, Germany
Precision Plus ProteinTM KaleidoscopeTM prestained protein standard	1610375	Bio-Rad, Munich, Germany
RNaseZAPTM	R2020-250ML	Sigma-Aldrich, Munich, Germany
SDS pellets	2326.1	Carl Roth, Karlsruhe, Germany
Sodium Fluoride	S7920-100G	Sigma-Aldrich, Munich, Germany
Sodium Orthovanadate	P0758L	New England Biolabs, Inc., Frankfurt am Main, Germany
SYBRTM Green PlatinumTM qPCR SuperMix-UDG	11733046	ThermoFisher Scientific Inc. Braunschweig, Germany
TEMED	2367.3	Th. Geyer, Renningen, Germany

Tricaine methanesulfonate	E10521	Sigma-Aldrich, Munich, Germany
Triethanolamine	90279-100ML	Sigma-Aldrich, Munich, Germany
Tri-Sodium citrate dihydrate	27833.294	VWR chemicals, Darmstadt, Germany
Triton-X 100	A4975.0500	AppliChem, Darmstadt, Germany
Trizma Base	T1503	Sigma-Aldrich, Munich, Germany
Tween 20	500-018-3	Sigma-Aldrich, Munich, Germany
Vi-Cell Reagent Coulter cleanz	8448222	Beckmann Coulter, Krefeld, Germany
Vi-Cell Reagent Isoton II	8448011	Beckmann Coulter, Krefeld, Germany
β-mercaptoethanol	39563	SERVA, Heidelberg, Germany

3.1.5 Buffers and Solutions

3.1.5.1. Stock solutions

Table 14. 20% SDS.

Ingredient	Amount	Final concentration
SDS	10 g	20% (w/v)
ddH_2O	added up to 50 ml	

Table 15. 1M Tris-HCl.

Ingredient	Amount	Final concentration
Trizma Base	12.1 g	1 M
HCl	added dropwise	to pH 7.6
ddH_2O	added up to 100 ml	

Table 16. 1M NaCl.

Ingredient	Amount	Final concentration
NaCl	5.8 g	1 M
ddH_2O	added up to 100 ml	

3.1.5.2 Cell lysis solutions

10X phosphatase and 10X protease inhibitor stocks were prepared as follows: 1 tablet of PhosSTOP or cOmplete Protease inhibitor were solved in 1 ml ddH_2O separately and stored at -20°C.

Table 17. RIPA buffer for cell lysis

Ingredient	Amount	Final concentration
1M Tris-HCl	2.5 ml	25 mM, pH 7.6
1M NaCl	10 ml	100 mM
NP-40	1 ml	1% (v/v)
Sodium deoxycholate	1 g	1% (w/v)
20% SDS in H_2O	0.5 ml	0.1% (v/v)
ddH_2O	added up to 100 ml	
10x PhosphoSTOP	added just before use	1X
10x cOmplete Protease inhibitor	added just before use	1X

Table 18. Cell lysis buffer for proteomic sample preparation.

Ingredient	Amount	Final concentration
RIPA Buffer	10 ml	
1M Sodium Fluoride	100 µl	10mM
1M Sodium Orthovandate	10 µl	1mM
Benzonase	100 µl	250 U/ml
DNase I	10 µl	10 U/ml
PhosphoSTOP	1 pill	1X
cOmplete Protease inhibitor	1 pill	1X

Table 19. 4x Laemmli buffer for protein loading.

Ingredient	Amount	Final concentration
0.5 M Tris-HCl, pH 6.8	10 ml	62.5 mM Tris/HCl
Glycerol	8 ml	20% (v/v)
20% SDS in H_2O	8 ml	4% (w/v)
Bromophenol blue	2 mg	5 %
ddH_2O	added up to 40 ml	
β-mercaptoethanol	added just before use	5% (v/v)

3.1.5.3 TBS and TBS-T

Table 20. 10X TBS

Ingredient	Amount	Final concentration
Trizma Base	120 g	200 mM
NaCl	400 g	1.37 M
HCl	added dropwise until pH 7.5	
ddH_2O	added up to 5 L	

Table 21. 1X TBS-T

Ingredient	Volume	Final concentration
10X TBS, pH 7.5	100 ml	20 mM Trizma Base, 137 mM NaCl
Tween-20	1 ml	0.1% (v/v)
ddH_2O	added up to 1 L	

3.1.5.4 Staining solutions

Table 22. Coomassie Brilliant Blue staining for SDS gels.

Ingredient	Amount	Final concentration
Brilliant Blue G	500 mg	0.05% (w/v)
Isopropanol	250 ml	25% (v/v)
Acetic acid	100 ml	10% (v/v)
ddH_2O	added up to 1 L	

Table 23. Ponceau staining for membranes.

Ingredient	Amount	Final concentration
Ponceau S Solution	5 ml	10% (v/v)

ddH_2O	45 ml

3.1.5.5 Blocking buffers

Table 24. 5% milk in TBS-T as blocking solution. Stored at 4°C up to 1 week.

Ingredient	Amount	Final concentration
Non-fat dry milk	5 g	5% (w/v)
1x TBS-T	added up to 100 ml	

Table 25. 5% BSA in TBS-T as blocking solution. Stored at 4°C up to 1 week.

Ingredient	Amount	Final concentration
BSA	5 g	5% (w/v)
1x TBS-T	added up to 100 ml	

3.1.5.6 E3 zebrafish embryo buffer

Table 26. 50X E3 zebrafish embryo buffer.

Ingredient	Amount	Final concentration
NaCl	16.61 g	5 mM
KCl	0.63 g	0.17 mM
CaCl2·2H2O	2.43 g	0.33 mM
$MgSO_4$	1.99 g	0.33 mM
NaOH	added dropwise	to pH 7.2
ddH_2O	added up to 1 L	

Table 27. 1X E3 buffer.

Ingredient	Amount	Final concentration
50X E3 buffer	20 ml	2% (v/v)
ddH_2O	880 ml	

3.1.6 Fluorescent dyes

Table 28. Fluorescent dyes.

Dyes	Specificity	Color	Catalog No.	Supplier
TMRE	Cell permeant mito-chondrial membrane potential stain	Red-orange	ab113852	Abcam, Cambridge, UK
Hoechst 33342	Cell permeant DNA stain	Blue	H1399	ThermoFisher Scientific Inc. Braunschweig, Germany
RedDot2	Cell impermeant DNA stain	Far red	40061-1	Biotium, San Francisco Bay Area, USA
Vybrant DID	Cell permeant lipophilic stain	Far red	V22887	ThermoFisher Scientific Inc. Braunschweig, Germany
CM-DiI	Cell permeant lipophilic stain	Red	V22888	ThermoFisher Scientific Inc. Braunschweig, Germany

3.1.7 Consumables

Table 29. Consumables.

Article	Catalog No.	Supplier
4–20% Mini-PROTEAN® TGX™ Precast Protein Gels, 10-well	4561094	Bio-Rad, Munich, Germany
4–20% Mini-PROTEAN® TGX™ Precast Protein Gels, 15-well	4561096	Bio-Rad, Munich, Germany
7.5% Mini-PROTEAN® TGX™ Precast Protein Gels, 10-well	4561023	Bio-Rad, Munich, Germany
7.5% Mini-PROTEAN® TGX™ Precast Protein Gels, 15-well	4561026	Bio-Rad, Munich, Germany
Conical tubes, 15 ml	188271	ThermoFisher Scientific Inc., Waltham, MA, USA
Conical tubes, 50 ml	2098	ThermoFisher Scientific Inc., Waltham, MA, USA
Corning® Costar® ultra-low attachment Multiple Well Plates, 12 wells	CLS3471-24EA	Sigma-Aldrich, Munich, Germany
Corning® Costar® non-treated well plates, 48 wells	351178	Sigma-Aldrich, Munich, Germany
Cryo Vials 2 ml	E315.1	Carl Roth, Karlsruhe, Germany
D300e Digital dispenser dispenshead casettes, D4+	30097371	Tecan, Männerdorf, Switzerland
D300e Digital dispenser dispenshead casettes, T8+	30097370	Tecan, Männerdorf, Switzerland
Falcon® 5mL Round Bottom Polystyrene Test Tube (FACS Tubes)	10186360	ThermoFisher Scientific Inc., Waltham, MA, USA
Falcon™ Polystyrene Microplates, 6 well	353046	ThermoFisher Scientific Inc., Waltham, MA, USA
Falcon™ Standard Tissue Culture Dishes, 10 cm	353003	ThermoFisher Scientific Inc., Waltham, MA, USA
Glassware	SCHOTT AG, Mainz, Germany	SCHOTT AG, Mainz, Germany
Hashimoto zebrafish imaging 96-well plates	HDK-ZFA101-02a	Hashimoto Electronic Industry Co., Ltd., Japan
Immun-Blot® PVDF Membrane	1620177	Bio-Rad, Munich, Germany
Microplates, 384-well, round bottom, black with clear bottom	3830	Corning, Corning, NY, USA
Millex-GS Syringe Filter 0.22 µm, sterile	SLGS033SS	Sigma-Aldrich, Munich, Germany
Pasteurpipettes, Glas 230 mm	12908	WU Mainz, Bamberg, Germany
Pipet tips, refillable, 10 µl	961-001-20	Steinbrenner Laborsysteme, Wiesenbach, Germany
Pipet tips, refillable, 200 µl	961-201-20	Steinbrenner Laborsysteme, Wiesenbach, Germany
Pipet tips, refillable, 1000 µl	961-1002-7	Steinbrenner Laborsysteme, Wiesenbach, Germany

Pipet tips, sterile, 10 µl	07-613-8300	Nerbe plus, Winsen/Luhe, Germany
Pipet tips, sterile, 100 µl	07-642-8300	Nerbe plus, Winsen/Luhe, Germany
Pipet tips, sterile, 1000 µl	06-693-5300	Nerbe plus, Winsen/Luhe, Germany
Pipet tips, sterile, 20 µl	07-622-8300	Nerbe plus, Winsen/Luhe, Germany
Pipet tips, sterile, 200 µl	07-662-8300	Nerbe plus, Winsen/Luhe, Germany
Reaction tubes, 0.5 ml	30121023	Eppendorf, Hamburg, Germany
Reaction tubes, 1.5 ml	72.690.001	Sarstedt, Nürnbrecht, Germany
Reaction tubes, 1.5 ml	30120086	Eppendorf, Hamburg, Germany
Reaction tubes, 2 ml	30120094	Eppendorf, Hamburg, Germany
Sapphire PCR tubes, 0.2 ml	683201	Greiner Bio-One GmbH, Frickenhausen, Germany
Serological pipettes, 5 ml	4487	Sigma-Aldrich, Munich, Germany
Serological pipettes, 10 ml	4488	Sigma-Aldrich, Munich, Germany
Serological pipettes, 25 ml	4489	Sigma-Aldrich, Munich, Germany
T25 tissue culture flask	690175	Greiner Bio-One GmbH, Frickenhausen, Germany
T75 tissue culture flask	658175	Greiner Bio-One GmbH, Frickenhausen, Germany
T175 tissue culture flask	660175	Greiner Bio-One GmbH, Frickenhausen, Germany
T25 tissue culture flask, for suspension cells	83.3910.502	Sarstedt, Nürnbrecht, Germany
T75 tissue culture flask, for suspension cells	83.3911.502	Sarstedt, Nürnbrecht, Germany
T175 tissue culture flask, for suspension cells	83.3912.502	Sarstedt, Nürnbrecht, Germany
Vi-CELL® 4 ml Sample Vials	383721	Beckmann Coulter, Krefeld, Germany

3.1.8 Kits

Table 30. Kits.

Article	Catalog No.	Supplier
Agilent RNA 6000 Nano Kit	5067-1511	Aligent, Santa Clara, CA, USA
Agilent RNA 6000 Nano Ladder	5067-1529	Aligent, Santa Clara, CA, USA
Amersham ECL Prime Western Blotting Detection Reagent	RPN2232	Sigma-Aldrich, Munich, Germany
Caspase-3/7 Assay Kit, fluorometric	ab39383	Abcam, Cambridge, UK
CellTiterGlo 2.0	G9243	Promega, Madison, WI, USA
PierceTM BCA Protein Assay Kit	23227	ThermoFisher Scientific Inc. Braunschweig, Germany
QIAamp® DNA Mini Kit	51304	Qiagen, Hilden, Germany
RNase free DNase Set	79254	Qiagen, Hilden, Germany
RNeasy Mini Kit	74104	Qiagen, Hilden, Germany
Trans-Blot Turbo RTA Mini 0.45 µM LF PVDF Transfer Kit	1704274	Bio-Rad, Hercules, CA, US

Venor® GenM Classic Mycoplasma Detection Kit	11-1250	Minerva Biolabs, Berlin, Germany

3.1.9 Instruments and devices

Table 31. Instruments and devices.

Instrument	Supplier
2100 Bioanalyzer	Aligent, Santa Clara, CA, USA
Azure c400 imaging system	Azure Biosystems, Dublin, CA, USA
BarnsteadTM GenPureTM xCAD Plus Ultrapure water purification system	ThermoFisher Scientific Inc. Braunschweig, Germany
Benchtop centrifuge Micro Star 17R	VWR International, Radnor, PA, USA
CellCamper® Mini	neoLab Migge GmbH, Heidelberg, Germany
Centrifuge 5810 R	Eppendorf, Hamburg, Germany
Cryo freezing container Nalgene® Cryo 1°C "Mr. Frosty"	ThermoFisher Scientific Inc. Braunschweig, Germany
D300e Digital dispenser	Tecan, Männerdorf, Switzerland
Microliter pipette 0.1-2.5 µl, 0.5-10 µl, 2-20 µl, 20-200 µl, 100-1000 µl	Gilson, Middleton, WI, USA
FemtoJet 4i Microinjector	Eppendorf, Hamburg, Germany
FLUOstar Omega automated plate reader	BMG Labtech, Ortenberg, Germany
FLUOstar OPTIMA automated plate reader	BMG Labtech, Ortenberg, Germany
Hamilton syringe	Hamilton Company, Reno, NV, USA
Heat sealer "Folio"	Severin Elektro, Sundern, Germany
Heating block Thermomixer® Comfort	Eppendorf, Hamburg, Germany
ImageXpress Micro Confocal High-Content Imaging System	Molecular Devices, San Jose, CA, USA
Incubator Heraeus B6420	Heraeus, Leverkusen, Germany
LSM 710 confocal microscope	Zeiss, Oberkochen, Germany
Magnetic stirrer with heating MR-3001	Heidolph Instruments, Schwabach, Germany
Microwave Severin MW 7869	Severin Elektro, Sundern, Germany
Mosquito Liquid Handling System	SPT Labtech, Melbourn, UK
Motorized stereo microscope (Leica M205 FA)	Leica Microsystems, Germany
Multi-axle rotating mixer TRM 56	IDL GmbH, Nidderau, Germany
Nano-Drop ND-1000 spectrophotometer	PEQLab, Erlangen, Germany
NovaSeq 6000 System	Illumina, San Diego, CA, USA
pH meter SevenCompact	Mettler-Toledo, Gießen, Germany
Pipetboy acu 2	INTEGRA Biosciences, Zizers, Switzerland
Refrigerator with freezer	Liebher, Biberach and der Riß, Germany
Rocking platform WT 16	Biometra, Göttinger, Germany
StoragePod	Roylan Development, UK
Test tube shaker Reax Top	Heidolph Instruments, Schwabach, Germany
Tissue culture incubator "C200"	Labotect, Rosdorf, Germany
Tissue culture incubator "CB220"	Binder GmbH, Tuttlingen, Germany
Tissue culture sterile bench "MaxiSafe 2030i"	ThermoScientific, Waltham, MA, USA
Tissue culture sterile bench "Safe2020"	ThermoScientific, Waltham, MA, USA
Trans-Blot Turbo Transfer System	Bio-Rad, Hercules, CA, US

Ultra-low temperature freezer	ThermoFisher Scientific Inc. Braunschweig, Germany
Vacuum concentrator "Concentrator plus"	Eppendorf, Hamburg, Germany
Vi-CELL XR automated cell counter	Beckmann Coulter, Brea, CA, USA
Vortexer IKA VF2	IKA Janke & Kunkel, Staufen im Breisgau, Germany
VWR ® Shaking water bath (18L)	VWR chemicals, Darmstadt, Germany

3.1.10 Software

Table 32. Software.

Software	Supplier
ABI 7500 software v2.3	Applied Biosystems, ThermoFisher Scientific Inc. Braunschweig, Germany
Azure c400 acquisition software	Azure Biosystems, Dublin, CA, USA
BioRender	BioRender
CellProfiler v.4.1.3	Broad Institute, Cambridge, MA, USA
CellProfiler Analyst v.3.0.4	Broad Institute, Cambridge, MA, USA
D300e Digital dispenser control software	Tecan, Männerdorf, Switzerland
GraphPad Prism v10.0.2	GraphPad Software Inc, San Diego, CA, USA
ImageJ v2.9.0	National Institutes of Health
Living Image Software Version 4.4	PerkinElmer, Waltham, MA, US
MaxQuant software v1.6.17.0	Max Planck Institute of Biochemistry, Martinsried, Germany
MetaExpress 6.5.559 Molecular Devices	San Jose, CA, USA
Microsoft Office 2019	Microsoft, Redmond, WA, USA
Mosquito software: v4.1	SPT Labtech, Melbourn, UK
Omega Microplate reader software v5.11R4	BMG Labtech, Ortenberg, Germany
OPTIMA Microplate reader software v2.20R2	BMG Labtech, Ortenberg, Germany
R 4.2.2	The R Foundation, Vienna, Austria
RStudio v2023.12.0	RStudio, Boston, MA, USA
Vi-CELLTM XR 2.03 software	Beckmann Coulter, Brea, CA, USA
Zotero	Zotero

3.1.11 Databases and online tools

Table 33. Databases and online tools.

Database	Website
iTReX: interactive Therapy Response eXploration v1.3.0	https://itrex.kitz-heidelberg.de/iTReX/
R2 Genomics Analysis and Visualization Platform	https://hgserver1.amc.nl/
ShinyGO 0.80	http://bioinformatics.sdstate.edu/go/
Ensembl	https://www.ensembl.org/index.html
NCBI	https://www.ncbi.nlm.nih.gov/
Gene Ontology Enrichment Analysis	https://geneontology.org/
Enrichr: a comprehensive gene set enrichment analysis web server	https://maayanlab.cloud/Enrichr/enrich

SynergyFinder+	https://synergyfinder.org/
ChatGPT 4.0	https://chatgpt.com/
Perplexity	https://www.perplexity.ai/
DeepL	https://www.deepl.com/en/translator
Connected Papers	https://www.connectedpapers.com/
String	https://string-db.org/
Blood-Brain-Barrier-Drug-Penetration-Predictions (BDPP)	https://unite-bdpp.dkfz.de

3.2 Methods

3.2.1 Cell culture

The cell lines and models were maintained in a humidified environment with 5% CO_2 at 37°C. All the cell culture experiments were performed under sterile conditions as well as with sterile consumables under laminar flow unless stated otherwise.

3.2.1.1. Propagation of cells

Majority of the cell models used in the project were maintained in hydrophobic (low attachment) T25, T75 and T175 flasks, where they formed spheroids either adherent or in suspension (**Table 34**). The spheroids were replenished with fresh medium every 2-3 days. When reached 70-80% confluence, and/or the core of the spheroids started turning brown (necrosis), they were dissociated. If the spheroids were adherent, the flasks were added with the respective dissociation reagent (**Table 34**). In case of spheroids growing in suspension, the cells were collected into 50 ml conical tubes, centrifuged at 500g for 5 minutes and the resulting cell pellet was resuspended with the respective dissociation agent according to **Table 34**. After incubation for 5 minutes (min) at 37°C, the cells in the flasks were also collected into 50 ml conical tubes and pipetted in slow mode a few times until single cell suspension was obtained, which was checked under microscope. Upon resuspension with 10 ml tumor stem medium (TSM) base, the cells were split according to a defined ratio described in **Table 34** unless seeded for an experiment, and centrifuged at 500g for 5 min. The resulting pellet was resuspended in TSM complete and transferred to a new flask.

The rest of the cells were maintained in regular tissue culture flasks, where they grew adherent, and passaged once or twice a week when 70-80% confluence was reached. For passaging, the supernatant was decanted, and the cells were washed with PBS before being detached with Trypsin/EDTA. Following incubation for 5 min at 37°C, the enzymatic reaction was stopped using the respective medium containing FCS with thrice the amount of trypsin. The cells were seeded in a new cell culture flask according to their respective splitting ratio described in **Table 34**.

Table 34. Cell culture conditions.

Cell models	Adherence	Dissociation agent	Splitting ratio	Type of flask
HSJD-DIPG-007	Suspension, spheroids	Accumax	1:10	Low attachment
SU-DIPG-17	Adherent, spheroids	TrypLE	1:30	Low attachment

SU-DIPG-19	Semi-adherent, spheroids	TrypLE	1:10	Low attachment
SU-DIPG-25	Suspension, spheroids	TrypLE	1:5	Low attachment
SU-DIPG-13	Suspension, spheroids	Accumax	1:3	Low attachment
SU-DIPG-4	Adherent, spheroids	TrypLE	1:20	Low attachment
SU-DIPG-21	Suspension, spheroids	TrypLE	1:5	Low attachment
SU-pSCG1	Suspension, spheroids	TrypLE	1:5	Low attachment
SJ-DIPGX9	Suspension, spheroids	TrypLE	1:2	Low attachment
KNS42	Adherent	0.05% Trypsin/EDTA	1:20	Regular
BT278	Semi-adherent, spheroids	TrypLE	1:2	Low attachment
INF_R_1073_relapse1	Semi-adherent, spheroids	TrypLE	1:2	Low attachment
SJ-G2	Adherent	0.05% Trypsin/EDTA	1:20	Regular
SU-pcGBM2	Suspension, spheroids	TrypLE	1:2	Low attachment
Isogenic cell lines	Suspension, spheroids	Accumax	1:10	Low attachment
VH7/human fibroblasts	Adherent	0.05% Trypsin/EDTA	1:5	Regular
Fetal astrocytes	Adherent	0.05% Trypsin/EDTA	1:2	Regular, Matrigel coating (1:150) in DMEM w/o supplements
HMC3 (microglia)	Adherent	0.05% Trypsin/EDTA	1:10	Regular

3.2.1.2. Freezing and thawing cells

Before freezing, the cells were expanded into T175 flasks and maintained until 80% confluence was reached. The TSM complete growing suspension cells were centrifuged at 500g for 5 min. After the supernatant was discarded, the cell pellet was resuspended in 10 ml ice cold Synth-a-freeze cryopreservation medium. The adherent cells growing in TSM complete were dissociated using their respective dissociation reagent as described in **Table 34**. Following resuspension with TSM base and centrifugation at 500g for 5 min, the supernatant was descanted, and the resulting cell pellet was mixed with 10 ml ice cold Synth-a-freeze cryopreservation medium. 1 ml of the suspension were aliquoted into 10 cryovials, which were frozen at -80°C freezer in a cryogenic container (Mr. Frosty). The next day, the cryovials were transferred to one of the respective cell storage boxes at -80°C freezer.

For the freezing of the remaining cells, the cells were trypsinized, and their cell number and the viability were assessed using Vi-CELL XR automated cell counter. 1-2 x 10^6 cells/ml were frozen in their respective freezing medium (**Table 6**).

For thawing, the cells were defrosted in 37°C water bath until little ice piece remained in the cryovial and then resuspended in 10 ml cell culture media after being completely thawed. Next, the cells were

centrifuged for 5 min at 500g and supernatant containing freezing medium was discarded. The resulting cell pellet was resuspended in fresh medium and seeded to a well of ultra-low-attachment 6-well plate (spheroids) or to a regular T25 flask (non-spheroids) (**Table 34**).

3.2.1.3 Authentication and contamination testing of cell lines

The cell lines were subjected to comprehensive contamination screening using the Multiplex Cell Contamination Test (McCT) and authenticated via the Multiplex Cell Line Authentication (MCA) test (Multiplexion GmbH, Friedrichshafen, Germany). To conduct the McCT, 10^6 cells were collected and centrifuged at 500g for 5 min at tabletop centrifuge. The pellet was resuspended in 100 µl PBS and incubated at 95°C for 15 min. After centrifugation at 20,000g for 5 min, the supernatant was transferred to a new tube. For MCA test, DNA was isolated from 10^6 cells using the QIAmp DNA Mini Kit according to manufacturer's instructions. DNA amount was quantified by NanoDrop and diluted to 30 ng/ml in 30 µl using DNase and RNase-free water. Both McCT and MCA samples were stored at 4°C until the analysis.

3.2.1.4. Routine mycoplasma check

Cell lines underwent routine monitoring for mycoplasma contamination via polymerase chain reaction (PCR) monthly, utilizing the Venor®GeM kit (Minerva Biolabs). In this procedure, 200 µl of the cell culture supernatant were transferred to a 1.5 ml reaction tube and centrifuged at 500g for 5 min to pellet down the cells. The supernatant was subjected to 95°C incubation for 5 min and stored at cold room (4°C) until the analysis, which had been performed by one of the technical assistants in the lab.

3.2.2 Epigenetic drug library printing and screening

3.2.2.1 Epigenetic drug library printing

The epigenetic drug library contains 102 compounds (**Table 7**), which arrived in vials in a 96-well package. They were all dissolved in DMSO and came in the same stock concentration of 10 mM, except for Tazemetostat (2 mM) and Valproic acid (VPA), the latter was dissolved in water to the stock concentration of 1 M. Each compound, except VPA was pipetted to the TECAN D300e dispenser, which dispensed 5 µl of compounds into total of four 384-well long bottom plates in a concentration range. Each compound was printed in replicates in a dose response series in 10-fold dilutions at five different concentrations. Literature research was conducted to optimize the concentration range for each compound according to their C_{max}[184] *in vivo* if there were clinical data for the compounds. If not, the concentration range was defined based on *ex vivo* and *in vitro* findings. The compound concentrations mainly ranged from 30,000 nM to 3 nM or 3,000 nM to 0.3 nM. In addition to the epigenetic drugs, benzethonium chloride (BztCl; 300 µM) and staurosporine (STS; 250 µM) were printed on the plates as positive (dead) controls (**Table 10**) and dimethyl sulfoxide (DMSO; final concentration 0.3%) as a negative control. These plates are the so-called source plates were kept in StoragePods (Roylan Development) which is filled with dry and inert gas to prevent damaging exposure of compounds to moisture and oxygen. The Mosquito HTS liquid handling system (ttp LabTech) used source plates containing 5 µl of each compound and stamped up to four identical assay plates (384-well round-bottom plates) from one source plate in one run with 75 nl of each drug in the same layout /concentration

range as the source plate. VPA was printed on assay plates with TECAN D300e dispenser to the final concentration range from 1,000,000 nM to 100 nM. The assay plates were used to create dose-response profile of each cell model through metabolic activity assay.

3.2.2.2 Metabolic activity assay

Metabolic activity was determined using a single-reagent assay, CellTiter-Glo (CTG) 2.0. The assay aims at detecting the amount of viable cells by measuring adenosine triphosphate (ATP), a marker indicative of cellular metabolic activity. The luminescent signal obtained from the assay is directly correlated with the abundance of viable cells.

3.2.2.2.1 Seeding density optimization

To assess optimal seeding density for each cell model, cells were seeded at two-fold dilutions in six different densities ranging from 62 to 2000 cells in 25 µl per well in 384-well round-bottom plates in quintuplicate. Five additional wells were kept as blank control, which were only added with 25 µl of the media of the respective cell model. The cells grew as 3D spheroids in the wells. Upon incubation for 72 hours (h), the plates and the CTG reagent of CTG 2.0 kit were brought to room temperature. Next, 15 µl of the CTG reagent were added to each well. Following that the plates were shaken on a bench-top plate shaker for 5 min and incubated at room temperature for 15 min, the metabolic activity was measured as luminescence signal using TECAN Spark plate reader pre-warmed to 28°C. The results were normalized to the mean value of the blank controls. The linear relationship between increasing number of cells and signal (relative light unit, RLU) were considered while deciding on the optimal seeding density (**Table 35**).

3.2.2.3 Assessing drug sensitivity

To examine the drug response, the cells were seeded onto ready-to-use drug-printed assay plates according to their corresponding seeding densities (**Table 35**), incubated for 72h and then with CTG substrate to measure cell viability as described in **3.2.2.2.1 Seeding density optimization**. The results were analyzed using a Shiny App containing an R package, named iTReX (https://itrex.kitz-heidelberg.de/iTReX/)[185]. iTReX computes an extended version of the drug sensitivity score (DSS) based on advanced five-parameter log-logistic equation fit to dose-response curves. This asymmetric scoring method called, DSS_{asym}, quantifies drug sensitivities for each cell model and compound.

Cell model	Seeding density per well (25 µl)
BT278	1000
KNS42	500
HSJD-DIPG-007	750
SU-DIPG-19	1000
SU-DIPG-13	750
SU-DIPG-25	1000
SU-DIPG-21	750
SU-DIPG-17	750
SU-DIPG-4	1000
SJ-DIPG-X9	750
SU-pSCG1	750
SU-pcGBM2	500
SJ-G2	500
INF_R_1073_relapse1	1000
Fetal astrocytes	1000
HMC3	1000
VH7	2000

Table 35. Seeding densities for metabolic activity assays. 384-well round bottom plates were used, where cells formed 3D spheroids. Incubation time was 72h.

3.2.3 TDSU drug library printing and combination screens

3.2.3.1 TDSU drug library printing

The Translational Drug Screening Unit (TDSU) drug library used in combination screens is based on the one generated by Peterziel et al., 2022 featuring originally 76 drugs relevant to cancer treatment[169]. An extended version of the library comprising 86 compounds was used in this project (**Table 8**). The compounds of the library were printed on 384-well long-bottom plates as described in **3.2.2.1 Epigenetic drug library printing** by another doctoral student, Sonja Herter, in the lab. Each of the four plates contained drugs at five different concentrations centered around their respective C_{max}[184]. Additionally, each plate included STS and BztCl as dead controls (positive controls), in addition to negative control wells containing DMSO. One of the source plates were added with 11 more epigenetic compounds from the drug classes of the identified epigenetic hits (CDK9i, BETi, AURKi) in a similar way to test the interaction between two epigenetic compounds (**Table 9**). Then assay plates were produced by replicating all four source plates using the Mosquito HTS liquid handling system.

3.2.3.2 Printing of the combination partner

The TDSU compounds were printed in a concentration range in duplicates on the two halves of a 384-well round-bottom assay plates. To one of the two halves, the epigenetic combination partner of interest was added at 25% inhibitory concentration (IC25) for the respective cell model to be screened (**Table 36**). With this, each TDSU drug library compound was screened as a single agent and in combination with one of the epigenetic hits.

Table 36. Cell models analyzed in combination screens and the combination partners.

Cell model	Combination partner analyzed in combination screen with TDSU drug library/IC25 (nM)		
HSJD-DIPG-007	atuveciclib/565.6	mivebresib/7.6	alisertib/9.8
SU-DIPG-17	atuveciclib/744.2	mivebresib/18.8	alisertib/30.1
SU-DIPG-19	atuveciclib/471.7	mivebresib/3.5	alisertib/221.8
SU-DIPG-25	atuveciclib/433	mivebresib/15.7	alisertib/9.3

3.2.3.3 Examining compound combination sensitivity

Four H3K27M mutant cell models were picked, which were HSJD-DIPG-007, SU-DIPG-17, SU-DIPG-19 and SU-DIPG-25. The experimental setup was the same as described in **3.2.2.3 Assessing drug sensitivity**. The raw data obtained from metabolic activity assay was run on iTreX[185], which provided two types of DSS_{asym}: DSS_{asym}_mono and DSS_{asym}_combo for single agent and combination treatments, respectively.

3.2.3 Synergy screens

Synergistic interaction between two compounds was investigated using two different methods: multiple-ray design and matrix design. Metabolic activity was measured as a readout in both methods.

3.2.3.1 Synergy screen with multiple-ray design

For the evaluation of potential synergistic interaction between atuveciclib (CDK9i) and BMS-986158 (BETi) for H3K27M DMG cell models, the ray design approach was employed with seven rays. This method utilizes a set of fixed ratios to combine the compounds. Each ray design contained seven rays:

- Two rays corresponded to each drug alone (single agent rays).
  - Rays 0 and 1 were assigned to the IC50s of atuveciclib (CDK9i) and BMS-986158 (BETi), respectively for each individual cell model.
- Five rays consisted of five concentrations of both drugs combined in a fixed proportion unique to each ray with respect to their IC50s (combination rays).
  - 4 to 1: Four parts atuveciclib (CDK9i) and one part BMS-986158 (BETi).
  - 1.86 to 1: 1.86 parts atuveciclib (CDK9i) and one part BMS-986158 (BETi).
  - 1 to 1: Equivalent ray consisting of equal parts of each compound.
  - 1 to 1.86: One part atuveciclib (CDK9i) and 1.86 part BMS-986158 (BETi).
  - 1 to 4: One part atuveciclib (CDK9i) and four parts BMS-986158 (BETi).
- For each combination, the drugs were serially diluted into seven levels, centered around the IC50 for each drug, thereby covering a range from the minimal to maximal effective concentrations. This design allowed for a detailed dose-response curve, facilitating the identification of dose-dependent synergistic, antagonistic, or additive effects.
  - Minimum (min) and maximum (max) concentration tested were 0 to 30,000 nM for atuveciclib (CDK9i) and 0 to 3,000 nM for BMS-986158 (BETi).
  - Dilution factors varied for each cell model to stay within min and max concentrations.
    - 100, 10, 3, 1, 0.3, 0.1 and 0.03 for HSJD-DIPG-007 and SU-DIPG-17.
    - 8, 4, 2, 1, 0.5, 0.25 and 0.125 for SU-DIPG-19.
    - 31, 10, 3, 1, 0.3, 0.1 and 0.03 for SU-DIPG-25.

The efficacy of drug combinations was quantitatively assessed using metabolic activity assay for the stated four cell models, which were also investigated in combination screens (**Table 36**). The degree of synergy based on the results from two replicates was calculated using Loewe model[186] by Dr. Tim Holland-Letz. The model exploited the interaction index (ii) to evaluate interaction effects. An ii less than 1 indicated synergy, equal to 1 indicated an additive effect, and greater than 1 suggested antagonism.

The analysis from Dr. Tim Holland-Letz included IC50 values corresponding to each ray, based on which the concentrations of combination partners were determined given that the proportion of each compound was predefined. This helped delineate the concentrations of both compounds used in combo low treatment specific for each cell model.

The multiple-ray design method was chosen to determine the synergistic ratios between the two compounds, which could potentially form a basis for the design of *in vivo* zebrafish xenograft experiments.

3.2.3.2 Synergy screen with matrix design

For the investigation of probable synergistic interaction between KB-0742 (CDK9i) and BMS-986158 (BETi) or CC-90010 (BETi) was investigated with 7x7 matrix design using SynergyFinder+[187]. Each concentration of KB-0742 (CDK9i) was combined with each concentration of either of the BETis. Only SU-DIPG-17 was examined in this experiment. The interaction between the compounds was measured employing Loewe model. The 2D synergy maps generated by SynergyFinder+ displayed synergistic and antagonistic dose regions in red and green colors, respectively. The heatmaps also helped identify the most synergistic areas.

3.2.4 Western Blot

3.2.4.1 Cell lysate preparation

HSJD-DIPG-007 cells were seeded according to **Table 37**, and treated according to **Table 38**. For cell lysis, cells were washed with ice-cold PBS once following harvesting, and lysed in 150-200 µl RIPA buffer (**Table 17**). Lysates were incubated on ice for 30 min, centrifuged at maximum speed for 30 min at 4°C, and the supernatant of each sample was transferred to a new 1.5 ml tube.

Table 37. Seeding densities in all experiments.

Method	Plate format	Cell model	Seeding density
Epigenetic drug library screen	384-well round bottom	All cell models	**Table 35**
Combination screens	384-well round bottom	HSJD-DIPG-007, SU-DIPG-17, SU-DIPG-19, SU-DIPG-25	**Table 35**
Synergy screens	384-well round bottom	HSJD-DIPG-007, SU-DIPG-17, SU-DIPG-19, SU-DIPG-25	**Table 35**
HCM imaging	384-well round bottom	SU-DIPG-17, HSJD-DIPG-007, KNS42, HMC3	**Table 35**
Sample generation for WB	Ultra-low attachment 6-well	HSJD-DIPG-007	10^6/2 ml
Sample generation for RNAseq	Ultra-low attachment 6-well	HSJD-DIPG-007, SU-DIPG-17, SU-DIPG-19, SU-DIPG-25	10^6/2 ml in triplicates

Sample generation for MS/MS proteomics	Ultra-low attachment 6-well	HSJD-DIPG-007, SU-DIPG-17, SU-DIPG-19, SU-DIPG-25, INF_R_1073_relapse1	10^6/2 ml in triplicates
Caspase-3/7 assay	Ultra-low attachment 6-well	HSJD-DIPG-007, SU-DIPG-17, SU-DIPG-25	10^6/2 ml
Soft-agar colony formation assay	6-well	SU-DIPG-17	8,000
Flow cytometry	Ultra-low attachment 6-well	HSJD-DIPG-007	10^6/2 ml in 6 wells per treatment

Table 38. Concentrations used in *in vitro* assays.

Cell model	**Compound concentration (nM)**					
	IC50 for atuveciclib (CDK9i)	**IC50 for BMS-986158 (BETi)**	**Combo low (combination reaches to 50% inhibition)**		**Combo high**	
HSJD-DIPG-007	850	27	atuveciclib (CDK9i)	155	atuveciclib (CDK9i)	850
			BMS-986158 (BETi)	5.5	BMS-986158 (BETi)	27
SU-DIPG-17	1522	21	atuveciclib (CDK9i)	277	atuveciclib (CDK9i)	1522
			BMS-986158 (BETi)	4	BMS-986158 (BETi)	21
SU-DIPG-25	716	103	atuveciclib (CDK9i)	54	atuveciclib (CDK9i)	716
			BMS-986158 (BETi)	83	BMS-986158 (BETi)	103

3.2.4.2 Measurement of protein concentration

Protein concentrations were measured utilizing the Pierce™ BCA Protein Assay Kit as per the instructions provided by the manufacturer. A range of protein standards, using albumin supplied in the kit from 2000 µg/ml down to 25 µg/ml, was prepared in the appropriate lysis buffers (RIPA, Caspase-3/7 assay buffer). These standards were consistently maintained on ice and stored at -20°C when not in use. Samples were diluted in ratios from 1:2 to 1:6 with their specific lysis buffers to align the concentrations within the range of the standard curve. 5 µl of each sample or standard were pipetted into a clear, flat-bottom 96-well plate in triplicate, and then 200 µl of the BCA working solution (combining reagent A and reagent B in a 50:1 ratio) was added. Following a 30 min incubation at 37°C, the colorimetric change, indicative of the protein amount, was assessed using FLUOstar OPTIMA plate reader by measuring the absorbance at 570 nm.

3.2.4.3 Gel electrophoresis and immunoblotting

SDS-polyacrylamide gel electrophoresis (SDS-PAGE) was conducted to separate proteins based on their molecular weight using pre-cast gels from Bio-Rad (4-20% and 7.5%). 20-30 µl of 10 µg protein per sample were loaded in 10-comb gels, and 15 µl of 10 µg protein in 15-comb gels. For all the gels, the Precision Plus Protein™ Kaleidoscope™ Prestained Protein Standard ladder was also loaded to predict the sample protein molecular weight. The gel electrophoresis was run in an electrophoresis chamber containing 1:10 diluted 10X Tris-SDS Running Buffer from Bio-Rad at 100 V.

PVDF membranes were activated in either ethanol or methanol for 1-2 min and kept wet in 1:10 diluted 10X Transfer Buffer from Bio-Rad until the transfer. Membrane and gel were sponged between Trans-Blot Turbo RTA Transfer Kit pads soaked in 1X BioRad Transfer Buffer. The proteins were transferred to a PVDF membrane from the SDS-PAGE gel using Trans-Blot Turbo RTA Mini 0.45 µM PVDF Transfer Kit with the Trans-Blot Turbo Transfer System for 10 min at 1.3 A (one mini gel) or 2.5 A (two mini gels) and up to 25 V.

Following the transfer, the SDS-PAGE gel was stained with Coomassie stain (**Table 22**) for 30 min at room temperature to decipher whether all the proteins could be transferred. The membrane was immersed in absolute ethanol for 1 min and stained with Ponceau (**Table 23**) for 5 min at room temperature to detect the transferred proteins.

After the Ponceau staining, the membrane was blocked in 5% milk (**Table 24**) or 5% BSA (**Table 25**) for 1h at room temperature. Then, the membrane was incubated with the primary antibody (**Table 11**) overnight (O/N) at 4°C. Horse radish peroxidase (HRP) conjugated secondary antibody (**Table 12**) incubation was conducted at room temperature for 2h. The membrane was washed with TBS-T (**Table 21**) three times for 5 min after both antibody incubations. The detection of antibody binding was achieved through the chemiluminescence produced by enhanced chemiluminescence (ECL) substrates upon interaction with HRP, which was captured using an Azure Imaging System 400. Images were analyzed using ImageJ.

3.2.5 Caspase-3/7 activity assay

Caspase-3/7 activity assay was performed using Caspase-3/7 kit (**Table 30**), which depicted potential apoptotic induction in H3K27M DMG models (HSJD-DIPG-007, SU-DIPG-17 and SU-DIPG-25) under mono- and combination therapy. The cells were seeded as detailed in **Table 37**, and treated subsequently according to **Table 38**. After 24h incubation, the cells were harvested and pelleted at 500 g at 4°C in 2 ml reaction tubes. The cell pellets were washed with ice-cold PBS and spinned down at 2000 g for 5 min at 4°C. The pellets were lysed in 65 µl ice-cold caspase assay cell lysis buffer on ice for 15 min.

To quantify the protein amount, BCA was performed with 1:2 diluted lysates and standards prepared in caspase assay cell lysis buffer as explained in **3.2.4.2 Measurement of protein concentration**. All the samples were diluted to 50 µg in 50 µl lysis buffer. 50 µl of lysis buffer were used as blank. The samples and the blank controls were mixed with 50 µl 2x reaction buffer containing fresh 10 mM DTT. Lastly, 5 µl of the substrate were added to each sample and blank, and mixed thoroughly by pipetting.

The samples and the blank control were transferred in technical duplicates of 50 µl into a black flat-bottom 96-well plate. Subsequently, the plate was subjected to fluorescent emission measurement using a pre-warmed FLUOstar OPTIMA plate reader at 37°C, with readings taken every 10 min over a 3h period (20 cycles). The plate reader was configured for excitation at 380 nm and emission detection at 520 nm, with a gain setting of 1400. Following the assay, the software integrated with the BMG Reader Control Software was utilized to determine the time window exhibiting linear increase in fluorescent signal, and the slope of this linear increase was calculated accordingly. Graphs were plotted using GraphPad Prism v10.0.2. This experiment was repeated thrice for each cell model.

3.2.6 Soft-agar colony formation assay (Soft-agar CFA)

To assess the impact of drugs on the growth of cells in an anchorage-independent manner, soft agar CFA was conducted. Initially, a 3% sterile agar solution was melted at 45°C and combined with TSM complete (**Table 6**), resulting in a final concentration of 0.6%. Subsequently, 2 ml of this mixture were added to each well of a 6-well plate, serving as the base layer. After the bottom layer was solidified, the upper layer, containing 8,000 SU-DIPG-17 cells together with varying drug concentrations (**Table 38**), were mixed with a 3% agar solution and TSM complete to achieve a final agar concentration of 0.3%. This top layer was then poured over the base layer in each well. Upon the solidification of the top layer, the plates were incubated at 37°C, 5% CO_2. One day after the seeding and every three days, 200 µl of TSM complete were added to each well to prevent the agar and the cells from drying. After 12 days, colonies were stained with 200 µl of MTT at a final concentration of 1 mg/ml O/N at 37°C. The next day, each well was visualized with Azure Imaging System 400. Each treatment was tested in duplicates. Images were generated using ImageJ.

3.2.7 High content microscopy imaging

To examine the cytostatic and cytotoxic effect of the treatments, high content microscopy (HCM) imaging was performed. SU-DIPG-17, HSJD-DIPG-007, KNS42 and HMC3 cells were stained with TMRE (final concentration 100 nM) and seeded in 384-well round-bottom plates according to **Table 37** in 14 replicates. 24h later, the spheroids were imaged using ImageXpress Micro Confocal High-Content Imaging System with 10x objective and Cy3 channel, and treated subsequently according to **Table 38** with Tecan D300 drug dispenser. Both KNS42 and HMC3 were subjected to treatment conditions of HSJD-DIPG-007 and SU-DIPG-17 (**Table 38**). 300 µM BztCl was used as a dead control and DMSO as a negative control. 72h after the treatment, each well was added with 25 µl of TSM complete (**Table 6**) containing 2X RedDot2 and 10 µg/ml Hoechst (**Table 28**), where they were diluted 1:2 more, and incubated at 37°C, 5% CO_2 for 30 min. Following incubation with the dyes, the plates were imaged again using the same settings including Cy5 and DAPI channels being activated. Image analysis was performed using CellProfiler for spheroid area measurement and dead cell quantification, for the latter CellProfiler Analyst was also employed.

3.2.8 RNA sequencing

3.2.8.1 Sample generation

Gene expression analysis was conducted to decipher the mechanism of action behind the compound and compound combination effect on H3K27M DMGs. HSJD-DIPG-007, SU-DIPG-17, SU-DIPG-19 and SU-DIPG-25 cells were seeded and subsequently treated as indicated **Table 37** and **Table 39**, respectively in three technical and five biological replicates. 24h later, the cells were harvested and pelleted down by centrifugation at 500g for 5 min. The resulting pellet was washed with ice-cold PBS thrice and RNA was extracted using RNeasy Mini Kit with on-column DNA digestion according to the manufacturer's instructions. RNA concentration was measured using Nano-Drop ND-1000 spectrophotometer. RNA integrity representing the RNA quality was measured using 2100 Bioanalyzer and Agilent RNA 6000 Nano Kit according to the manufacturer's instructions.

Table 39. Treatment conditions used in omics analyses. Concentrations refer to IC50 for the respective cell model.

Cell model	Compound concentration (nM)			
	atuveciclib (CDK9i)	BMS-986158 (BETi)	Combo low	
HSJD-DIPG-007	850	27	atuveciclib (CDK9i)	155
			BMS-986158 (BETi)	5.5
SU-DIPG-17	1522	21	atuveciclib (CDK9i)	277
			BMS-986158 (BETi)	4
SU-DIPG-19	726	483	atuveciclib (CDK9i)	208
			BMS-986158 (BETi)	130
SU-DIPG-25	716	103	atuveciclib (CDK9i)	54
			BMS-986158 (BETi)	83

3.2.8.2 RNA sequencing

Total of 80 RNA samples were diluted to a final concentration of 60 ng/µl in 40 µl nuclease-free water based on Nano-Drop results for submission to Next-Generation Sequencing (NGS) Core Facility at the DKFZ, where the sequencing was conducted. Briefly, sequencing libraries were constructed using the Illumina TruSeq mRNA Stranded Kit, adhering to the guidelines provided by the manufacturer. mRNA was isolated from 500 ng of total RNA via oligo(dT) beads. Subsequently, the poly(A) containing RNA was broken down into 150 bp fragments, synthesized into complementary DNA (cDNA), end-repaired, adenylated at the 3' end, adapter-ligated, and PCR-amplified for 15 cycles. The completed libraries were then undergone quality control (QC) analysis using Qubit and TapeStation. 150 bp paired-end sequencing was carried out by an Illumina NovaSeq 6000, following the manufacturer's protocol.

3.2.8.3 Data analysis

The resulting FASTq files were subjected to downstream analysis involving read-trimming, alignment to the hg19/GRCh37 human genome and calculation of raw read counts and transcript per million (TPM) values by the One Touch Pipeline (OTP)[188] at the DKFZ. Both the raw data and TPM values of 80 samples were uploaded to R2: Genomics Analysis and Data Visualization Platform[189] for subsequent gene expression analyses.

3.2.9 LC-MS/MS proteomics

3.2.9.1 Sample generation

The same cells analyzed in RNA sequencing (RNAseq) were seeded, treated under the same conditions and harvested as described in **3.2.8.1 Sample generation**. Additionally, INF_R_1073_relapse1 (H3 WT) cells were seeded according to **Table 37** and treated using the treatment conditions of each H3K27M DMG model as detailed in **Table 39**. This way one to one comparison between H3 WT and H3K27M pHGG cells was ensured. Following the ice-cold PBS washing of the pellets, the cells were lysed in 100 µl lysis buffer (**Table 18**) and proceeded as highlighted in **3.2.4.1 Cell lysate preparation**. Four biological replicates were generated per cell model and treatment condition. Protein concentration of 128 1:4 diluted samples was measured using PierceTM BCA Protein Assay Kit according to the manufacturer's instructions as detailed in **3.2.4.2 Measurement of protein concentration**.

3.2.9.2 Sample processing

The protein samples were diluted to 500 ng/µl final concentration in 40 µl lysis buffer (**Table 18**) for submission to Proteomics Core Facility at the DKFZ, where the liquid chromatography-mass spectrometry (LC-MS/MS) analysis took place. Below is the text from the Proteomics Core Facility describing how they have processed the samples:

"*Proteins (10 µg) were trypsin digested using an AssayMAP Bravo liquid handling system (Agilent technologies) running the autoSP3 protocol according to Müller et al.*[190].

A LC-MS/MS analysis was carried out on an Ultimate 3000 UPLC system (Thermo Fisher Scientific) directly connected to an Orbitrap Exploris 480 mass spectrometer for a total of 120 min. Peptides were online desalted on a trapping cartridge (Acclaim PepMap300 C18, 5µm, 300Å wide pore; Thermo Fisher Scientific) for 3 min using 30 µl/min flow of 0.05% TFA in water. The analytical multistep gradient (300 nl/min) was performed using a nanoEase MZ Peptide analytical column (300Å, 1.7 µm, 75 µm x 200 mm, Waters) using solvent A (0.1% formic acid in water) and solvent B (0.1% formic acid in acetonitrile). For 102 min the concentration of B was linearly ramped from 4% to 30%, followed by a quick ramp to 78%, after 2 min the concentration of B was lowered to 2% and a 10 min equilibration step appended. Eluted peptides were analyzed in the mass spectrometer using data independent acquisition (DIA) mode. A full scan at 120,000 (120k) resolution (380-1400 m/z, 300% AGC target, 45 ms maxIT) was followed by 40 windows of variable width covering the mass range of 400-1000 m/z for fragment spectrum acquisition (collision energy 28%, resolution 30k and the maximum injection time was 54 milliseconds (ms) with and AGC target of 1000%).

Analysis of DIA RAW files was performed with Spectronaut (Biognosys, version 17.1.221229.55965) in directDIA+ (deep) library-free mode. Default settings were applied with the following adaptions. Within the Pulsar Search in Peptides the Max Peptide Length was set to 35, in Result Filters the Peptide Charge was enabled and the Max Charge set to 6 and the Min Charge set to 2. Within DIA Analysis under Identification the Precursor PEP Cutoff was set to 0.01, the Protein Qvalue Cutoff (Run) set to 0.01 and the Protein PEP Cutoff set to 0.05. In Quantification the Proteotypicity Filter was set to Only Protein Group Specific, the Corss-Run Normalization was disabled, the Quantification window was set to Not Synchronized and the Major Group Quantity was set to Sum peptide quantity. The data was searched

against the human proteome from Uniprot (human reference database with one protein sequence per gene, containing 20,591 unique entries from first of March 2023) and the contaminants FASTA from MaxQuant (246 unique entries from twenty-second of December 2022).”

3.2.10 Radiosensitization analysis

To explore the potential radiosensitization effect of combo low, metabolic activity assay and CFA were conducted in collaboration with Prof. Marlon Veldwijk in UniKlinikum Mannheim. All the experiments in this section were repeated three times.

3.2.10.1 Plating efficiency test

Plating efficiency of HSJD-DIPG-007, SU-DIPG-17, SU-DIPG-19, SU-pcGBM2, BT278 and INF_R_1073_relapse1 was determined by Prof. Veldwijk as described in Veldwijk et al., 2011[191].

3.2.10.2 Radiosensitivity assessment via colony formation assay

Radiosensitivity of HSJD-DIPG-007, SU-DIPG-17 and SU-DIPG-19 was assessed by Prof. Veldwijk’s group according to Furth et al., 1981[192] performing a colony formation assay.

3.2.10.3 Metabolic activity analysis of combo low in conjunction with radiotherapy

To examine optimal drug combinations, which can potentially sensitize the H3K27M DMG models to irradiation, metabolic activity assay was performed. In brief, HSJD-DIPG-007, SU-DIPG-19 and SU-DIPG-25 cells were seeded according to **Table 35** in drug-printed 384-well round-bottom plates. To form a dose-response curve, a layout was prepared similar to the one described in **3.2.3.1 Synergy screen with multiple-ray design** specific for each cell model. The plates included BztCl and DMSO as positive and negative control, respectively. Each cell model was analyzed in three plates, each of which received different Gy doses (SF100 (0 Gy), SF75 (IC25) and SF50 (IC50)) predetermined in **3.2.10.2 Radiosensitivity assessment via colony formation assay** 24h after being seeded and incubated with drug combinations. 72-96h after irradiation, metabolic activity assay was performed using CTG as described **3.2.2.2 Metabolic activity assay**. The results were analyzed and plotted using GraphPad Prism v10.0.2.

3.2.10.4 Radiosensitization exploration via colony formation assay

H3K27M DMG models, HSJD-DIPG-007 and SU-DIPG-17 cells, were seeded in 96-well plates and treated subsequently according to (**Table 40**). 24h later, they were subjected to radiotherapy (RT) in Gy doses of 0, 2, 4, 8 and 10. SU-pcGBM2 (H3 WT) was also analyzed to demonstrate that presence of H3K27M mutation is the sensitizing factor to RT when subjected to combo low treatment. For SU-pcGBM2, the highest concentrations of atuveciclib (CDK9i) and BMS-986158 (BETi) used in combo low treatments of HSJD-DIPG-007 and SU-DIPG-17 were applied (**Table 40**).

Table 40. Compound doses used in radiosensitization assay.

Cell model	Compound concentration (nM)	
	Combo low	
HSJD-DIPG-007	atuveciclib (CDK9i)	155
	BMS-986158 (BETi)	5.5
SU-DIPG-17	atuveciclib (CDK9i)	277
	BMS-986158 (BETi)	4
SU-pcGBM2	atuveciclib (CDK9i)	277
	BMS-986158 (BETi)	5.5

3.2.11 Exploration of DNA damage induction in H3K27M DMG cell model under treatment

The experiments explained here were performed in collaboration with Prof. Dr. Oliver Krämer at UniMedizin Mainz.

3.2.11.1 DNA damage investigation with WB

HSJD-DIPG-007 cells were seeded according to **Table 37** and subsequently treated with atuveciclib (CDK9i), BMS-986158 (BETi) and combo high as detailed in **Table 38**. Additionally, 1 mM hydroxyurea was used as a positive control for DNA damage analysis, and non-treated cells were kept as a negative control. Moreover, 0.1% DMSO treatment was kept as a solvent control. 16h later, the cells were harvested, centrifuged at 500g for 5 min, the pellet was washed with ice-cold PBS once, pelleted down at the same conditions, snapped frozen on dry ice and kept at -80°C. The samples were analyzed in WB for γH2A.X, PARP1 cleavage, pChk1 and ACTB by Prof. Krämer's technician as described in Pons, M., et al.[193].

3.2.11.2 DNA damage investigation with flow cytometry

HSJD-DIPG-007 cells were seeded according to **Table 37** and subsequently treated with atuveciclib (CDK9i), BMS-986158 (BETi) and combo high as detailed in **Table 38**. Additionally, 1 mM hydroxyurea was used as a positive control for DNA damage analysis, and non-treated cells were kept as a negative control. Moreover, 0.1% DMSO treatment was kept as a solvent control. 16h later, the cells were collected into 15 ml tubes, centrifuged at 500g for 5 min, dissociated with 1ml Accumax as described in **3.2.1.1. Propagation of cells.** Resulting cell pellets were resuspended in 200 µl PBS and were prefixed with 2 ml ice cold 1% paraformaldehyde (PFA) in PBS for 15 min. Then, 5 ml PBS were added, and the cells were centrifuged at 300g for 5 min. After washing with PBS and centrifugation steps were repeated, the pellets were resuspended with 200 µl PBS, added with 2 ml ice cold 80% EtOH (-20°C) and kept on ice while being transported to Mainz for flow cytometry analysis. Next, the cells were added with 5 ml PBS and centrifuged at 300g for 5min. The resulting pellets were resuspended with 5 ml PBS and incubated at room temperature for 5 min. After centrifugation, the pellets were permeabilized with 1 ml 0.25% Triton X-100 in PBS and incubated on ice for 5 min. Next, tubes were added with 5 ml PBS and centrifuged. The pellets were resuspended in 100 µl 1% BSA in PBS containing 0.5 µg anti-γH2A.X Ab and incubated at room temperature with gentle agitation for 2h. Next, the cells were added with 1 ml 1% BSA in PBS and centrifuged. The pellets were resuspended in 100 µl 1% BSA in PBS containing 3.33 µg Alexa Fluor® 488-conjugated goat secondary Ab and incubated at room temperature

with gentle agitation in dark for 1h. Next, the cells were added with 1 ml 1% BSA in PBS and centrifuged. The pellets were resuspended in 500 µl PBS containing 10 µg/ml PI and 100 µg/ml RNase, incubated for 30 min at 37°C in the dark and the cells were analyzed in flow cytometry measuring green (530 nm) and red (>590 nm) fluorescence using blue light excitation (488 nm) for γH2A.X and PI stainings, respectively with the help of Prof. Krämer's PhD student, Andreas Mieland.

3.2.12 Toxicity assay, xenotransplantation and drug treatment in zebrafish embryo

To validate the effect of the compounds and their combination *in vivo*, the zebrafish xenografts were used.

3.2.12.1 Zebrafish embryo toxicity assay

Maximum tolerated dose (MTD) and lethal dose (LD) of both atuveciclib (CDK9i) and BMS-986158 (BETi), as well as their combination were determined in a toxicity assay using zebrafish embryos. This experiment was performed by our MD student, Charlotte Gatzweiler. The concentrations of atuveciclib (CDK9i) and BMS-986158 (BETi) used in the toxicity analysis were mentioned in the respective figure, and that of different combinations of these compounds were detailed in **Table 41**.

Table 41. Compound combination concentrations used in zebrafish embryo toxicity analysis.

Combination	atuveciclib (CDK9i)	BMS-986158 (BETi)
1	10 µM	0.25 µM
2	7 µM	0.325 µM
3	13 µM	0.175 µM
4	16 µM	0.1 µM
5	20 µM	0.5 µM
6	50 µM	0.5 µM

Upon collection of zebrafish eggs, they were washed, and incubated in a petri dish with 1X E3 embryonic buffer (**Table 27**) at 28.5°C. At 24h post-fertilization (hpf), the buffer was replaced with 1X E3 embryonic buffer containing 0.2 mM 1-phenyl-2-thiourea (PTU buffer) to inhibit pigmentation.

Zebrafish embryos were treated at 2 days post-fertilization (dpf) in 48-well plates with increasing drug concentrations in PTU buffer and solvent control (DMSO). Effective drug concentrations are generally 10-to 20-fold higher in the zebrafish embryo xenograft model compared to cell culture experiments[194–196]. Therefore, drug concentrations were adjusted to 10 times the *in vitro* metabolic IC50s (e.g., IC50 atuveciclib (CDK9i) = 700-1500 nM; 10-fold = 7-15 µM). During the treatment period (2 dpf to 5 dpf), the embryos were maintained at 34°C. Three embryos were analyzed per treatment condition. Imaging was conducted at 3 dpf and 5 dpf using a stereo microscope. Embryos were monitored for toxicity indicators such as morphological changes (curvature of body, edema), mortality, and responsiveness to external stimuli. MTD was identified as the highest concentration tested that did not result in toxicity signs, and LD as the dose which resulted in mortality.

3.2.12.2 Zebrafish embryo xenotransplantation

The experiments in this and following section (**3.2.12.3 Zebrafish embryo xenograft imaging and treatment**) were conducted by Dr. Sara Najafi in our lab. HSJD-DIPG-007 and KNS42 cells were dissociated as previously described **3.2.1.1. Propagation of cells**. The number of cells was assessed using Vi-CELL XR automated cell counter, subsequently 10^6 viable cells/ml were stained with CM-DiI or DiD (**Table 28**) according to manufacturer's guidelines. In brief, cells were incubated at 37°C for 10 min, then centrifuged and washed three times with FCS-free RPMI medium without phenol red. Subsequently, cells were resuspended in 1 ml of the same medium and incubated with 1 µl of Benzonase for 10 min at room temperature. Following an additional centrifugation, the cells were resuspended to a density of 10^8 cells/ml. A 40 µm cell strainer was used for HSJD-DIPG-007 cells prior to labelling besides described steps.

During microinjections, cells were kept on ice and protected from light. Embryos were anesthetized using 0.02% (w/v) tricaine diluted in PTU buffer. 10 µL of cell suspension were loaded into each capillary and injected into the yolk sac of the embryos using an Eppendorf FemtoJet microinjector and a stereomicroscope. Post-injection, tumor cell bearing zebrafish embryos were identified and maintained at 34°C.

3.2.12.3 Zebrafish embryo xenograft imaging and treatment

1-day post-injection (dpi), tumor bearing zebrafish embryos were placed in 96-well Hashimoto zebrafish imaging plates and imaged with HCM at 34°C with 4x objective by acquiring multiple stacks to evaluate tumor volume. Following imaging, embryos were treated with compounds diluted in PTU for 48h in non-treated 48-well plates at 34°C. 3 dpi, the embryos were anesthetized using 0.02% (w/v) tricaine in PTU buffer and imaged using HCM at 34°C in Hashimoto plates. The change in tumor volume after treatment was evaluated with an automated analysis pipeline created in ImageJ.

The zebrafish-adapted Response Evaluation Criteria in Solid Tumors (RECIST)[196,197] was utilized to calculate and illustrate the drug response. For a tumor to be classified as having progressive disease (PD), its volume must increase by at least 20%. Conversely, for a tumor to be classified as having a partial response (PR), its volume must decrease by more than 30%.

The plots were generated using GraphPad Prism v10.0.2 by me.

3.2.13 Statistical analyses

Drug sensitivity evaluations of epigenetic drug library and compound combination screens following metabolic activity assays was performed using iTReX app (https://itrex.kitz-heidelberg.de/iTReX/)[185], which computed DSS_{asym} for mono and combination treatments, Z', IC25 and IC50, and generated dose-response curves. Hierarchical clustering heat map and PCA analyses of the epigenetic drug screening were performed by Dr. Duy Nguyan. The multiple-ray design screen metabolic activity assay raw data were analyzed using a Shiny App containing an R package designed by Dr. Tim Holland-Letz. RNAseq data was uploaded and analyzed in R2 genomics Analysis and Visualization Platform (https://hgserver1.amc.nl/)[189]. Proteomic data analyses were conducted using ShinyGO0.80

(http://bioinformatics.sdstate.edu/go/)[198] All other statistical analyses were conducted in GraphPad Prism v10.0.2 or R studio (version 4.2.2). The statistical test details and the number of biological replicates for each experiment were detailed in the respective figure legends. Significance was defined as p-value or adjusted (adj.) p-value < 0.05.

3.2.14 The use of artificial intelligence

ChatGPT4 was used to proofread part of the text in this thesis. It was only used for editing purposes, the context was not generated by it. All unpublished, sensitive information was anonymized during the proofreading of the text to prevent its disclosure. It was also employed to write R codes for data analysis, specifically for omics part. DeepL was used to translate the summary to German, which was then proofread by my friend, Anna Hartley.

4 Results

4.1 Establishment of the epigenetic drug library to target H3K27M DMGs

DMGs with H3K27M mutation harbor drastic changes in their epigenome due to polycomb repressive complex 2 (PRC2) sequestration and resulting global decrease in H3K27me3, a post-translational modification (PTM) that is associated with inactive transcription. Furthermore, an increase in H3K27ac on H3 WT is reported in these tumors[47], which is linked to open chromatin and active transcription. Owing to these alterations in the epigenome, H3K27M DMG is considered an epigenetic disease with transcriptional vulnerability. In consequence, a therapy specifically targeting the epigenome might be a promising strategy to tackle this disease. Accordingly, I aimed at identifying epigenetically-acting drugs selectively targeting H3K27M DMG culture models.

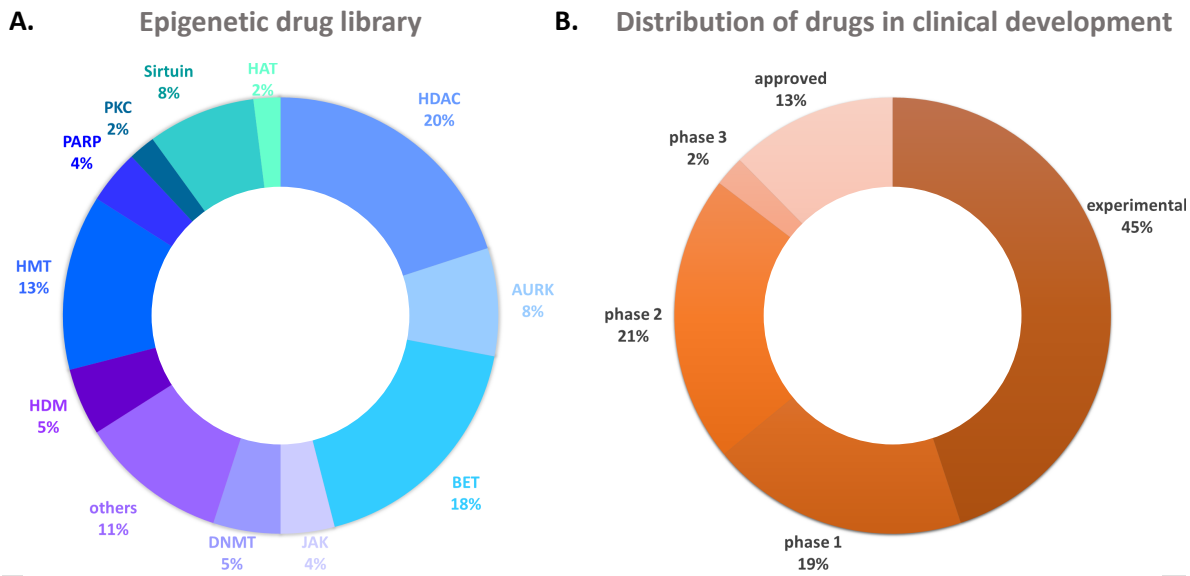

Figure 4. Epigenetic drug library. (**A**) Pie diagram of drug targets and (**B**) the proportion of compound in clinical development. HAT: histone acetyltransferase; HDAC: histone deacetylase; AURK: aurora kinase; BET: bromodomain and extra terminal domain protein; JAK: janus kinase; DNMT: DNA methyltransferase; HDM: histone demethylase; HMT: histone methyltransferase; PARP: Poly (ADP-ribose) polymerase; PKC: protein kinase C.

A drug library, consisting of 102 compounds, was designed and generated by considering various epigenetic regulators from the drug classes of histone acetyltransferase (HAT), histone methyltransferase (HMT), histone demethylase (HDM), histone deacetylase (HDAC), bromodomain and extraterminal domain (BET) containing proteins, DNA methyltransferase (DNMT), aurora kinase (AURK), poly (ADP-ribose) polymerase (PARP), protein kinase C (PKC) and sirtuin inhibitors. Some of the small molecule inhibitors in this library presented as a single member drug class, such as atuveciclib (CDK9i) and MBQ-167 (Rac/Cdc42 inhibitor) (**Figure 4A**). The majority of these compounds were experimental, some were in clinical trials or Food and Drug Administration (FDA) and European Medicines Agency (EMA) approved (**Figure 4B**). The compounds of this library were selected by scientists of the department, before the start of my doctoral studies. Literature research was conducted by me for each compound to define a concentration range centering around their maximum plasma concentration (C_{max}) when applicable. If C_{max} was not available, a range was set based on *in vitro* studies. The library additionally

included two death controls (positive controls), staurosporine (STS, an apoptosis inducer)[199] and benzethonium chloride (BztCl, detergent), as well as dimethyl sulfoxide (DMSO) as a solvent (negative) control. The final drug list with concentration ranges is depicted in **Table 7**.

Prior to the epigenetic drug library screening of each individual cell model in 384-well round-bottom plates, the following pre-tests were performed. To determine the optimal seeding density, metabolic activity assays using CellTiter-Glo (CTG) were employed for each cell model. Moreover, the efficiency of drug dispensing of different volumes by Mosquito HTS liquid handling system was analyzed. For the latter, the responsiveness of selected cell models to the death controls, BztCl and STS, was examined, which indicated the sensitivity level of the cells to the killing compounds. DMSO was used as a negative control.

Optimization of seeding density for each cell model that underwent drug screening was a crucial step for the quality of the assay. Based on the linear relationship between the increasing number of cells and luminescence signal from the CTG (**Figure S1A**), the optimal number of cells to be seeded was determined (**Table 35**) as described in **3.2.2.2.1 Seeding density optimization**.

STS was dispensed in three different volumes, 25 nl, 50 nl and 75 nl at a fixed concentration range, along with BztCl and DMSO at a single concentration with Mosquito HTS liquid handling system. There was no significant difference on STS effect between different dispensing volumes (**Figure S1B**). As higher compound concentrations could be dispensed with 75 nl, this volume was picked as a dispensing volume for all the compounds tested in 384-well plates in the scope of this project.

4.2 Epigenetic drug screen identified CDK9i, BETi and AURKi as top hits for H3K27M DMG models

Having determined optimal seeding densities, a metabolic activity assay was performed after 72h epigenetic drug library exposure for 14 pHGG models with different H3 mutation status (nine H3.3/H3.1K27M, two H3G34R/V, three H3 WT) alongside three non-malignant cell lines (VH7 human juvenile fibroblasts, human fetal astrocytes, HMC3 immortalized human microglia) (**Table 4**).

4.2.1 All models passed quality control

The screen was subject to a stringent set of criteria to determine its usability for subsequent analyses. These criteria were pivotal in assessing the assay performance and consistency, serving as a benchmark for its reliability. The predefined thresholds for these criteria were as follows:

- DMSO raw count was set at a minimum value of 5000 (luminometer-specific threshold).
- Z-prime (Z'), a measure of statistical effect size, was required to be equal to or greater than 0.5.
- The correlation coefficient (R) for replicates needed to exceed 0.7.
- The ratio of the negative control (DMSO), to the positive control (BztCl), had to surpass 7.

If the screen met all these criteria, it was considered reliable, warranting further analytical exploration. Conversely, failure to meet any of these standards necessitated the repetition of the experiment to

ensure the robustness of the results. This approach ensured that only assays with demonstrated reliability proceed to further stages of analysis, thereby enhancing the overall quality of the experimental findings. All cell models passed the QC criteria for downstream analyses (**see Appendix** for further details).

4.2.2 Metabolic activity assay found mivebresib, atuveciclib and alisertib as lead compounds specifically targeting H3K27M DMGs

The drug effect on cell viability was assessed as drug sensitivity score (DSS_{asym}), which was calculated based on 5-paramter integral (5PL) scoring model incorporating the asymmetry coefficient (asym) in addition to the original 4-parameter integral scoring model (4PL) factors. These parameters include the x-coordinate at the inflection point (Xmid), the Hill slope (Slope), the lower and upper asymptotes (Rmin and Rmax, respectively), and the activity threshold (Amin)[185]. The analyses were performed in an automated fashion through the lab-internal iTreX application[185].

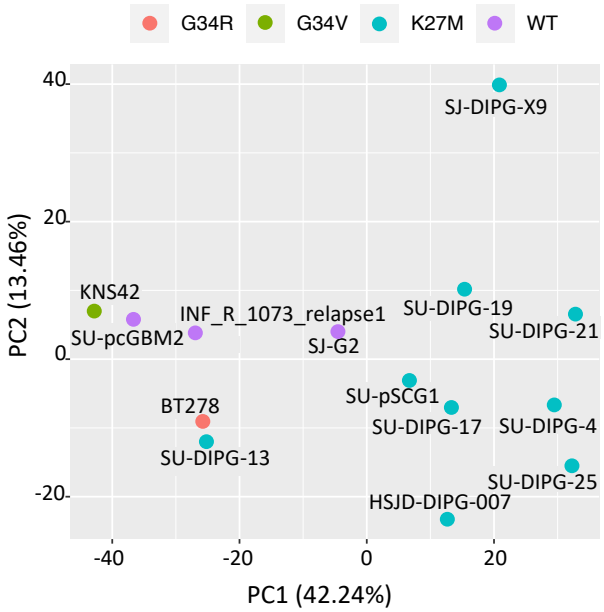

Figure 5. H3K27M DMG models are clustered by PCA. The PCA plot was generated using the DSS_{asym} values of cell models obtained from epigenetic drug library screens. Blue: H3K27M, purple: H3 WT, red: H3G34R, green: H3G34V.

For each cell model, DSS_{asym} for each individual drug was determined. These DSS_{asym} values were subjected to principal component analysis (PCA) (**Figure 5**) to reduce the dimensionality of the data, facilitating easier analysis and preprocessing. The PCA plot revealed that the majority of H3K27M DMG models clustered together and were separated from the rest of the non-H3K27M pHGG models by principal component 1 (PC1) explaining 42% of the variance. This separation suggested that certain drugs had significantly different potency on tumor cells harboring H3K27M mutation.

To pinpoint the compounds resulting in distinctive sensitivity profile for H3K27M DMG cell models, an unsupervised hierarchical clustering heatmap based on DSS_{asym} values was generated (**Figure 6**). The heatmap classified the cell models into two main clusters, one predominantly containing H3K27M DMG models, with the sole exception being SJ-G2 (H3 WT). Only one H3K27M DMG model (SU-DIPG-13) was grouped in the other cluster. Moreover, the compounds were sorted into two primary groups, with the first group encompassing approximately 95% of all drugs, which was further subdivided into two arms. The upper arm, comprising 26 compounds (**Figure 7A**), demonstrated significantly higher sensitization effect on the H3K27M DMG cell models (**Figure 7B**). An in-depth examination of this segment revealed that the majority of these 26 compounds were classified under the drug categories of DNMT (3.9%), JAK (7.7%), AURK (15.4%), BET (15.4%), and HDAC (38.5%) inhibitors. Notably, 50% of all HDAC and AURK inhibitors and 25% of all BET inhibitors were present in the upper arm, indicating an enrichment of HDAC and AURK inhibitors, while the representation of BET inhibitors remained constant. Consequently, the HDAC, AURK, and BET inhibitor classes were identified as the primary hit drug classes. To

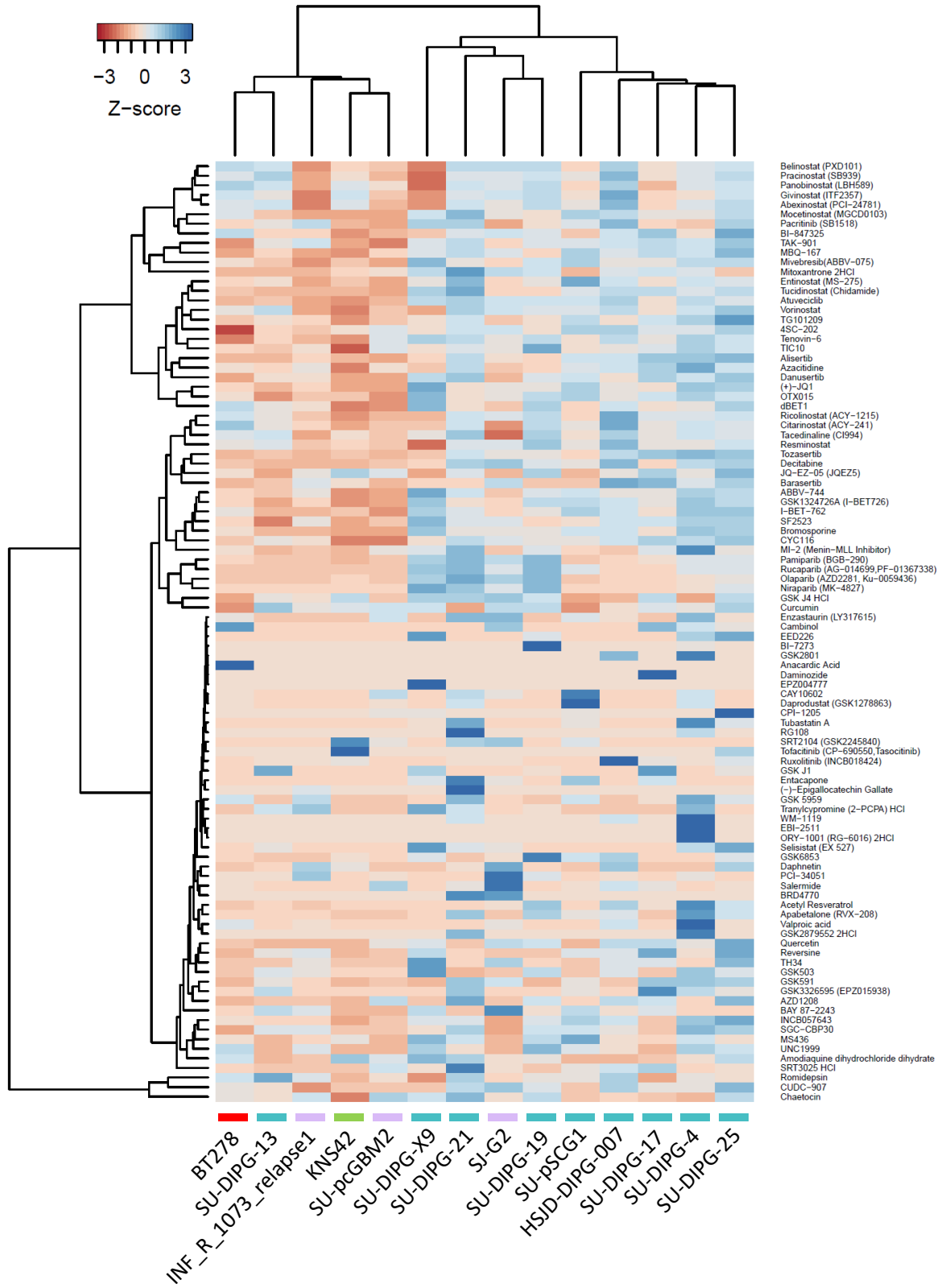

Figure 6. The compound effect on pHGG models visualized by unsupervised hierarchical clustering heatmap. The heatmap was generated based on the sensitivity of the cell models (listed at the bottom, n=14) to the epigenetic drug library (on the right, n=102). Z-score was calculated for each compound across all cell models. A high value indicates sensitivity of a cell model for the respective compound.

decipher the most effective compounds for the cells, specific criteria were employed: a drug needed to achieve a DSS_{asym} of at least 10 in H3K27M DMG cell models, a condition met by all 26 compounds. The delta DSS_{asym} (ΔDSS_{asym}) was determined by deducting the average DSS_{asym} for H3 WT (**Figure 7C**) or H3G34R/V mutant pHGG models (**Figure 7D**) from that of H3K27M DMG models, which had to be at least 5, narrowing the list down to 11 compounds. For these 11 drugs, a selective DSS_{asym} ($sDSS_{asym}$) was calculated by subtracting the mean DSS_{asym} of non-malignant control cells from that of H3K27M DMG cells, which had to be also at least 5 (**Figure 7E**). Ultimately, two HDACis (entinostat, tucidinostat), three AURKis (TAK-901, danusertib, alisertib), and four BETis (mivebresib, dBET1, OTX015, (+)-JQ1), along with two other compounds (atuveciclib (CDK9i) and MBQ-167 (Rac/Cdc42 inhibitor)), were shortlisted. Among these, mivebresib (BETi), alisertib (AURKi) and atuveciclib (CDK9i) exhibited the most significant effect size and showed promise, with all advancing to Phase I/II clinical trials (**NCT02391480**, **NCT01898078** and **NCT02345382**, respectively), which then have been completed. Both atuveciclib (CDK9i) and mivebresib (BETi) reached 100% inhibition for all four cell models. The potency of alisertib (AURKi) was less pronounced, as it did not achieve complete inhibition in HSJD-DIPG-007 and SU-DIPG-19. DSS_{asym} values were above 10 for all compounds and the four selected H3K27M cell models, except for SU-DIPG-19, for which alisertib (AURKi) could only attain DSS_{asym} value of 9.4 (**Figure 9**).

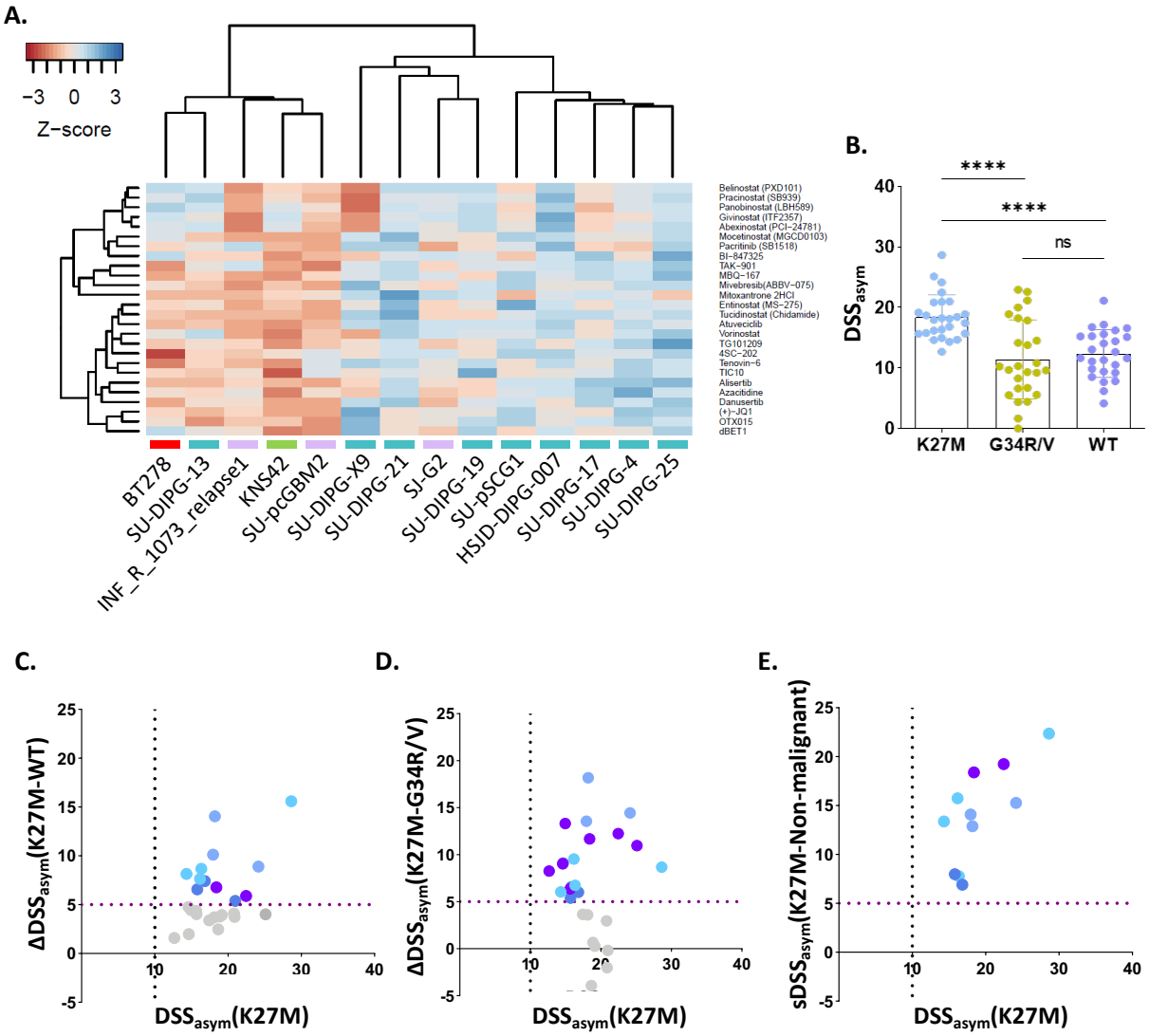

Figure 7. Analysis on the upper arm of the hierarchical clustering heatmap. **(A)** The upper arm comprising 26 compounds. **(B)** Significant selectivity of the 26 compounds for H3K27M cell models. The mean DSS_{asym} values were calculated for each compound within each mutation group. Scatter plot with bar shows mean with standard deviation (SD). Statistics were calculated using one-way ANOVA followed by Tukey's test. ****p<0.0001; ns: not significant. **(C)** The compounds passing DSSasym(K27M) of 10 and ΔDSS_{asym}(K27M-WT) of 5. ΔDSS_{asym} for H3K27M versus H3 WT was calculated by subtracting the mean DSS_{asym} values of H3 WT pHGG models from those of H3K27M DMG models for all 26 compounds, and plotted against DSS_{asym} values of H3K27M models. **(D)** The compounds passing DSS_{asym}(K27M) of 10 and ΔDSS_{asym}(K27M-G34R/V) of 5. ΔDSS_{asym} for H3K27M vs H3G34R/V was calculated by subtracting mean DSS_{asym} values of H3G34R/V DHG models from that of H3K27M DMG models for all 26 compounds, and plotted against DSS values of H3K27M models. (**E**) The compounds passing DSS_{asym}(K27M) of 10 and $sDSS_{asym}$(K27M-Non-malignant) of 5. $sDSS_{asym}$ was calculated by subtracting the mean DSS_{asym} values of non-malignant cell models from H3K27M DMG models for 11 shortlisted compounds. Thresholds of five and 10 are depicted for ΔDSS_{asym}/$sDSS_{asym}$ and DSS_{asym}, respectively. The grey dots indicate the compounds which did not fulfill the cut off criteria. The compounds meeting the criteria were color coded based on their drug classes: blue for BETi, lilac for AURKi, dark purple for HDACi, magenta for others.

4.3 Identification of CDK9i plus BETi as optimal drug combination

Given that monotherapies frequently lead to resistance in cancer patients[200,201], my objective was to develop a combination therapy that could offer improved effectiveness and diminish the potential toxicities associated with treatments using single agents. After pinpointing promising epigenetic hit compounds, I conducted further screening based on metabolic activity measurements. In this phase, each hit compound was individually paired with Translational Drug Screening Unite (TDSU) drug library containing 86 clinically relevant drugs to assess their combined effects.

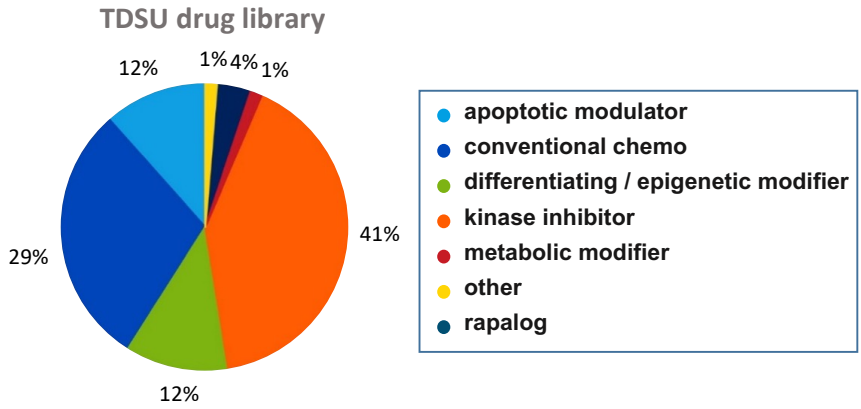

Figure 8. Composition of the TDSU drug library. Adapted from *Peterziel et al., 2022*[169].

The TDSU library has been generated by the INFORM Translational Drug Screening Unite (TDSU) of the department to profile the drug sensitivity of patient-derived fresh tissue cultures obtained through the international precision oncology program INFORM[169]. This library was comprised predominantly of conventional chemotherapeutics and kinase inhibitors (**Figure 8**), which are mainly FDA and EMA approved or in late phase clinical trials. Additionally, 11 more compounds from the drug classes of CDK9, AURK and BET inhibitors (**Table 9**), not represented in the epigenetic drug library but active in clinical trials, were added to this library. Each compound of the TDSU drug library was screened as a single agent and in combination with one of the epigenetic hits (atuveciclib (CDK9i), mivebresib (BETi), alisertib (AURKi)) on one single plate. The hit compounds were combined with the TDSU drug library at 25% inhibitory concentration (IC25) for the respective cell model screened (**Table 36**).

For the combination screen, four H3K27M DMG were selected based on their sensitivity to the epigenetic hits (**Figure 9**) and their resemblance of the patient cohort. These cell models were HSJD-DIPG-007, SU-DIPG-17, SU-DIPG-19 and SU-DIPG-25, and contained H3.3K27M mutation, which is more commonly observed in the DMG patients compared with H3.1/H3.2K27M[15]. Except for SU-DIPG-19, all harbored a *MYC* amplification (**Table 4**). Please **see Appendix** for the dose response curves of non-H3K27M models for atuveciclib (CDK9i), mivebresib (BETi) and alisertib (AURKi).

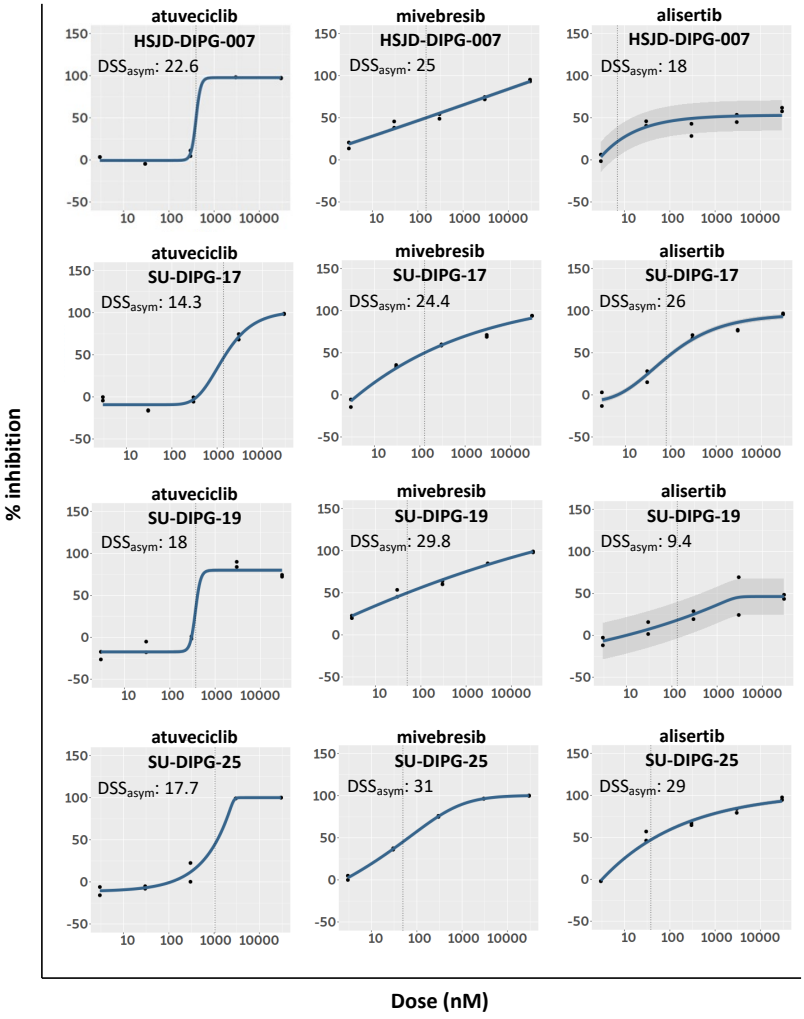

Figure 9. Dose-response curves of the epigenetic hits for four H3K27M DMG cell models selected for the combination screens. y-axis represents the percentage inhibition and x-axis demonstrates the compound concentrations in nM. DSS_{asym} values corresponding to each treatment and cell model are shown on each graph.

In a similar way to the epigenetic drug library screen, the metabolic activity readouts were analyzed for two types of DSS_{asym} values: DSS_{asym}_mono assessing single agent activity and DSS_{asym}_combo evaluating compound combination potency by the iTReX application. Drugs were shortlisted if DSS_{asym}_mono was greater than 10 and the difference between DSS_{asym}_combo and DSS_{asym}_mono, drug combination DSS_{asym} ($dcDSS_{asym}$), was greater than two. Based on these selection criteria, all four H3K27M DMG models responded best to the combination of CDK9 and BET inhibitors. Combination with atuveciclib (CDK9i) narrowed down 11 compounds, among which four of them were BETis (BMS-986158, CC-90010, CPI-0610, I-BET151) (**Figure 10A**). Similarly, combination with mivebresib (BETi) enhanced the sensitivity of the cells to CDK9is (CYC065, AZD4573, KB-0742, zotiraciclib) (**Figure 10B**). Alisertib (AURKi) did not sensitize the cells to any specific drug class (**Figure 10C**). Detailed analysis revealed that, all four H3K27M DMG cell models demonstrated greatest sensitivity to the BETis when combined with atuveciclib (CDK9i) (**Figure 10D**), as evidenced by their elevated $dcDSS_{asym}$ values. Moreover, the combination of BMS-986158 (BETi) with atuveciclib (CDK9i) yielded the highest $dcDSS_{asym}$ (**Figure 10A**), suggesting that atuveciclib (CDK9i) notably elevated the sensitivity of the cell models to BMS-986158 (BETi). Overall, the combination of CDK9i and BETi appeared to be the most

beneficial treatment for H3K27M DMG models. Owing to the highest $dcDSS_{asym}$ observed for BMS-986158, this BETi was selected as a combination partner to atuveciclib (CDK9i).

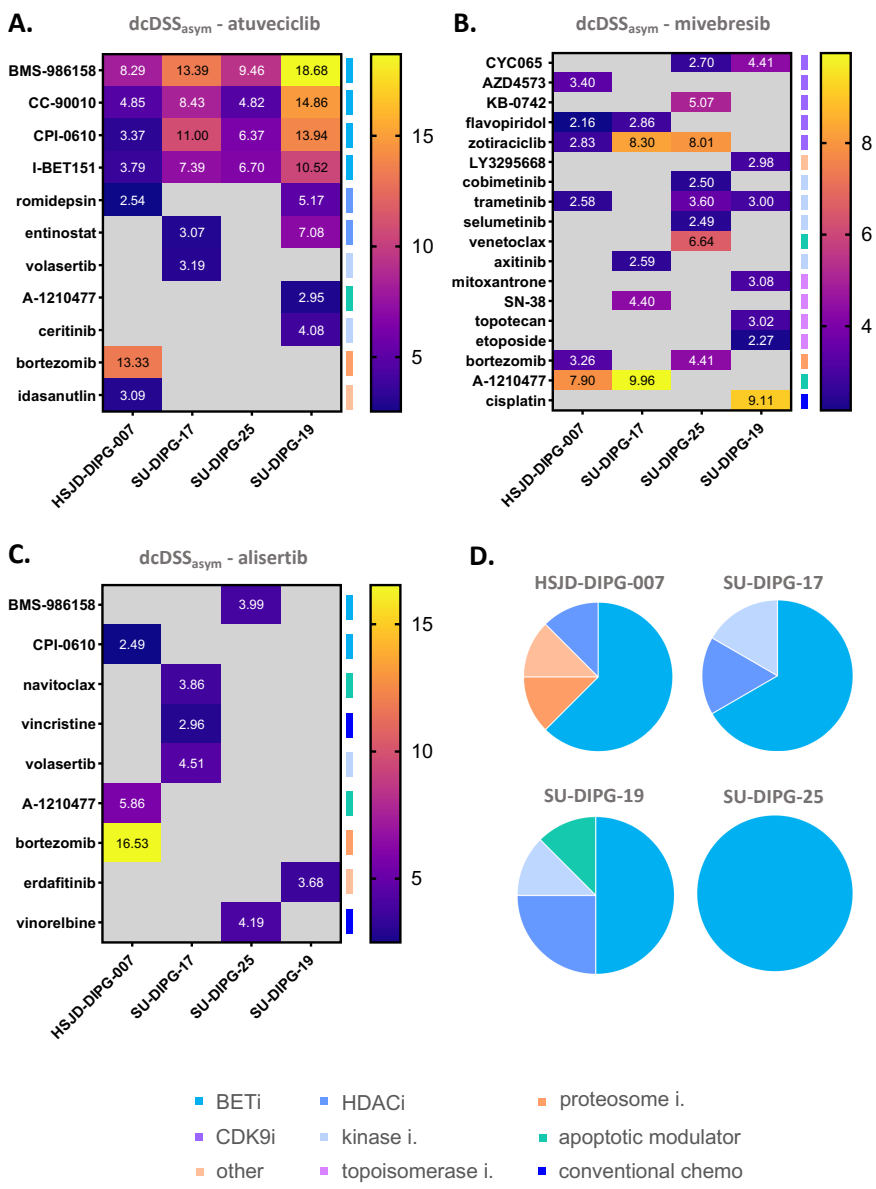

Figure 10. Compound combination screen with epigenetic hits and TDSU drug library. $dcDSS_{asym}$ values of compounds the sensitivity of which increased when combined with **(A)** atuveciclib (CDK9i), **(B)** mivebresib (BETi) and **(C)** alisertib (AURKi) demonstrated as heatmaps. $dcDSS_{asym}$ values were calculated by subtracting the DSS values of the single agent effect of the TDSU library compounds from that of their combined effect with individual epigenetic hits. The compounds presented on the heatmap passed the selection criteria of DSS_{asym}_mono > 10 and $dcDSS_{asym}$ > 2, analyzed separately for four H3K27M DMG cell models. **(D)** Pie charts of drug classes showing elevated potency when combined with atuveciclib for each H3K27M model. Drug classes are color coded for pie charts and indicated next to each heatmap.

4.3.1 Synergy screens with multiple-ray design approach demonstrated that atuveciclib and BMS-986158 synergize for H3K27M DMG

To determine the synergistic effect of the drug pairs, which also has the benefit to reduce the dose and the toxicity[202,203] as well as to circumvent incidence of drug resistance[204], I performed synergy screens for the combination of atuveciclib (CDK9i) and BMS-986158 (BETi). The multiple-ray design approach was employed to elucidate the optimal dose ratio. This methodological approach involved the exploration of predetermined fixed ratios of the compounds on four H3K27M DMG models, HSJD-DIPG-007, SU-DIPG-17, SU-DIPG-19 and SU-DIPG-25. Five ratios, based on which the two compounds

were combined, were analyzed. Similar to the previous screens, metabolic activity assay was performed, and the readout was run on a Shiny App containing an R program designed by Dr. Tim Holland-Letz. The Shiny App analyzed the synergistic interactions between the two compounds based on Loewe additivity model[186]. For all four models, a synergism was detected (interaction index (ii) < 1) for all the ratios (**Figure 11**). For individual analyses of each cell model, please **see Appendix.** According to this finding, atuveciclib (CDK9i) and BMS-986158 (BETi) were selected as a combination treatment for H3K27M DMG throughout this study. For further experiments, the ratio of 0.50 reaching to 50% inhibition was picked as one of the combination treatments (combo low), based on which the two drugs were combined equivalently according to their IC50 values for the respective cell model (**Table 39**).

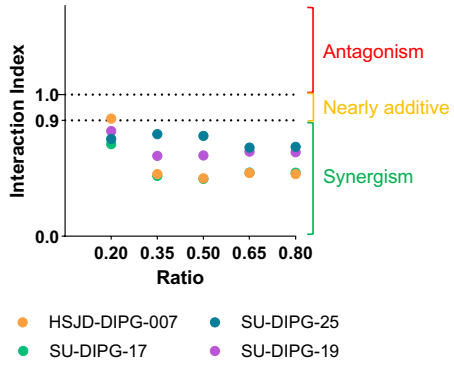

Figure 11. Synergism between atuveciclib (CDK9i) and BMS-986158 (BETi) for four H3K27M DMG cell models at 50% inhibition. Atuveciclib and BMS-986158 were combined in different ratios as depicted on x-axis. y-axis illustrates the interaction index as a measure of the synergy scores. Three days after the cells were seeded, metabolic activity was assessed. ii < 1, synergism; ii = 1, additivity; ii > 1, antagonism. n=2.

4.4 Combination treatment with atuveciclib and BMS-986158 specifically targets H3K27M DMG *in vitro*

Having identified a promising combination treatment with atuveciclib (CDK9i) and BMS-986158 (BETi) for H3K27M DMG models, I investigated the specificity and the mechanism of the compounds and their combination on pHGG cell models with various H3 mutation status *in vitro*. For the single agent treatments, I used the IC50 concentrations for the respective cell model (**Table 38**). Two combinations were analyzed, combo low and combo high (one to one combination of the two drugs at their IC50) unless stated otherwise. By using combo low, combination reaching to 50% inhibition, my objective was to show that combining lower doses of the two compounds could achieve the same level of potency (50% inhibition) as higher doses of each agent when administered alone.

4.4.1 Atuveciclib and BMS-986158 displayed on-target activity in H3K27M DMG cell models

The decrease in Serine2 (S2) phosphorylation of RNAPII C-terminal domain (CTD) is used as a biomarker for the assessment of CDK9 inhibitor effect[54]. Moreover, it was demonstrated for hematological malignancies and some solid tumors that both CDK9 and BET inhibitors result in reduced *MYC* expression as mentioned before. Besides that, HEXIM1 protein level has been analyzed as a pharmacodynamic (PD) biomarker to assess BET inhibitor effect[205,206]. Consequently, I conducted WB analyses with both single agent and combination treatments across various time points to determine when the

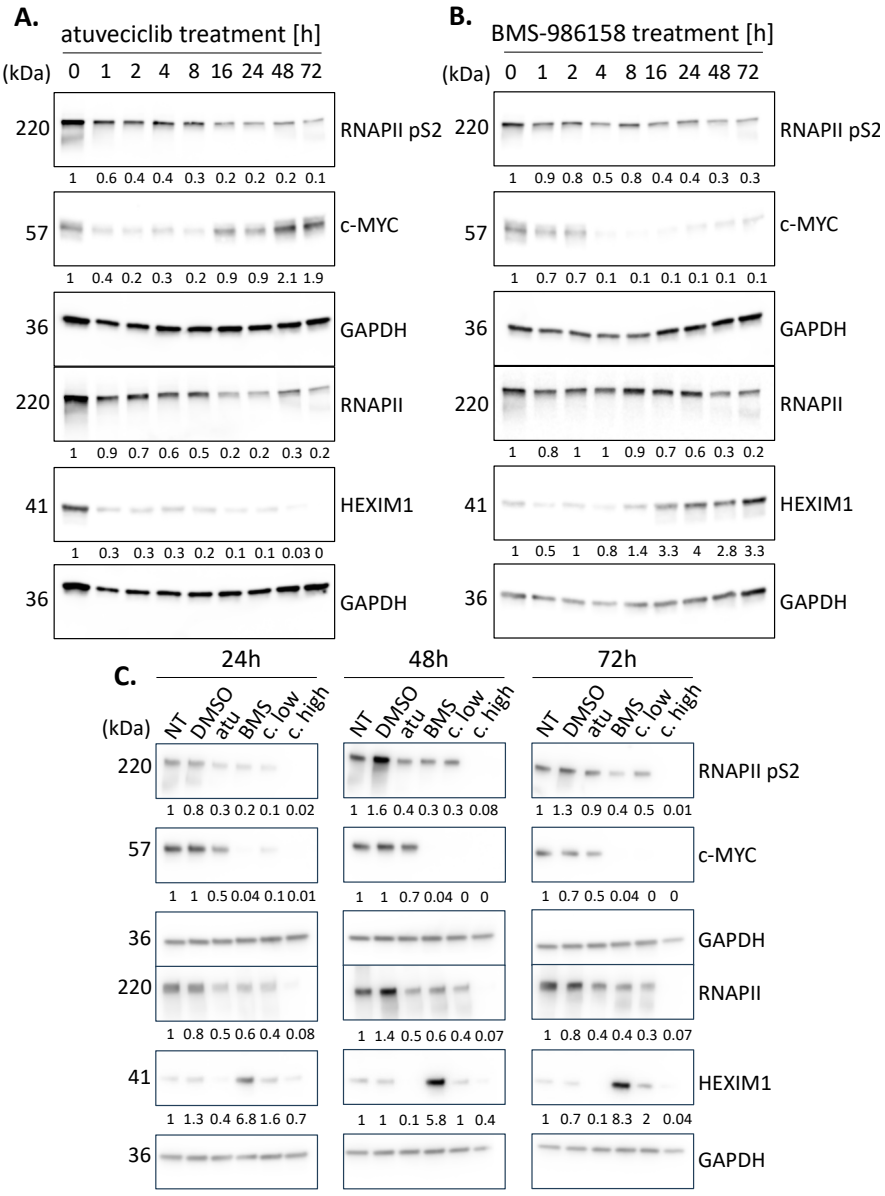

Figure 12. On-target analysis of the effects of atuveciclib (CDK9i), BMS-986158 (BETi) and combination treatments in WB. The levels of RNAPII pS2, c-MYC, RNAPII and HEXIM1 were analyzed for treatments (**A**) 850 nM of atuveciclib (CDK9i) and (**B**) 27 nM of BMS-986158 (BETi) on HSJD-DIPG-007 (H3K27M) cells over the course of time. GAPDH was used as a loading control. (**C**) HSJD-DIPG-007 (H3K27M) cells treated with 0.1% DMSO, 850 nM of atuveciclib (atu), 27 nM of BMS-986158 (BMS), combo low (c. low; 155 nM atu + 5.5 nM BMS) and combo high (c. high; 850 nM atu + 27 nM BMS) for 24h, 48h and 72h. Non-treated (NT) cells were kept as a negative control. WB was performed for RNAPII pS2, c-MYC, RNAPII pS2, HEXIM1 and GAPDH. The numbers beneath the specified proteins represent densitometric evaluations of protein expression, normalized to the loading control. The protein levels of untreated cells were set as 1. n=1.

treatments begin to exert their effects. I observed that atuveciclib (CDK9i) reduced the phosphorylation of RNAPII CTD S2 (RNAPII pS2) as early as 1h post-treatment, achieving nearly total inhibition by 72h. The expression of RNAPII itself also decreased upon atuveciclib (CDK9i) treatment hinting transcriptional process impairment resulting in reduced levels of protein-coding mRNAs (**Figure 12A**). Similarly, treatment with BMS-986158 (BETi) also led to a decrease in RNAPII pS2, although the effect was less pronounced compared to the reduction observed with atuveciclib (CDK9i) treatment. RNAPII levels remained largely stable until 16h after BMS-986158 (BETi) treatment initiation (**Figure 12B**).

MYC expression was observed to decrease 1h following atuveciclib (CDK9i) treatment and began to rise again 16h after the treatment (**Figure 12A**). This pattern may be associated with the cells adapting to the plates post-seeding and subsequently initiating proliferative signaling rather than as a result of CDK9 inhibition. In cells treated with BMS-986158 (BETi), MYC levels drastically decreased beginning 4h after treatment, which is likely to disrupt cell cycle regulation (**Figure 12B**). Moreover, HEXIM1 levels continuously increased following BMS-986158 (BETi) treatment correlating with literature[157] (**Figure 12B**). The elevation in HEXIM1 protein levels observed after BET inhibition is likely to play a

crucial role in regulating gene expression associated with cell cycle control and apoptosis contributing to antiproliferative effects. On the other hand, CDK9 inhibition diminishes the activity of P-TEFb, thereby reducing the requirement for HEXIM1 to regulate P-TEFb. As a result, HEXIM1 levels decline as observed with atuveciclib (CDK9i) treatment (**Figure 12A**) since the transcriptional elongation is hampered due to decreased RNAPII activity.

Another WB analysis was conducted to compare the combination treatment effect to that of single agent treatments. It was found that combo low decreased the levels of RNAPII pS2 and RNAPII comparable to atuveciclib (CDK9i) and BMS-986158 (BETi), while the combo high treatment completely diminished them (**Figure 12C**). The expression of c-MYC was also reduced with combo low treatment, which was abolished even more with combo high (**Figure 12C**). For combo low treatment, HEXIM1 expression was higher and lower compared to atuveciclib (CDK9i) and BMS-986158 (BETi), respectively as expected since it resembles the effect of the single agent treatments alone. Combo high decreased the expression of HEXIM1 almost entirely 24h onwards (**Figure 12C**).

4.4.2 High content microscopy analysis revealed that the combination treatment led to complete remission in H3K27M DMG cell models

For the characterization of the potency and specificity of the compound combination *in vitro* for H3K27M DMG cell models, a high content microscope (HCM) imaging was performed in 3D. I chose two H3K27M DMG cell models, SU-DIPG-17 and HSJD-DIPG-007, and treated them with atuveciclib (CDK9i) and BMS-986158 (BETi) as monotherapies, as well as in combination. The same treatment conditions tested on SU-DIPG-17 and HSJD-DIPG-007 were further analyzed on KNS42 (H3G34V) and HMC3 (microglia) cell lines to ensure the specificity of the treatment effect for H3K27M DMG. This assay was intended to detect spheroid area change

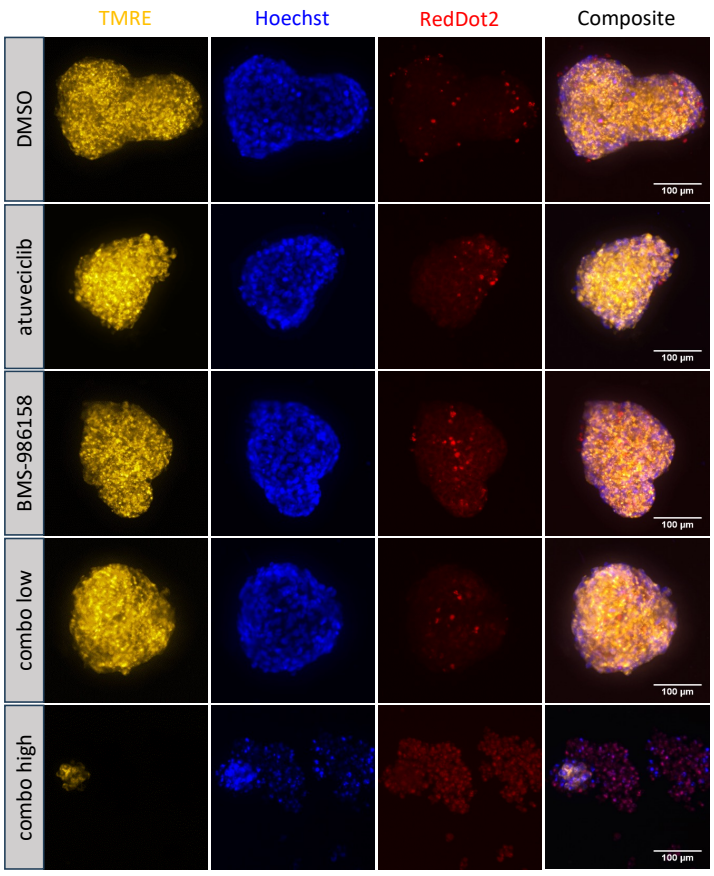

Figure 13. Representative HCM images of SU-DIPG-17 (H3K27M) spheroids treated with different conditions for 72h. Cells were pre-stained with TMRE prior to seeding in 384-well round-bottom plates where they formed 3D spheroids. DNA intercalating dye Hoechst33342 and cell-impermeable dye RedDot2 were added just before the imaging. DMSO was used as a solvent control. Atuveciclib (CDK9i) and BMS-986158 (BETi) were given as a single agent at IC50 for SU-DIPG-17, 1522 nM and 21 nM, respectively. Combo low represents the combination of 277 nM atuveciclib (CDK9i) and 4 nM BMS-986158 (BETi) as predetermined in the synergy screens. Combo high corresponds to the combination of 1522 nM atuveciclib (CDK9i) and 21 nM BMS-986158 (BETi). The scale is the same for all the images with scale bar indicating 100 µm.

from baseline upon treatment based on TMRE live staining, and cell death with Hoechst and RedDot2 staining.

SU-DIPG-17 (H3K27M) cells significantly slowed down the proliferation and achieved a smaller spheroid area when treated with atuveciclib (CDK9i) and BMS-986158 (BETi) compared to solvent control (DMSO). Combo low behaved similar but was slightly less potent compared to single agent treatments. Combo high resulted in almost a full remission (**Figure 13**). The RedDot2 staining clearly demonstrated that while the single agent treatments and the combo low did not induce considerable cell death compared to DMSO, combo high effectively eradicated nearly all the cells (**Figure 13**). Please **see Appendix** for images belonging to other cell models screened.

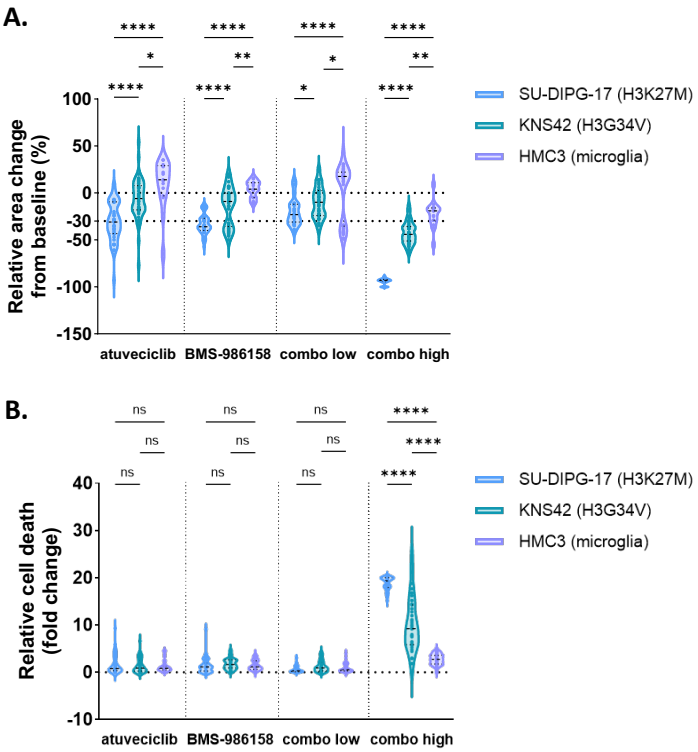

Figure 14. HCM imaging analysis depicting spheroid area change from baseline and cell death. The treatment conditions applied were 1522 nM atuveciclib (CDK9i), 21 nM BMS-986158 (BETi), combo low (277 nM atuveciclib + 4 nM BMS-986158) and combo high (1522 nM atuveciclib + 21 nM BMS-986158). DMSO was kept as a solvent (negative) control. **(A)** Spheroid area change from baseline calculated for each treatment and normalized to the solvent control of the respective cell model. **(B)** The number of death cells were counted for each treatment and normalized to the solvent control of the respective cell model. The data from three biological replicates are pooled for each graph. Statistics were calculated using two-way ANOVA followed by Tukey's test. *p<0.05; **p<0.01; ***p<0.001; ****p<0.0001; ns: not significant. n=3.

Detailed spheroid area analysis for SU-DIPG-17 (H3K27M), KNS42 (H3G34V) and HMC3 (microglia) showed that atuveciclib (CDK9i) and BMS-986158 (BETi) single agent treatments, administered at IC50 concentration for SU-DIPG-17 (H3K27M), facilitated approximately 50% reduction in spheroid area relative to solvent control (**Figure 14A**). Combo low resulted in a similar effect with a less pronounced potency (**Figure 14A**). Combo high expedited 100% partial response (PR) (**Figure 14A**), which is characterized by a minimum reduction of 30% in the total diameters of target lesions (spheroid area in this case), using the baseline sum diameters as a reference according to response evaluation criteria in solid tumors (RECIST)[197] modified for cell culture spheroids. In contrast, the reduction in spheroid area relative to solvent control was less pronounced for KNS42 (H3G34V) and HMC3 (microglia) under the same treatment conditions of SU-DIPG-17 (H3K27M) (**Figure 14A).** Moreover, it was observed that the combo high was significantly and specifically more cytocidal for SU-DIPG-17 (H3K27M) compared with KNS42 (H3G34V) and HMC3 (microglia) whereas there was no significant difference detected between these cell models under single agent treatments and combo low (**Figure 14B**). Similarly, HSJD-DIPG-007 (H3K27M) spheroid area shrank more when treated with combo high compared with KNS42 (H3G34V) and HMC3 (microglia), which were treated with the same

conditions as HSJD-DIPG-007 (H3K27M) (**Figure S2A**). Furthermore, the combo high resulted in significantly higher cell death for HSJD-DIPG-007 (H3K27M) (**Figure S2B**).

Overall, I found that the effect of monotherapies on H3K27M DMG models was cytostatic, while combo high facilitated cell death, which was much less pronounced in non-H3K27M models. Combo low elicited an effect size comparable to that of single agents.

4.4.3 Combinatorial treatment induced apoptosis in H3K27M DMG cell models

Having discovered that the combo high induced cell death, I sought the mechanism of cell death and speculated that the observed effect was potentially attributable to apoptosis, given that both CDK9 and BET inhibitors are recognized for their capability of inducing apoptosis[207–209].

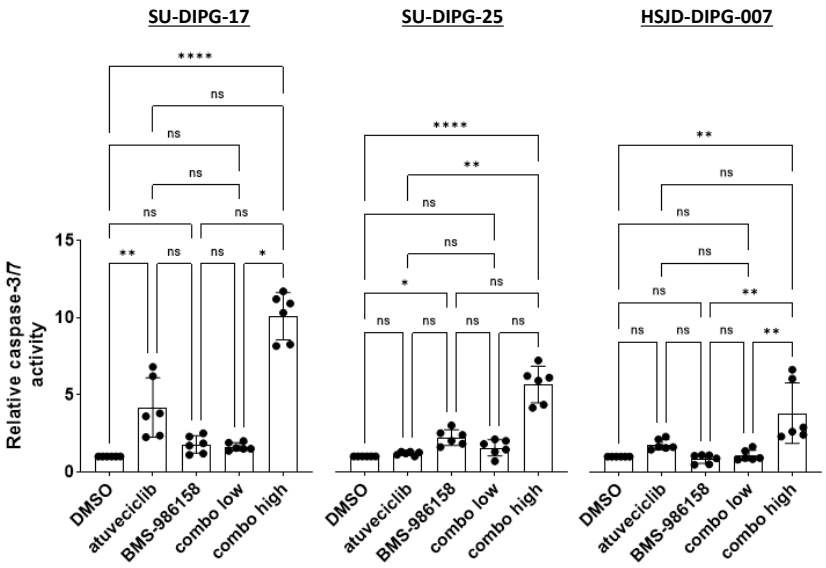

Figure 15. Caspase-3/7 activity analysis of H3K27M DMG cell models upon treatment. The cells were treated according to **Table 38** for 24h before harvested. DMSO was given as a solvent control. Kruskal-Wallis test was performed for the statistical analysis. *p<0.05; **p<0.01; ***p<0.001; ****p<0.0001; ns: not significant. n=3.

To detect apoptosis, I performed a caspase-3/7 activity assay with three H3K27M DMG cell models, SU-DIPG-17, SU-DIPG-25 and HSJD-DIPG-007 upon 24h treatment. I found that the atuveciclib (CDK9i) alone induced caspase-3/7 activation, hence apoptosis, in SU-DIPG-17 but not in SU-DIPG-25. Although there was a slight increase in caspase-3/7 activity in HSJD-DIPG-007 after atuveciclib (CDK9i) treatment, it was not significant compared to the solvent control (DMSO). BMS-986158 (BETi) induced apoptosis when administered alone only in SU-DIPG-25. Combo low did not facilitate caspase-3/7 activity in any of the cell models, whereas combo high elicited apoptosis significantly in all cell models. Overall, single agent treatments demonstrated cell model specific apoptosis induction, whereas combo low did not induce any caspase-3/7 activity, indicating that its effect was mainly cytostatic for H3K27M DMG cell models. Correlating with the results of the HCM screen (**Figure 14B, Figure S2B**), combo high was detected to be cytocidal inducing apoptosis (**Figure 15**).

4.4.4 Combinatorial treatment prevented colony formation of H3K27M DMG in soft agar colony formation assay

One of the defining traits of malignant cells is their ability to grow independently of anchorage, which is a significant marker of tumorigenic potential and an indication of the capability of cells to initiate tumors. This characteristic allows cancer cells to thrive without the attachment to a solid surface, a

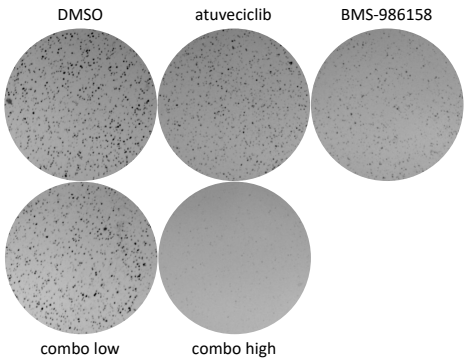

Figure 16. Soft-agar colony formation assay. 8,000 SU-DIPG-17 (H3K27M) cells were seeded on 0.3% soft-agar and subsequently treated with atuveciclib (CDK9i), BMS-986158 (BETi), combo low and combo high according to **Table 38**. DMSO was used as a solvent control. n=1.

fundamental deviation from normal cell behavior, which typically requires attachment for growth and survival[210]. In my study, I explored the effects of single agent and combination treatments on the anchorage-independent growth of SU-DIPG-17 (H3K27M) cells via soft agar CFA. This assay is a well-established method for evaluating the ability of cells to proliferate without substrate attachment, thereby mimicking the 3D growth environment of tumors[211]. The results of the treatments revealed that while the individual treatments atuveciclib (CDK9i), BMS-986158 (BETi) as well as the combo low, showed a reduction in colony formation relative to the solvent control, it was the combo high that proved most effective, completely inhibiting colony formation (**Figure 16**). Atuveciclib (CDK9i) and combo low diminished the colony formation almost to same extent. Unexpectedly, the effect of BMS-986158 (BETi), however, was more pronounced compared to atuveciclib (CDK9i) and combo low (**Figure 16**). This suggests that atuveciclib (CDK9i) and BMS-986158 (BETi) are acting through different mechanisms, and BMS-986158 (BETi) is crucial for preventing colony formation.

4.5 The combination of atuveciclib and BMS-986158 sensitized the H3K27M DMG cells to radiotherapy

As radiotherapy (RT) is the standard of care for DMG patients, I next sought whether the combination treatment would induce radiosensitization, or could be used in conjunction with RT. For that, I collaborated with Prof. Marlon Veldwijk. The data presented in this section are the results of experiments designed by me and performed by Marlon's team.

Before combining the drug treatment with RT, the radiosensitivity of three H3K27M DMG cell models, HSJD-DIPG-007, SU-DIPG-17, SU-DIPG-19, was investigated in the absence of compound combination treatment in a CFA. Each cell model exhibited varying degrees of sensitivity to irradiation, with SU-DIPG-19 showing the highest sensitivity and SU-DIPG-17 displaying the lowest to increasing radiation doses (**Figure 17A**). Surviving fraction (SF) 50 and 75 corresponding to IC50 and IC25, respectively was calculated for each cell model (**Table 42**) to be further analyzed in conjunction with compound combination. Similarly, the radiosensitivity of BT278 (H3G34R) and INF_R_1073_relapse1 (H3 WT) pHGG cell models was also attempted to be analyzed, however, it could not be detected due to the low plating efficiency of these cells, which is essential for a colony formation assay (CFA).

Subsequently, the effects of compound combinations along with RT were analyzed using a metabolic activity assay, which allowed for the evaluation of various compound and RT combinations in a robust way. SF50 and SF75 detected in CFA were used for the respective cell model. The goal was to identify optimal compound combinations inducing radiosensitivity to be further validated in CFA. It was essen-

tial to ensure that the observed reduction in metabolic activity resulted from the radiosensitizing effects of the compound combinations, rather than from the compound treatment alone. Thereby, every compound combination was tested also in the absence of RT. The cells were irradiated 24h after the compound treatment and incubated for 72-120h to cover at least two doubling times to observe the RT effect for the metabolic activity assay. As the sensitivity of SU-DIPG-19 cells to death control (BztCl) decreased in each experiment, they were excluded from further analyses of RT (**see Appendix** for the details of it). Concentrations used for combo low (**Table 40**) were examined in a dilution series to obtain a concentration range, and it was observed for both HSJD-DIPG-007 (**Figure S3**) and SU-DIPG-17 (**Figure S4**) that dilution factors of 3 and 10, hence the higher compound concentrations, facilitated complete inhibition even in the absence of RT (SF100). This finding indicated that these concentrations were too high to estimate the benefit of combination with RT. Compound combination administered alone at dilution factor of 1 resulted in reduced proliferation, which decreased slightly more in combination with RT. Dilution factors of 0.3 and 0.1 clearly distinguished between the 0 Gy, SF50, and SF75 doses. Administering the compound combination at these dilution factors without RT did not cause inhibition. However, when used in conjunction with RT, the treatment of cells with the combo low led to a substantial reduction in metabolic activity, achieving nearly 50% inhibition. Accordingly, combo low was further evaluated in a CFA with the dilution factors of 1, 0.3 and 0.1.

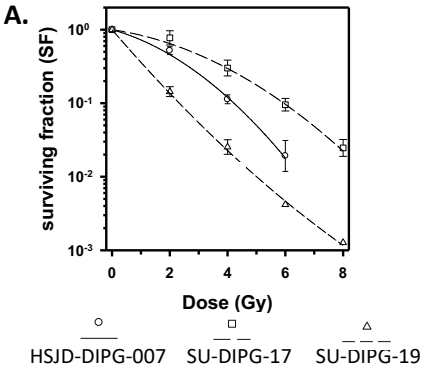

Table 42. Calculated SF50 and SF75 values for H3K27M DMG cell models.

	HSJD-DIPG-007	SU-DIPG-17	SU-DIPG-19
SF50 (IC50)	1.8 Gy	2.8 Gy	0.7 Gy
SF75 (IC25)	0.9 Gy	1.5 Gy	0.3 Gy

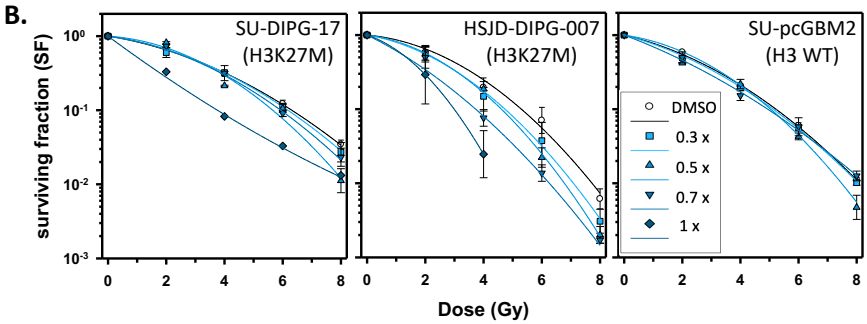

Figure 17. Radiosensitivity and radiosensitization analyses. (**A**) Radiosensitivity assessment of three H3K27M DMG cell models in a CFA. y-axis demonstrates Gy doses applied and x-axis shows surviving fraction (SF). n=3. (**B**) Radiosensitization examination conducted using two H3K27M DMG models, HSJD-DIPG-007 and SU-DIPG-17, and one H3 WT pHGG model, SU-pcGBM2 in a CFA. Combo low treatment conditions detailed in **Table 40** were tested in a concentration range. In the 1x condition for SU-DIPG-17, atuveciclib (CDK9i) was administered at 277 nM alongside BMS-986158 (BETi) at 4 nM. Conversely, for HSJD-DIPG-007 under the 1x condition, atuveciclib (CDK9i) was delivered at 155 nM with BMS-986158 (BETi) at 5.5 nM. For the H3 WT model SU-pcGBM2, atuveciclib (CDK9i) was given at 277 nM together with BMS-986158 (BETi) at 5.5 nM in the 1x condition, The 0.7x, 0.5x, and 0.3x concentrations were derived by multiplying the drug concentrations in the 1x condition of each respective cell model by 0.7, 0.5, and 0.3, respectively. DMSO was used as a negative control. y-axis demonstrates Gy doses applied and x-axis shows surviving fraction (SF) for all three pHGG models. n=3.

Given that the incubation period in a CFA is longer than in a metabolic activity assay, treatment effects are more discernible as cells undergo multiple replications. Consequently, it was anticipated that using dilution factors of 0.1 and 0.3 in combination with RT would produce a more pronounced effect in the CFA compared to the metabolic activity assay. Interestingly, the CFA validations performed for HSJD-DIPG-007 and SU-DIPG-17 demonstrated that dilution factor of 0.1 did not create any difference when administered alone or in combination with RT. Therefore, it was excluded from further analyses. Instead, more dilution factors were added spanning 0.3 and 1 to preserve the concentration range. The additive effect of the compound combination in conjunction with RT was clearly observed up to dilution factor of 0.7 for SU-DIPG-17, for which the curves overlapped. The highest dose of the compound combination, at dilution factor of 1, resulted in a linear survival curve separated from the rest, demonstrating that even a minor increase in radiation dose corresponded to a proportional increase in the effect (**Figure 17B**). Notably, radiosensitizing effect of the compound combination was evident for HSJD-DIPG-007 (**Figure 17B**), indicating that the compound combination therapy in conjunction with RT improved clonogenic cell death.

As the compound combination was structured based on the data of H3K27M DMG cell models and it was aimed to test the specificity of the combination therapy for H3K27M DMG throughout this study, I also examined SU-pcGBM2 (H3 WT) cells in a CFA to assess whether the compound combination would induce radiosensitization in a pHGG cell model which does not harbor H3K27M mutation. The analysis demonstrated that the compound combination did not sensitize these cells for radiotherapy (**Figure 17B**), which further signifies potential for use alongside radiation therapy for H3K27M DMG.

4.6 Multi-omics analysis identified the MoA of atuveciclib, BMS-986158 and their combination for H3K27M DMG cell models

Following the initial characterization of the single agent and combination treatments, I conducted bulk RNA sequencing (RNAseq) and mass spectrometry (MS) based protein analyses to elucidate the underlying mechanism of action (MoA) of atuveciclib (CDK9i) and BMS 986158 (BETi), as well as that of their synergistic effect observed for H3K27M DMG models. To achieve this, I employed four H3K27M DMG models, HSJD-DIPG-007, SU-DIPG-17, SU-DIPG-19 and SU-DIPG-25, and treated them with solvent control (DMSO), atuveciclib (CDK9i) and BMS-986158 (BETi), and the combo low for 24h. The concentrations administered for both single agents and the combo low were calibrated to induce a 50% inhibition after 72h, a level specific and unique for each cell model. This resulted in a uniform effect size across all cell types as a comparative baseline. The reason why the combo low was selected as the combination treatment, but not combo high, was to avoid apoptosis induction in the cells, as this would trigger rapid and global decay of messenger RNAs (mRNAs) before other cellular processes, such as DNA fragmentation[212]. Furthermore, inducing apoptosis could mask the actual expression level of apoptosis-related genes, such as caspases, *BCL-2* family and *TP53*[213]. Moreover, it was aimed to detect the mechanism resulting in the synergistic effect of the two compounds by treating the H3K27M DMG cells with combo low.

For proteomics alone, an additional H3 WT pHGG cell model, INF_R_1073_relapse1, was included and subjected to the same individual treatment conditions as the four H3K27M DMG cell models, enabling a pairwise comparison between each mutant and the WT model.

4.6.1 The samples passed quality control pre- and post-omics analyses

Quality control analyses were conducted on each replicate data to identify potential batch effects that could have arisen from sample generation, the use of different biological replicates, and the sequencing order during RNAseq and proteomic analyses.

Prior to RNAseq, a Bioanalyzer analysis of RNA samples was performed, which revealed that each sample achieved a high RNA integrity number (RIN), approaching 10, indicating that the RNA samples were intact and of high quality (**see Appendix** for further details). t-Distributed Stochastic Neighbor Embedding (t-SNE) of the RNAseq data of 80 samples indicated that the cell models clustered according to their intrinsic biological characteristics rather than the treatments applied (**Figure S5A**). Biological replicates for each condition clustered closely together, with the exception of one replicate from the atuveciclib (CDK9i) treated SU-DIPG-17 cells, suggesting the absence of batch effects. SU-DIPG-17 outlier was excluded from further analysis.

MS analysis of cell lysates identified between 8,000 and 9,000 proteins, with 7,000 to 8,300 of these quantified across all 128 samples submitted. The threshold for protein quantity set for further analysis was 5,000, which all samples met (**see Appendix** for further details). Uniform Manifold Approximation and Projection (UMAP) performed with proteomic data highlighted that the H3K27M cell models clustered together, also based on their intrinsic features, and were distinct from INF_R_1073_relapse1 (H3 WT) samples (**Figure S5B**). Six samples belonging to various treatments of SU-DIPG-17, SU-DIPG-19 and SU-DIPG-25 grouped with INF_R_1073_relapse1 (H3 WT) samples, hence excluded from further analysis (**see Appendix** for more details).

4.6.2 Gene expression analysis identified that DNA damage response pathways were negatively regulated by atuveciclib and BMS-986158

RNAseq raw counts for each sample were uploaded on R2: Genomics Analysis and Visualization Program (http://r2.amc.nl) for further analysis with dataset name: Exp DIPG - Oehme - 80 - DESeq2_rlog - io2312, and were subjected to DESeq2 analysis to identify differentially expressed genes between each treatments vs DMSO. Kyoto Encyclopedia of Genes and Genomes (KEGG) pathway analysis of pooled data of all four atuveciclib (CDK9i) treated H3K27M DMG cell models found that DNA replication was downregulated, as well as RNA transport, proteosome and mitogen-activated protein kinase (MAPK) signaling pathway. Importantly, DNA damage response (DDR) pathways such as mismatch repair, homologous recombination, base excision repair, and non-homologous end joining were downregulated (**Figure 18A**). Gene Set Enrichment Analysis (GSEA) based on Molecular Signature Database (MSigDB) Human collections Hallmarks 2020 gene sets displayed that E2F and MYC targets, both associated with DNA replication and cell proliferation, were significantly downregulated (**Figure 18B**). Decrease in the expression of mitotic spindle target genes suggests that cell division was negatively regulated (**Figure 18B**).

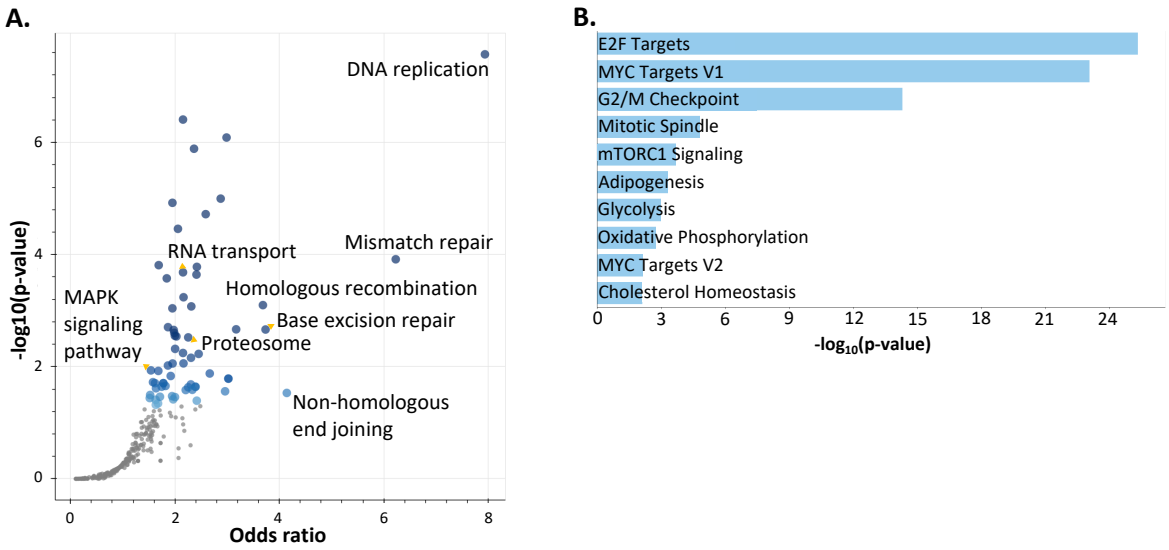

Figure 18. Pathway analysis of the pooled RNAseq data of downregulated genes upon atuveciclib (CDK9i) treatment. (**A**) KEGG pathway analysis of negatively regulated pathways under CDK9 inhibition depicted as a volcano plot. Each point represents a single term, plotted by the corresponding odds ratio (x-axis) and -$\log_{10}$(p-value) (y-axis) from the enrichment results of the input query gene set. The larger and darker-colored the point, the more significantly enriched the input gene set is for the term. (**B**) Enrichment analysis of gene expression data using MSigDB Hallmarks 2020, presented as a bar chart showing the significance of pathway enrichment.

Similarly, BMS-986158 (BETi) resulted in downregulation of DNA replication and cell cycle. DDR pathways were also dysregulated, though to a lesser extent compared to atuveciclib (CDK9i) treatment (**Figure 19A**). Downregulation of purine and pyrimidine metabolism (**Figure 19A**) also hints that cell proliferation was negatively affected due to depletion of nucleotide pools essential for DNA and RNA synthesis. This can facilitate cell cycle arrest and reduced cell proliferation, impacting tissue growth and repair[214]. KEGG analysis of BMS-986158 (BETi) treatment demonstrated that it upregulated autophagy and lysosome pathways (**Figure 19B**) indicating increased activation of autophagy pathways and enhanced lysosomal function in H3K27M DMG cell models. This could aid in the degradation of cancer cells or in the elimination of defective proteins and organelles that might contribute to cancer progression[215]. GSEA supported KEGG pathway analysis by showing that MYC and E2F targets were downregulated (**Figure 19C**), as observed for atuveciclib (CDK9i) treatment.

Combo low treatment displayed combined characteristics of atuveciclib (CDK9i) and BMS-986158 (BETi). DNA replication and cell cycle were downregulated, as well as purine and pyrimidine metabolism (**Figure 20A**), and macroautophagy was upregulated (**Figure 20B**) according to KEGG pathway analysis. The expression of genes associated with cell cycle were differentially regulated between combo low and solvent control treatment for all four H3K27M DMG cell models (**Figure 21**). Differently from the single agent treatments, spliceosome was downregulated with combo low treatment (**Figure 20A**), which can lead to the accumulation of R-loops (RNA-DNA hybrids) that are a significant source of genomic instability and DNA damage[216,217]. Similarly to purine and pyrimidine metabolism, downregulation of one-carbon metabolism observed for combo low is also linked to decrease nucleotide synthesis, as well as methylation reactions and energy production[218].

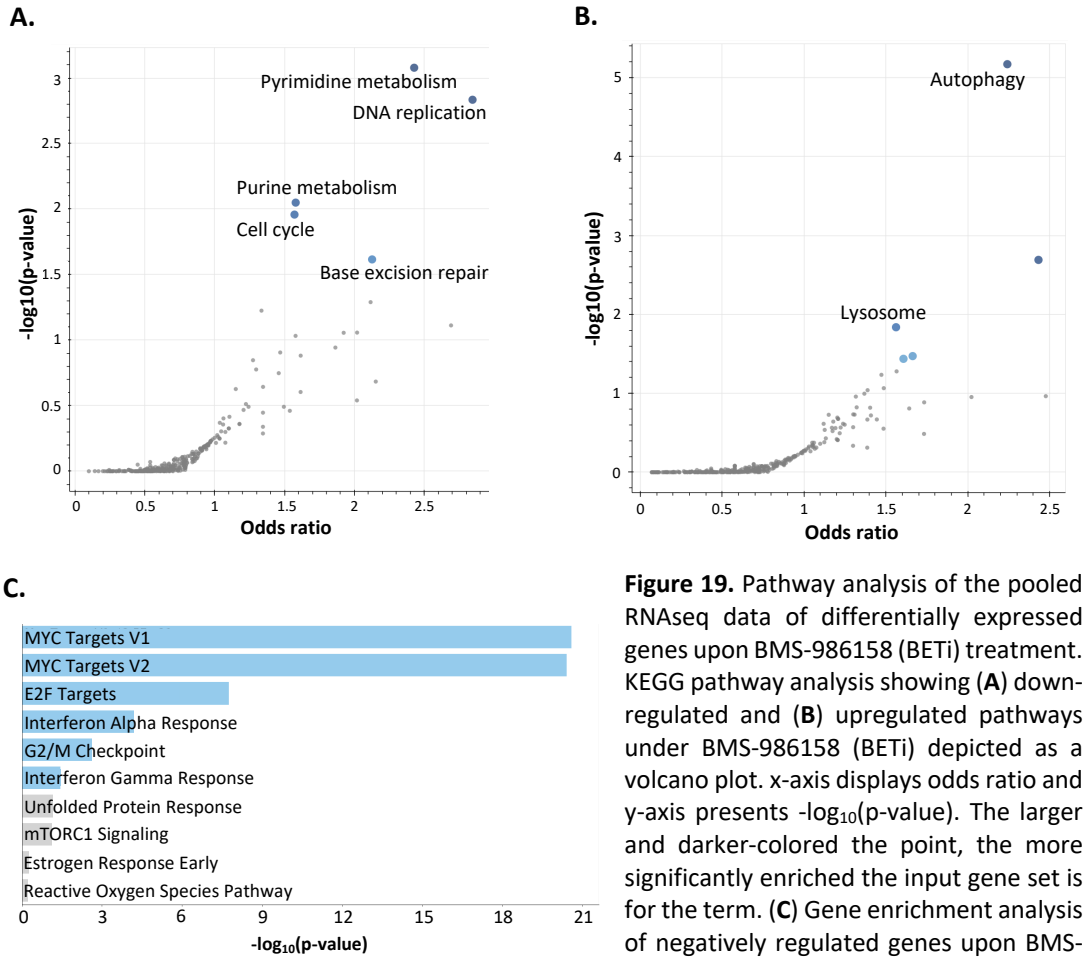

Figure 19. Pathway analysis of the pooled RNAseq data of differentially expressed genes upon BMS-986158 (BETi) treatment. KEGG pathway analysis showing (**A**) down-regulated and (**B**) upregulated pathways under BMS-986158 (BETi) depicted as a volcano plot. x-axis displays odds ratio and y-axis presents -$\log_{10}$(p-value). The larger and darker-colored the point, the more significantly enriched the input gene set is for the term. (**C**) Gene enrichment analysis of negatively regulated genes upon BMS-986158 (BETi) treatment using MSigDB Hallmarks 2020, illustrated as a bar chart.

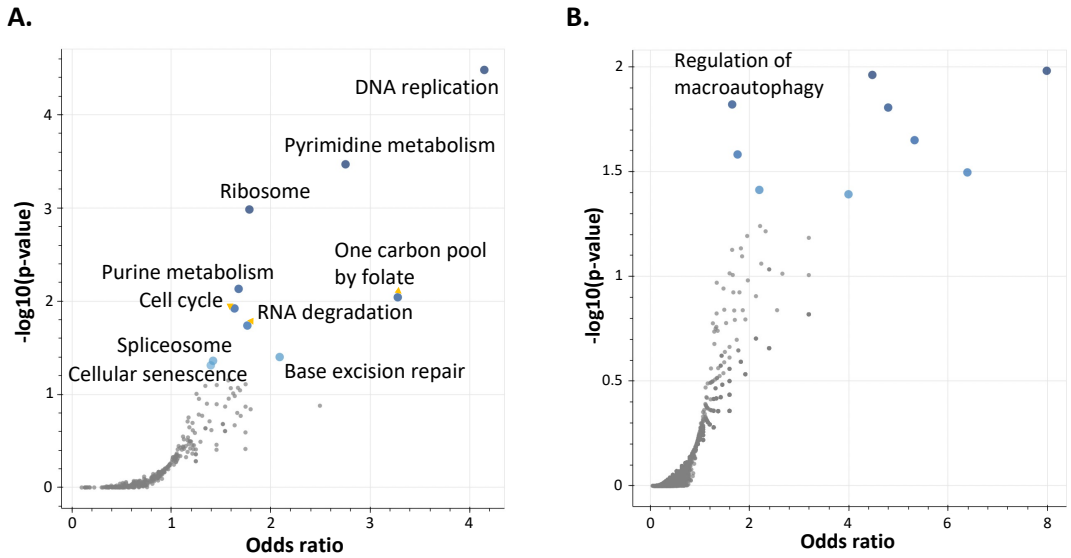

Figure 20. Pathway analysis of the pooled RNAseq data of differentially expressed genes following combo low treatment. KEGG pathway analysis of (**A**) downregulated and (**B**) upregulated pathways under combo low treatment shown as a volcano plot. x-axis displays odds

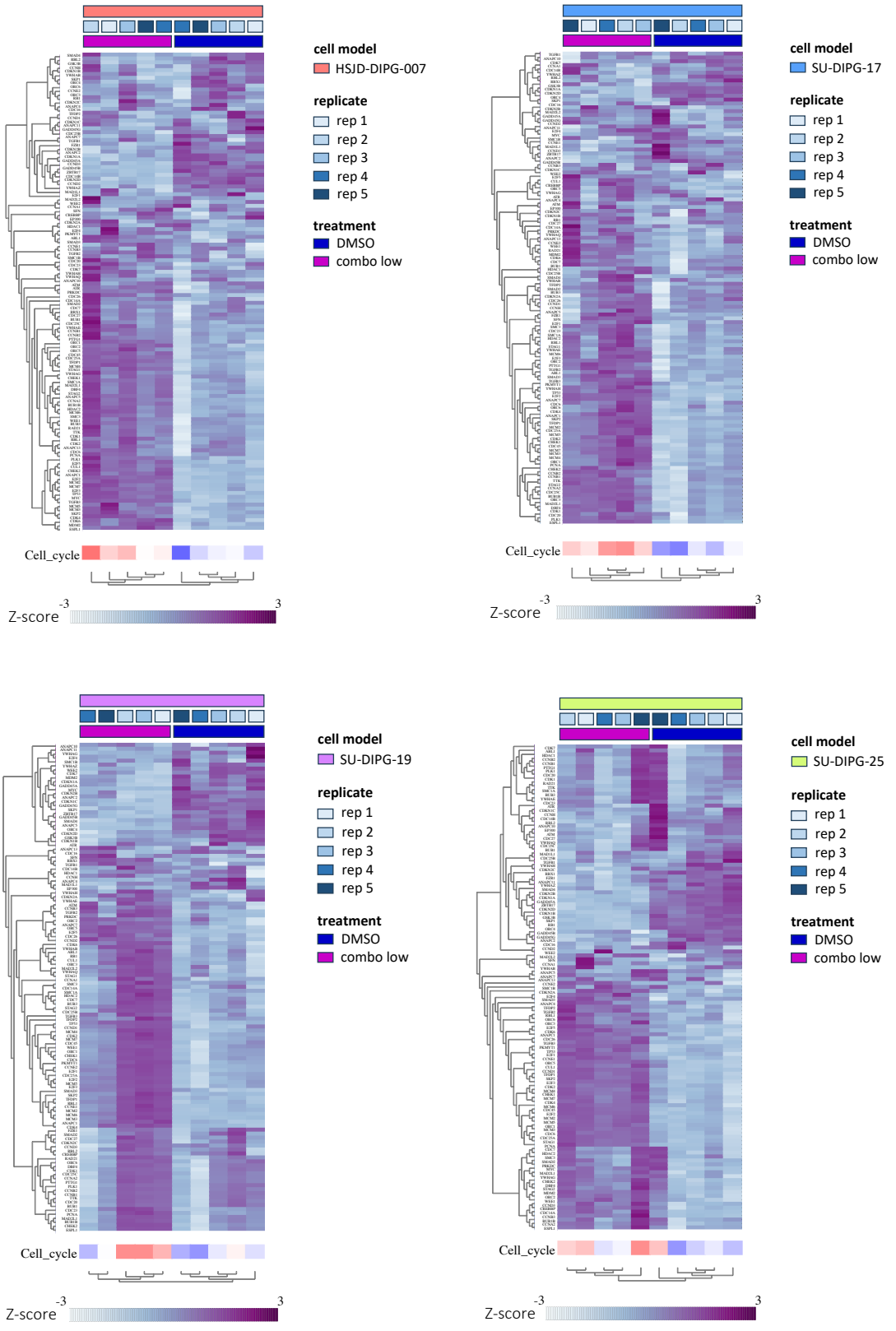

Figure 21. Hierarchical clustering heatmap of KEGG cell cycle pathway genes for all four H3K27M DMG cell models under combo low and DMSO treatments. Overall differential changes in KEGG cell cycle pathway were depicted below the heatmaps for each replicate (rep). Blue and red boxes represent negative and positive regulation, respectively.

Both CDK9 and BET inhibitors are known to decrease *MYC* expression in diverse hematological malignancies *in vitro*, such as diffuse large B-cell lymphoma[219] and hepatocellular carcinoma[220]. Accordingly, I analyzed the *MYC* expression level under different treatments across cell models. Atuveciclib (CDK9i) treatment did not alter *MYC* expression in any of the four cell models (**Figure 22**), correlating with the WB results (**Figure 12A**). BMS-986158 (BETi) treatment resulted in four-fold reduction in HSJD-DIPG-007 and approximately two-fold in SU-DIPG-25 (**Figure 22**). No change was observed for SU-DIPG-17 and SU-DIPG-19 (**Figure 22**). Combo low had a similar effect as BMS-986158 (BETi) for HSJD-DIPG-007 (**Figure 22**). These findings suggest that atuveciclib (CDK9i) did not change *MYC* expression in H3K27M DMG *in vitro* in the first 24h and BMS-986158 (BETi) had a cell model specific effect for *MYC* expression. On the other hand, MYC target genes were downregulated under both single agent and combo low treatments in HSJD-DIPG-007 (**Figure S6A**), SU-DIPG-17 (**Figure S6B**), SU-DIPG-19 (**Figure S6C**) and SU-DIPG-25 (**Figure S6D**).

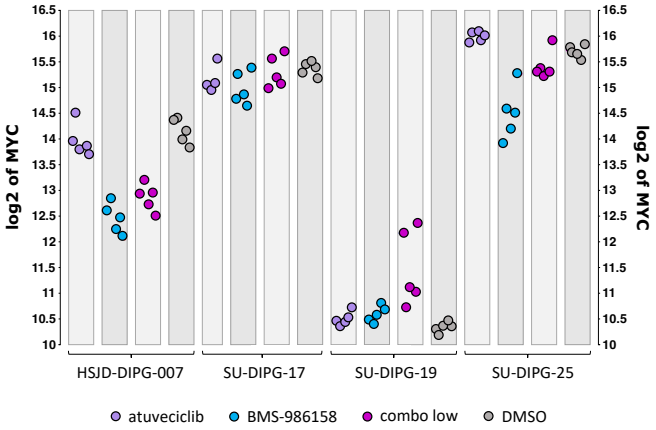

Figure 22. *MYC* expression in four H3K27M DMG cell models under different treatments. Each treatment is color-coded.

Overall, RNAseq conducted on H3K27M DMG cell models demonstrated that the two inhibitors downregulated essential cellular pathways such as DDR, spliceosome function, and the metabolism of purines and pyrimidines, which are vital for cancer cell proliferation and survival. Additionally, both inhibitors effectively inhibited DNA replication, potentially leading to cell cycle arrest. Notably, BMS-986158 (BETi) also upregulated autophagy and lysosomal pathways, distinguishing itself with a unique therapeutic mechanism that not only impedes critical functions in cancer cells but also enhances cellular clean-up process. This dual action could provide a comprehensive approach to cancer therapy by simultaneously disrupting cancer cell growth and promoting the degradation of defective cellular components.

4.6.3 Proteomics analysis confirmed gene expression findings

One of the objectives of the LC-MS/MS analysis was to assess whether the treatments affected H3K27M and H3 WT models differently. KEGG pathway analysis of the downregulated proteins demonstrated that the treatments had similar effects on these cells. Pooled data of atuveciclib (CDK9i) treated H3K27M DMG models showed that pathways associated with cell cycle and transcription were downregulated (**Figure 23A**), which were also observed for that of INF_R_1073_relapse1 (H3 WT) (**Figure 23B**). Gene ontology (GO) analysis for biological processes highlighted that DNA repair was negatively regulated in the cells independent of H3K27 status under atuveciclib (CDK9i) treatment (**Figure S7A** and **Figure S7B**).

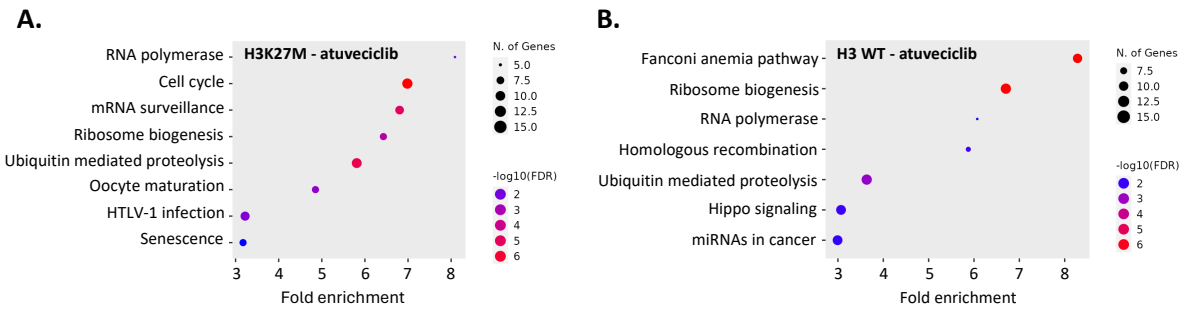

Figure 23. Downregulated pathways under atuveciclib (CDK9i) treatment in (**A**) H3K27M and (**B**) H3 WT models. Each point represents a pathway, plotted against fold enrichment on the x-axis. Point color indicates the statistical significance of enrichment -$\log_{10}$(FDR) value from two to six, light purple to dark red, and size reflects the number of involved genes (N. of Genes), emphasizing pathways with greater biological impact and gene involvement.

KEGG pathway analysis for BMS-986158 (BETi) data displayed that few pathways were downregulated in H3K27M models (**Figure 24A**). On the other hand, many GO terms associated with transcription (**Figure S8A** and **Figure S8B**) was negatively regulated independent of the presence of H3K27M mutation. Moreover, upregulation of autophagy was observed for BMS-986158 (BETi) treated H3K27M models (**Figure S8C**), similar to transcriptomics results (**Figure 19B**). The pathways highlighted for pooled analysis of H3 WT data suggest a disruption in processes like cell cycle regulation, signaling pathways (like epidermal growth factor receptor family, ERBB), and cellular transport mechanisms. Downregulation in aminoacyl-transfer RNA (tRNA) biosynthesis might suggest effects on protein synthesis, essential for cell growth and maintenance. The observed downregulation patterns could be associated with specific disease states, cellular stress responses, or other physiological or pathological conditions. Alterations in Fanconi anemia pathway could indicate a response to DNA damage (**Figure 24B**).

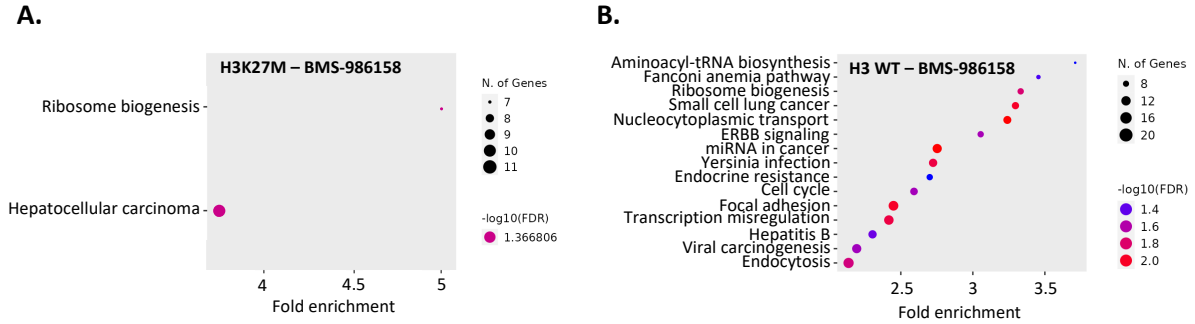

Figure 24. Downregulated pathways under BMS-986158 (BETi) treatment in (**A**) H3K27M and (**B**) H3 WT models. Each point represents a pathway, plotted against fold enrichment on the x-axis. Point color indicates the statistical significance of enrichment -$\log_{10}$(FDR) value from two to six, light purple to dark red, and size reflects the number of involved genes (N. of Genes), emphasizing pathways with greater biological impact and gene involvement.

Combo low impact on both H3K27M (**Figure 25A, Figure S9A**) and H3 WT models (**Figure 25B, Figure S9B**) were comparable showcasing crucial cellular processes related to cell division, DNA repair, and protein regulation being significantly influenced by downregulation.

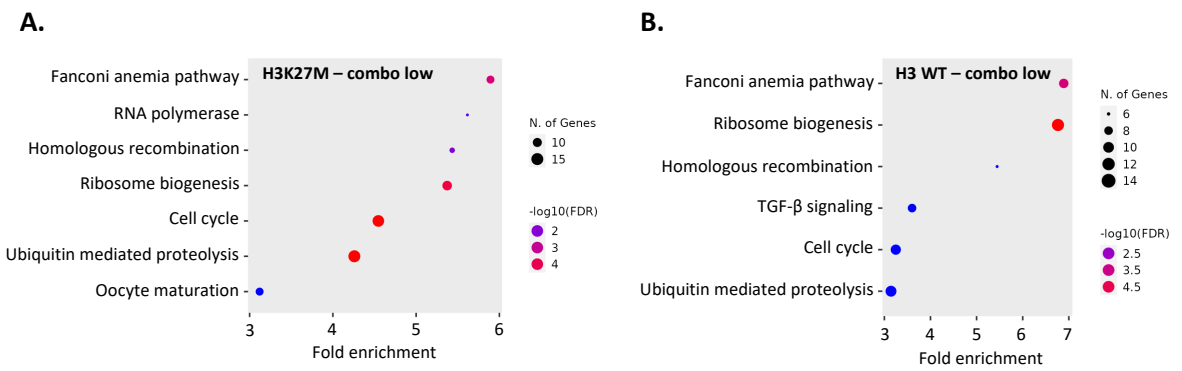

Figure 25. Downregulated pathways under combo low treatment in (**A**) H3K27M and (**B**) H3 WT models. Each point represents a pathway, plotted against fold enrichment on the x-axis. Point color indicates the statistical significance of enrichment -$\log_{10}$(FDR) value from two to six, light purple to dark red, and size reflects the number of involved genes (N. of Genes), emphasizing pathways with greater biological impact and gene involvement.

Overall, proteomics results correlated with that of transcriptomics, and highlighted that combination of atuveciclib (CDK9i) and BMS-986158 (BETi) negatively affected cell cycle, transcription and DNA repair in pHGG cells, however this was regardless of the H3K27 status of the models examined.

4.7 DNA damage exploration displayed increased γH2A.X level under combo high treatment

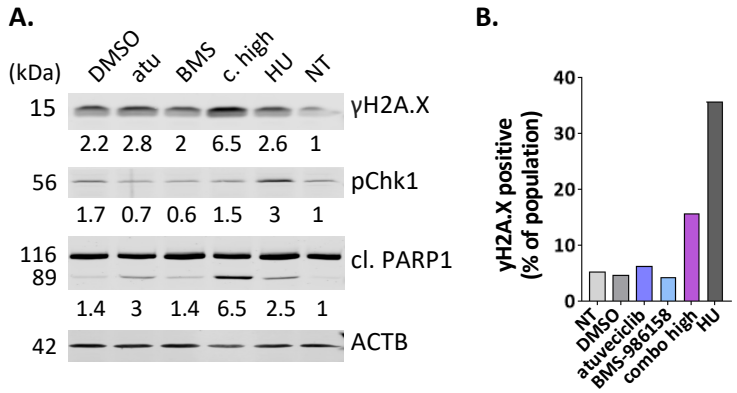

Figure 26. DNA damage and apoptosis induction by combo high. HSJD-DIPG-007 (H3K27M) cells treated with 850 nM atuveciclib (atu; CDK9i), 27 nM BMS-986158 (BMS; BETi) and combo high (155 nM atu + 5.5 nM BMS) for 16h. 1 mM HU and 0.1% DMSO were kept as positive and negative (solvent) controls, respectively. Non-treated (NT) cells were also tested to examine the effect of DMSO. **(A)** Immunoblots showing γH2A.x, pChk1 and cleaved (cl.) PARP1. ACTB (β-actin) served as a loading control. The numbers beneath the specified proteins represent densitometric evaluations of protein expression, normalized to the loading control. The protein levels of NT cells were set as 1. Data was generated and provided by Prof. Krämer's group. **(B)** Flow cytometry analysis showing γH2A.x positive populations for each treatment. n=1. Data was generated by the help of Prof. Krämer's group.

To understand whether the CDK9 and BET inhibition induces DNA damage in H3K27M DMG cells, WB and flow cytometry analyses were performed to measure γH2A.X levels, which is a well-known marker for DNA damage[221]. HSJD-DIPG-007 (H3K27M) cells were treated with atuveciclib (CDK9i), BMS-986158 (BETi) and combo high for 16h. Hydroxyurea (HU) and DMSO were kept as positive and negative controls, respectively. Both methods displayed that HSJD-DIPG-007 (H3K27M) cells exhibited intrinsic DNA damage, which increased under combo high treatment as evidenced by elevated γH2A.X levels in WB (**Figure 26A**) and flow cytometry (**Figure 26B**) experiments. Checkpoint kinase 1 phosphoryla-

tion (pChk1) was assessed to monitor DDR pathway activation[222]. While HU increased the phosphorylation of Chk1, atuveciclib (CDK9i), BMS-986158 (BETi) and combo high did not elevate pChk1 levels (**Figure 26A**), suggesting that DDR pathways were not activated, in line with RNAseq findings showing the negative regulation of cell cycle checkpoints. Moreover, combo high facilitated PARP1 cleavage (**Figure 26A**), which is a well-established marker for apoptosis[223,224], confirming the results of caspase-3/7 activity assay. Altogether, combo high induced DNA damage and apoptosis.

4.8 Compound combination was potent *in vivo* in zebrafish embryo xenograft model

Zebrafish embryo xenograft models have emerged as a valuable tool in cancer research, particularly for predicting drug responses *in vivo*. The use of zebrafish embryos, specifically through injections into the yolk sac, offers a unique platform for observing the effects of potential anticancer compounds on human cancer cells. This method leverages the transparent nature of zebrafish embryos, allowing for real-time visualization of tumor progression and metastasis, as well as the direct observation of drug effects on tumors[225,226]. Moreover, the genetic and physiological similarities between zebrafish and humans make this model particularly useful for studying cancer biology and drug metabolism. Researchers can utilize genetically engineered or chemically treated zebrafish to explore specific pathways and the genetic basis of drug resistance. The model is also highly scalable, enabling medium- to high-throughput screening of drugs, which is cost-effective and efficient[227]. In line with this, I investigated the compound combination effect on different pHGG cell models *in vivo* using zebrafish embryos. Before investigating the compound effect on the xenografts, the toxicity of the drugs and their combinations was assessed on zebrafish embryos. This part of the experiments was performed by an MD student of the lab, Charlotte Gatzweiler, based on my experimental design. Maximum tolerated dose (MTD) and lethal dose (LD) for BMS-986158 (BETi) were determined to be 0.5 µM and 2.5 µM, respectively (**Figure S10**). Atuveciclib (CDK9i) was not lethal in the applied concentrations (up to 50 µM) (**Figure S10**). As their combination was of interest, a toxicity analysis was performed with the combinations of the two compounds in different ratios as also tested in the synergy screens (**Table 41**). When 0.5 µM of BMS-986158 (BETi) and 20 µM and 50 µM atuveciclib (CDK9i), were applied to the buffer surrounding the embryos, they exhibited morphological changes, hence these combinations were considered toxic (**Figure S11**). Zebrafish embryos injected with either fluorescently labelled HSJD-DIPG-007 (H3K27M) or KNS42 (H3G34V) were incubated in buffer containing a non-toxic combination with 7 µM atuveciclib (CDK9i) and 0.325 µM BMS-986158 (BETi) for 48h (**Figure 27A**). Of note, it is a common rule of thumb that approximately 1:10 to 1:20 of the drug is taken up by the embryos and reaching the tumor[226]. Preliminary results demonstrated that the combination therapy resulted in significant shrinkage of HSJD-DIPG-007 (H3K27M) cell mass in the yolk sac of zebrafish embryos (**Figure 27B**, **Figure S12A)** ($p = 0.0011$), which was not the case for the KNS42 (H3G34V) model (**Figure 27C, Figure S12B**) ($p = 0.8537$) This further supported the specificity of the combination therapy for H3K27M DMG and hold potential for subsequent mouse xenograft studies. Please **see Appendix** for representative images of zebrafish early larvae bearing HSJD-DIPG-007 (H3K27M) and KNS42 (H3G34V) cells.

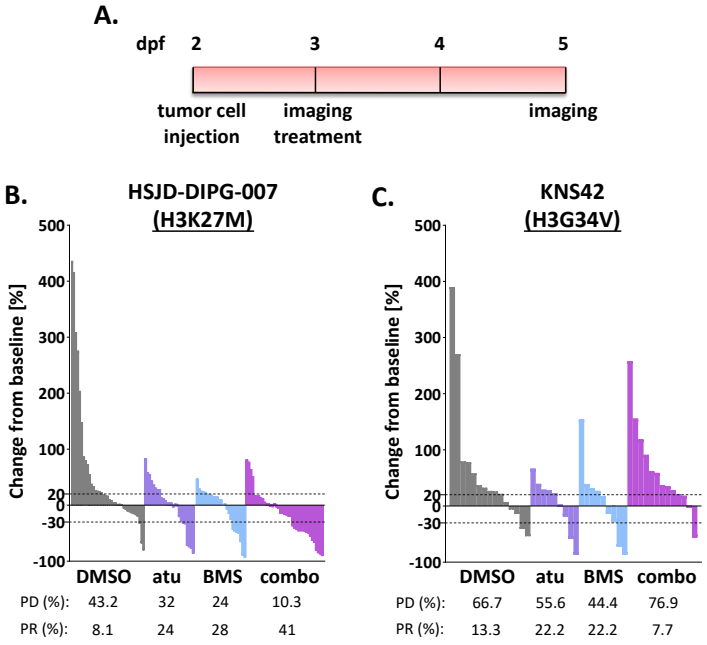

Figure 27. Waterfall plot demonstrating the change in tumor volume (%) from baseline for each individual zebrafish embryo xenograft. (**A**) Timeline of *in vivo* zebrafish embryo xenograft experiments. Zebrafish embryos were injected with fluorescently labelled. Waterfall plots showing change in tumor volume for individual zebrafish larvae bearing (**B**) HSJD-DIPG-007 (H3K27M) and (**C**) KNS42 (H3G34V), and treated with 7 µM atuveciclib (CDK9i), 0.325 µM BMS-986158 (BETi), their combination and 0.1% DMSO as a solvent control. n = 9-39 fish per treatment group. Progressive disease (PD) indicates percentages of the population showing 20% increase from baseline. Partial response (PR) displays 30% decrease from baseline.

4.9 Blood brain barrier penetrability of atuveciclib and BMS-986158 was calculated to be moderate

The blood-brain barrier (BBB) serves as a defense mechanism, protecting the brain from harmful effects of drugs and foreign molecules. Nonetheless, it is vital for treatments targeting neurological conditions to penetrate the brain at therapeutic levels[228]. Therefore, I investigated the BBB penetrability of atuveciclib (CDK9i) and BMS-986158 (BETi) with support of the group of Dr. Kristian Pajtler. They have calculated BBB scores for the compounds of interest based on *Gupta et al.*[228], which assesses passive diffusion across the BBB by incorporating seven physicochemical characteristics: the number of aromatic rings, number of heavy atoms, molecular weight, number of hydrogen bond acceptors, number of hydrogen bond donors, topological polar surface area, and pK_a[184]. The BBB score ranged from a low probability of penetrating the BBB (BBB score approaching 0) to a high probability (BBB score approaching 6), demonstrating that a higher BBB score is indicative of an increased likelihood of crossing the BBB[184,228]. The scores for atuveciclib (CDK9i) and BMS-986158 (BETi) were determined to be 2.03 and 2.73, respectively, corresponding to a moderate BBB penetrability (**Table 43**). Despite that, they remain promising for clinical applications as this presents an opportunity for structural remodeling of these compounds to enhance their BBB penetrability.

Table 43. BBB scores of atuveciclib (CDK9i) and BMS-986158 (BETi).

Compound	BBB score
atuveciclib (CDK9i)	2.03 (moderate)
BMS-986158 (BETi)	2.73 (moderate)

4.10 The effect of blood brain barrier penetrant CDK9i, KB-0742, on H3K27M DMG was found to be similar to atuveciclib

During the course of this study, two compounds, atuveciclib (CDK9i) and BMS-986158 (BETi) were rigorously tested across various assays with the ultimate goal being to advance a potential combination therapy to clinical trials. A partnership was established with a pharmaceutical company, Kronos Bio., that produces KB-0742 compound similar in class to atuveciclib (CDK9i). Leveraging this collaboration, I analyzed KB-0742 (CDK9i), which is currently in clinical trials and BBB penetrant (BBB score of 4.06, high penetrability), using same pHGG cell models with different H3 mutation status. This allowed me to directly compare the effects of a clinically relevant drug with my results, providing a comprehensive understanding of their relative performances and informing future clinical applications. The metabolic activity assay results of KB-0742 (CDK9i) resembled that of atuveciclib (CDK9i), achieving high DSS_{asym} values, between 14 and 18, and 100% inhibition in H3K27M DMG cell models (**Figure 28**). In contrast to atuveciclib (CDK9i), KB-0742 (CDK9i) required higher concentrations to achieve 50% inhibition.

Furthermore, I examined the synergistic effect of KB-0742 (CDK9i) with two BET inhibitors, BMS-986158 and CC-90010, which is known to be BBB penetrant[229,230] on SU-DIPG-17 (H3K27M). The interaction between KB-0742 (CDK9i) and BMS-986158 (BETi) (**Figure S13A**), as well as KB-0742 (CDK9i) and CC-90010 (BETi) (**Figure S13B**), was primarily additive, though the synergism was achieved with the combination of few concentrations.

Overall, KB-0742 (CDK9i) showed promise for further investigation *in vivo* and subsequent progression to clinical trials.

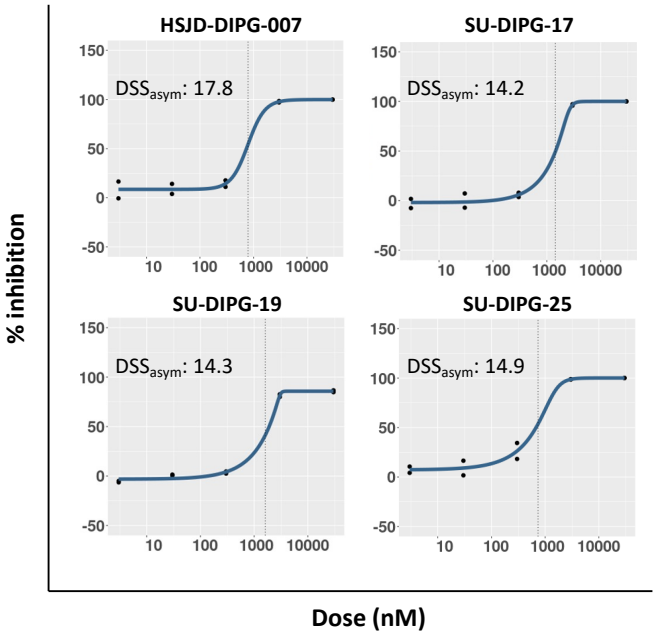

Figure 28. Dose-response curves of KB-0742 (CDK9i) for four H3K27M DMG cell models. y-axis represents the percentage inhibition and x-axis demonstrates the compound concentrations in nM. DSS_{asym} values corresponding to each cell model are shown on each graph.

5 Discussion

Treating pediatric patients with DMG presents significant challenges, primarily owing to the aggressive nature of the tumor, complex biology, and critical location in the brain. These tumors are often situated in vital midline structures such as the thalamus, brainstem, and spinal cord, where surgical interventions are inadvisable due to the high severe neurological damage risk. The resistance of these tumors to conventional treatments such as chemotherapy and radiotherapy further complicates clinical management. Although radiation may temporarily alleviate symptoms, it falls short of being curative, and chemotherapy tends to be ineffective in halting disease progression or significantly prolonging life[231,232]. To date, no chemotherapeutic agents, immunotherapies, or molecularly targeted treatments could extend survival for children suffering from DMG. Additionally, the effectiveness of these therapies is often limited by inadequate penetration of the BBB and the resistance mechanisms developed by DMGs. Recent studies have identified epigenetic dysregulation often resulting from K27M point mutation in one of two histone genes, *H3F3A* or *HIST1H3B*, which rewires the epigenome, enhancing the oncogenic potential of these tumors[233]. While it was initially discovered that the H3K27M mutation acted by sequestering and inactivating the PRC2 enzyme, more recent research suggests that residual PRC2 activity is maintained[234]. Moreover, the activity of PRC2 is necessary for sustaining a stem cell-like state in these cancer cells. The involvement of the H3K27M mutation in super enhancer-like elements, which reshape the enhancer landscape, together with the accumulation of PRC2 at tumor suppressor genes, leads to a notable block in differentiation and a continuous cycle of proliferation. These characteristics are crucial in propelling the oncogenic properties of DMG cells harboring the H3K27M mutation[233–236]. Given the substantial role epigenetic alterations play in the pathogenesis of H3K27M DMGs, epigenetic therapy emerges as a particularly promising approach. Consequently, the development and application of epigenetic therapies could offer a breakthrough in treating this devastating pediatric cancer, shifting the current therapeutic paradigm and potentially prolong OS.

5.1 Compound screens

I compared the drug sensitivity of 14 patient-derived HGG cell models and three non-malignant control cell lines through high-throughput epigenetic drug library screening of 102 compounds. Atuveciclib (CDK9i), mivebresib (BETi) alisertib (AURKi) were selected as hit compounds specifically targeting H3K27M DMGs, which also advanced into clinical trials. In non-H3K27M pHGG cell models, these inhibitors resulted in notably low DSS_{asym} values and relatively high IC50s. The shared mode of action among BET, CDK9 and AURK inhibitors lies in their capacity to disrupt essential regulatory pathways governing cell cycle progression and cell survival. By targeting distinct elements within these pathways, these inhibitors prompt cell cycle arrest and apoptosis, effectively curbing the proliferation of cancer cells. Specifically, BET inhibitors hinder transcriptional regulation by blocking the assembly of transcriptional complexes[160,237]. CDK9 inhibitors suppress transcription elongation, which results in reduced levels of anti-apoptotic proteins[54,92,119]. AURK inhibitors disrupt mitotic activities, inducing chromosomal instability and subsequent cell death[238]. Together, the reason why these inhibitors came up as hits for H3K27M DMGs could be that they all play a crucial role in impeding the proliferation and

survival of these cells by influencing transcription regulation and cell cycle mechanisms. This observation could indicate that H3K27M DMGs are particularly vulnerable to disruptions in transcriptional machinery and pathways associated with cell cycle regulation. Such susceptibility suggests that these tumors rely heavily on specific transcriptional and cell cycle pathways for their growth and proliferation. Consequently, targeting these processes with discovered epigenetic hits may offer a strategic approach to inhibit tumor progression and potentially enhance therapeutic outcomes.

Resistance to single agent therapies in cancer treatment poses a significant challenge in clinical oncology. The primary issue is that cancer cells exhibit a high degree of genetic and epigenetic diversity, which provides a reservoir of variations that some cells can exploit to survive even when exposed to potent therapeutics. Over time, these surviving cells proliferate, leading to the development of a resistant tumor. Mechanisms of resistance include the upregulation of drug efflux pumps, repair of drug-induced DNA damage, and activation of alternative survival pathways. These resistance mechanisms can be acquired as the tumor evolves in response to the selective pressure exerted by the therapy[239,240]. This complexity underscores the need for multi-faceted treatment strategies that combine agents targeting different pathways to reduce the likelihood of resistance development and achieve more durable responses in cancer therapy. In line with this, I aimed to develop a combination therapy for H3K27M DMGs. I focused on four DMG cell models harboring the K27M mutation in their histone H3.3, which most closely represent the patient cohort[15]. It was found through combination screens with TDSU drug library and identified epigenetic hits that the combination of atuveciclib (CDK9i) and BMS-986158 (BETi) was the most efficacious. A synergistic interaction between these two compounds was also observed for all H3K27M DMG cell models tested. CDK9 and BET inhibitors display distinct toxicity profiles that require careful management in clinical environments. They demonstrate hematological side effects, such as neutropenia[241] and thrombocytopenia[242], which may restrict their use in clinical settings. However, the synergistic effect observed between the two inhibitors holds promise for refining dosage regimens to enhance their effectiveness and reduce the toxicity of these inhibitors in treating H3K27M DMGs.

It was additionally noted that SU-DIPG-25 (H3K27M) cells exhibited increased sensitivity to kinase inhibitors, particularly MEK inhibitors such as cobimetinib, trametinib, selumetinib, when these were used in combination with mivebresib (BETi). The distinctive sensitivity of SU-DIPG-25 cells to combined regimen of MEK inhibitors and a BETi might be attributed to their specific genetic background, which includes a Neurofibromatosis Type 1 (*NF1*) mutation. This genetic alterations have been documented to confer increased susceptibility to the combination of MEK and BET inhibitors in other cancer types, such as malignant peripheral nerve sheath tumors[243]. Due to the modest increase in sensitivity, indicative of additivity, this phenomenon was not explored further.

5.2 Molecular characterization of atuveciclib, BMS-986158 and their combination

Analyzing the effects of single agent and combination treatments was vital for understanding how the therapy could impact the cellular and molecular mechanisms within the tumor. This way, I aimed to decipher which pathways were affected, which genes were upregulated or downregulated, and how the cells adapted or succumbed to therapy. This was crucial for evaluating and validating the efficacy

of the treatment. Overall, such analyses could help me understand potential mechanism of action of the combination therapy in targeting H3K27M DMGs. Throughout this study, I used atuveciclib (CDK9i) and BMS-986158 (BETi) at their respective half-maximal inhibitory concentrations (IC50s), which were different for all H3K27M DMG cell models. Using the IC50 for each model tailored the dosage to the individual sensitivity of each cell model, which could vary due to differences in cell type, genetic background, or expression levels of targets or other proteins even though they all share H3K27M mutation. This method was informative in understanding how each cell model responded to a dose that was specifically effective for it, potentially mirroring a more clinically relevant scenario where treatment is personalized. This approach was also useful for evaluating the mechanism of action or dynamics of apoptosis at an optimally effective concentration for each model. Moreover, these IC50s were also applied on non-H3K27M models, which allowed for a direct comparison of the effect of the compounds and help identify differences in sensitivity and resistance across H3K27M and non-H3K27M cell models.

5.2.1 Mode of cell death

While metabolic activity assay performed over the course of compound screens offered significant advantages for high-throughput screening and initial assessments of the drug effects, it presented notable limitations that I had to address to accurately characterize the therapy. Primarily, the metabolic activity assay provided an indirect measure of cell viability, essentially based on metabolic activity, which does not necessarily correlate with cell proliferation or death. As a result, the observed reduction in metabolic activity could be due to factors other than cytotoxicity, such as cellular senescence or quiescence[244]. To distinguish between cytostatic and cytotoxic effects of the single agent and combination treatments, I performed high content microscopy (HCM) imaging of 3D spheroids to mimic the tumor physiology more closely. Both single agents elicited minimal cytotoxicity, which was not significantly distinguishable from the effect of solvent control. On the other hand, combo high (one to one combination of the two drugs at their IC50 for the respective H3K27M DMG cell models, SU-DIPG-17 and HSJD-DIPG-007) facilitated complete response in H3K27M DMG models by inducing cell death as evidenced by the augmented number of RedDot2 positive cells. Combo low (combination reaching to 50% inhibition) demonstrated a potency comparable to the single agent treatments, further showcasing the synergistic interaction.

Although the HCM imaging of the spheroids was conducted in 3D through the acquisition of z-stacks spanning each spheroid, the analysis was limited to 2D due to computational constraints. The analysis of 3D images demands extensive computational resources for processing and feature extraction, as well as substantial technical expertise. Consequently, only the maximum intensity projection images were utilized for analyses. Nevertheless, quantifying dead cells remained a challenge; the segmentation of cells within the compact structures of 3D spheroids required meticulous optimizations to more accurately reflect cell death in the 2D representations. For the scope of this project, 2D analysis was sufficient; however, acquired 3D images provide an opportunity to develop new image analysis techniques within the lab.

While the lead compounds alone were selective for H3K27M DMG cell models and not for non-H3K27M models as proven by low DSS_{asym} values and high IC50s obtained for non-H3K27M models, it was still necessary to validate the specificity of the combination therapy for H3K27M DMG cell models.

Therefore, HCM imaging was also employed to characterize the selectivity and specificity of the combination treatment for H3K27M DMG. In line with this, a H3G34V diffuse hemispheric glioma (DHG) (KNS42) and a non-malignant cell model (HMC3) were included in the analysis in addition to two H3K27M DMG models. I observed more pronounced cell death and spheroid shrinkage for H3K27M DMG cell models, supporting my hypothesis. However, it is necessary to further strengthen these findings by analyzing also H3 WT pHGG models.

Understanding how a treatment induces cell death provides insights into its mechanism of action. Apoptosis is particularly significant since it allows for regulated cell death, which minimizes potential harm to surrounding tissue[245]. Moreover, apoptotic cells are typically cleared by the body more efficiently, reducing the risk of an inflammatory response that can promote metastasis and tumor growth[246]. I discovered that combo high activated caspase-3/7 in all H3K27M DMG cell models tested fitting to known properties of CDK9[247] and BET[248] inhibitors, which are widely recognized for their apoptosis-inducing capabilities[54,160,207,209,215]. The difference between combo high and the single agent treatments was not significant, which can be attributed to the low statistical power of non-parametric tests, that had to be applied owing to the small sample size. Only, SU-DIPG-25 cells were undergone caspase-3/7 activation when treated with BMS-986158 (BETi) although a non-significant increase was also observed for SU-DIPG-17. Similarly, atuveciclib (CDK9i) significantly elevated caspase-3/7 activity only in SU-DIPG-17 cells. Moreover, combo high elicited PARP1 cleavage in HSJD-DIPG-007. Together, this data suggests that combo high induced apoptosis in H3K27M DMG models tested.

Even with the same H3K27M mutation, differences in the genetic landscape could affect how each cell model responds to treatment. SU-DIPG-25 harbors *MET* amplification and *NF1* mutation in addition to *TP53* mutation and *MYC* amplification. The latter two mutations are also observed for SU-DIPG-17, but not the former two. HSJD-DIPG-007 also contains *MYC* amplification plus *PPM1D*, *ACVR1*, *PIK3CA* mutations, as well as *CCND2* amplification (**Table 4**). Based on limited information on the genomic profile of these cells, it could be argued that presence of *NF1* mutation and/or *MET* amplification may potentiate apoptosis induction upon BET inhibition in SU-DIPG-25 model. Additionally, the amplification of *MET* proto-oncogene and mutation in the *NF1* tumor suppressor gene could render this model less susceptible to apoptosis through CDK9 inhibition. Although atuveciclib (CDK9i) and BMS-986158 (BETi) individually induced only low levels of caspase-3/7 activation in different cell models, it was their combination that consistently elicited higher caspase-3/7 activity across all examined cells. This observation suggests that each inhibitor targets distinct but complementary pathways essential for cell survival. Individually, the activity of these pathways appears to be compensable; cells can bypass the inhibition of one pathway by relying on the other. This compensatory mechanism likely accounts for the lower levels of caspase-3/7 activity observed when either inhibitor was used alone. However, when both inhibitors were applied concurrently, the cellular capacity for compensation was overwhelmed, leading to a significant increase in caspase-3/7 activity despite the mutations harbored in either *TP53* or *PPM1D* genes. Mutation in *PPM1D* often results in overactivation of its protein negatively regulating p53 acting like p53 mutation[249,250], which could lead to suppression of apoptosis[251–253]. Despite that, the increased caspase-3/7 activity and PARP1 cleavage could be attributed to that when cells are overwhelmed due to stress induced by treatments, p73 can be triggered[254], leading to the activation of pro-apoptotic genes. Similarly, p63 can activate some p53 target genes in the absence of p53[255]. The synergistic effect between the two inhibitors on apoptosis induction underscores the complexity of the signaling networks within H3K27M DMGs and highlights the potential advantage of

simultaneously targeting multiple pathways by a combination therapy. This strategy could be particularly effective in overcoming the acquired resistance that often limits the efficacy of single-agent therapies in clinical settings.

The specificity of the combination treatment towards H3K27M DMG was further validated *in vivo* using zebrafish embryo xenograft models. The experiments were conducted with two cell models harboring either H3K27M or H3G34V mutations. However, more analyses should be performed also with H3 WT pHGG models to further strengthen the findings. To enhance the understanding of the combination treatment effects, including its pharmacokinetics (PK), pharmacodynamics (PD), and blood-brain barrier (BBB) penetrability, further *in vivo* evaluations will be conducted using a mouse model. Notably, the upcoming *in vivo* studies will incorporate KB-0742 (CDK9i) instead of atuveciclib (CDK9i). This adjustment is predicated on improved clinical tolerability, reduced side effects and better BBB penetrability, aiming to optimize therapeutic outcomes while maintaining the mechanistic integrity of the initial combination.

5.2.2 Mode of action

Identifying the genes and pathways differentially regulated by single-agent treatments, as well as understanding how their combination induces cell death, was of high interest. Additionally, elucidating the mechanisms of synergy between these agents was critical, as it could provide deeper insights into the biology of H3K27M DMGs.

5.2.2.1 Mode of action of BET inhibition

BET protein family, which includes BRD2, BRD3, BRD4, and BRDT, functions as chromatin readers and facilitators of transcription. These proteins recognize acetylated histones through their bromodomains, recruiting the transcription elongation complex to enhance RNA polymerase II (RNAPII) mediated transcription of genes, as well as oncogenes such as *MYC*[256–258]. BRD4, being the ubiquitously expressed[144] and most extensively researched member of the BET protein family, plays a crucial role[257,258]. In DMGs, H3K27M interacts with H3K27ac to form heterotypic nucleosomes that BRD4 targets at super-enhancers, extensive clusters of enhancers characterized by high transcription factor binding[234]. These super-enhancers regulate genes critical to cellular identity, which are often oncogenic drivers in cancer cells[259]. Therefore, cells in DMGs are highly susceptible to the transcriptional interference[260]. In this study, I conducted bulk RNAseq and proteomics to understand the mechanism of action. Chromatin immunoprecipitation sequencing (ChIPseq) could also be conducted to explore the interaction between BRD4 and histone proteins, aiming to identify the expression of which genes is influenced when H3K27M DMG cells are treated with BETi. Transcriptomics results displayed that DNA replication and cell cycle, as well as purine and pyrimidine metabolism and base excision repair (BER) pathways were negatively regulated by BMS-986158 (BETi) treatment in H3K27M DMG cell models. Purines and pyrimidines are essential components in DNA repair mechanisms. Inhibiting purine synthesis has been shown to disrupt DNA repair processes and enhance the sensitivity of H3K27M DMG cells to radiation therapy. Conversely, pyrimidines are considered to have a more limited role in DNA repair and radiotherapy resistance than purines[261]. These insights underscore the importance of purines, especially regarding DNA repair and resistance to therapy in H3K27M DMGs. The downregulation of the base excision repair (BER) pathway can significantly impact cellular function and genomic

stability. BER is an essential DNA repair mechanism tasked with proofreading damaged bases resulting from deamination, oxidation, and alkylation. If these bases are not repaired, they can lead to mutations and DNA strand breaks, jeopardizing genomic integrity[262]. Downregulation of this pathway could elevate DNA damage accumulation in H3K27M DMG cell models, leading to genomic instability and potentially triggering cell death. Downregulation of DNA replication and cell cycle emphasizes that the ability of these cells to proliferate was impaired, which could facilitate cell cycle arrest, thereby inhibiting growth and progression. Furthermore, Gene Ontology (GO) term analysis for biological processes of proteomic data demonstrated that RNAseq results were reflected at the protein level as evidenced by the observed negative impact of BMS-986158 (BETi) treatment on DNA repair, replication and proliferation. The reason why the pathway analysis of proteomic data for H3K27M models under BMS-986158 (BETi) treatment did not show enrichment for the ontologies identified in GO term analysis could be that GO offers a broader categorization of gene functions and more detailed functional analysis[263] compared to a pathway analysis. Moreover, gene expression analysis provided a more comprehensive elaboration on the effect of BMS-986158 (BETi) on H3K27M DMG models, which can be attributed to that RNAseq can detect even low-abundance transcripts as RNA is amplified during library preparation, which is not the case for proteins[264]. Therefore, proteomics generally has lower sensitivity due to the challenges in detecting proteins that are present at low concentrations or those that are masked by more abundant proteins[265]. Thus, the differences in sensitivity in both methods could be the underlying reason why more information was obtained from RNAseq data.

5.2.2.2 Mode of action of CDK9 inhibition

H3K27M mutation in DMG results in global loss of H3K27me2 and H3K27me3. Moreover, the mutant histones, by forming heterotypic nucleosomes with H3 WT, facilitate elevated levels of H3K27ac, which is associated with euchromatin and active transcription[49,234,266,267] and BRD4 recruitment to chromatin[234,137,73]. BRD4, in turn, recruits CDK9, which, together with Cyclin T1, constitutes the positive transcription elongation factor b (P-TEFb), that is essential for the transcription elongation of nascent mRNA strands through the phosphorylation of RNA Polymerase II (RNAPII). This kinase plays a key role in controlling several cellular processes such as proliferation, survival, cell cycle regulation, DNA damage repair, and metastasis, all of which are crucial for the growth[54,92,268]. In line with the literature, RNAseq data showed that inhibition of CDK9 with atuveciclib downregulated DNA replication, similar to BMS-986158 (BETi) effect, as well as DDR pathways, such as non-homologous end joining (NHEJ) and homologous recombination (HR). Proteomics analysis did not converge on any DDR pathway being differentially regulated in H3K27M DMG cell models under atuveciclib (CDK9i) treatment; however, GO term analysis indicated that DNA repair regulation was negatively regulated. Using atuveciclib (CDK9i) to downregulate these DNA repair pathways could potentially increase DNA damage in H3K27M DMG cells by suppressing key proteins involved in NHEJ and HR, essential for repairing DNA double-strand breaks (DSB). The accumulation of non-repaired DSBs makes these cells susceptible to cell death and sensitive to DNA-damaging treatments, such as radiation and chemotherapy. Additionally, the accumulated DNA damage can induce apoptosis, which could explain the increased caspase-3/7 activation observed for some of the H3K27M DMG models. Furthermore, Nepomuceno et al. discovered that CDK9 interacts with and phosphorylates breast cancer type 1 susceptibility protein (BRCA1), a critical protein involved in HR repair. Inhibition of CDK9 with short hairpin RNA (shRNA) hinders the recruitment of BRCA1 to DNA damage sites and disrupts its subsequent HR functions, including DNA end resection and DNA repair protein RAD51 homolog 1 (RAD51) loading[269]. To prove the

hypothesis that HR is dysfunctional after CDK9 inhibition, an IP analysis could be conducted to display that CDK9 interacts with BRCA1, and this interaction is disrupted upon atuveciclib (CDK9i) treatment in H3K27M DMG cells. Moreover, the levels of key proteins involved in NHEJ (e.g. Ku70, Ku80)[270] and HR (e.g. RAD51, BRCA1/2)[271] could be measured in a WB before and after atuveciclib (CDK9i) treatment across different time points.

Several studies have highlighted CDK9 as a promising therapeutic target in cancer cells, given its crucial function in the transcriptional regulation of genes that facilitate tumor growth and survival. Inhibiting CDK9 has demonstrated potential in preclinical models by decreasing the transcription of these oncogenes, such as *MYC*, which in turn disrupts tumor cell proliferation and survival[272,131,273,274]. However, the RNAseq data, as well as the time point analysis conducted in WB of atuveciclib (CDK9i) treated H3K27M DMG cell models highlighted that MYC levels did not change. This observation suggests that cytostatic effect of atuveciclib (CDK9i) on H3K27M DMG cell models was independent of MYC expression, which recapitulated the findings of another study where the authors investigated the same compound on H3K27M DMG cells[275].

5.2.2.3 The effect of the inhibitors on cell cycle

According to the gene expression analysis of H3K27M DMG cell models treated with BMS-986158 (BETi), although the expression of *MYC* decreased only in SU-DIPG-25 and HSJD-DIPG-007, as confirmed by WB for the latter, the MYC target genes were downregulated across all four cell models along with E2F target genes. Atuveciclib (CDK9i) also negatively regulated MYC and E2F target genes. Both E2F and MYC target genes play a crucial role in the drive of expression of genes required for the cell cycle phase transitions and initiation of DNA replication[276–278]. Moreover, proteomics confirmed that cell cycle pathway and nuclear replication events were downregulated under all tested treatments. These observations highlight the negative effect of the BET and CDK9 inhibition on the cell cycle. H3.3K27M mutation often co-segregates with *TP53* mutation in DMGs[15] (**Figure 1**), and in fact, except for SU-DIPG-19, all the cell models analyzed in the omics analyses harbor either *TP53* mutation (SU-DIPG-17, SU-DIPG-25) or *PPM1D* mutation (HSJD-DIPG-007) (**Table 4**), which negatively regulates p53[249,250]. It has been demonstrated that both *PPM1D* and *TP53* mutations can override normal cell cycle checkpoints, allowing continuous proliferation[250,279]. Consequently, it is probable that these cells cannot be arrested at any cell cycle phase although further experiments, such as flow cytometry, are required to prove that.

5.2.2.4 The effect of the inhibitors on DNA damage

In the S-phase of the cell cycle, the coordination between chromatin regions actively transcribing RNA and advancing replication forks is crucial. If the regulation and synchronization of transcription or replication are disrupted, it can lead to a misalignment of these chromatin-related processes. This desynchronization may cause formation of R-loops (RNA:DNA hybrids) due to annealing of nascent RNA with its DNA template, resulting in a three-stranded structure[280–282,159]. When RNAPII is stalled due to e.g. CDK9 inhibition, the nascent RNA can re-anneal with its template strand, forming an R-loop that anchors RNAPII to the chromatin. During S-phase, these R-loop-bound transcription machinery acts as an obstacle to advancing replication forks[283,284]. When these R-loops remain unresolved, they can cause collisions of the transcription complex with the replication machinery, leading to replication fork

collapse and DSBs[159,284,285,286]. BRD4 activates CDK9 through its C-terminal domain (CTD), triggering a phosphorylation event that is crucial for efficient transcription elongation[287–289]. Previous studies have demonstrated that the depletion of BRD4 following a BETi results in reduced RNAPII traveling ratios, suggesting that RNAPII becomes paused on the chromatin[290]. Additionally, direct chemical inhibition of CDK9 has been shown to cause RNAPII stalling and an increase in R-loop formation[285,291]. Moreover, spliceosomes could resolve the R-loops with proper pre-mRNA splicing and when downregulated, as observed for combo low treatment, R-loop accumulates[216,217]. In the light of these findings, I hypothesize that both BET and CDK9 inhibition could facilitate R-loop formation, which further causes DNA damage in H3K27M DMG cell models. In fact, when used in combination, both inhibitors synergistically increased the DNA damage accumulation, as evident by increased γH2A.X levels detected in WB and flow cytometry, which cannot be repaired due to the downregulation of genes essential for DNA damage repair. The detection of R-loops is facilitated by several methods, each with its strengths and limitations. While S9.6 mAb[292] and RNase H1-based[293] methods are commonly used, they face challenges related to specificity, sensitivity, and technical implementation. S9.6 mAb binds to RNA:DNA hybrids, but can also recognize double stranded RNAs (dsRNAs), leading to false positive results[294]. Overexpression of RNase H1 can be used to manipulate R-loop levels, while catalytically-dead versions of RNase H1 or its hybrid binding domain (HBD) can be employed for R-loop detection in imaging and immunoprecipitation assays[295]. Nevertheless, potential interference with endogenous RNase H1 activity poses a challenge to the method[294].

5.2.3 Specificity of combinatorial treatment with CDK9i and BETi towards H3K27M DMG

To ensure the accurate expression of transcriptional programs in specific cell types or developmental stages, polycomb repressive complex 2 (PRC2) antagonizes with the epigenetic regulators that facilitate gene expression[296]. PRC2 opposes some chromatin regulators such as CREB-binding protein (CBP), which is involved in mediating H3K27ac[297]. Research has demonstrated that malignant peripheral nerve sheath tumors (MPNSTs) are vulnerable to compounds that induce aberrant transcription, due to the loss of function of PRC2 and the subsequent reduction in H3K27me2/3 (a repressive mark) and corresponding increase in H3K27ac (an activating mark) observed in these tumors[298]. Similarly, the H3K27M mutation in DMGs creates a unique epigenetic landscape due to decreased PRC2 function, which results in transcriptional dependencies[260], leading to a decrease in H3K27me2/3 and an increase in H3K27ac compared to pHGGs without the H3K27M mutation[234,299,64]. This shift occurs despite the fact that the H3K27M mutant protein only constitutes 3-17% of the total H3 proteins[64]. The increased H3K27ac in H3K27M DMGs colocalizes with BRD proteins at transcriptionally activated genes. This interaction contributes to the activation of transcription by recruiting P-TEFb and RNAPII[234,290]. The increase in H3K27ac provides more binding sites for BRDs, making H3K27M DMGs more dependent on BRD-mediated transcription, hence more vulnerable to BETis and drugs impairing transcription, such as CDK9i. The combination of CDK9 and BET inhibition could exhibit synthetic lethality in H3K27M DMG cells by capitalizing on their transcriptional vulnerabilities. This combinatorial treatment simultaneously disrupts transcriptional regulation and DNA damage response (DDR) pathways, leading to the accumulation of lethal DNA damage. I hypothesize that if H3K27M DMG cells cannot be arrested at any cell cycle phase - either due to the underlying mutations discussed above or as an effect of the inhibitors, which has to be investigated further - and are unable to repair DNA-strand breaks, then

DNA damage will accumulate as the cells undergo mitosis. This could ultimately lead to mitotic catastrophe. Mitotic catastrophe is an antiproliferative mechanism that takes place during defective or unsuccessful mitosis. It is marked by distinct nuclear changes, including multinucleation and micronucleation, which are used as morphological indicators for its detection[300]. Although the signaling pathways that elicit mitotic catastrophe are still poorly understood, it is known that in clinical practice, effectively inducing mitotic catastrophe necessitates both the initiation of DNA damage and the inhibition of molecular pathways that govern cell cycle arrest and DNA damage repair[301,302]. If mitotic catastrophe results in a lethal outcome, it triggers apoptosis, necrosis, or autophagy, and apoptosis and autophagy are capable of regulating each other[302–304]. The upregulation of autophagy observed in multiomics analysis of BMS-986158 (BETi) treated H3K27M DMG cell models could be attributed to mitotic catastrophe induction. Although further investigation is required, such as morphology analysis of cell nucleus with and without treatment, for the characterization of mitotic catastrophe, it is probable that the combinatorial inhibition of CDK9 and BET enhances mitotic catastrophe and eventually pushes the cells to apoptotic cell death.

The design of the proteomic analysis included testing a H3 WT pHGG cell model to shed light onto the differences between H3K27M and H3 WT models in response to the treatment. However, the inhibitors elicited similar alterations in both H3K27M and H3 WT models, such as negative regulation of DNA repair, replication and transcription. Therefore, a more comprehensive analysis is required, such as ChIPseq, to stratify the genes affected by the treatments in pHGG models with different H3 mutation status. Additionally, although HCM screens discussed in **5.2.1 Mode of cell death** indicated that the combo high was more specific for H3K27M DMG models, it would be still required to test H3 WT pHGG models, e.g. the one analyzed in proteomics, to further strengthen the findings. Furthermore, DDR proteins alongside γH2A.X could be monitored in WB for pHGG models with various H3 mutation profiles to assess the differences in the DNA damage accumulation and repair.

5.2.4 Sensitization to radiotherapy

The downregulation of purine metabolism and DDR pathways were also observed when H3K27M DMG cells were treated with combo low. In this instance, the reason why the radiosensitivity observed for HSJD-DIPG-007 (H3K27M) cell model under combo low treatment can be attributed to a decrease in DNA repair capacity of the cells. SU-DIPG-17 (H3K27M) demonstrated rather an additivity when treated with combo low and radiation therapy (RT), which could be because this model was originated from a patient who had undergone RT (**Table 4**). Consequently, SU-DIPG-17 might have developed resistance against RT. Moreover, in the absence of the compound treatment, this model demonstrated the lowest radiosensitivity compared to other H3K27M DMG cell models derived from patients who had not received RT. Additionally, SU-pcGBM2 (H3 WT) was not sensitized to RT when treated with combo low, suggesting that combination of RT with inhibition of CDK9 and BET could exploit synthetic lethality in H3K27M DMGs.

The reason why additional cell models with different H3 mutation status were not included in the radiosensitization analysis is that most of the cells exhibited limited plating efficiency, rendering them unsuitable for investigation in a colony formation assay, which was crucial for this phase of analysis.

6 Conclusion & Outlook

The main objective of this project was to develop a combination therapy specifically targeting H3K27M DMGs, with the potential for clinical application. Epigenetic drug library screen identified atuveciclib (CDK9i), mivebresib (BETi) and alisertib (AURKi) as lead compounds specifically targeting H3K27M DMG cell models. These compounds were further screened in combination with TDSU library, which revealed that the sensitivity of H3K27M DMG cell models to BETis increased when these inhibitors were combined with atuveciclib (CDK9i). BMS-986158 (BETi) was selected as the combination partner to atuveciclib (CDK9i) as its DSS_{asym} value increased the most, hence the sensitivity, compared with other BETis screened in conjunction with atuveciclib (CDK9i). Synergy analysis with multiple-ray design approach confirmed the synergistic interaction between atuveciclib (CDK9i) and BMS-986158 (BETi) for all four H3K27M DMG cell models.

High-content microscopy imaging displayed that the combo high elicited cytotoxicity in H3K27M DMG models, which was found to be the result of caspase-3/7 activation, indicative for apoptosis. Single-agent treatments were identified to be rather cytostatic. *In vitro* specificity of the combination treatment was further validated *in vivo* using zebrafish xenograft models. Combo high prevented colony formation in anchorage-independent soft-agar colony formation assay. A combination therapy using lower doses of atuveciclib (CDK9i) and BMS-986158 (BETi), referred to as combo low, achieved the same effect size as higher doses of these two inhibitors used individually. This finding not only underscored the synergistic interaction between the compounds but also highlighted the potential for strategic dose adjustments to mitigate toxicity. The ability to optimize dosages is crucial, as it could help enhance the patient safety and treatment efficacy, potentially broadening the therapeutic window in clinical setting.

Multi-omics analyses demonstrated that DNA replication and cell cycle associated genes were negatively regulated by atuveciclib (CDK9i), BMS-986158 (BETi) and combo low. Moreover, different DDR pathways were downregulated by these inhibitors, suggesting a complementary inhibitory role on DNA damage repair. WB and flow cytometry analyses displayed that combo high resulted in DNA damage accumulation. Future experiments will focus on the hypothesis that the H3K27M DMG models undergo mitotic catastrophe as a result of DNA damage accumulation and insufficient repair. To more deeply understand the differences in sensitivity to the combinatorial treatment, assays will cover also the H3G34V/R and H3 WT pHGG models.

Moreover, it was demonstrated that the combination therapy radiosensitized one of the H3K27M DMG cell models, potentially resulting in synthetic lethality due to the downregulation of DDR pathways. Since either synergism or additivity was observed for the H3K27M DMG models screened, the combination therapy appears to be safe for use with RT.

Altogether, the combinatorial treatment with CDK9 and BET inhibitors exploits the transcriptional vulnerability of H3K27M DMGs, which display decreased H3K27me2/3 and increased H3K27ac due to the compromised function of PRC2. These inhibitors target multiple points in the transcriptional regulation, leading to synergistic effects including downregulation of DNA replication and potentially cell cycle arrest, accumulation of DNA damage and induction of apoptosis. This enhances the overall specificity and efficacy of the combination treatment against H3K27M DMGs.

The last but not least, the first steps in the initiation of clinical trials were taken by establishing a collaboration with Kronos Bio. Company, which produces a BBB penetrant CDK9i, KB-0742. This compound is being investigated with H3K27M DMG models *in vitro* in combination with BETis. To thoroughly explore the clinical potential of the CDK9 and BET inhibitor combination, *in vivo* mouse experiments are planned with KB-0742 (CDK9i) and BMS-986158 (BETi). These experiments will evaluate BBB penetrability, on-target effects of the compounds (RNAPII pS2 and HEXIM1 levels) and survival following the combination treatment. If promising, clinical trials will begin.

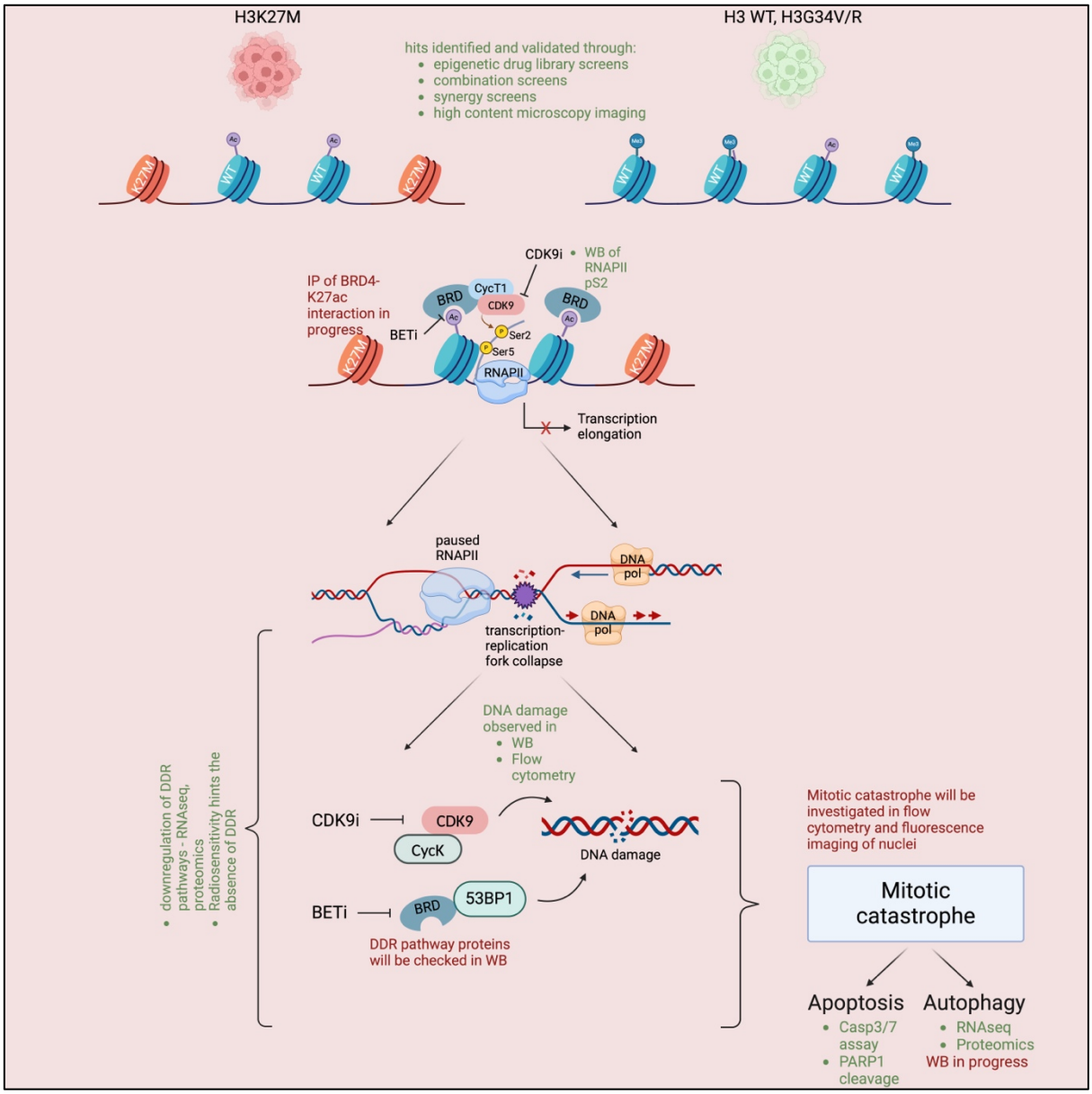

Figure 29. Graphical explanation of CDK9i and BETi combination effect on H3K27M DMG. The experiments leading to the mechanistic explanation are in green and experiments to be performed are in red. K27M mutant histones portrayed in orange, WT histones are in blue. CycT1, Cyclin T1; CycK: Cyclin K; 53BP1: p53-binding protein 1; DNA pol: DNA polymerase.

Supplementary Figures

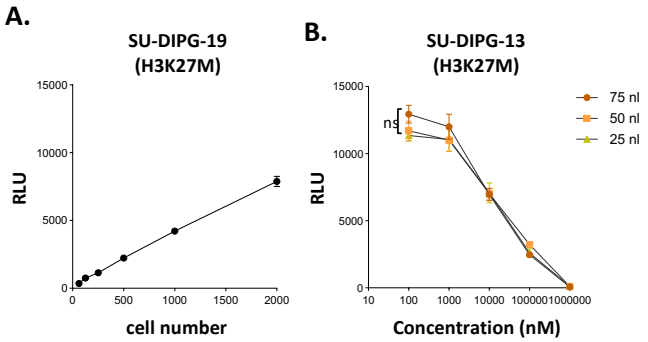

Figure S1. Cell titer and drug dispensing volume controls. **(A)** SU-DIPG-19 (H3K27M) cells were seeded in two-fold dilutions at six different densities, incubated for 72h and subjected to CTG. The data were normalized to that of blank control. The linear relationship between increasing number of cells and increasing luminescence signal (relative light unit, RLU) demonstrated the optimal cell number to be seeded. **(B)** STS was tested in three different volume, 25 nl, 50 nl and 75 nl at a concentration range. SU-DIPG-13 (H3K27M) cells were seeded according to **Table 35**, and incubated with pre-dispensed STS for 72h before CTG. Statistics were calculated with non-parametric Friedman test followed by Dunn's multiple comparison. ns: not significant.

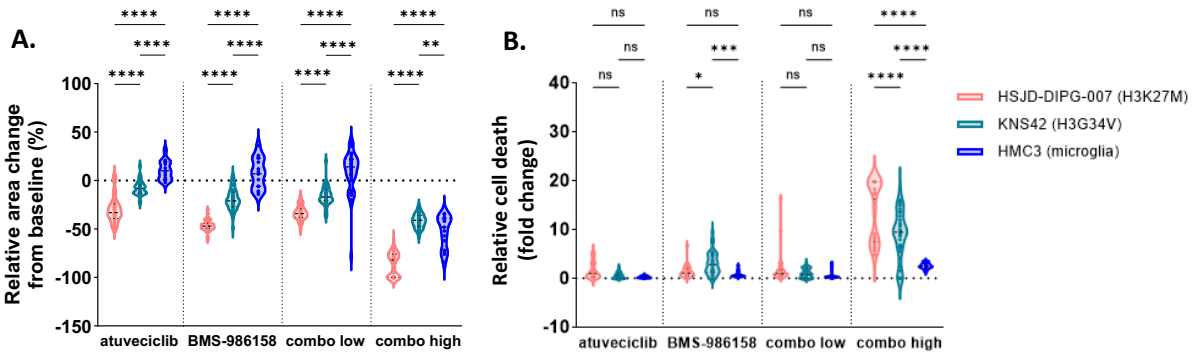

Figure S2. HCM image analysis depicting spheroid area change from baseline and cell death. Treatment conditions belonged to that of HSJD-DIPG-007 (H3K27M), and were as follows: 850 nM atuveciclib (CDK9i), 27 nM BMS-986158 (BETi), combo low (155 nM atuveciclib + 5.5 nM BMS-986158) and combo high (850 nM atuveciclib + 27 nM BMS-986158). DMSO was kept as a solvent (negative) control. **(A)** Spheroid area change from baseline calculated for each treatment and normalized to the solvent control of the respective cell model. **(B)** The number of death cells were counted for each treatment and normalized to the solvent control of the respective cell model. The data from three biological replicates are pooled for each graph. Statistics were calculated using two-way ANOVA followed by Tukey's test. *p<0.05; **p<0.01; ***p<0.001; ****p<0.0001; ns: not significant. n=3.

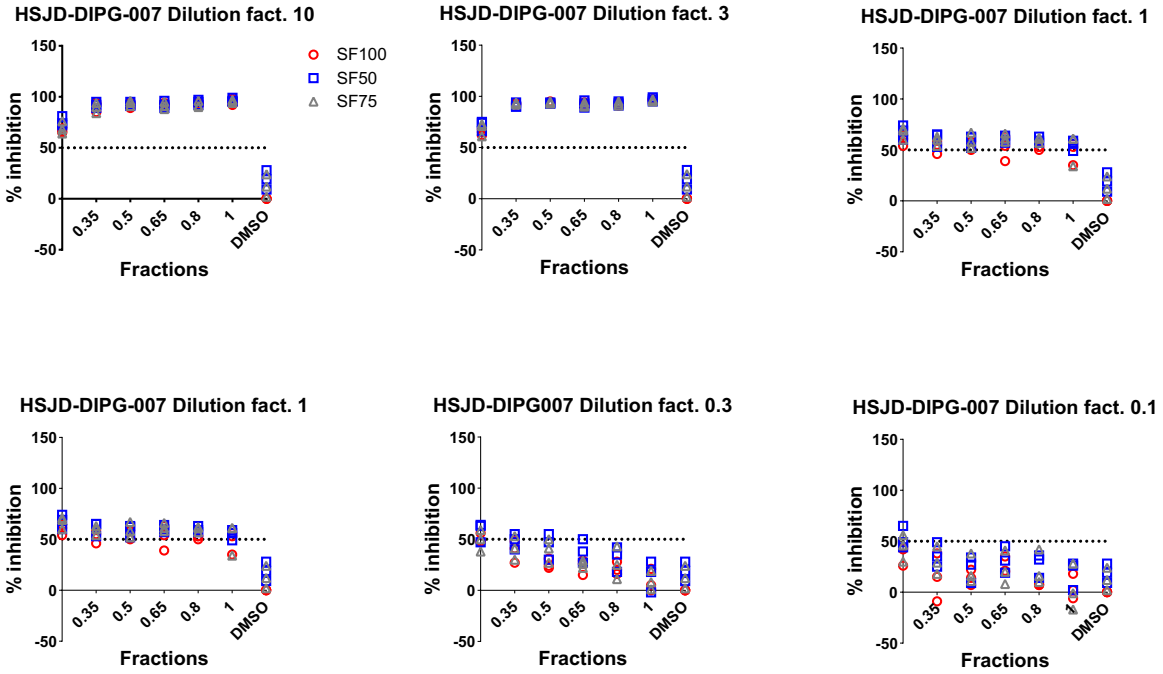

Figure S3. Radiosensitization assessment of combo low on HSJD-DIPG-007 (H3K27M) cells conducted using a metabolic activity assay. Different dilution factors (10, 3, 1, 0.3, 0.1) were employed to create a concentration range. Dilution factor of 1 corresponds to standard combo low (155 nM atuveciclib + 5.5 nM BMS-986158). Dilution factors were multiplied by the standard combo low concentration to give rise to new concentrations.

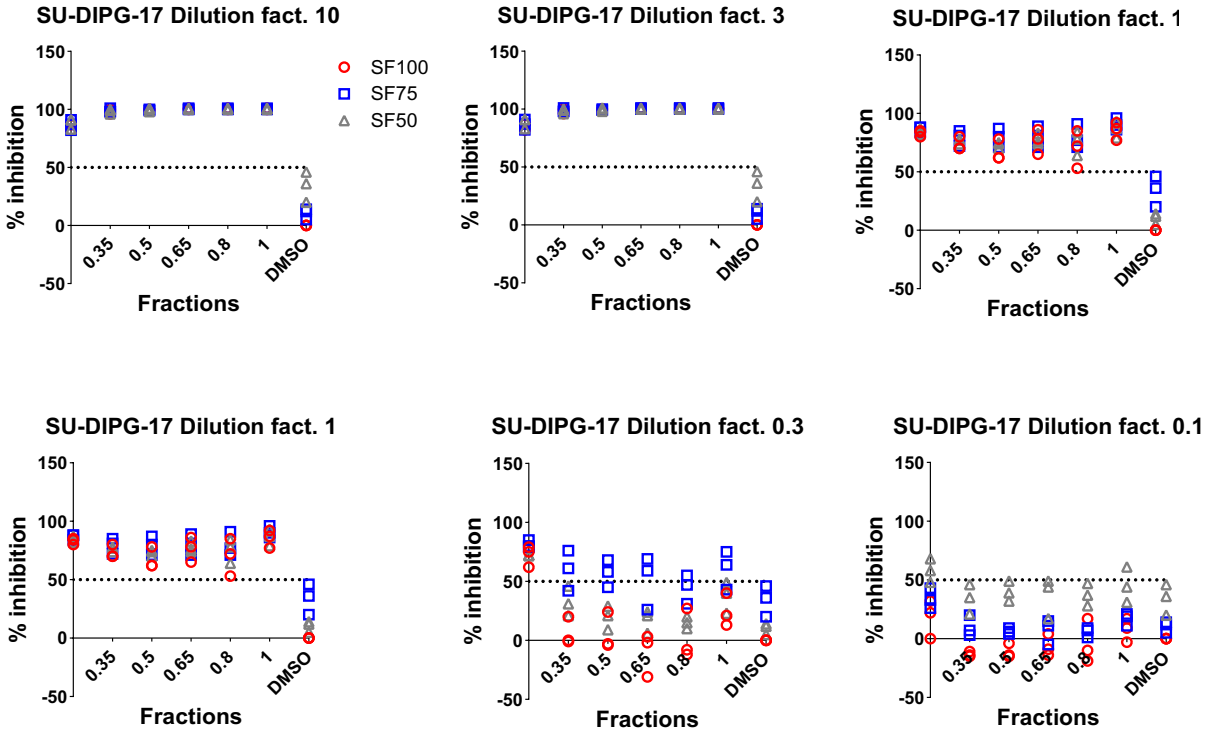

Figure S4. Radiosensitization assessment of combo low on SU-DIPG-17 (H3K27M) cells conducted using a metabolic activity assay. Different dilution factors (10, 3, 1, 0.3, 0.1) were employed to create a concentration range. Dilution factor of 1 corresponds to standard combo low (277 nM atuveciclib + 4 nM BMS-986158). Dilution factors were multiplied by the standard combo low concentration to give rise to new concentrations.

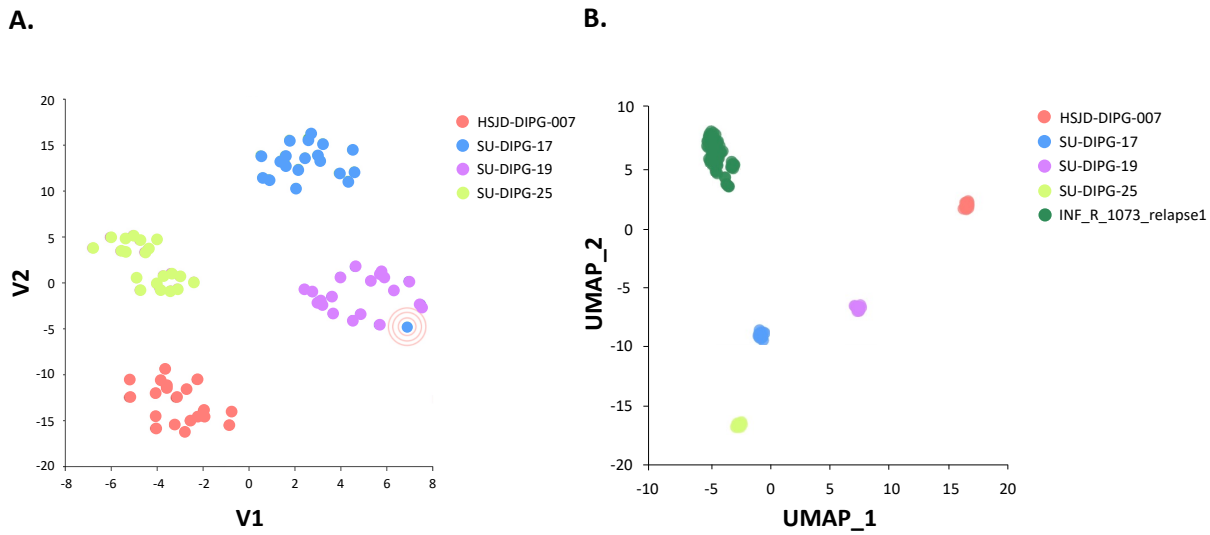

Figure S5. Quality check of bulk RNAseq and LC-MS/MS proteomic data. The cells were treated according to **Table 39**, and analyzed in five and four biological replicates in RNAseq and proteomic, respectively. (**A**) t-SNE plot of RNAseq data of 80 samples was generated in R2: Genomics Analysis and Visualization Platform. Only SU-DIPG-17 atuveciclib replicate 2, highlighted in red circles, was detected as an outlier and excluded from the analysis. (**B**) UMAP of proteomic data of 128 samples was plotted using RStudio.

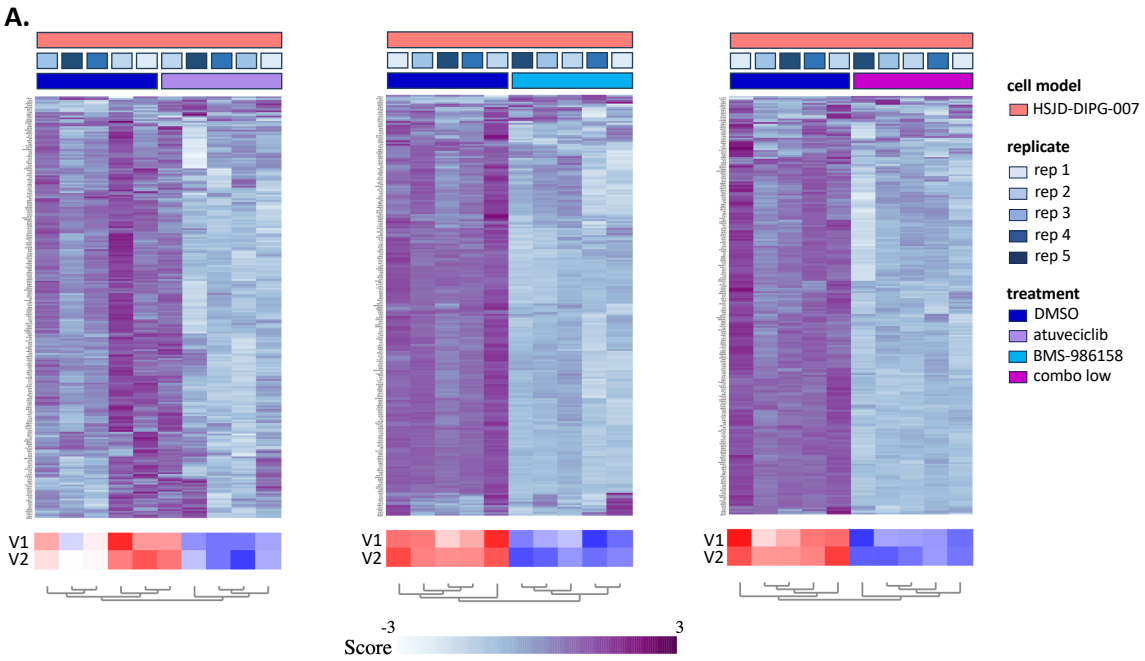
A.
V1
V2
-3
3
Score
cell model
HSJD-DIPG-007
replicate
rep 1
rep 2
rep 3
rep 4
rep 5
treatment
DMSO
atuveciclib
BMS-986158
combo low

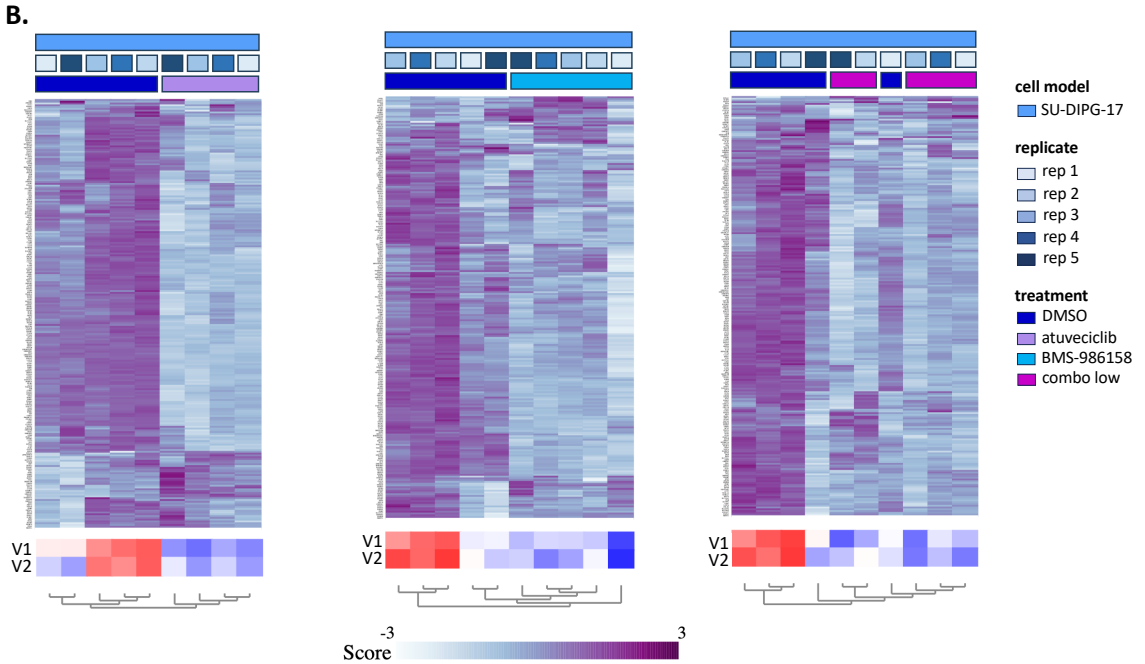
B.
V1
V2
-3
3
Score
cell model
SU-DIPG-17
replicate
rep 1
rep 2
rep 3
rep 4
rep 5
treatment
DMSO
atuveciclib
BMS-986158
combo low

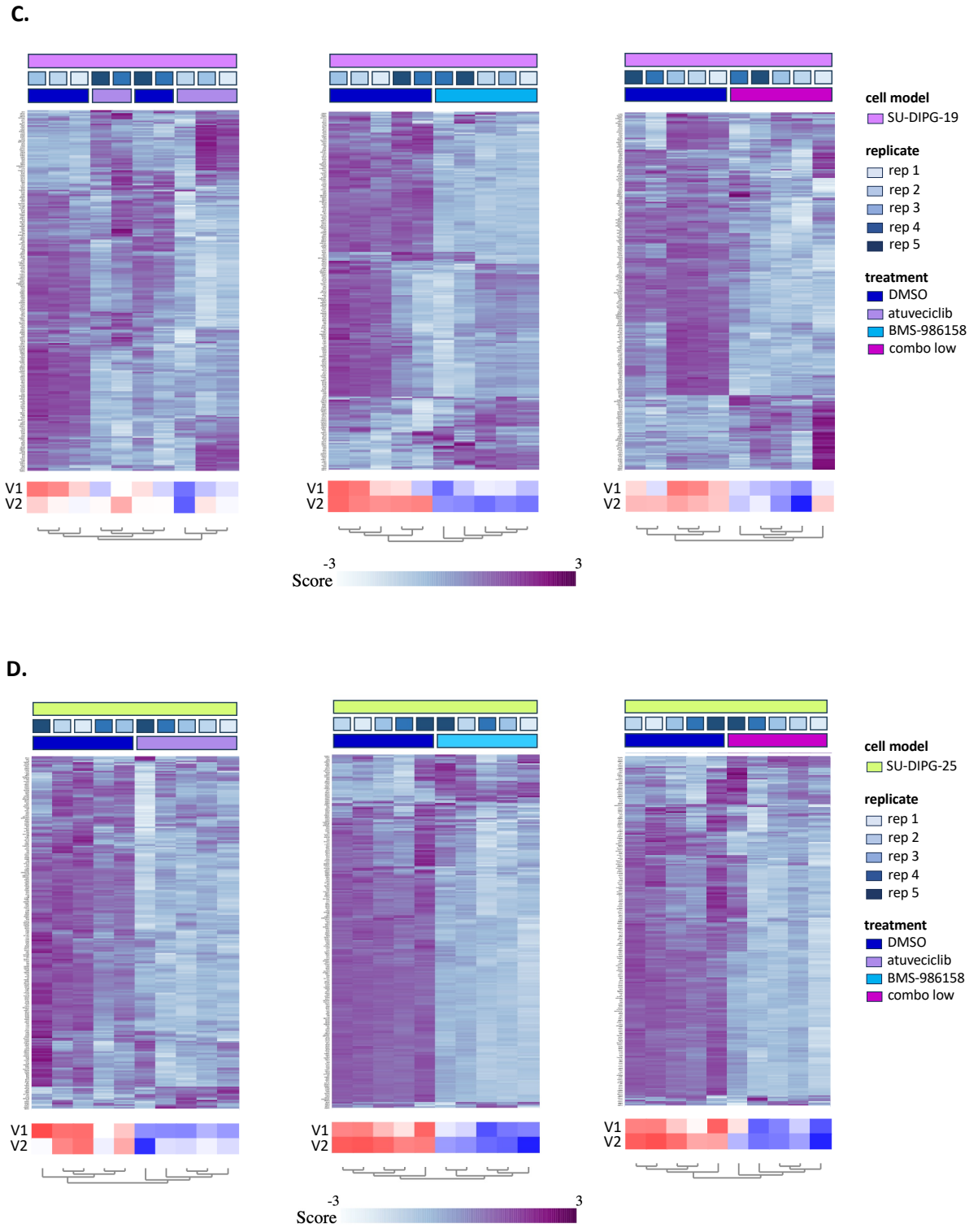

Figure S6. Hierarchical clustering heatmap using Z-score based on MSigDB HALLMARK MYC Targets version 1 (V1) and 2 (V2) for **(A)** HSJD-DIPG-007, **(B)** SU-DIPG-17, **(C)** SU-DIPG-19 and **(D)** SU-DIPG-25. Each treatment group was compared with DMSO. Overall differential changes in V1 and V2 were depicted below the heatmaps for each replicate (rep). Blue and red boxes represent negative and positive regulation, respectively.

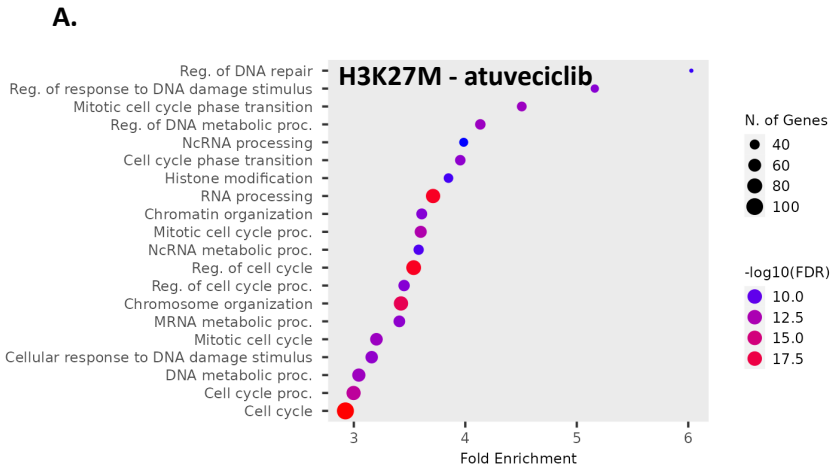

Figure S7. GO term analysis for biological processes displaying downregulated ontologies in (**A**) H3K27M DMG and (**B**) H3 WT pHGG models under atuveciclib (CDK9i) treatment.

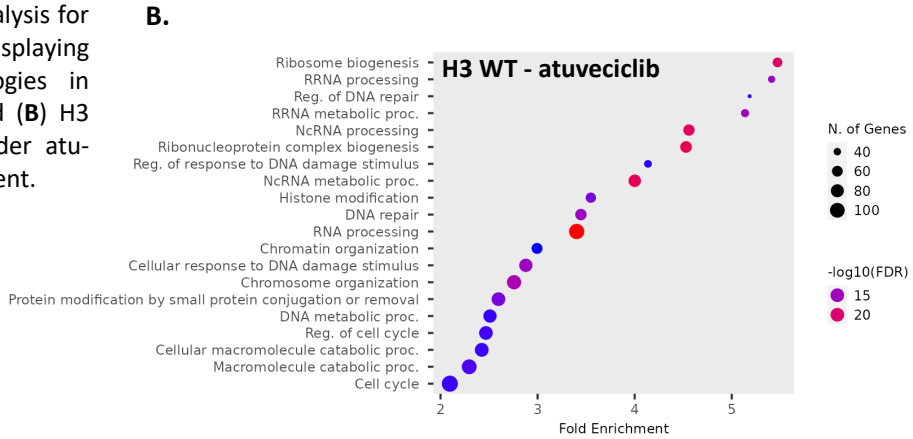

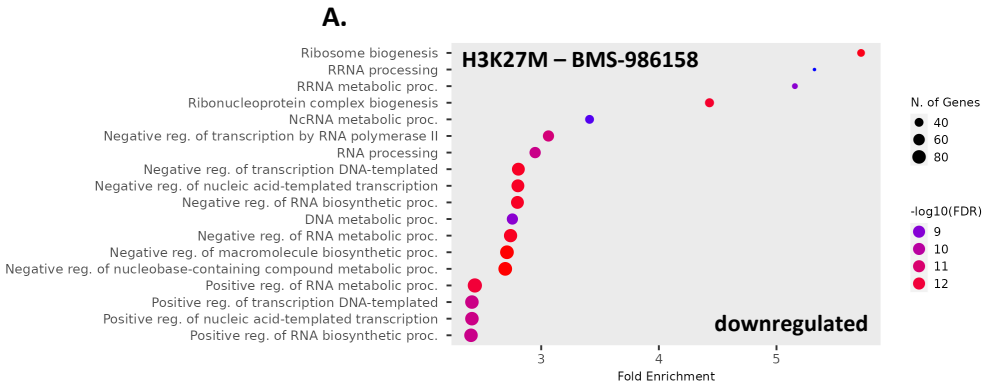

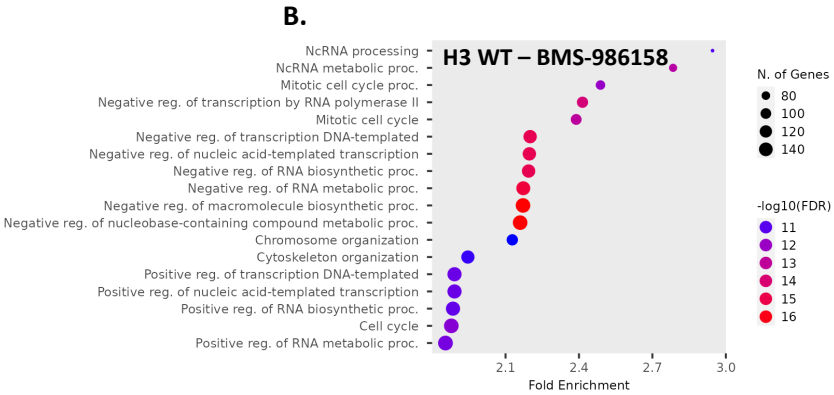

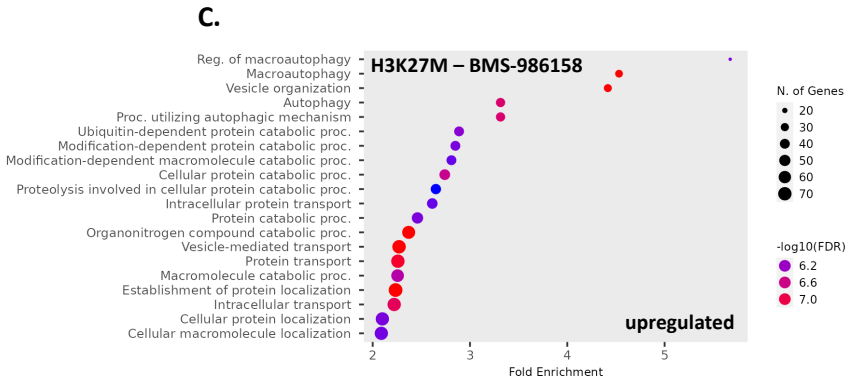

Figure S8. GO term analysis for biological processes showing negatively regulated ontologies in (**A**) H3K27M DMG and (**B**) H3 WT pHGG models, and (**C**) upregulated ontologies under BMS-986158 (BETi) treatment for H3K27M DMG models.

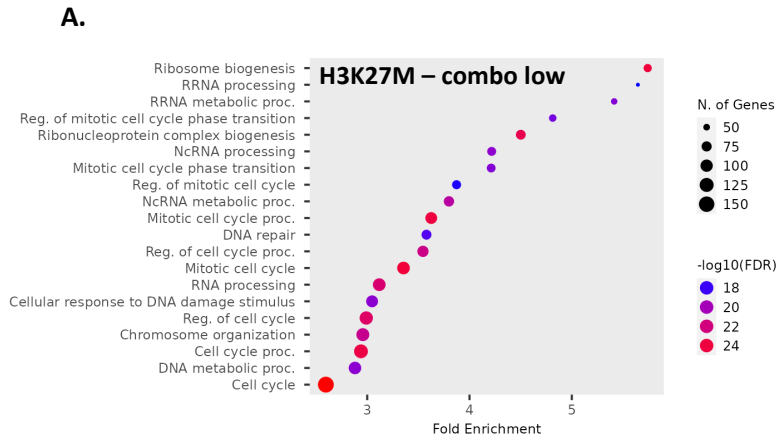

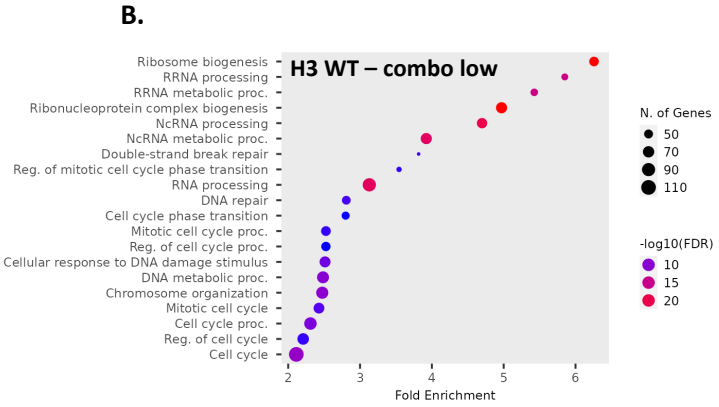

Figure S9. GO term analysis for biological processes demonstrating downregulated ontologies in (**A**) H3K27M DMG and (**B**) H3 WT pHGG models under combo low treatment.

Compound		Embryo 1	Embryo 2	Embryo 3	Results
DMSO 1:1000	Day 1				All healthy
	Day 3	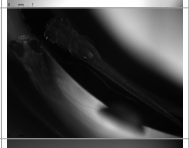			All healthy
DMSO 1:200	Day 1				All healthy
	Day 3		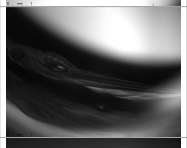	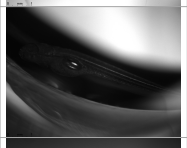	All healthy
Atuvecliclib 1µM	Day 1				All healthy
	Day 3		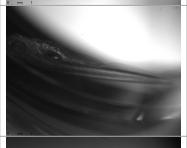		All healthy
Atuvecliclib 5µM	Day 1				All healthy
	Day 3	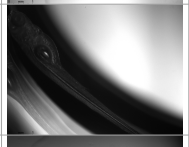	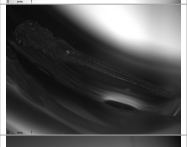		All healthy
Atuvecliclib 10µM	Day 1				All healthy
	Day 3				All healthy
Atuvecliclib 20µM	Day 1		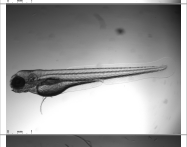		All healthy
	Day 3		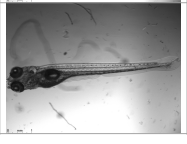	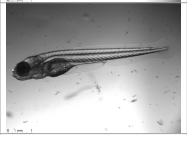	All healthy

Compound		Embryo 1	Embryo 2	Embryo 3	Results
Atuvecliclib 50µM	Day 1				All healthy
	Day 3		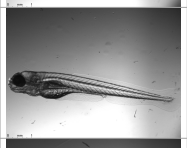		All healthy
BMS-986158 200nM	Day 1				All healthy
	Day 3	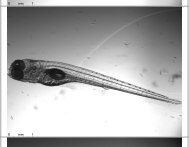			All healthy
BMS-986158 500nM	Day 1				All healthy
	Day 3			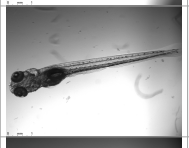	All healthy
BMS-986158 1000nM	Day 1				All healthy
	Day 3				Alive, but morphology changes
BMS-986158 2500nM	Day 1				Alive, but morphology changes
	Day 3				Dead
BMS-986158 5000nM	Day 1				Dead
	Day 3		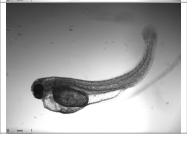	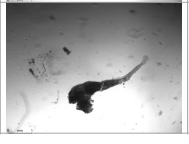	Dead

Figure S10. Toxicity analysis of atuveciclib (CDK9i) and BMS-986158 (BETi) on zebrafish embryos.

Concentration		Embryo 1	Embryo 2	Embryo 3	remarks
DMSO	Day 1				All healthy
	Day 3	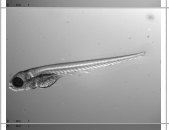			All healthy
Combo 1	Day 1	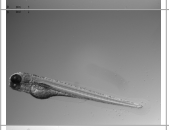	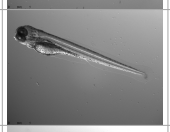	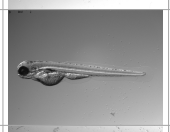	All healthy
	Day 3		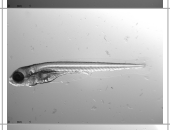	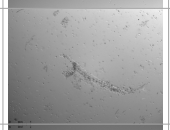	1,2 healthy 3 dead
Combo 2	Day 1	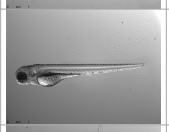	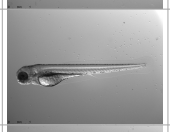		All healthy
	Day 3	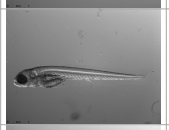		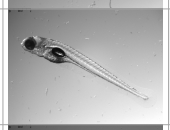	All healthy
Combo 3	Day 1	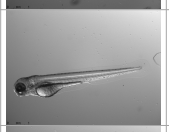	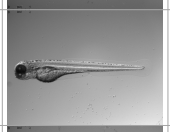	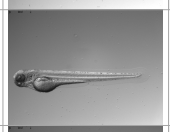	All healthy
	Day 3	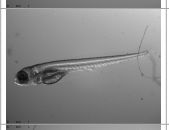	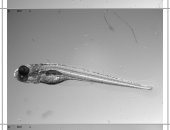	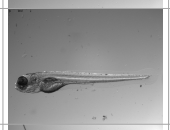	All healthy
Combo 4	Day 1				All healthy
	Day 3	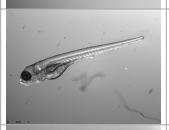	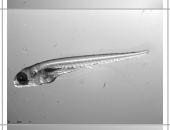		All healthy
Combo 5	Day 1				1,3 healthy 2 slightly curved
	Day 3		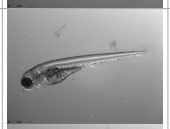		All slightly curved, no major changes
Combo 6	Day 1	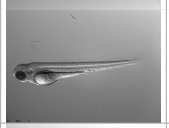			1 healthy 2,3 slightly curved
	Day 3	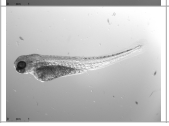	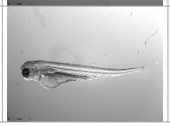	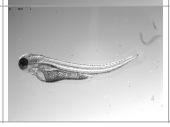	Morphology changes

Figure S11. Toxicity analysis of six different combination treatments with atuveciclib (CDK9i) and BMS-986158 (BETi) on zebrafish embryos according to **Table 41**.

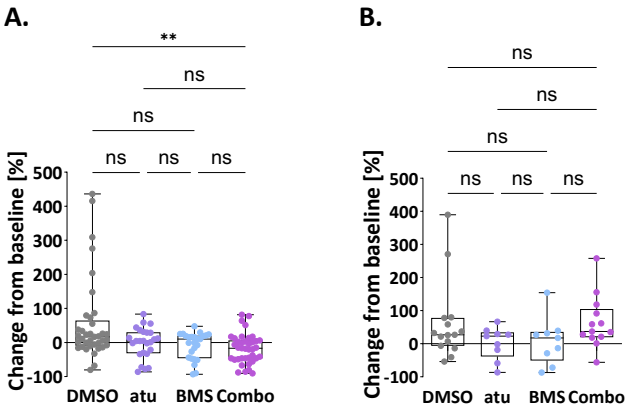

Figure S12. Box-dot plots of zebrafish xenograft data for (**A**) HSJD-DIPG-007 (H3K27M) and (**B**) KNS42 (H3G34V). Kruskal-Wallis test was performed to calculate statistics. **p<0.01; ns: not significant.

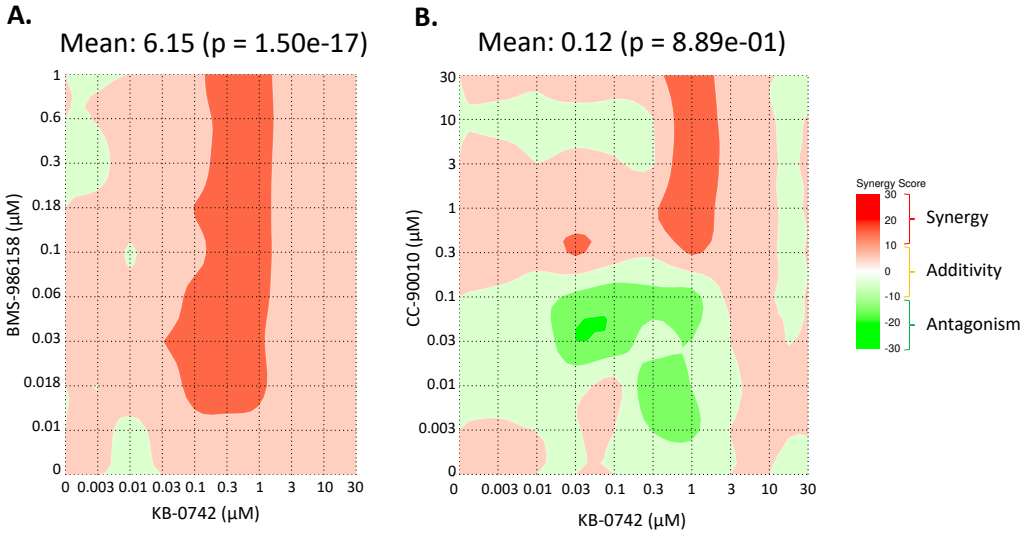

Figure S13. Synergy screen with KB-0742 (CDK9i) and BETis using a matrix design. (**A**) BMS-986158 and (**B**) CC-90010 were tested as BETis. The synergy calculation was performed based on Loewe model and plotted on SynergyFinder+

Appendix

HSJD-DIPG-007_p1

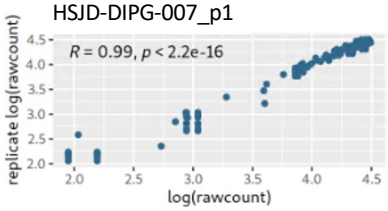

HSJD-DIPG-007_p2

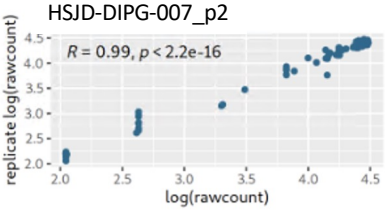

HSJD-DIPG-007_p3

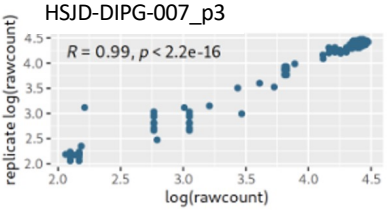

HSJD-DIPG-007_p4

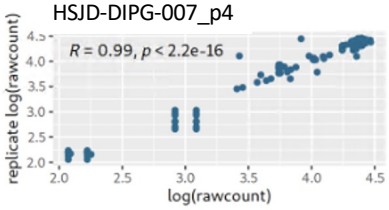

HSJD-DIPG-007	Z'
p1	0.88
p2	0.71
p3	0.86
p4	0.85

SU-DIPG-17_p1

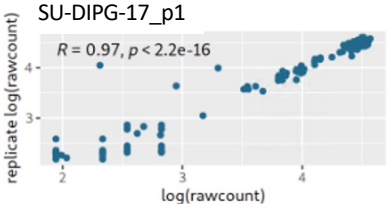

SU-DIPG-17_p2

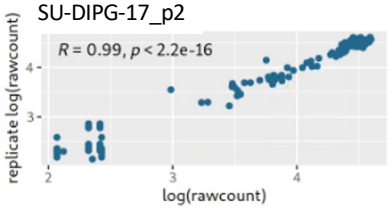

SU-DIPG-17_p3

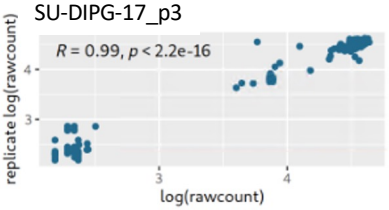

SU-DIPG-17_p4

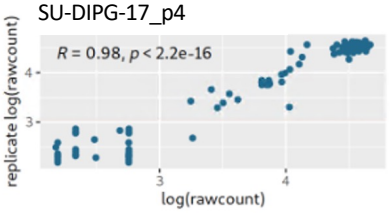

SU-DIPG-17	Z'
p1	0.84
p2	0.78
p3	0.80
p4	0.77

SU-DIPG-19_p1

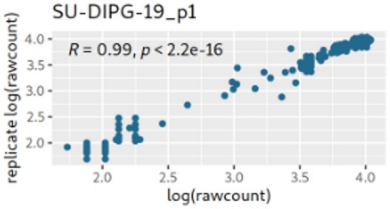

SU-DIPG-19_p2

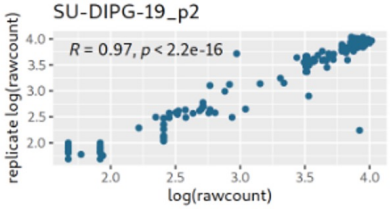

SU-DIPG-19_p3

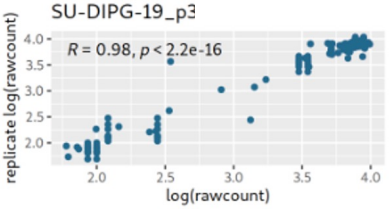

SU-DIPG-19_p4

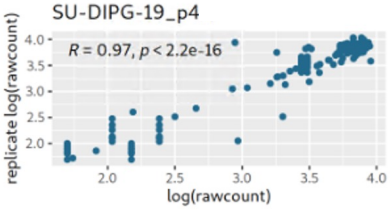

SU-DIPG-19	Z'
p1	0.67
p2	0.52
p3	0.72
p4	0.77

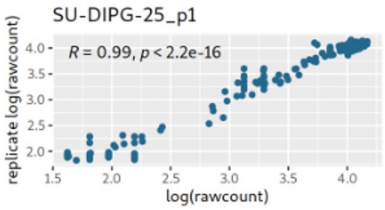

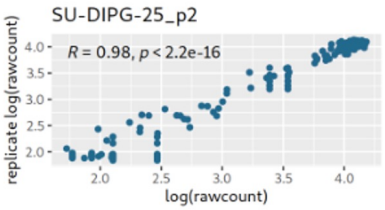

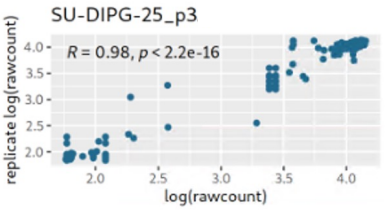

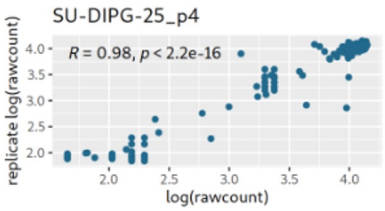

SU-DIPG-25	Z'
p1	0.81
p2	0.78
p3	0.74
p4	0.72

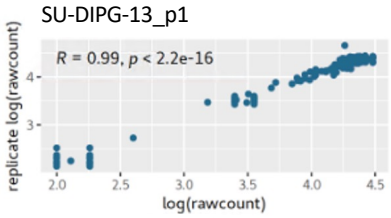

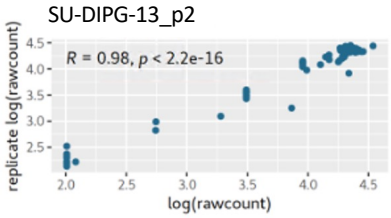

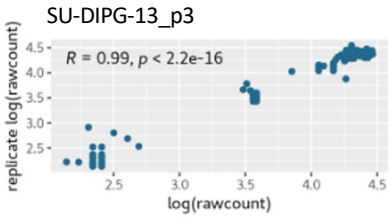

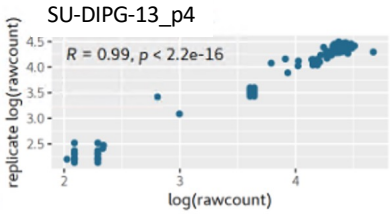

SU-DIPG-13	Z'
p1	0.57
p2	0.61
p3	0.77
p4	0.82

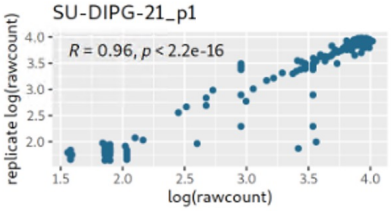

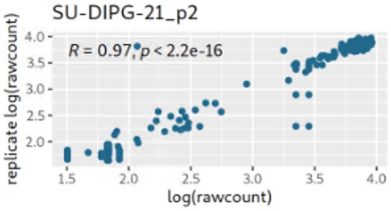

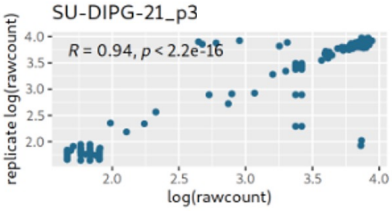

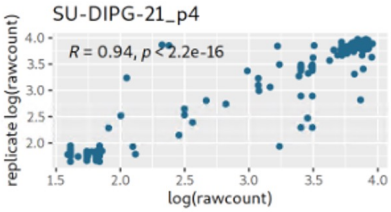

SU-DIPG-21	Z'
p1	0.85
p2	0.88
p3	0.70
p4	0.71

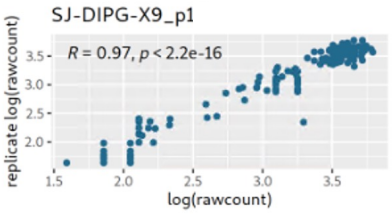

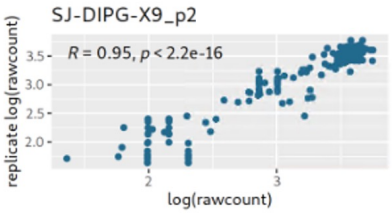

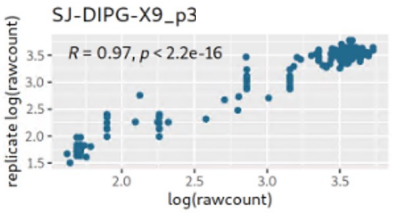

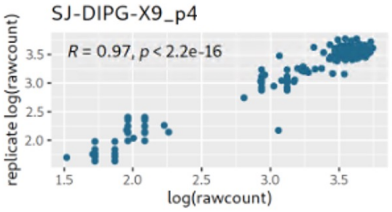

SJ-DIPG-X9	Z'
p1	0.74
p2	0.52
p3	0.69
p4	0.53

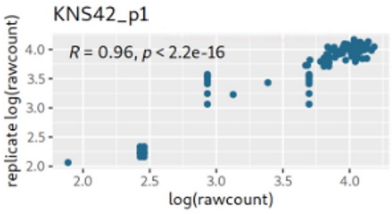

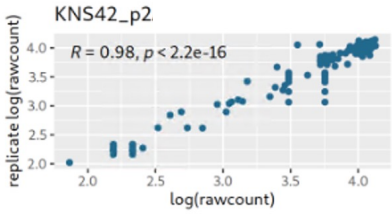

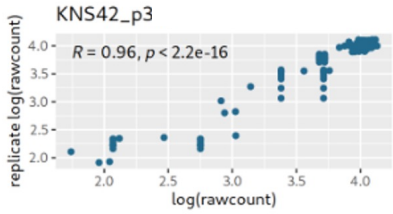

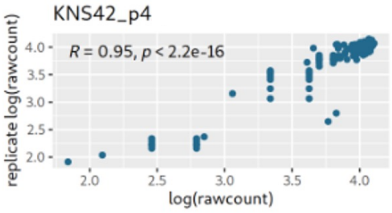

KNS42	Z'
p1	0.69
p2	0.77
p3	0.76
p4	0.64

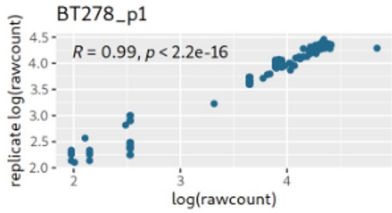

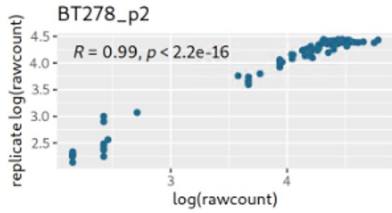

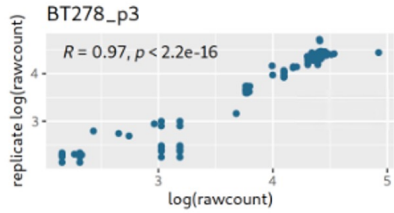

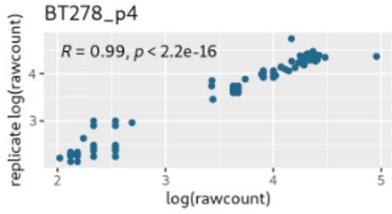

BT278	Z'
p1	0.84
p2	0.72
p3	0.79
p4	0.84

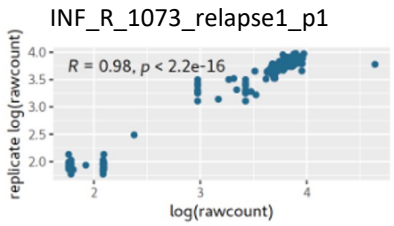

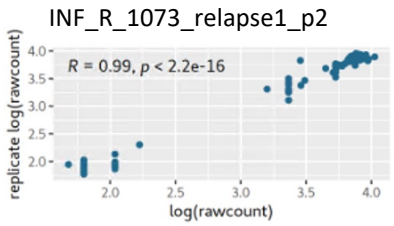

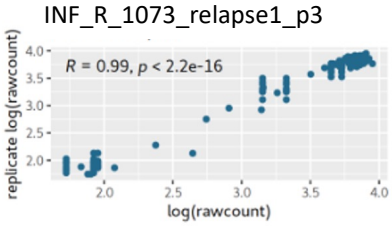

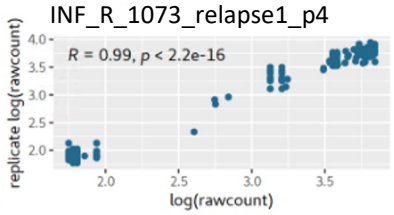

INF_R_1073_relapse1	Z'
p1	0.74
p2	0.76
p3	0.75
p4	0.76

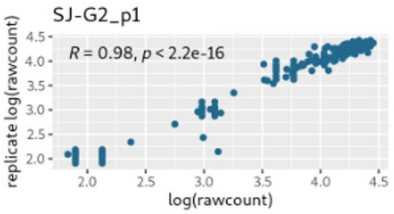

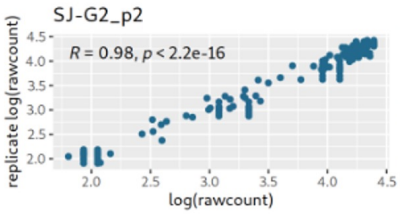

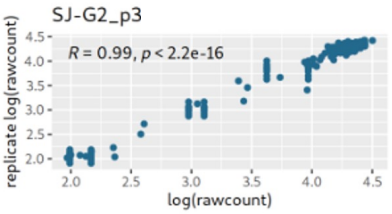

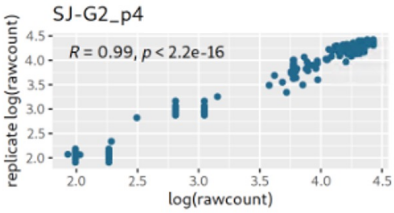

SJ-G2	Z'
p1	0.49
p2	0.68
p3	0.68
p4	0.67

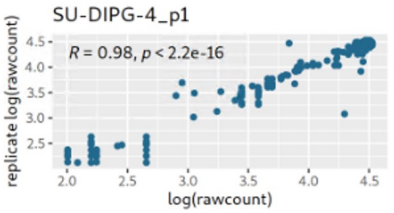

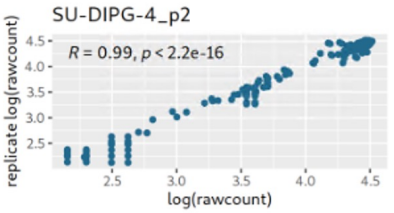

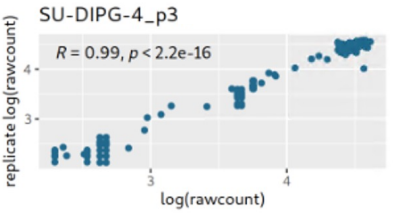

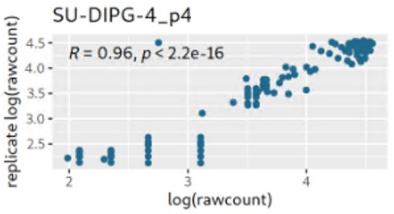

SU-DIPG-4	Z'
p1	0.69
p2	0.85
p3	0.83
p4	0.66

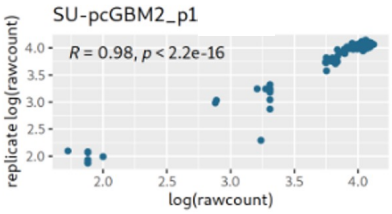

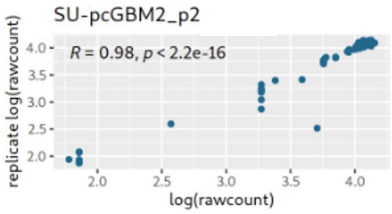

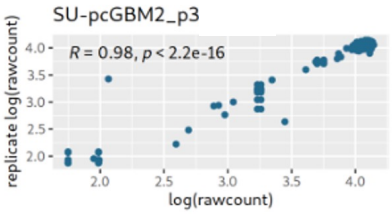

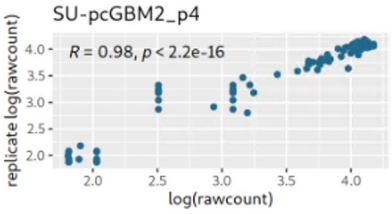

SU-pcGBM2	Z'
p1	0.82
p2	0.83
p3	0.83
p4	0.79

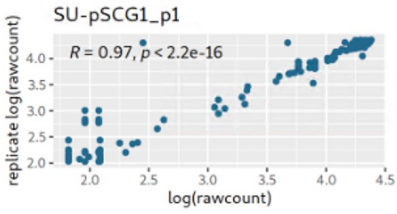

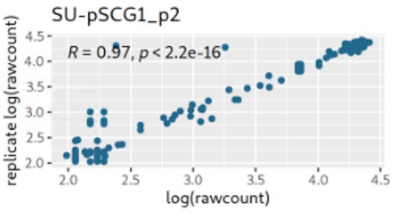

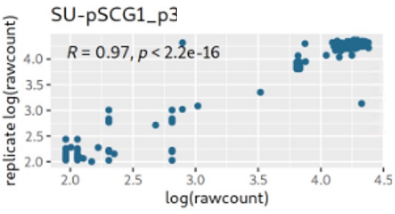

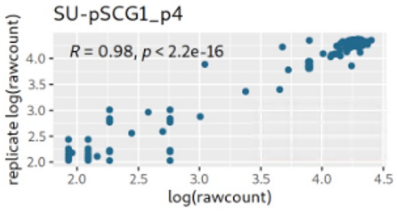

SU-pSCG1	Z'
p1	0.81
p2	0.71
p3	0.82
p4	0.47

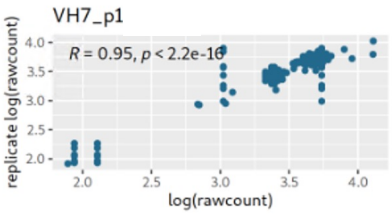

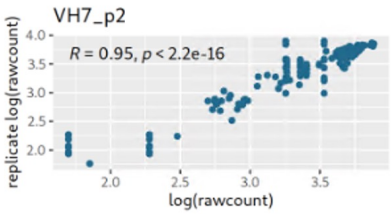

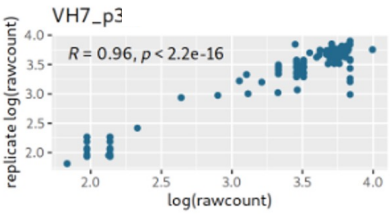

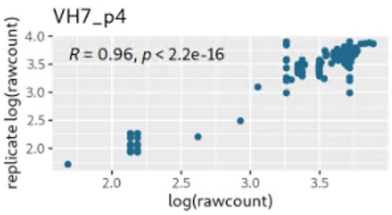

VH7	Z'
p1	0.52
p2	0.65
p3	0.70
p4	0.69

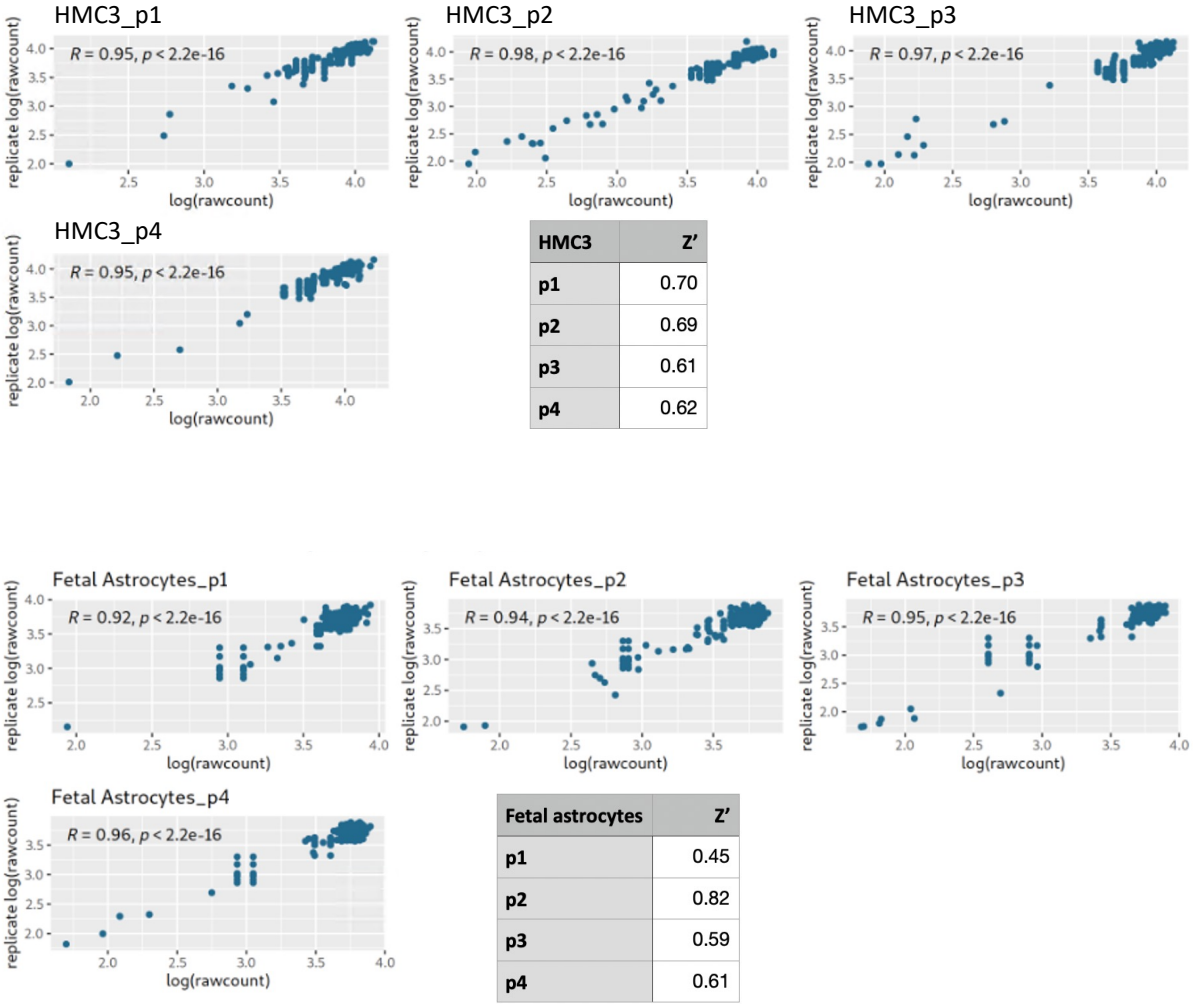

HMC3	Z'
p1	0.70
p2	0.69
p3	0.61
p4	0.62

Fetal astrocytes	Z'
p1	0.45
p2	0.82
p3	0.59
p4	0.61

Appendix Figure 1. QC data of all cell models screened with epigenetic drug library. The drugs were dispensed into four plates depicted as p1, p2, p3 and p4. Four graphs demonstrate correlation between replicates in each plate, and the table illustrates Z' for each plate. 1=Z': an ideal assay; 1>Z'≥0.5: an excellent assay; 0.5>Z'>0: a marginal assay; Z'=0: a non-ideal assay; Z'<0: data is impossible to use. The data were generated using iTReX shiny app.

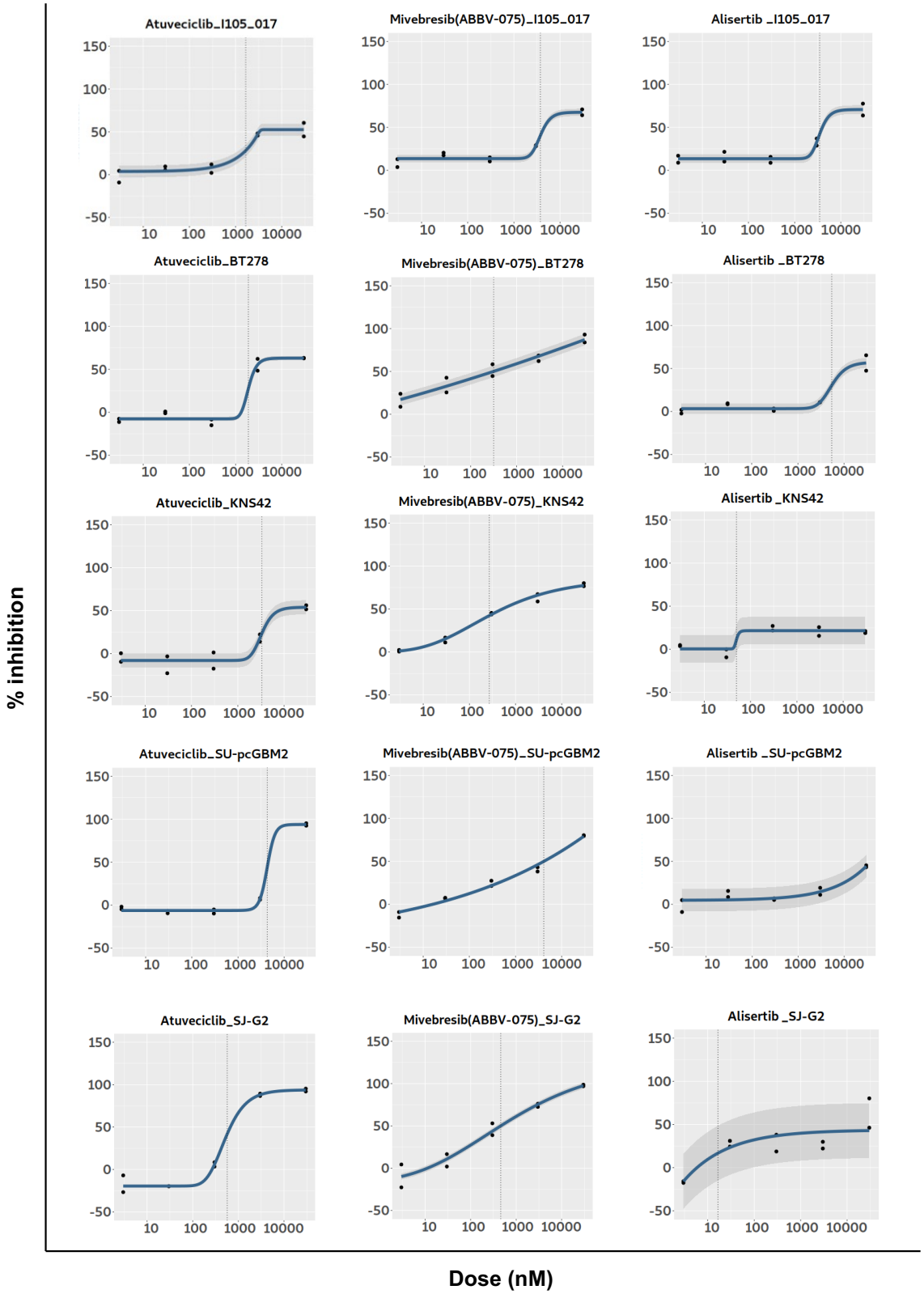

Appendix Figure 2. Dose response curves of non-H3K27M pHGG cell models for atuveciclib (CDK9i), mivebresib (BETi) and alisertib (AURKi).

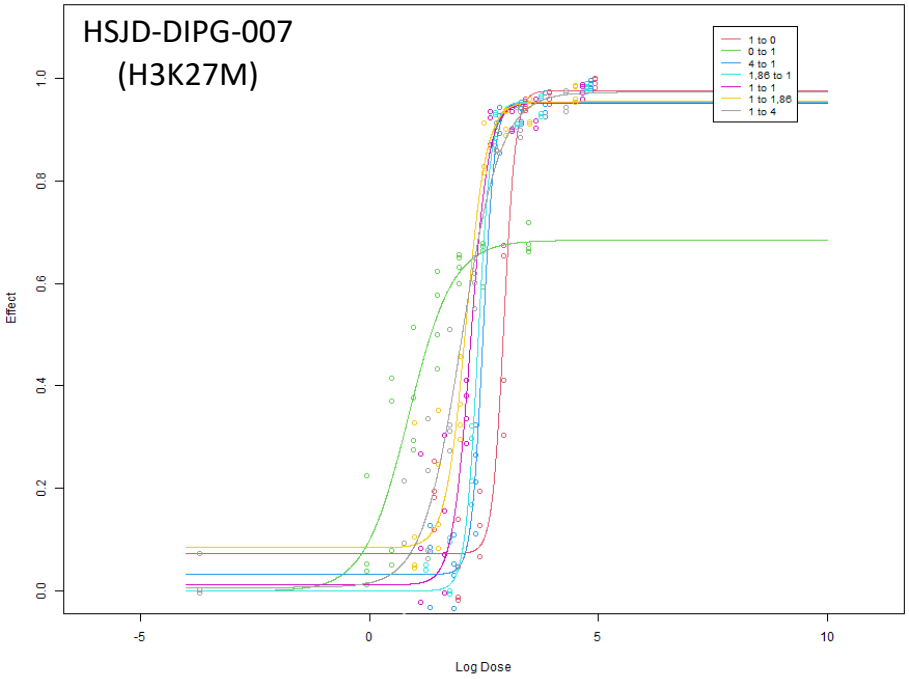
HSJD-DIPG-007
(H3K27M)
1 to 0
0 to 1
4 to 1
1,86 to 1
1 to 1
1 to 1,86
1 to 4
Effect
Log Dose

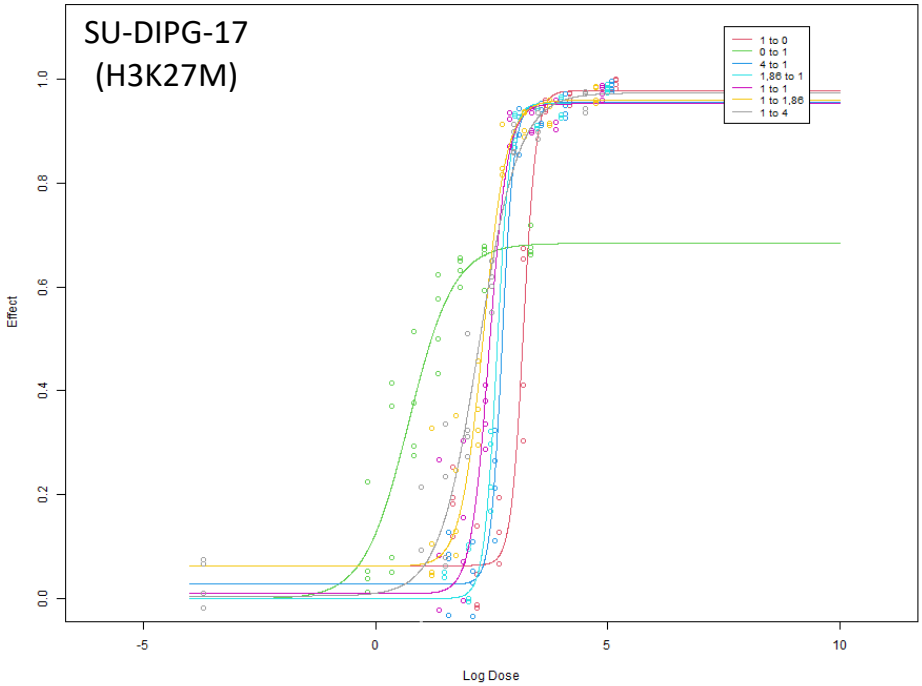
SU-DIPG-17
(H3K27M)
1 to 0
0 to 1
4 to 1
1,86 to 1
1 to 1
1 to 1,86
1 to 4
Effect
Log Dose

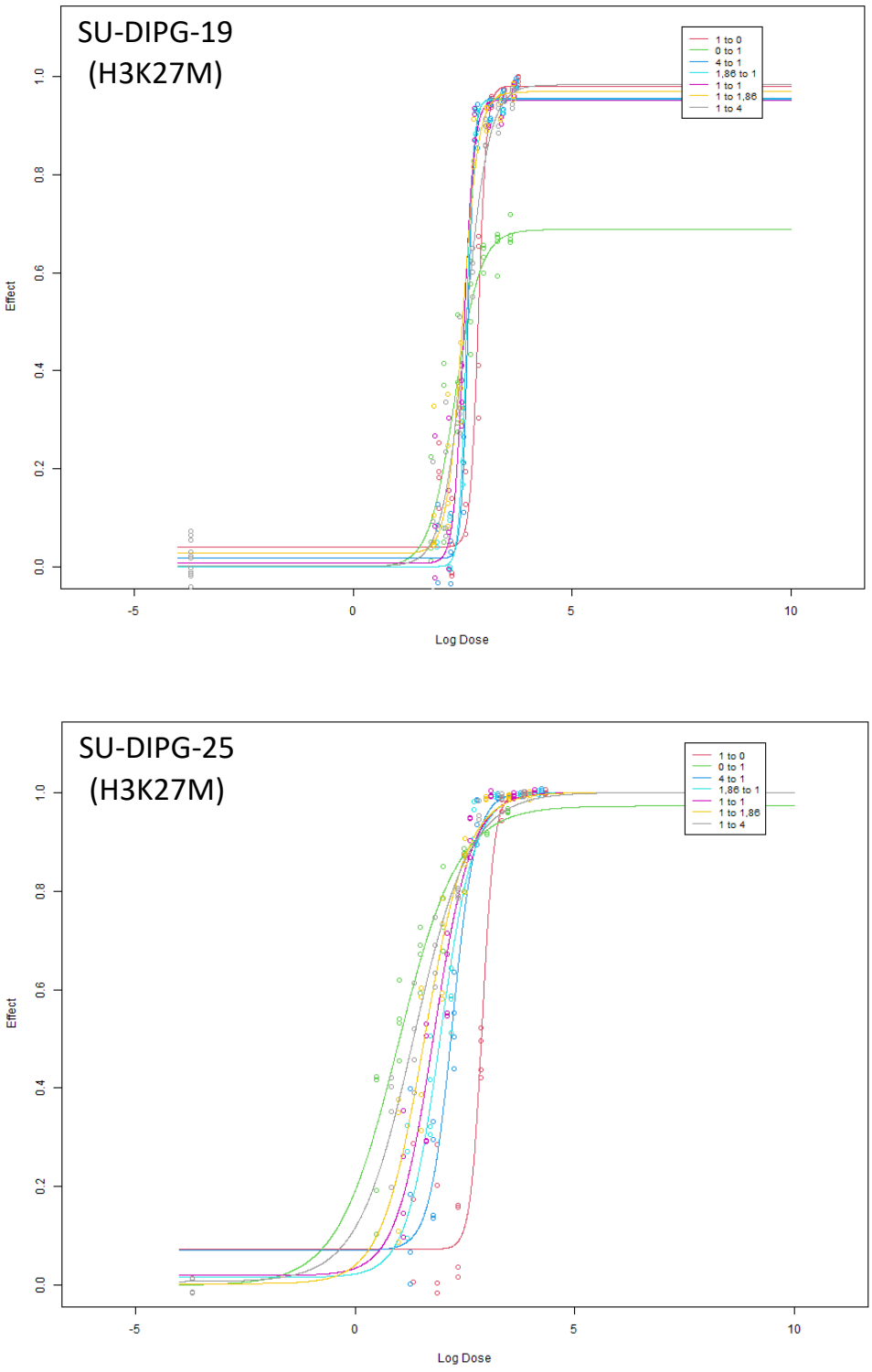

Appendix Figure 3. Separate synergy plots for four H3K27M DMG models tested in synergy screens with 7-ray approach. The y-axis represents the inhibition, 1 being IC100, 0 being IC0, and x-axis shows the logarithm base 10 of concentrations used in nM. The ratios of atuveciclib (CDK9i) and BMS-986158 (BETi) were depicted in boxes in each plot.

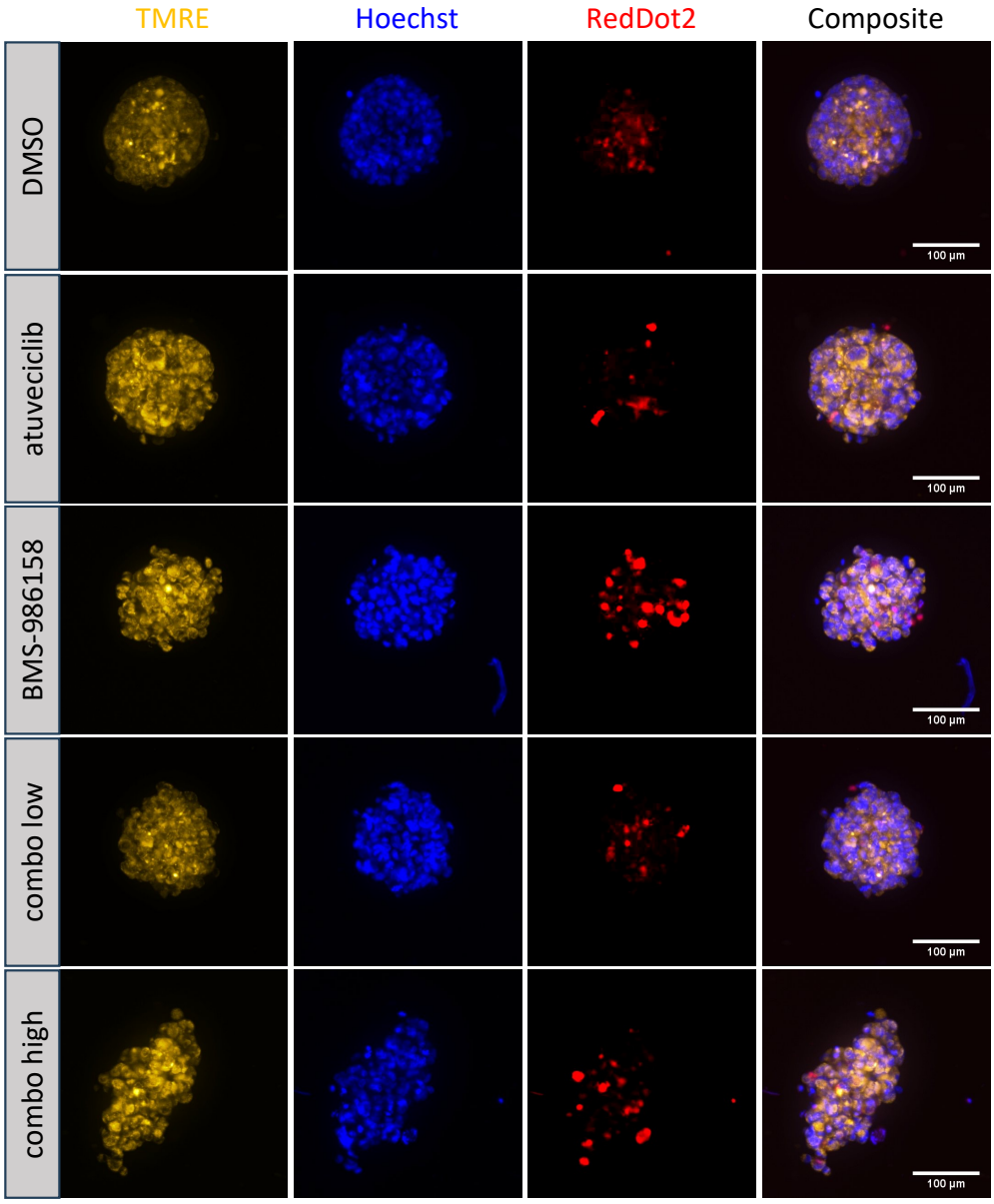

Appendix Figure 4. HCM analysis of KNS42 (H3G34V) cells with the treatment conditions of SU-DIPG-17 (H3K27M) as detailed in **Table 38**. TMRE stains the metabolically active cells, Hoechst stains nuclei and RedDot2 is a cell impermeant dye, staining only the dead cells. Composite is the merged images of all three channels.

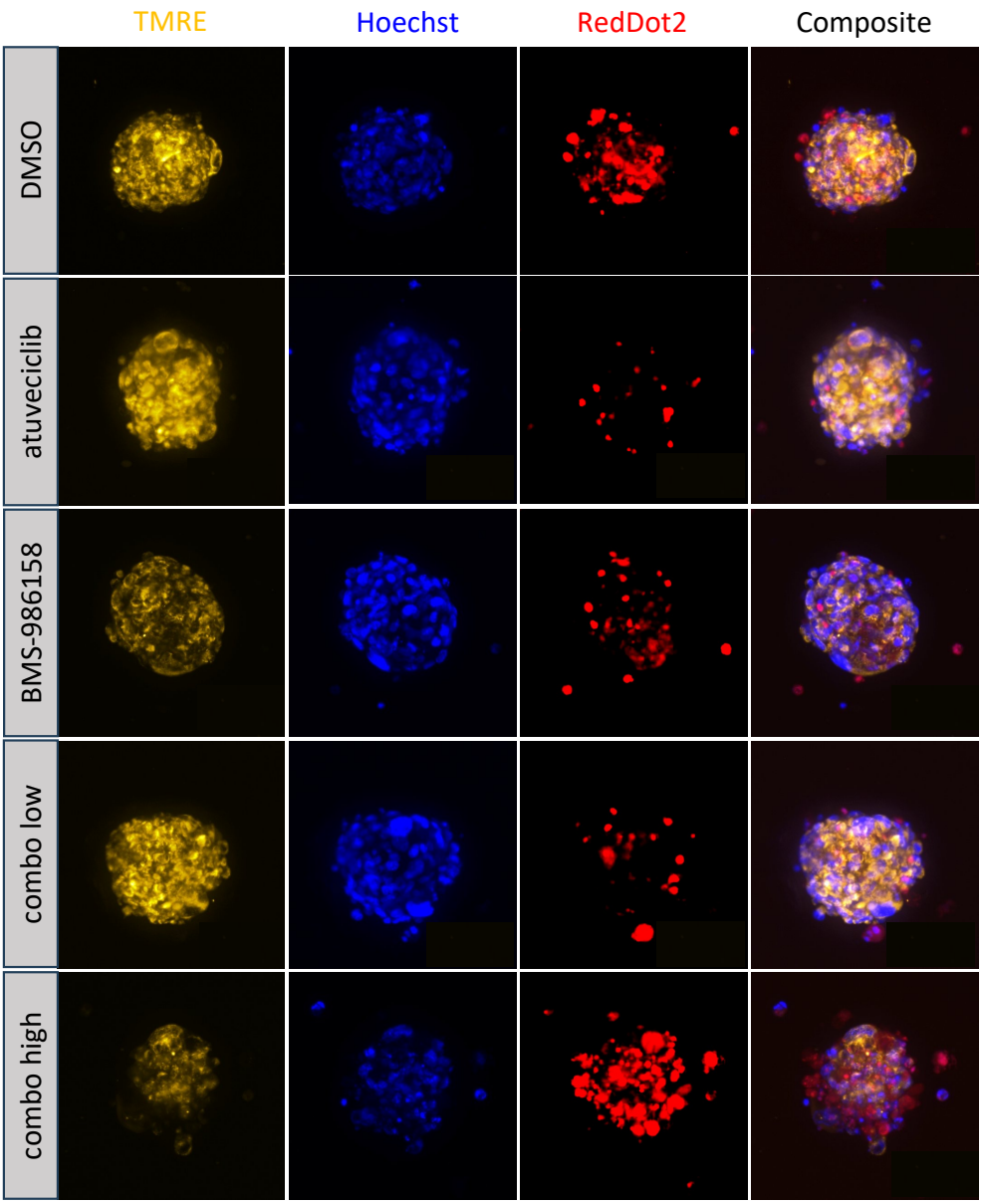

Appendix Figure 5. HCM analysis of HMC3 (microglia) cells under the treatment conditions of SU-DIPG-17 (H3K27M) according to **Table 38**. TMRE stains the metabolically active cells, Hoechst stains nuclei and RedDot2 is a cell impermeant dye, staining only the dead cells. Composite is the merged images of all three channels.

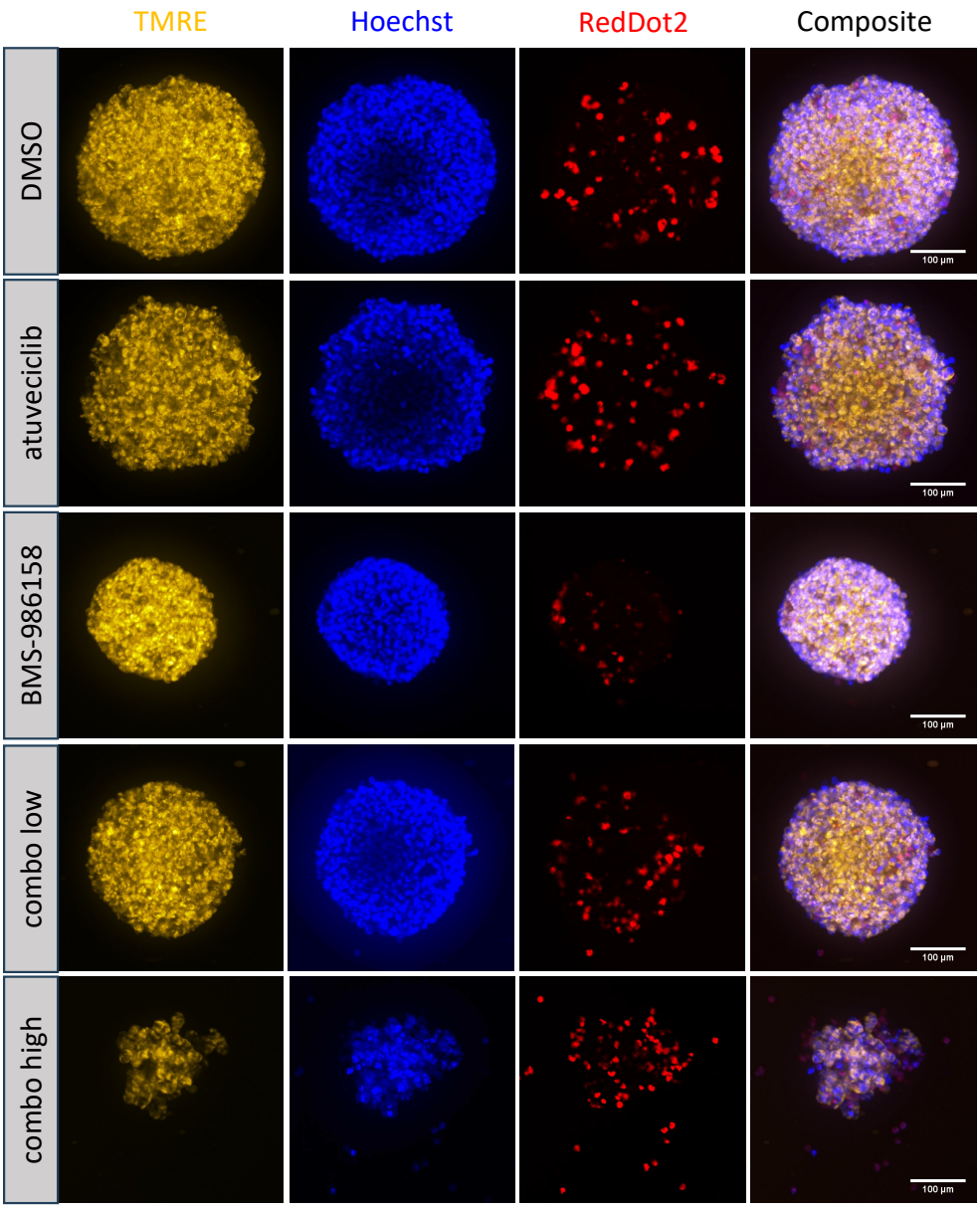

Appendix Figure 6. HCM analysis of HSJD-DIPG-007 (H3K27M) cells under different treatments. The concentrations used for each treatment were detailed in **Table 38**. TMRE stains the metabolically active cells, Hoechst stains nuclei and RedDot2 is a cell impermeant dye, staining only the dead cells. Composite is the merged images of all three channels.

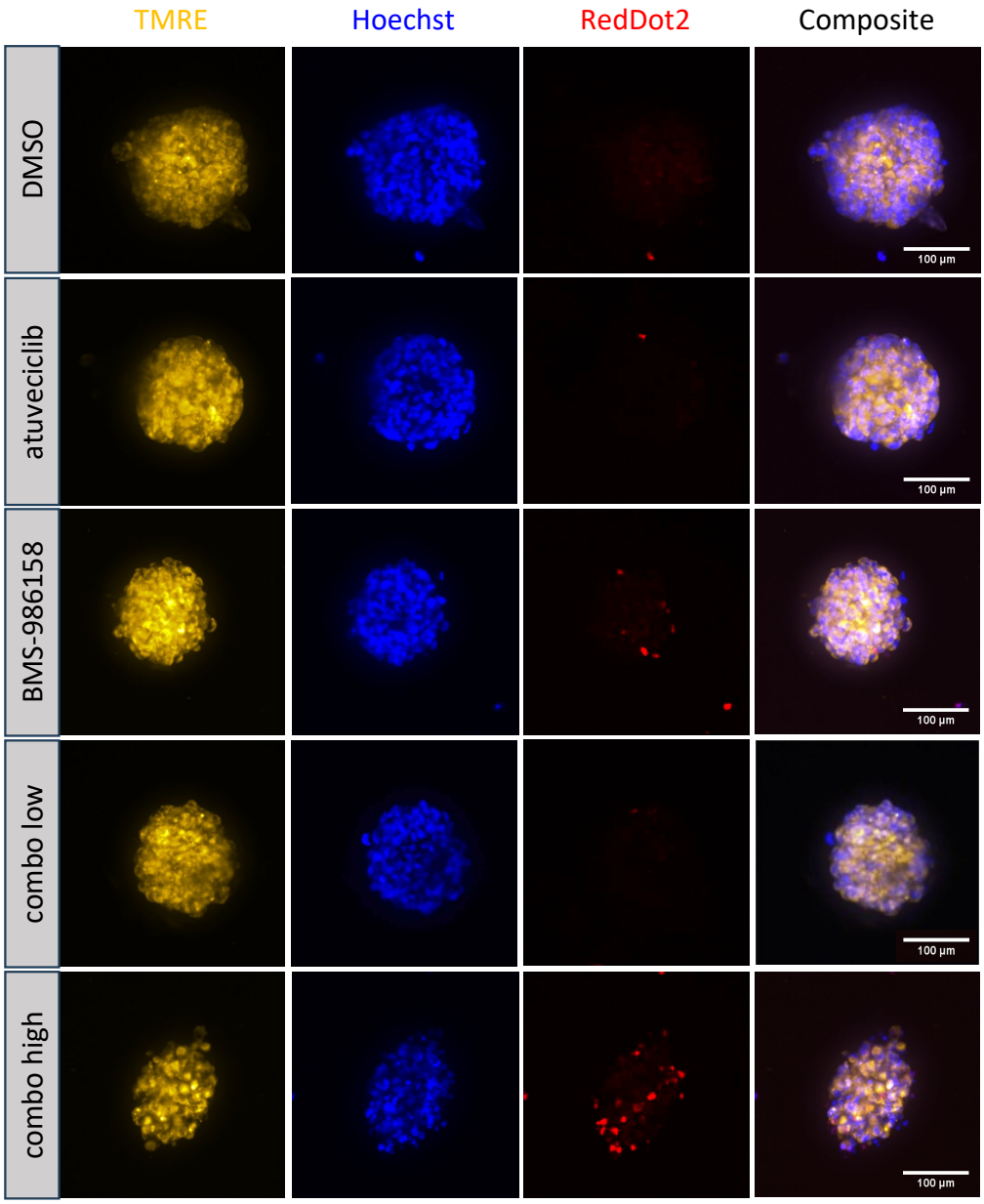

Appendix Figure 7. HCM analysis of KNS42 (H3G34V) model under the treatment conditions of HSJD-DIPG-007 (H3K27M) according to **Table 38**. TMRE stains the metabolically active cells, Hoechst stains nuclei and RedDot2 is a cell impermeant dye, staining only the dead cells. Composite is the merged images of all three channels.

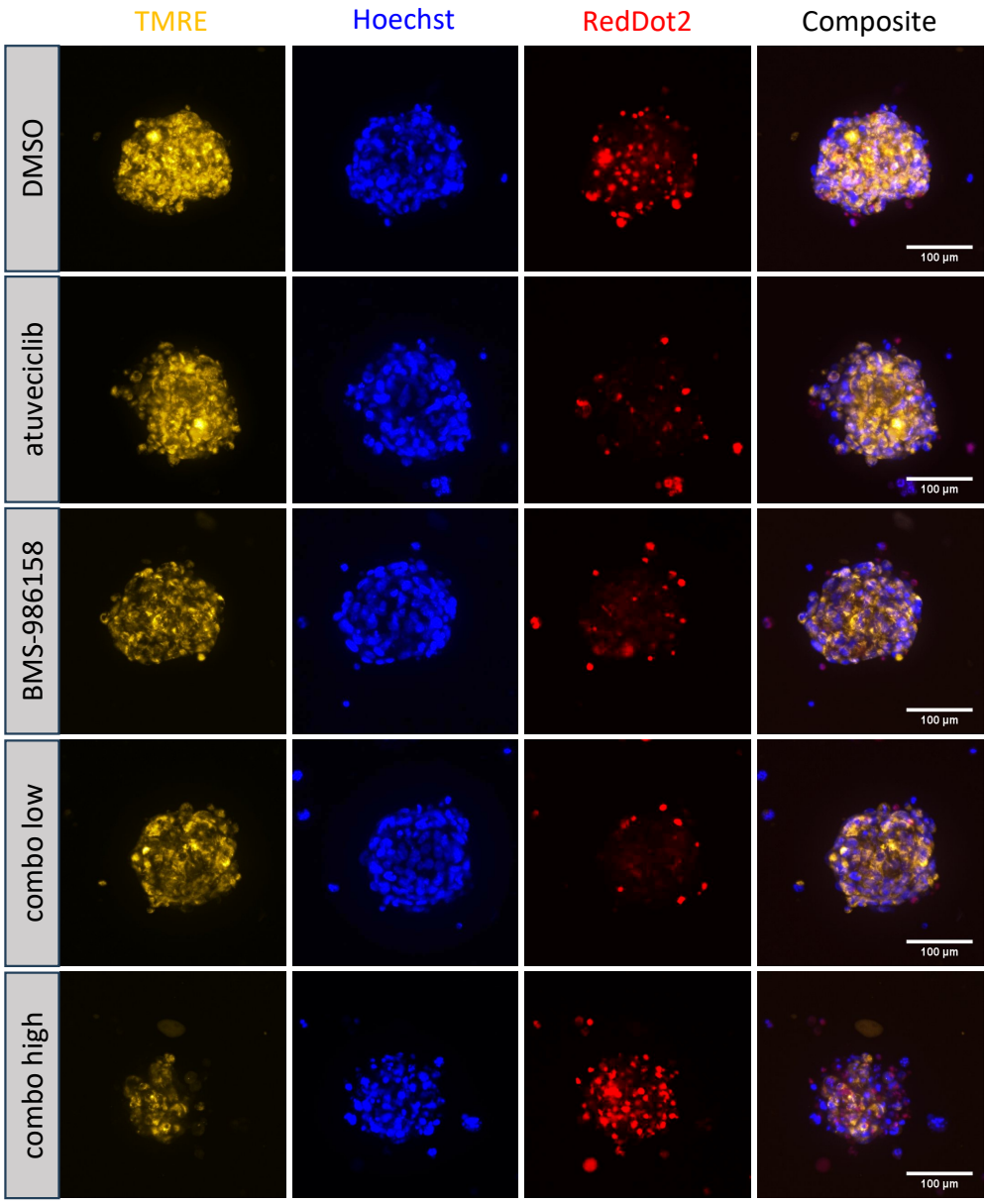

Appendix Figure 8. HCM analysis of HMC3 (microglia) under the treatment conditions of HSJD-DIPG-007 (H3K27M) according to **Table 38**. TMRE stains the metabolically active cells, Hoechst stains nuclei and RedDot2 is a cell impermeant dye, staining only the dead cells. Composite is the merged images of all three channels.

1st exp – Gy 0 (SF0)

	BztCl	DMSO	
mean	811	15825.1	Z'= 0.55
std	172.0	2059.3	

2nd exp – Gy 0 (SF0)

	BztCl	DMSO	
mean	2092.5	11235.6	Z'= 0.48
std	131.7	1451.8	

1st exp – Gy 0.5 (SF75) → *23 %*

	BztCl	DMSO	
mean	1066.00	12166.8	Z'= 0.53
std	145.6	1595.9	

2nd exp – Gy 0.5 (SF75) → *30 %*

	BztCl	DMSO	
mean	2920.50	7869.2	Z'= 0.31
std	195.1	943.7	

1st exp – Gy 1 (SF50) → *38 %*

	BztCl	DMSO	
mean	942.60	9751.7	Z'= 0.58
std	116.1	1113.0	

2nd exp – Gy 1 (SF50) → *49 %*

	BztCl	DMSO	
mean	3084.83	5687.2	Z'= -0.09
std	187.6	754.8	

Appendix Figure 9. Radiosensitization experiments conducted on SU-DIPG-19 (H3K27M). Each table represents a single plate, and they demonstrate counts detected for BztCl and DMSO in 1st and 2nd experiment (exp). Z' was calculated as a QC criterion. Gray (Gy) doses used for each plate are mentioned above each table.

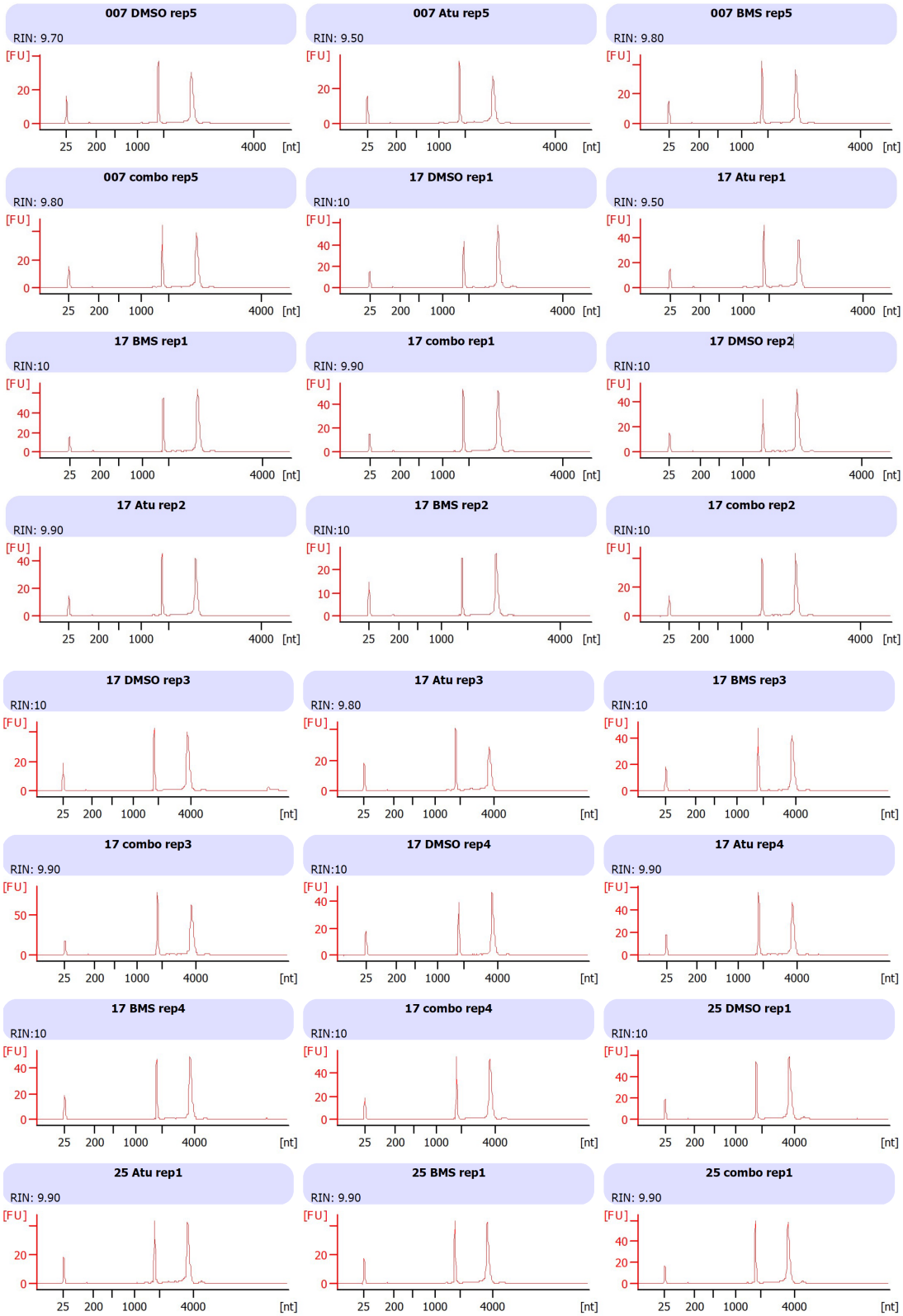
007 DMSO rep5
RIN: 9.70
007 Atu rep5
RIN: 9.50
007 BMS rep5
RIN: 9.80
007 combo rep5
RIN: 9.80
17 DMSO rep1
RIN:10
17 Atu rep1
RIN: 9.50
17 BMS rep1
RIN:10
17 combo rep1
RIN: 9.90
17 DMSO rep2
RIN:10
17 Atu rep2
RIN: 9.90
17 BMS rep2
RIN:10
17 combo rep2
RIN:10
17 DMSO rep3
RIN:10
17 Atu rep3
RIN: 9.80
17 BMS rep3
RIN:10
17 combo rep3
RIN: 9.90
17 DMSO rep4
RIN:10
17 Atu rep4
RIN: 9.90
17 BMS rep4
RIN:10
17 combo rep4
RIN:10
25 DMSO rep1
RIN:10
25 Atu rep1
RIN: 9.90
25 BMS rep1
RIN: 9.90
25 combo rep1
RIN: 9.90
[FU]
[nt]
25
200
1000
4000

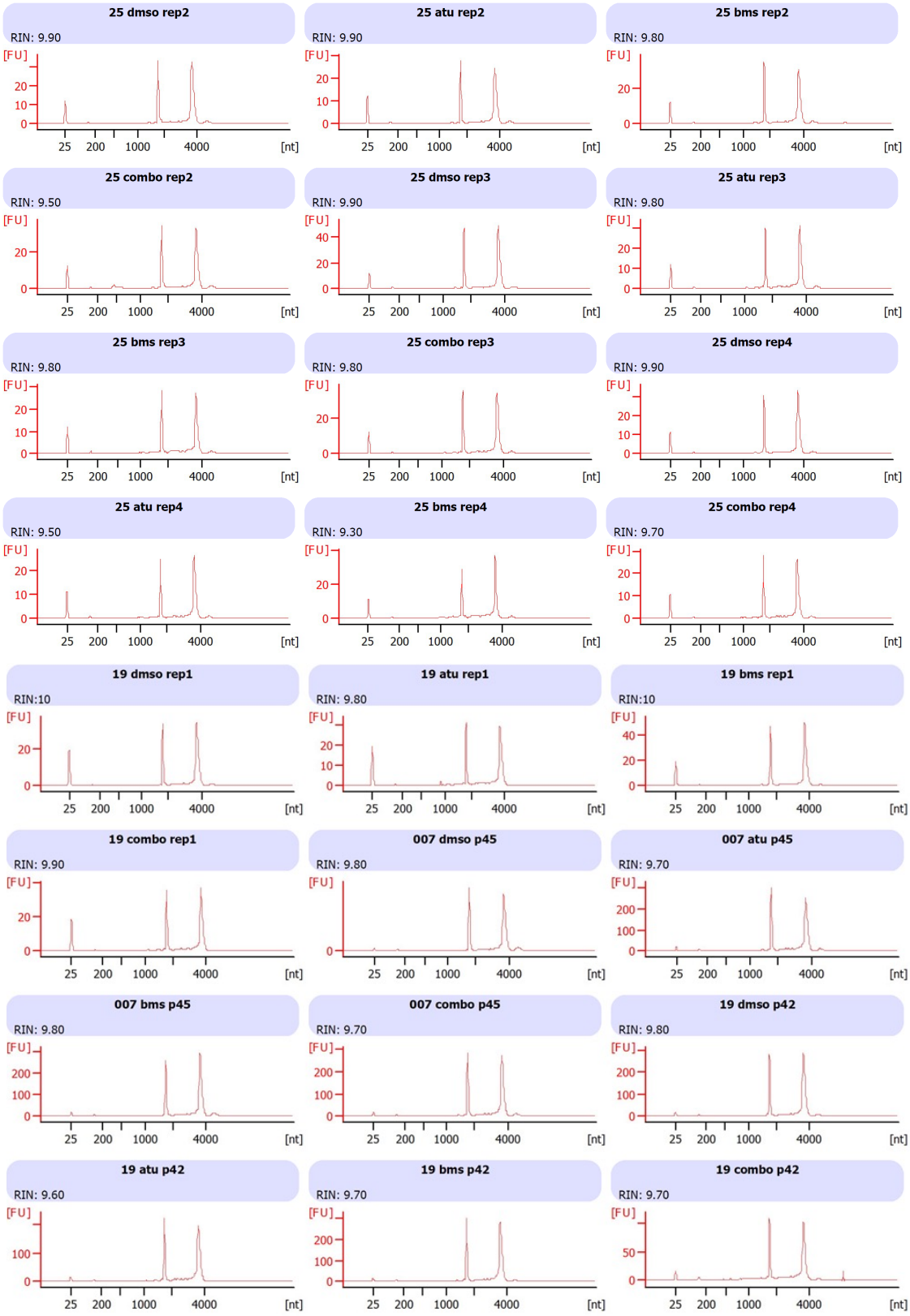
25 dmso rep2
RIN: 9.90
25 atu rep2
RIN: 9.90
25 bms rep2
RIN: 9.80
25 combo rep2
RIN: 9.50
25 dmso rep3
RIN: 9.90
25 atu rep3
RIN: 9.80
25 bms rep3
RIN: 9.80
25 combo rep3
RIN: 9.80
25 dmso rep4
RIN: 9.90
25 atu rep4
RIN: 9.50
25 bms rep4
RIN: 9.30
25 combo rep4
RIN: 9.70
19 dmso rep1
RIN:10
19 atu rep1
RIN: 9.80
19 bms rep1
RIN:10
19 combo rep1
RIN: 9.90
007 dmso p45
RIN: 9.80
007 atu p45
RIN: 9.70
007 bms p45
RIN: 9.80
007 combo p45
RIN: 9.70
19 dmso p42
RIN: 9.80
19 atu p42
RIN: 9.60
19 bms p42
RIN: 9.70
19 combo p42
RIN: 9.70
[FU]
[nt]
25
200
1000
4000

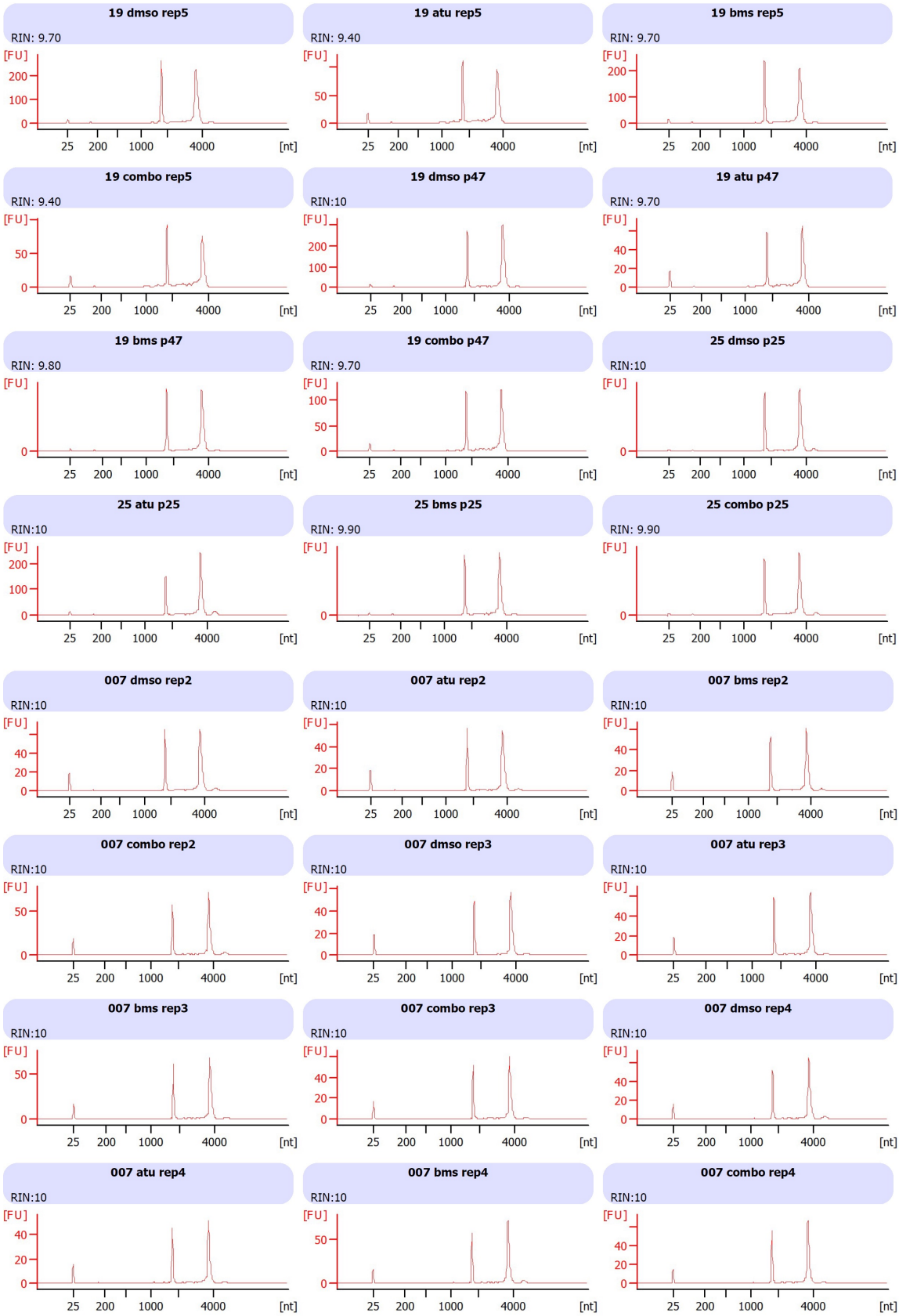
19 dmso rep5
RIN: 9.70
19 atu rep5
RIN: 9.40
19 bms rep5
RIN: 9.70
19 combo rep5
RIN: 9.40
19 dmso p47
RIN:10
19 atu p47
RIN: 9.70
19 bms p47
RIN: 9.80
19 combo p47
RIN: 9.70
25 dmso p25
RIN:10
25 atu p25
RIN:10
25 bms p25
RIN: 9.90
25 combo p25
RIN: 9.90
007 dmso rep2
RIN:10
007 atu rep2
RIN:10
007 bms rep2
RIN:10
007 combo rep2
RIN:10
007 dmso rep3
RIN:10
007 atu rep3
RIN:10
007 bms rep3
RIN:10
007 combo rep3
RIN:10
007 dmso rep4
RIN:10
007 atu rep4
RIN:10
007 bms rep4
RIN:10
007 combo rep4
RIN:10
[FU]
[nt]
25
200
1000
4000

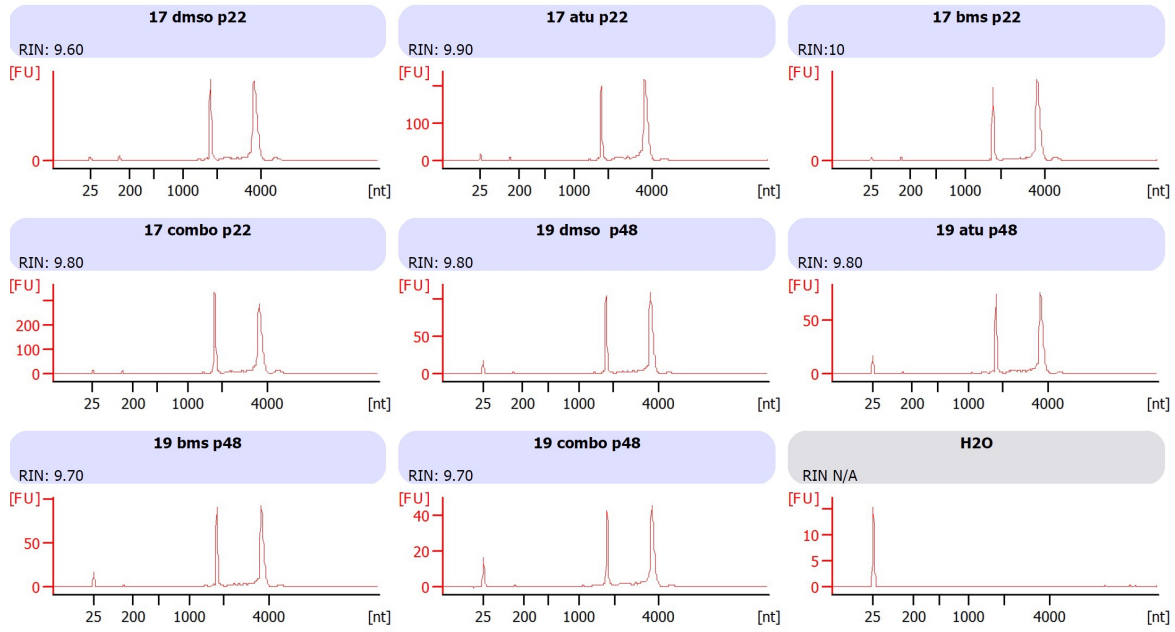

Appendix Figure 10. Bioanalyzer QC check of RNA samples submitted for RNAseq. RIN: RNA integrity number.

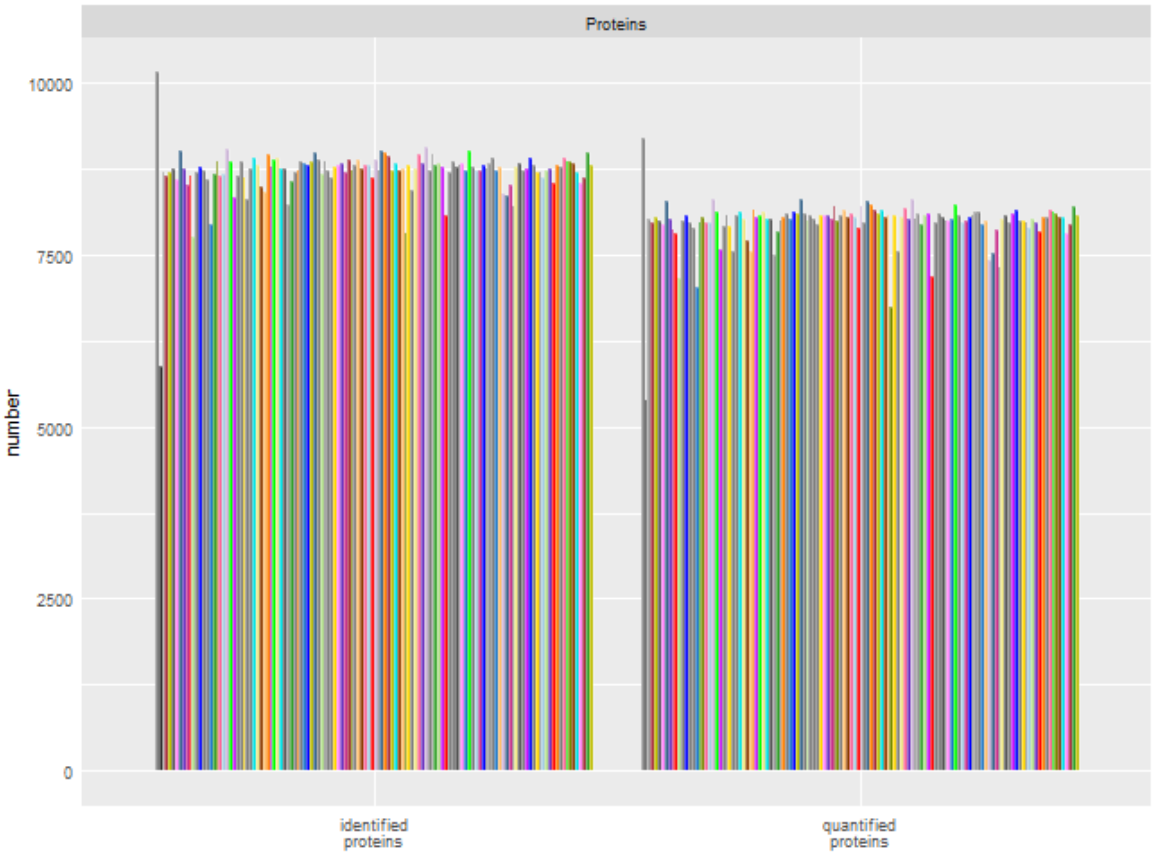

Appendix Figure 11. Identified and quantified proteins in LC-MS/MS. Each bar represents an individual sample.

UMAP cluster	Sample Name	Treatment	Cell model	H3 status	Replicate
1	Atu_25_WT_rep3	atuveciclib	SU-DIPG-25	H3 WT	rep-3
1	BMS_7_WT_rep1	BMS-986158	HSJD-DIPG-007	H3 WT	rep-1
1	Atu_19_WT_rep2	atuveciclib	SU-DIPG-19	H3 WT	rep-2
1	Atu_17_WT_rep4	atuveciclib	SU-DIPG-17	H3 WT	rep-4
1	BMS_17_WT_rep1	BMS-986158	SU-DIPG-17	H3 WT	rep-1
1	DMSO_17_WT_rep4	DMSO	SU-DIPG-17	H3 WT	rep-4
1	syn_7_WT_rep1	combo low	HSJD-DIPG-007	H3 WT	rep-1
1	syn_17_WT_rep4	combo low	SU-DIPG-17	H3 WT	rep-4
1	Atu_17_mut_rep4	atuveciclib	SU-DIPG-17	H3K27M	rep-4
1	DMSO_25_WT_rep2	DMSO	SU-DIPG-25	H3 WT	rep-2
1	Atu_7_WT_rep3	atuveciclib	HSJD-DIPG-007	H3 WT	rep-3
1	syn_25_WT_rep2	combo low	SU-DIPG-25	H3 WT	rep-2
1	syn_19_WT_rep3	combo low	SU-DIPG-19	H3 WT	rep-3
1	DMSO_19_WT_rep1	DMSO	SU-DIPG-19	H3 WT	rep-1
1	BMS_25_WT_rep2	BMS-986158	SU-DIPG-25	H3 WT	rep-2
1	DMSO_7_WT_rep1	DMSO	HSJD-DIPG-007	H3 WT	rep-1
1	BMS_19_WT_rep3	BMS-986158	SU-DIPG-19	H3 WT	rep-3
1	BMS_25_WT_rep3	BMS-986158	SU-DIPG-25	H3 WT	rep-3
1	DMSO_19_WT_rep3	DMSO	SU-DIPG-19	H3 WT	rep-3
1	Atu_25_WT_rep2	atuveciclib	SU-DIPG-25	H3 WT	rep-2
1	BMS_25_mut_rep4	BMS-986158	SU-DIPG-25	H3K27M	rep-4
1	syn_19_WT_rep4	combo low	SU-DIPG-19	H3 WT	rep-4
1	syn_25_WT_rep4	combo low	SU-DIPG-25	H3 WT	rep-4
1	DMSO_17_WT_rep1	DMSO	SU-DIPG-17	H3 WT	rep-1
1	BMS_17_WT_rep3	BMS-986158	SU-DIPG-17	H3 WT	rep-3
1	syn_17_WT_rep2	combo low	SU-DIPG-17	H3 WT	rep-2
1	syn_7_WT_rep4	combo low	HSJD-DIPG-007	H3 WT	rep-4
1	BMS_7_WT_rep4	BMS-986158	HSJD-DIPG-007	H3 WT	rep-4
1	Atu_19_WT_rep1	atuveciclib	SU-DIPG-19	H3 WT	rep-1
1	DMSO_25_WT_rep1	DMSO	SU-DIPG-25	H3 WT	rep-1
1	BMS_19_WT_rep4	BMS-986158	SU-DIPG-19	H3 WT	rep-4
1	DMSO_7_WT_rep3	DMSO	HSJD-DIPG-007	H3 WT	rep-3
1	Atu_7_WT_rep4	atuveciclib	HSJD-DIPG-007	H3 WT	rep-4
1	Atu_17_WT_rep3	atuveciclib	SU-DIPG-17	H3 WT	rep-3
1	syn_17_WT_rep3	combo low	SU-DIPG-17	H3 WT	rep-3
1	DMSO_19_WT_rep4	DMSO	SU-DIPG-19	H3 WT	rep-4
1	DMSO_7_WT_rep4	DMSO	HSJD-DIPG-007	H3 WT	rep-4
1	BMS_19_WT_rep1	BMS-986158	SU-DIPG-19	H3 WT	rep-1
1	DMSO_25_WT_rep3	DMSO	SU-DIPG-25	H3 WT	rep-3
1	syn_19_mut_rep1	combo low	SU-DIPG-19	H3K27M	rep-1
1	BMS_25_WT_rep1	BMS-986158	SU-DIPG-25	H3 WT	rep-1
1	Atu_19_WT_rep4	atuveciclib	SU-DIPG-19	H3 WT	rep-4
1	syn_25_WT_rep3	combo low	SU-DIPG-25	H3 WT	rep-3
1	BMS_17_WT_rep4	BMS-986158	SU-DIPG-17	H3 WT	rep-4
1	Atu_17_WT_rep1	atuveciclib	SU-DIPG-17	H3 WT	rep-1
1	syn_19_WT_rep2	combo low	SU-DIPG-19	H3 WT	rep-2
1	Atu_25_WT_rep4	atuveciclib	SU-DIPG-25	H3 WT	rep-4
1	syn_7_WT_rep3	combo low	HSJD-DIPG-007	H3 WT	rep-3
1	BMS_7_WT_rep3	BMS-986158	HSJD-DIPG-007	H3 WT	rep-3
1	Atu_7_WT_rep1	atuveciclib	HSJD-DIPG-007	H3 WT	rep-1
1	DMSO_17_WT_rep2	DMSO	SU-DIPG-17	H3 WT	rep-2
1	BMS_19_WT_rep2	BMS-986158	SU-DIPG-19	H3 WT	rep-2
1	BMS_19_mut_rep3	BMS-986158	SU-DIPG-19	H3K27M	rep-3
1	DMSO_19_mut_rep2	DMSO	SU-DIPG-19	H3K27M	rep-2
1	syn_25_mut_rep4	combo low	SU-DIPG-25	H3K27M	rep-4
1	BMS_25_WT_rep4	BMS-986158	SU-DIPG-25	H3 WT	rep-4
1	Atu_25_WT_rep1	atuveciclib	SU-DIPG-25	H3 WT	rep-1

1	syn_17_WT_rep1	combo low	SU-DIPG-17	H3 WT	rep-1
1	DMSO_17_WT_rep3	DMSO	SU-DIPG-17	H3 WT	rep-3
1	syn_7_WT_rep2	combo low	HSJD-DIPG-007	H3 WT	rep-2
1	syn_19_WT_rep1	combo low	SU-DIPG-19	H3 WT	rep-1
1	Atu_7_WT_rep2	atuveciclib	HSJD-DIPG-007	H3 WT	rep-2
1	BMS_17_WT_rep2	BMS-986158	SU-DIPG-17	H3 WT	rep-2
1	Atu_19_WT_rep3	atuveciclib	SU-DIPG-19	H3 WT	rep-3
1	Atu_17_WT_rep2	atuveciclib	SU-DIPG-17	H3 WT	rep-2
1	syn_25_WT_rep1	combo low	SU-DIPG-25	H3 WT	rep-1
1	DMSO_25_WT_rep4	DMSO	SU-DIPG-25	H3 WT	rep-4
1	DMSO_7_WT_rep2	DMSO	HSJD-DIPG-007	H3 WT	rep-2
1	DMSO_19_WT_rep2	DMSO	SU-DIPG-19	H3 WT	rep-2
1	BMS_7_WT_rep2	BMS-986158	HSJD-DIPG-007	H3 WT	rep-2

UMAP cluster	**Sample Name**	**Treatment**	**Cell model**	**H3 status**	**Replicate**
2	DMSO_7_mut_rep1	DMSO	HSJD-DIPG-007	H3K27M	rep-1
2	BMS_7_mut_rep3	BMS-986158	HSJD-DIPG-007	H3K27M	rep-3
2	Atu_7_mut_rep1	atuveciclib	HSJD-DIPG-007	H3K27M	rep-1
2	syn_7_mut_rep1	combo low	HSJD-DIPG-007	H3K27M	rep-1
2	DMSO_7_mut_rep4	DMSO	HSJD-DIPG-007	H3K27M	rep-4
2	syn_7_mut_rep3	combo low	HSJD-DIPG-007	H3K27M	rep-3
2	Atu_7_mut_rep3	atuveciclib	HSJD-DIPG-007	H3K27M	rep-3
2	BMS_7_mut_rep4	BMS-986158	HSJD-DIPG-007	H3K27M	rep-4
2	DMSO_7_mut_rep2	DMSO	HSJD-DIPG-007	H3K27M	rep-2
2	Atu_7_mut_rep2	atuveciclib	HSJD-DIPG-007	H3K27M	rep-2
2	syn_7_mut_rep2	combo low	HSJD-DIPG-007	H3K27M	rep-2
2	BMS_7_mut_rep1	BMS-986158	HSJD-DIPG-007	H3K27M	rep-1
2	syn_7_mut_rep4	combo low	HSJD-DIPG-007	H3K27M	rep-4
2	BMS_7_mut_rep2	BMS-986158	HSJD-DIPG-007	H3K27M	rep-2
2	Atu_7_mut_rep4	atuveciclib	HSJD-DIPG-007	H3K27M	rep-4
2	DMSO_7_mut_rep3	DMSO	HSJD-DIPG-007	H3K27M	rep-3

UMAP cluster	Sample Name	Treatment	Cell model	H3 status	Replicate
3	DMSO_19_mut_rep4	DMSO	SU-DIPG-19	H3K27M	rep-4
3	syn_19_mut_rep2	combo low	SU-DIPG-19	H3K27M	rep-2
3	Atu_19_mut_rep3	atuveciclib	SU-DIPG-19	H3K27M	rep-3
3	BMS_19_mut_rep2	BMS-986158	SU-DIPG-19	H3K27M	rep-2
3	Atu_19_mut_rep1	atuveciclib	SU-DIPG-19	H3K27M	rep-1
3	DMSO_19_mut_rep1	DMSO	SU-DIPG-19	H3K27M	rep-1
3	syn_19_mut_rep3	combo low	SU-DIPG-19	H3K27M	rep-3
3	BMS_19_mut_rep4	BMS-986158	SU-DIPG-19	H3K27M	rep-4
3	DMSO_19_mut_rep3	DMSO	SU-DIPG-19	H3K27M	rep-3
3	BMS_19_mut_rep1	BMS-986158	SU-DIPG-19	H3K27M	rep-1
3	Atu_19_mut_rep2	atuveciclib	SU-DIPG-19	H3K27M	rep-2
3	syn_19_mut_rep4	combo low	SU-DIPG-19	H3K27M	rep-4
3	Atu_19_mut_rep4	atuveciclib	SU-DIPG-19	H3K27M	rep-4

UMAP cluster	Sample Name	Treatment	Cell model	H3 status	Replicate
4	syn_17_mut_rep2	combo low	SU-DIPG-17	H3K27M	rep-2
4	BMS_17_mut_rep1	BMS-986158	SU-DIPG-17	H3K27M	rep-1
4	DMSO_17_mut_rep3	DMSO	SU-DIPG-17	H3K27M	rep-3
4	DMSO_17_mut_rep4	DMSO	SU-DIPG-17	H3K27M	rep-4
4	Atu_17_mut_rep3	atuveciclib	SU-DIPG-17	H3K27M	rep-3
4	syn_17_mut_rep4	combo low	SU-DIPG-17	H3K27M	rep-4
4	BMS_17_mut_rep2	BMS-986158	SU-DIPG-17	H3K27M	rep-2
4	syn_17_mut_rep3	combo low	SU-DIPG-17	H3K27M	rep-3
4	BMS_17_mut_rep4	BMS-986158	SU-DIPG-17	H3K27M	rep-4
4	DMSO_17_mut_rep2	DMSO	SU-DIPG-17	H3K27M	rep-2
4	Atu_17_mut_rep2	atuveciclib	SU-DIPG-17	H3K27M	rep-2
4	Atu_17_mut_rep1	atuveciclib	SU-DIPG-17	H3K27M	rep-1
4	DMSO_17_mut_rep1	DMSO	SU-DIPG-17	H3K27M	rep-1
4	BMS_17_mut_rep3	BMS-986158	SU-DIPG-17	H3K27M	rep-3
4	syn_17_mut_rep1	combo low	SU-DIPG-17	H3K27M	rep-1

UMAP cluster	Sample Name	Treatment	Cell model	H3 status	Replicate
5	BMS_25_mut_rep3	BMS-986158	SU-DIPG-25	H3K27M	rep-3
5	DMSO_25_mut_rep3	DMSO	SU-DIPG-25	H3K27M	rep-3
5	syn_25_mut_rep2	combo low	SU-DIPG-25	H3K27M	rep-2
5	Atu_25_mut_rep2	atuveciclib	SU-DIPG-25	H3K27M	rep-2
5	DMSO_25_mut_rep4	DMSO	SU-DIPG-25	H3K27M	rep-4
5	Atu_25_mut_rep1	atuveciclib	SU-DIPG-25	H3K27M	rep-1
5	syn_25_mut_rep1	combo low	SU-DIPG-25	H3K27M	rep-1
5	Atu_25_mut_rep3	atuveciclib	SU-DIPG-25	H3K27M	rep-3
5	BMS_25_mut_rep1	BMS-986158	SU-DIPG-25	H3K27M	rep-1
5	syn_25_mut_rep3	combo low	SU-DIPG-25	H3K27M	rep-3
5	DMSO_25_mut_rep2	DMSO	SU-DIPG-25	H3K27M	rep-2
5	BMS_25_mut_rep2	BMS-986158	SU-DIPG-25	H3K27M	rep-2
5	Atu_25_mut_rep4	atuveciclib	SU-DIPG-25	H3K27M	rep-4
5	DMSO_25_mut_rep1	DMSO	SU-DIPG-25	H3K27M	rep-1

Appendix Figure 12. UMAP clusters of 128 samples, which were undergone proteomic analysis. Yellow marked samples showcase that they did not cluster with the other replicates of the same cell model and treatment.

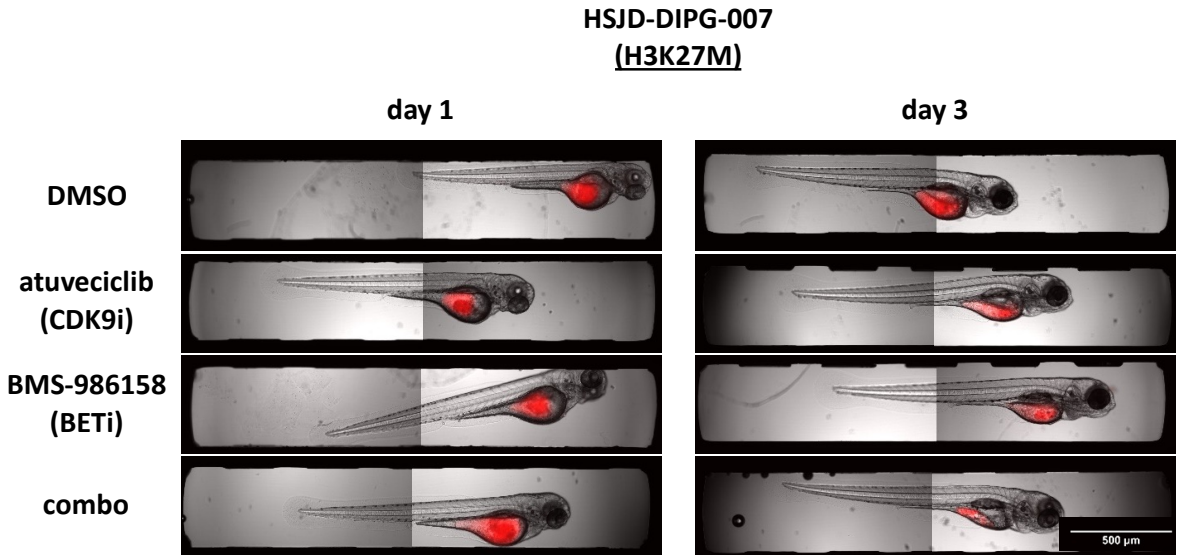

Appendix Figure 13. Representative images of a zebrafish early larvae engrafted with DiD stained HSJD-DIPG-007 (H3K27M) cells in the yolk sac. 7 µM atuveciclib (CDK9i) and 0.325 µM BMS-986158 (BETi) were applied as single agent and for the combination (combo) treatments for two days. The fish were imaged on day 1 (1 dpi, 3 dpf), before treatment, and on day 3 (3 dpi, 5 dpf), after treatment to assess the change in cell mass volume.

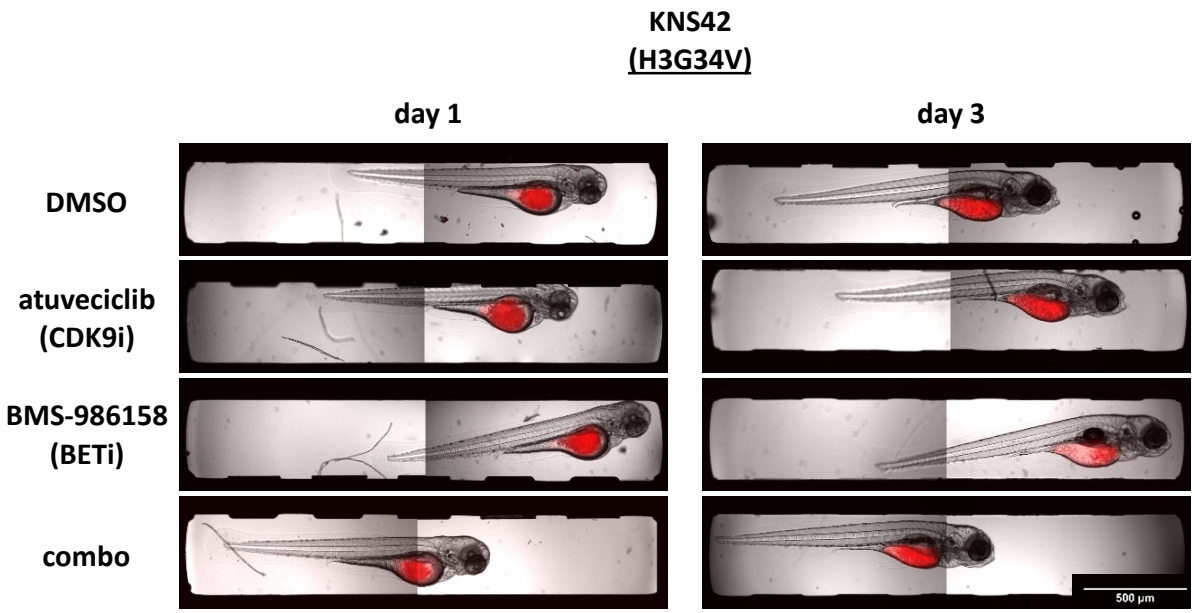

Appendix Figure 14. Representative images of a zebrafish early larvae engrafted with DiD stained KNS42 (H3G34V) cells in the yolk sac. 7 µM atuveciclib (CDK9i) and 0.325 µM BMS-986158 (BETi) were applied as single agent and for the combination (combo) treatments for two days. The fish were imaged on day 1 (1 dpi, 3 dpf), before treatment, and on day 3 (3 dpi, 5 dpf), after treatment to assess the change in cell mass volume.

References

1. Force, L. M. *et al.* The global burden of childhood and adolescent cancer in 2017: an analysis of the Global Burden of Disease Study 2017. *The Lancet Oncology* **20**, 1211–1225 (2019).
2. Kattner, P. *et al.* Compare and contrast: pediatric cancer versus adult malignancies. *Cancer Metastasis Rev* **38**, 673–682 (2019).
3. Liu, F., Xiong, Q.-W., Wang, J.-H. & Peng, W.-X. Roles of lncRNAs in childhood cancer: Current landscape and future perspectives. *Front. Oncol.* **13**, 1060107 (2023).
4. Davis, F. G., Bruner, J. M. & Surawicz, T. S. The Rationale for Standardized Registration and Reporting of Brain and Central Nervous System Tumors in Population-Based Cancer Registries. *Neuroepidemiology* **16**, 308–316 (1997).
5. Wrensch, M. Epidemiology of primary brain tumors: Current concepts and review of the literature. *Neuro-Oncology* **4**, 278–299 (2002).
6. Ward, E., DeSantis, C., Robbins, A., Kohler, B. & Jemal, A. Childhood and adolescent cancer statistics, 2014. *CA A Cancer J Clinicians* **64**, 83–103 (2014).
7. Steliarova-Foucher, E. *et al.* International incidence of childhood cancer, 2001–10: a population-based registry study. *The Lancet Oncology* **18**, 719–731 (2017).
8. Bauchet, L. *et al.* Clinical epidemiology for childhood primary central nervous system tumors. *J Neurooncol* **92**, 87–98 (2009).
9. Peris-Bonet, R. *et al.* Childhood central nervous system tumours – incidence and survival in Europe (1978–1997): Report from Automated Childhood Cancer Information System project. *European Journal of Cancer* **42**, 2064–2080 (2006).
10. Ostrom, Q. T. *et al.* Alex's Lemonade Stand Foundation Infant and Childhood Primary Brain and Central Nervous System Tumors Diagnosed in the United States in 2007–2011. *Neuro-Oncology* **16**, x1–x36 (2015).
11. Funakoshi, Y. *et al.* Pediatric Glioma: An Update of Diagnosis, Biology, and Treatment. *Cancers* **13**, 758 (2021).
12. Damodharan, S. & Puccetti, D. Pediatric Central Nervous System Tumor Overview and Emerging Treatment Considerations. *Brain Sciences* **13**, 1106 (2023).
13. Hauser, P. Classification and Treatment of Pediatric Gliomas in the Molecular Era. *Children* **8**, 739 (2021).
14. Ward, E., DeSantis, C., Robbins, A., Kohler, B. & Jemal, A. Childhood and adolescent cancer statistics, 2014. *CA A Cancer J Clinicians* **64**, 83–103 (2014).
15. Mackay, A. *et al.* Integrated Molecular Meta-Analysis of 1,000 Pediatric High-Grade and Diffuse Intrinsic Pontine Glioma. *Cancer Cell* **32**, 520-537.e5 (2017).
16. Da-Veiga, M.-A., Rogister, B., Lombard, A., Neirinckx, V. & Piette, C. Glioma Stem Cells in Pediatric High-Grade Gliomas: From Current Knowledge to Future Perspectives. *Cancers* **14**, 2296 (2022).

17. Aggarwal, P. *et al.* Pediatric versus adult high grade glioma: Immunotherapeutic and genomic considerations. *Front. Immunol.* **13**, 1038096 (2022).

18. Voon, H. P. J. & Wong, L. H. Chromatin mutations in pediatric high grade gliomas. *Front. Oncol.* **12**, 1104129 (2023).

19. Saratsis, A. M., Knowles, T., Petrovic, A. & Nazarian, J. H3K27M Mutant Glioma: Disease Definition and Biological Underpinnings. *Neuro-Oncology* noad164 (2023) doi:10.1093/neuonc/noad164.

20. Louis, D. N. *et al.* The 2021 WHO Classification of Tumors of the Central Nervous System: a summary. *Neuro-Oncology* **23**, 1231–1251 (2021).

21. Guidi, M. *et al.* Genetic signature and treatment of pediatric high-grade glioma. *Mol Clin Oncol* **14**, 70 (2021).

22. Filbin, M. G. *et al.* Developmental and oncogenic programs in H3K27M gliomas dissected by single-cell RNA-seq. *Science* **360**, 331–335 (2018).

23. Aziz-Bose, R. & Monje, M. Diffuse intrinsic pontine glioma: molecular landscape and emerging therapeutic targets. *Current Opinion in Oncology* **31**, 522–530 (2019).

24. Liu, I. *et al.* The landscape of tumor cell states and spatial organization in H3-K27M mutant diffuse midline glioma across age and location. *Nat Genet* **54**, 1881–1894 (2022).

25. Mariño-Ramírez, L., Kann, M. G., Shoemaker, B. A. & Landsman, D. Histone structure and nucleosome stability. *Expert Review of Proteomics* **2**, 719–729 (2005).

26. Van Holde, K. E. *Chromatin: Springer Series in Molecular Biology*. (Springer-Verlag, New York, 1988).

27. Van Holde, K. & Zlatanova, J. Chromatin Higher Order Structure: Chasing a Mirage? *Journal of Biological Chemistry* **270**, 8373–8376 (1995).

28. Luger, K., Mäder, A. W., Richmond, R. K., Sargent, D. F. & Richmond, T. J. Crystal structure of the nucleosome core particle at 2.8 Å resolution. *Nature* **389**, 251–260 (1997).

29. Ederveen, T. H. A., Mandemaker, I. K. & Logie, C. The human histone H3 complement anno 2011. *Biochimica et Biophysica Acta (BBA) - Gene Regulatory Mechanisms* **1809**, 577–586 (2011).

30. Wu, R. S., Tsai, S. & Bonner, W. M. Patterns of histone variant synthesis can distinguish G0 from G1 cells. *Cell* **31**, 367–374 (1982).

31. Ahmad, K. & Henikoff, S. The Histone Variant H3.3 Marks Active Chromatin by Replication-Independent Nucleosome Assembly. *Molecular Cell* **9**, 1191–1200 (2002).

32. Lewis, P. W., Elsaesser, S. J., Noh, K.-M., Stadler, S. C. & Allis, C. D. Daxx is an H3.3-specific histone chaperone and cooperates with ATRX in replication-independent chromatin assembly at telomeres. *Proc. Natl. Acad. Sci. U.S.A.* **107**, 14075–14080 (2010).

33. Goldberg, A. D. *et al.* Distinct Factors Control Histone Variant H3.3 Localization at Specific Genomic Regions. *Cell* **140**, 678–691 (2010).

34. Wong, L. H. *et al.* ATRX interacts with H3.3 in maintaining telomere structural integrity in pluripotent embryonic stem cells. *Genome Res.* **20**, 351–360 (2010).

35. Elsässer, S. J., Noh, K.-M., Diaz, N., Allis, C. D. & Banaszynski, L. A. Histone H3.3 is required for endogenous retroviral element silencing in embryonic stem cells. *Nature* **522**, 240–244 (2015).

36. Johnson, K. *et al.* B cell–specific loss of histone 3 lysine 9 methylation in the VH locus depends on Pax5. *Nat Immunol* **5**, 853–861 (2004).

37. Filipescu, D., Szenker, E. & Almouzni, G. Developmental roles of histone H3 variants and their chaperones. *Trends in Genetics* **29**, 630–640 (2013).

38. Schwartzentruber, J. *et al.* Driver mutations in histone H3.3 and chromatin remodelling genes in paediatric glioblastoma. *Nature* **482**, 226–231 (2012).

39. Sturm, D. *et al.* Hotspot Mutations in H3F3A and IDH1 Define Distinct Epigenetic and Biological Subgroups of Glioblastoma. *Cancer Cell* **22**, 425–437 (2012).

40. Saratsis, A. M., Knowles, T., Petrovic, A. & Nazarian, J. H3K27M Mutant Glioma: Disease Definition and Biological Underpinnings. *Neuro-Oncology* noad164 (2023) doi:10.1093/neuonc/noad164.

41. St. Jude Children's Research Hospital–Washington University Pediatric Cancer Genome Project. Somatic histone H3 alterations in pediatric diffuse intrinsic pontine gliomas and non-brainstem glioblastomas. *Nat Genet* **44**, 251–253 (2012).

42. Bender, S. *et al.* Reduced H3K27me3 and DNA Hypomethylation Are Major Drivers of Gene Expression in K27M Mutant Pediatric High-Grade Gliomas. *Cancer Cell* **24**, 660–672 (2013).

43. Lewis, P. W. *et al.* Inhibition of PRC2 Activity by a Gain-of-Function H3 Mutation Found in Pediatric Glioblastoma. *Science* **340**, 857–861 (2013).

44. Margueron, R. & Reinberg, D. The Polycomb complex PRC2 and its mark in life. *Nature* **469**, 343–349 (2011).

45. Justin, N. *et al.* Structural basis of oncogenic histone H3K27M inhibition of human polycomb repressive complex 2. *Nat Commun* **7**, 11316 (2016).

46. Chan, K.-M. *et al.* The histone H3.3K27M mutation in pediatric glioma reprograms H3K27 methylation and gene expression. *Genes Dev.* **27**, 985–990 (2013).

47. Piunti, A. *et al.* Therapeutic targeting of polycomb and BET bromodomain proteins in diffuse intrinsic pontine gliomas. *Nat Med* **23**, 493–500 (2017).

48. Mohammad, F. *et al.* EZH2 is a potential therapeutic target for H3K27M-mutant pediatric gliomas. *Nat Med* **23**, 483–492 (2017).

49. Harutyunyan, A. S. *et al.* H3K27M induces defective chromatin spread of PRC2-mediated repressive H3K27me2/me3 and is essential for glioma tumorigenesis. *Nat Commun* **10**, 1262 (2019).

50. Jain, S. U. *et al.* H3 K27M and EZHIP Impede H3K27-Methylation Spreading by Inhibiting Allosterically Stimulated PRC2. *Molecular Cell* **80**, 726-735.e7 (2020).

51. Krug, B. *et al.* Pervasive H3K27 Acetylation Leads to ERV Expression and a Therapeutic Vulnerability in H3K27M Gliomas. *Cancer Cell* **35**, 782-797.e8 (2019).

52. Herz, H.-M. *et al.* Histone H3 lysine-to-methionine mutants as a paradigm to study chromatin signaling. *Science* **345**, 1065–1070 (2014).

53. Brien, G. L. *et al.* Simultaneous disruption of PRC2 and enhancer function underlies histone H3.3-K27M oncogenic activity in human hindbrain neural stem cells. *Nat Genet* **53**, 1221–1232 (2021).

54. Anshabo, A. T., Milne, R., Wang, S. & Albrecht, H. CDK9: A Comprehensive Review of Its Biology, and Its Role as a Potential Target for Anti-Cancer Agents. *Front. Oncol.* **11**, 678559 (2021).

55. Castel, D. *et al.* Histone H3F3A and HIST1H3B K27M mutations define two subgroups of diffuse intrinsic pontine gliomas with different prognosis and phenotypes. *Acta Neuropathol* **130**, 815–827 (2015).

56. Hoffman, L. M. *et al.* Clinical, Radiologic, Pathologic, and Molecular Characteristics of Long-Term Survivors of Diffuse Intrinsic Pontine Glioma (DIPG): A Collaborative Report From the International and European Society for Pediatric Oncology DIPG Registries. *JCO* **36**, 1963–1972 (2018).

57. Vuong, H. G., Ngo, T. N. M., Le, H. T. & Dunn, I. F. The prognostic significance of HIST1H3B/C and H3F3A K27M mutations in diffuse midline gliomas is influenced by patient age. *J Neurooncol* **158**, 405–412 (2022).

58. Damodharan, S., Lara-Velazquez, M., Williamsen, B. C., Helgager, J. & Dey, M. Diffuse Intrinsic Pontine Glioma: Molecular Landscape, Evolving Treatment Strategies and Emerging Clinical Trials. *JPM* **12**, 840 (2022).

59. Lehnertz, B. *et al.* H3 K27M/I mutations promote context-dependent transformation in acute myeloid leukemia with RUNX1 alterations. *Blood* **130**, 2204–2214 (2017).

60. Sarthy, J. F. *et al.* Histone deposition pathways determine the chromatin landscapes of H3.1 and H3.3 K27M oncohistones. *eLife* **9**, e61090 (2020).

61. Nacev, B. A. *et al.* The expanding landscape of 'oncohistone' mutations in human cancers. *Nature* **567**, 473–478 (2019).

62. Aziz-Bose, R. & Monje, M. Diffuse intrinsic pontine glioma: molecular landscape and emerging therapeutic targets. *Current Opinion in Oncology* **31**, 522–530 (2019).

63. Hoeman, C. M. *et al.* ACVR1 R206H cooperates with H3.1K27M in promoting diffuse intrinsic pontine glioma pathogenesis. *Nat Commun* **10**, 1023 (2019).

64. Leszczynska, K. B., Jayaprakash, C., Kaminska, B. & Mieczkowski, J. Emerging Advances in Combinatorial Treatments of Epigenetically Altered Pediatric High-Grade H3K27M Gliomas. *Front. Genet.* **12**, 742561 (2021).

65. Taylor, K. R. *et al.* Recurrent activating ACVR1 mutations in diffuse intrinsic pontine glioma. *Nat Genet* **46**, 457–461 (2014).

66. Nagaraja, S. *et al.* Histone Variant and Cell Context Determine H3K27M Reprogramming of the Enhancer Landscape and Oncogenic State. *Molecular Cell* **76**, 965-980.e12 (2019).

67. Castel, D. *et al.* Transcriptomic and epigenetic profiling of 'diffuse midline gliomas, H3 K27M-mutant' discriminate two subgroups based on the type of histone H3 mutated and not supratentorial or infratentorial location. *acta neuropathol commun* **6**, 117 (2018).

68. Lowe, B. R., Maxham, L. A., Hamey, J. J., Wilkins, M. R. & Partridge, J. F. Histone H3 Mutations: An Updated View of Their Role in Chromatin Deregulation and Cancer. *Cancers* **11**, 660 (2019).

69. Voon, H. P. J. & Wong, L. H. Chromatin mutations in pediatric high grade gliomas. *Front. Oncol.* **12**, 1104129 (2023).

70. Crowell, C. *et al.* Systematic review of diffuse hemispheric glioma, H3 G34-mutant: Outcomes and associated clinical factors. *Neuro-Oncology Advances* **4**, vdac133 (2022).

71. Packer, R. J., Nicholson, H. S., Vezina, L. G. & Johnson, D. L. Brainstem gliomas. *Neurosurg Clin N Am* **3**, 863–879 (1992).

72. Vitanza, N. A. & Monje, M. Diffuse Intrinsic Pontine Glioma: From Diagnosis to Next-Generation Clinical Trials. *Curr Treat Options Neurol* **21**, 37 (2019).

73. Guerra-García, P. *et al.* Challenging the indiscriminate use of temozolomide in pediatric high-grade gliomas: A review of past, current, and emerging therapies. *Pediatric Blood & Cancer* **67**, e28011 (2020).

74. Abe, H. *et al.* MGMT Expression Contributes to Temozolomide Resistance in H3K27M-Mutant Diffuse Midline Gliomas and MGMT Silencing to Temozolomide Sensitivity in IDH-Mutant Gliomas. *Neurol. Med. Chir.(Tokyo)* **58**, 290–295 (2018).

75. Wierzbicki, K. *et al.* Targeting and Therapeutic Monitoring of H3K27M-Mutant Glioma. *Curr Oncol Rep* **22**, 19 (2020).

76. Oberoi, R. K. *et al.* Strategies to improve delivery of anticancer drugs across the blood–brain barrier to treat glioblastoma. *Neuro Oncol* **18**, 27–36 (2016).

77. Ballabh, P., Braun, A. & Nedergaard, M. The blood–brain barrier: an overview. *Neurobiology of Disease* **16**, 1–13 (2004).

78. Yang, Z., Sun, L., Chen, H., Sun, C. & Xia, L. New progress in the treatment of diffuse midline glioma with H3K27M alteration. *Heliyon* **10**, e24877 (2024).

79. Kline, C. *et al.* Upfront Biology-Guided Therapy in Diffuse Intrinsic Pontine Glioma: Therapeutic, Molecular, and Biomarker Outcomes from PNOC003. *Clinical Cancer Research* **28**, 3965–3978 (2022).

80. Damodharan, S., Lara-Velazquez, M., Williamsen, B. C., Helgager, J. & Dey, M. Diffuse Intrinsic Pontine Glioma: Molecular Landscape, Evolving Treatment Strategies and Emerging Clinical Trials. *JPM* **12**, 840 (2022).

81. Malumbres, M. Cyclin-dependent kinases. *Genome Biol* **15**, 122 (2014).

82. Malumbres, M. & Barbacid, M. Cell cycle, CDKs and cancer: a changing paradigm. *Nat Rev Cancer* **9**, 153–166 (2009).

83. Anshabo, A. T., Milne, R., Wang, S. & Albrecht, H. CDK9: A Comprehensive Review of Its Biology, and Its Role as a Potential Target for Anti-Cancer Agents. *Front. Oncol.* **11**, 678559 (2021).

84. Liu, H. & Herrmann, C. H. Differential localization and expression of the Cdk9 42k and 55k isoforms. *J Cell Physiol* **203**, 251–260 (2005).

85. Chao, S. H. & Price, D. H. Flavopiridol inactivates P-TEFb and blocks most RNA polymerase II transcription in vivo. *J Biol Chem* **276**, 31793–31799 (2001).

86. Jonkers, I., Kwak, H. & Lis, J. T. Genome-wide dynamics of Pol II elongation and its interplay with promoter proximal pausing, chromatin, and exons. *Elife* **3**, e02407 (2014).

87. Hochegger, H., Takeda, S. & Hunt, T. Cyclin-dependent kinases and cell-cycle transitions: does one fit all? *Nat Rev Mol Cell Biol* **9**, 910–916 (2008).

88. Wei, P., Garber, M. E., Fang, S. M., Fischer, W. H. & Jones, K. A. A novel CDK9-associated C-type cyclin interacts directly with HIV-1 Tat and mediates its high-affinity, loop-specific binding to TAR RNA. *Cell* **92**, 451–462 (1998).

89. Peng, J., Marshall, N. F. & Price, D. H. Identification of a cyclin subunit required for the function of Drosophila P-TEFb. *J Biol Chem* **273**, 13855–13860 (1998).

90. Lu, H. *et al.* Phase-separation mechanism for C-terminal hyperphosphorylation of RNA polymerase II. *Nature* **558**, 318–323 (2018).

91. Taube, R., Lin, X., Irwin, D., Fujinaga, K. & Peterlin, B. M. Interaction between P-TEFb and the C-terminal domain of RNA polymerase II activates transcriptional elongation from sites upstream or downstream of target genes. *Mol Cell Biol* **22**, 321–331 (2002).

92. Bacon, C. W. & D'Orso, I. CDK9: a signaling hub for transcriptional control. *Transcription* **10**, 57–75 (2019).

93. Brogie, J. E. & Price, D. H. Reconstitution of a functional 7SK snRNP. *Nucleic Acids Res* **45**, 6864–6880 (2017).

94. Barboric, M. *et al.* 7SK snRNP/P-TEFb couples transcription elongation with alternative splicing and is essential for vertebrate development. *Proc Natl Acad Sci U S A* **106**, 7798–7803 (2009).

95. Li, Q. *et al.* Analysis of the large inactive P-TEFb complex indicates that it contains one 7SK molecule, a dimer of HEXIM1 or HEXIM2, and two P-TEFb molecules containing Cdk9 phosphorylated at threonine 186. *J Biol Chem* **280**, 28819–28826 (2005).

96. Schulte, A. *et al.* Identification of a cyclin T-binding domain in Hexim1 and biochemical analysis of its binding competition with HIV-1 Tat. *J Biol Chem* **280**, 24968–24977 (2005).

97. Krueger, B. J. *et al.* LARP7 is a stable component of the 7SK snRNP while P-TEFb, HEXIM1 and hnRNP A1 are reversibly associated. *Nucleic Acids Res* **36**, 2219–2229 (2008).

98. Fujinaga, K. *et al.* PKC phosphorylates HEXIM1 and regulates P-TEFb activity. *Nucleic Acids Research* **40**, 9160–9170 (2012).

99. Saunders, A., Core, L. J. & Lis, J. T. Breaking barriers to transcription elongation. *Nat Rev Mol Cell Biol* **7**, 557–567 (2006).

100. Sims, R. J., Belotserkovskaya, R. & Reinberg, D. Elongation by RNA polymerase II: the short and long of it. *Genes Dev.* **18**, 2437–2468 (2004).

101. Zhou, Q., Li, T. & Price, D. H. RNA Polymerase II Elongation Control. *Annu. Rev. Biochem.* **81**, 119–143 (2012).

102. Marshall, N. F. & Price, D. H. Control of formation of two distinct classes of RNA polymerase II elongation complexes. *Mol. Cell. Biol.* **12**, 2078–2090 (1992).

103. Rahl, P. B. *et al.* c-Myc Regulates Transcriptional Pause Release. *Cell* **141**, 432–445 (2010).

104. Cicenas, J. & Valius, M. The CDK inhibitors in cancer research and therapy. *J Cancer Res Clin Oncol* **137**, 1409–1418 (2011).

105. Endicott, J. A., Noble, M. E. M. & Johnson, L. N. The Structural Basis for Control of Eukaryotic Protein Kinases. *Annu. Rev. Biochem.* **81**, 587–613 (2012).

106. Manning, G., Whyte, D. B., Martinez, R., Hunter, T. & Sudarsanam, S. The Protein Kinase Complement of the Human Genome. *Science* **298**, 1912–1934 (2002).

107. Malumbres, M. Cyclin-dependent kinases. *Genome Biol* **15**, 122 (2014).

108. Adelman, K. & Lis, J. T. Promoter-proximal pausing of RNA polymerase II: emerging roles in metazoans. *Nat Rev Genet* **13**, 720–731 (2012).

109. Yamaguchi, Y. *et al.* NELF, a Multisubunit Complex Containing RD, Cooperates with DSIF to Repress RNA Polymerase II Elongation. *Cell* **97**, 41–51 (1999).

110. Wada, T. Evidence that P-TEFb alleviates the negative effect of DSIF on RNA polymerase II-dependent transcription invitro. *The EMBO Journal* **17**, 7395–7403 (1998).

111. Zhu, Y. *et al.* Transcription elongation factor P-TEFb is required for HIV-1 Tat transactivation in vitro. *Genes Dev.* **11**, 2622–2632 (1997).

112. Fujinaga, K. *et al.* Dynamics of Human Immunodeficiency Virus Transcription: P-TEFb Phosphorylates RD and Dissociates Negative Effectors from the Transactivation Response Element. *Molecular and Cellular Biology* **24**, 787–795 (2004).

113. Shim, E. Y., Walker, A. K., Shi, Y. & Blackwell, T. K. CDK-9/cyclin T (P-TEFb) is required in two postinitiation pathways for transcription in the *C. elegans* embryo. *Genes Dev.* **16**, 2135–2146 (2002).

114. McCracken, S. *et al.* The C-terminal domain of RNA polymerase II couples mRNA processing to transcription. *Nature* **385**, 357–361 (1997).

115. Anshabo, A. T., Milne, R., Wang, S. & Albrecht, H. CDK9: A Comprehensive Review of Its Biology, and Its Role as a Potential Target for Anti-Cancer Agents. *Front. Oncol.* **11**, 678559 (2021).

116. Gu, B., Eick, D. & Bensaude, O. CTD serine-2 plays a critical role in splicing and termination factor recruitment to RNA polymerase II in vivo. *Nucleic Acids Research* **41**, 1591–1603 (2013).

117. Liang, K. *et al.* Characterization of Human Cyclin-Dependent Kinase 12 (CDK12) and CDK13 Complexes in C-Terminal Domain Phosphorylation, Gene Transcription, and RNA Processing. *Molecular and Cellular Biology* **35**, 928–938 (2015).

118. Devaiah, B. N. *et al.* BRD4 is an atypical kinase that phosphorylates Serine2 of the RNA Polymerase II carboxy-terminal domain. *Proc. Natl. Acad. Sci. U.S.A.* **109**, 6927–6932 (2012).

119. Laitem, C. *et al.* CDK9 inhibitors define elongation checkpoints at both ends of RNA polymerase II–transcribed genes. *Nat Struct Mol Biol* **22**, 396–403 (2015).

120. Sansó, M. *et al.* P-TEFb regulation of transcription termination factor Xrn2 revealed by a chemical genetic screen for Cdk9 substrates. *Genes Dev.* **30**, 117–131 (2016).

121. Parua, P. K. *et al.* A Cdk9–PP1 switch regulates the elongation–termination transition of RNA polymerase II. *Nature* **558**, 460–464 (2018).

122. Graña, X. *et al.* PITALRE, a nuclear CDC2-related protein kinase that phosphorylates the retinoblastoma protein in vitro. *Proc. Natl. Acad. Sci. U.S.A.* **91**, 3834–3838 (1994).

123. Bettencourt-Dias, M. *et al.* Genome-wide survey of protein kinases required for cell cycle progression. *Nature* **432**, 980–987 (2004).

124. Mochizuki, K. *et al.* The Bromodomain Protein Brd4 Stimulates G1 Gene Transcription and Promotes Progression to S Phase. *Journal of Biological Chemistry* **283**, 9040–9048 (2008).

125. Yang, Z., He, N. & Zhou, Q. Brd4 Recruits P-TEFb to Chromosomes at Late Mitosis To Promote G_1 Gene Expression and Cell Cycle Progression. *Molecular and Cellular Biology* **28**, 967–976 (2008).

126. Fu, T.-J., Peng, J., Lee, G., Price, D. H. & Flores, O. Cyclin K Functions as a CDK9 Regulatory Subunit and Participates in RNA Polymerase II Transcription. *Journal of Biological Chemistry* **274**, 34527–34530 (1999).

127. Lin, X., Taube, R., Fujinaga, K. & Peterlin, B. M. P-TEFb Containing Cyclin K and Cdk9 Can Activate Transcription via RNA. *Journal of Biological Chemistry* **277**, 16873–16878 (2002).

128. Mori, T. *et al.* Cyclin K as a Direct Transcriptional Target of the p53 Tumor Suppressor. *Neoplasia* **4**, 268–274 (2002).

129. Yu, D. S. *et al.* Cyclin-dependent kinase 9–cyclin K functions in the replication stress response. *EMBO Reports* **11**, 876–882 (2010).

130. Liu, H. *et al.* 55K isoform of CDK9 associates with Ku70 and is involved in DNA repair. *Biochemical and Biophysical Research Communications* **397**, 245–250 (2010).

131. Sonawane, Y. A. *et al.* Cyclin Dependent Kinase 9 Inhibitors for Cancer Therapy: Miniperspective. *J. Med. Chem.* **59**, 8667–8684 (2016).

132. Asghar, U., Witkiewicz, A. K., Turner, N. C. & Knudsen, E. S. The history and future of targeting cyclin-dependent kinases in cancer therapy. *Nat Rev Drug Discov* **14**, 130–146 (2015).

133. Brisard, D. *et al.* Antineoplastic effects of selective CDK9 inhibition with atuveciclib on cancer stem-like cells in triple-negative breast cancer. *Oncotarget* **9**, 37305–37318 (2018).

134. Dahl, N. A. *et al.* Super Elongation Complex as a Targetable Dependency in Diffuse Midline Glioma. *Cell Reports* **31**, 107485 (2020).

135. Lücking, U. *et al.* Identification of Atuveciclib (BAY 1143572), the First Highly Selective, Clinical PTEFb/CDK9 Inhibitor for the Treatment of Cancer. *ChemMedChem* **12**, 1776–1793 (2017).

136. Ranjan, A. *et al.* Targeting CDK9 for the Treatment of Glioblastoma. *Cancers* **13**, 3039 (2021).

137. Donati, B., Lorenzini, E. & Ciarrocchi, A. BRD4 and Cancer: going beyond transcriptional regulation. *Mol Cancer* **17**, 164 (2018).

138. Wu, S.-Y. & Chiang, C.-M. The Double Bromodomain-containing Chromatin Adaptor Brd4 and Transcriptional Regulation. *Journal of Biological Chemistry* **282**, 13141–13145 (2007).

139. Wu, S.-Y. *et al.* Opposing Functions of BRD4 Isoforms in Breast Cancer. *Molecular Cell* **78**, 1114-1132.e10 (2020).

140. Chiang, C.-M. Phospho-BRD4: transcription plasticity and drug targeting. *Drug Discovery Today: Technologies* **19**, 17–22 (2016).

141. Dhalluin, C. *et al.* Structure and ligand of a histone acetyltransferase bromodomain. *Nature* **399**, 491–496 (1999).

142. Rahman, S. *et al.* The Brd4 Extraterminal Domain Confers Transcription Activation Independent of pTEFb by Recruiting Multiple Proteins, Including NSD3. *Molecular and Cellular Biology* **31**, 2641–2652 (2011).

143. Wang, N., Wu, R., Tang, D. & Kang, R. The BET family in immunity and disease. *Sig Transduct Target Ther* **6**, 23 (2021).

144. Cheung, K. L., Kim, C. & Zhou, M.-M. The Functions of BET Proteins in Gene Transcription of Biology and Diseases. *Front. Mol. Biosci.* **8**, 728777 (2021).

145. Jang, M. K. *et al.* The Bromodomain Protein Brd4 Is a Positive Regulatory Component of P-TEFb and Stimulates RNA Polymerase II-Dependent Transcription. *Molecular Cell* **19**, 523–534 (2005).

146. Schröder, S. *et al.* Two-pronged Binding with Bromodomain-containing Protein 4 Liberates Positive Transcription Elongation Factor b from Inactive Ribonucleoprotein Complexes. *Journal of Biological Chemistry* **287**, 1090–1099 (2012).

147. Zheng, B. *et al.* Acute perturbation strategies in interrogating RNA polymerase II elongation factor function in gene expression. *Genes Dev.* **35**, 273–285 (2021).

148. Hsu, S. C. *et al.* The BET Protein BRD2 Cooperates with CTCF to Enforce Transcriptional and Architectural Boundaries. *Molecular Cell* **66**, 102-116.e7 (2017).

149. Cheung, K. L. *et al.* Distinct Roles of Brd2 and Brd4 in Potentiating the Transcriptional Program for Th17 Cell Differentiation. *Molecular Cell* **65**, 1068-1080.e5 (2017).

150. Wu, T., Kamikawa, Y. F. & Donohoe, M. E. Brd4's Bromodomains Mediate Histone H3 Acetylation and Chromatin Remodeling in Pluripotent Cells through P300 and Brg1. *Cell Reports* **25**, 1756–1771 (2018).

151. Qian, H. *et al.* Super-enhancers and the super-enhancer reader BRD4: tumorigenic factors and therapeutic targets. *Cell Death Discov.* **9**, 470 (2023).

152. Filippakopoulos, P. *et al.* Selective inhibition of BET bromodomains. *Nature* **468**, 1067–1073 (2010).

153. Lovén, J. *et al.* Selective Inhibition of Tumor Oncogenes by Disruption of Super-Enhancers. *Cell* **153**, 320–334 (2013).

154. Sansam, C. G. *et al.* A mechanism for epigenetic control of DNA replication. *Genes Dev.* **32**, 224–229 (2018).

155. Zhang, J. *et al.* BRD4 facilitates replication stress-induced DNA damage response. *Oncogene* **37**, 3763–3777 (2018).

156. Edwards, D. S. *et al.* BRD4 Prevents R-Loop Formation and Transcription-Replication Conflicts by Ensuring Efficient Transcription Elongation. *Cell Reports* **32**, 108166 (2020).

157. Bowry, A., Piberger, A. L., Rojas, P., Saponaro, M. & Petermann, E. BET Inhibition Induces HEXIM1- and RAD51-Dependent Conflicts between Transcription and Replication. *Cell Reports* **25**, 2061-2069.e4 (2018).

158. Kim, J. J. *et al.* Systematic bromodomain protein screens identify homologous recombination and R-loop suppression pathways involved in genome integrity. *Genes Dev.* **33**, 1751–1774 (2019).

159. Lam, F. C. *et al.* BRD4 prevents the accumulation of R-loops and protects against transcription–replication collision events and DNA damage. *Nat Commun* **11**, 4083 (2020).

160. To, K. K. W., Xing, E., Larue, R. C. & Li, P.-K. BET Bromodomain Inhibitors: Novel Design Strategies and Therapeutic Applications. *Molecules* **28**, 3043 (2023).

161. Hay, M., Thomas, D. W., Craighead, J. L., Economides, C. & Rosenthal, J. Clinical development success rates for investigational drugs. *Nat Biotechnol* **32**, 40–51 (2014).

162. Imamura, Y. *et al.* Comparison of 2D- and 3D-culture models as drug-testing platforms in breast cancer. *Oncology Reports* **33**, 1837–1843 (2015).

163. Kitaeva, K. V., Rutland, C. S., Rizvanov, A. A. & Solovyeva, V. V. Cell Culture Based in vitro Test Systems for Anticancer Drug Screening. *Front. Bioeng. Biotechnol.* **8**, 322 (2020).

164. Morash, M., Mitchell, H., Beltran, H., Elemento, O. & Pathak, J. The Role of Next-Generation Sequencing in Precision Medicine: A Review of Outcomes in Oncology. *JPM* **8**, 30 (2018).

165. Wong, M. *et al.* Whole genome, transcriptome and methylome profiling enhances actionable target discovery in high-risk pediatric cancer. *Nat Med* **26**, 1742–1753 (2020).

166. Abbott, L. S., Grover, S., Henning, J.-W., Oberoi, S. & Malkin, D. Access for adolescents and young adults with hard-to-cure cancer to PROFYLE: The pan-Canadian precision oncology pipeline. *JCO* **42**, 10012–10012 (2024).

167. Langenberg, K. P. S. *et al.* Implementation of paediatric precision oncology into clinical practice: The Individualized Therapies for Children with cancer program 'iTHER'. *European Journal of Cancer* **175**, 311–325 (2022).

168. Acanda De La Rocha, A. M. *et al.* Feasibility of functional precision medicine for guiding treatment of relapsed or refractory pediatric cancers. *Nat Med* **30**, 990–1000 (2024).

169. Peterziel, H. *et al.* Drug sensitivity profiling of 3D tumor tissue cultures in the pediatric precision oncology program INFORM. *npj Precis. Onc.* **6**, 94 (2022).

170. Wang, Z. *et al.* Towards functional precision oncology with human organoids. *The Lancet* **402**, 1526–1527 (2023).

171. Van Renterghem, A. W. J., Van De Haar, J. & Voest, E. E. Functional precision oncology using patient-derived assays: bridging genotype and phenotype. *Nat Rev Clin Oncol* **20**, 305–317 (2023).

172. Letai, A. Functional precision cancer medicine—moving beyond pure genomics. *Nat Med* **23**, 1028–1035 (2017).

173. Mohammad, F. *et al.* EZH2 is a potential therapeutic target for H3K27M-mutant pediatric gliomas. *Nat Med* **23**, 483–492 (2017).

174. Nagaraja, S. *et al.* Transcriptional Dependencies in Diffuse Intrinsic Pontine Glioma. *Cancer Cell* **31**, 635-652.e6 (2017).

175. Mount, C. W. *et al.* Potent antitumor efficacy of anti-GD2 CAR T cells in H3-K27M+ diffuse midline gliomas. *Nat Med* **24**, 572–579 (2018).

176. Qin, E. Y. *et al.* Neural Precursor-Derived Pleiotrophin Mediates Subventricular Zone Invasion by Glioma. *Cell* **170**, 845-859.e19 (2017).

177. Grasso, C. S. *et al.* Functionally defined therapeutic targets in diffuse intrinsic pontine glioma. *Nat Med* **21**, 555–559 (2015).

178. He, C. *et al.* Patient-Derived Orthotopic Xenografts and Cell Lines from Pediatric High-Grade Glioma Recapitulate the Heterogeneity of Histopathology, Molecular Signatures, and Drug Response. Preprint at https://doi.org/10.1101/2020.12.06.407973 (2020).

179. Takeshita, I. *et al.* Characteristics of an established human glioma cell line, KNS-42. *Neurol Med Chir (Tokyo)* **27**, 581–587 (1987).

180. Houghton, P. J. *et al.* Efficacy of topoisomerase I inhibitors, topotecan and irinotecan, administered at low dose levels in protracted schedules to mice bearing xenografts of human tumors. *Cancer Chemother Pharmacol* **36**, 393–403 (1995).

181. Grasso, C. S. *et al.* Functionally defined therapeutic targets in diffuse intrinsic pontine glioma. *Nat Med* **21**, 555–559 (2015).

182. Rettig, I. *et al.* Selective inhibition of HDAC8 decreases neuroblastoma growth in vitro and in vivo and enhances retinoic acid-mediated differentiation. *Cell Death Dis* **6**, e1657–e1657 (2015).

183. Janabi, N., Peudenier, S., Héron, B., Ng, K. H. & Tardieu, M. Establishment of human microglial cell lines after transfection of primary cultures of embryonic microglial cells with the SV40 large T antigen. *Neurosci Lett* **195**, 105–108 (1995).

184. Jamaladdin, N. *et al.* Key Pharmacokinetic Parameters of 74 Pediatric Anticancer Drugs Providing Assistance in Preclinical Studies. *Clin Pharma and Therapeutics* **114**, 904–913 (2023).

185. ElHarouni, D. *et al.* iTReX: Interactive exploration of mono- and combination therapy dose response profiling data. *Pharmacological Research* 105996 (2021) doi:10.1016/j.phrs.2021.105996.

186. Lederer, S., Dijkstra, T. M. H. & Heskes, T. Additive Dose Response Models: Explicit Formulation and the Loewe Additivity Consistency Condition. *Front. Pharmacol.* **9**, 31 (2018).

187. Zheng, S. *et al.* SynergyFinder Plus: Toward Better Interpretation and Annotation of Drug Combination Screening Datasets. *Genomics, Proteomics & Bioinformatics* **20**, 587–596 (2022).

188. Reisinger, E. *et al.* OTP: An automatized system for managing and processing NGS data. *Journal of Biotechnology* **261**, 53–62 (2017).

189. Koster, J. R2: Genomics Analysis and Visualization Platform. http://r2.amc.nl.

190. Müller, T. *et al.* Automated sample preparation with SP 3 for low-input clinical proteomics. *Molecular Systems Biology* **16**, e9111 (2020).

191. Veldwijk, M. R. *et al.* Overexpression of Manganese Superoxide Dismutase Does Not Increase Clonogenic Cell Survival Despite Effect on Apoptosis in Irradiated Lymphoblastoid Cells. *Radiation Research* **176**, 725–731 (2011).

192. Furth, E. E., Thilly, W. G., Penman, B. W., Liber, H. L. & Rand, W. M. Quantitative assay for mutation in diploid human lymphoblasts using microtiter plates. *Analytical Biochemistry* **110**, 1–8 (1981).

193. Pons, M. *et al.* Oncogenic Kinase Cascades Induce Molecular Mechanisms That Protect Leukemic Cell Models from Lethal Effects of De Novo dNTP Synthesis Inhibition. *Cancers* **13**, 3464 (2021).

194. Fior, R. *et al.* Single-cell functional and chemosensitive profiling of combinatorial colorectal therapy in zebrafish xenografts. *Proc. Natl. Acad. Sci. U.S.A.* **114**, (2017).

195. Wertman, J., Veinotte, C. J., Dellaire, G. & Berman, J. N. The Zebrafish Xenograft Platform: Evolution of a Novel Cancer Model and Preclinical Screening Tool. in *Cancer and Zebrafish* (ed. Langenau, D. M.) vol. 916 289–314 (Springer International Publishing, Cham, 2016).

196. Wrobel, J. K. *et al.* Rapid In Vivo Validation of HDAC Inhibitor-Based Treatments in Neuroblastoma Zebrafish Xenografts. *Pharmaceuticals* **13**, 345 (2020).

197. Eisenhauer, E. A. *et al.* New response evaluation criteria in solid tumours: Revised RECIST guideline (version 1.1). *European Journal of Cancer* **45**, 228–247 (2009).

198. Ge, S. X., Jung, D. & Yao, R. ShinyGO: a graphical gene-set enrichment tool for animals and plants. *Bioinformatics* **36**, 2628–2629 (2020).

199. Chae, H.-J. *et al.* Molecular mechanism of staurosporine-induced apoptosis in osteoblasts. *Pharmacological Research* **42**, 373–381 (2000).

200. Palmer, A. C. & Sorger, P. K. Combination Cancer Therapy Can Confer Benefit via Patient-to-Patient Variability without Drug Additivity or Synergy. *Cell* **171**, 1678-1691.e13 (2017).

201. Hwangbo, H., Patterson, S., Dai, A., Plana, D. & Palmer, A. C. Additivity predicts the efficacy of most approved combination therapies for advanced cancer. Preprint at https://doi.org/10.1101/2022.10.21.22281013 (2022).

202. Radic-Sarikas, B. *et al.* Lapatinib potentiates cytotoxicity of YM155 in neuroblastoma via inhibition of the ABCB1 efflux transporter. *Sci Rep* **7**, 3091 (2017).

203. Garman, K. A., Gelb, T., Urban, D., Hall, M. D. & Brownell, I. F. High-Throughput Matrix Synergy Screening Identifies Novel Therapeutic Combinations for Merkel Cell Carcinoma. *The FASEB Journal* **34**, 1–1 (2020).

204. Gao, S. *et al.* CRISPR screens identify cholesterol biosynthesis as a therapeutic target on stemness and drug resistance of colon cancer. *Oncogene* **40**, 6601–6613 (2021).

205. Gerlach, D. *et al.* The novel BET bromodomain inhibitor BI 894999 represses super-enhancer-associated transcription and synergizes with CDK9 inhibition in AML. *Oncogene* **37**, 2687–2701 (2018).

206. Shorstova, T., Foulkes, W. D. & Witcher, M. Achieving clinical success with BET inhibitors as anti-cancer agents. *Br J Cancer* **124**, 1478–1490 (2021).

207. Baker, E. K. *et al.* BET inhibitors induce apoptosis through a MYC independent mechanism and synergise with CDK inhibitors to kill osteosarcoma cells. *Sci Rep* **5**, 10120 (2015).

208. Cidado, J. *et al.* AZD4573 Is a Highly Selective CDK9 Inhibitor That Suppresses MCL-1 and Induces Apoptosis in Hematologic Cancer Cells. *Clinical Cancer Research* **26**, 922–934 (2020).

209. Huang, W.-L. *et al.* CDK9 Inhibitor Induces the Apoptosis of B-Cell Acute Lymphocytic Leukemia by Inhibiting c-Myc-Mediated Glycolytic Metabolism. *Front. Cell Dev. Biol.* **9**, 641271 (2021).

210. Deng, Z., Wang, H., Liu, J., Deng, Y. & Zhang, N. Comprehensive understanding of anchorage-independent survival and its implication in cancer metastasis. *Cell Death Dis* **12**, 629 (2021).

211. Horibata, S., Vo, T. V., Subramanian, V., Thompson, P. R. & Coonrod, S. A. Utilization of the Soft Agar Colony Formation Assay to Identify Inhibitors of Tumorigenicity in Breast Cancer Cells. *JoVE* 52727 (2015) doi:10.3791/52727.

212. Thomas, M. P. *et al.* Apoptosis Triggers Specific, Rapid, and Global mRNA Decay with 3′ Uridylated Intermediates Degraded by DIS3L2. *Cell Reports* **11**, 1079–1089 (2015).

213. Tadros, S. F., D'Souza, M., Zhu, X. & Frisina, R. D. Apoptosis-related genes change their expression with age and hearing loss in the mouse cochlea. *Apoptosis* **13**, 1303–1321 (2008).

214. Siddiqui, A. & Ceppi, P. A non-proliferative role of pyrimidine metabolism in cancer. *Molecular Metabolism* **35**, 100962 (2020).

215. Elshazly, A. M. & Gewirtz, D. A. Cytoprotective, Cytotoxic and Cytostatic Roles of Autophagy in Response to BET Inhibitors. *IJMS* **24**, 12669 (2023).

216. Naro, C., Bielli, P., Pagliarini, V. & Sette, C. The interplay between DNA damage response and RNA processing: the unexpected role of splicing factors as gatekeepers of genome stability. *Front. Genet.* **6**, (2015).

217. Ivanova, O. M. *et al.* Non-canonical functions of spliceosome components in cancer progression. *Cell Death Dis* **14**, 77 (2023).

218. Newman, A. C. & Maddocks, O. D. K. One-carbon metabolism in cancer. *Br J Cancer* **116**, 1499–1504 (2017).

219. Rowland, T. *et al.* Selective Targeting Cyclin-Dependent Kinase-9 (CDK9) Downmodulates c-MYC and Induces Apoptosis in Diffuse Large B-Cell Lymphoma (DLBCL) Cells. *Blood* **128**, 289–289 (2016).

220. Yin, Y. *et al.* EGFR signaling confers resistance to BET inhibition in hepatocellular carcinoma through stabilizing oncogenic MYC. *J Exp Clin Cancer Res* **38**, 83 (2019).

221. Mah, L.-J., El-Osta, A. & Karagiannis, T. C. γH2AX: a sensitive molecular marker of DNA damage and repair. *Leukemia* **24**, 679–686 (2010).

222. Zhang, Y. & Hunter, T. Roles of Chk1 in cell biology and cancer therapy. *Intl Journal of Cancer* **134**, 1013–1023 (2014).

223. Chaitanya, G. V., Alexander, J. S. & Babu, P. P. PARP-1 cleavage fragments: signatures of cell-death proteases in neurodegeneration. *Cell Commun Signal* **8**, 31 (2010).

224. Mashimo, M. *et al.* The 89-kDa PARP1 cleavage fragment serves as a cytoplasmic PAR carrier to induce AIF-mediated apoptosis. *Journal of Biological Chemistry* **296**, 100046 (2021).

225. Sturtzel, C. *et al.* Refined high-content imaging-based phenotypic drug screening in zebrafish xenografts. *npj Precis. Onc.* **7**, 44 (2023).

226. Wrobel, J. K. *et al.* Rapid In Vivo Validation of HDAC Inhibitor-Based Treatments in Neuroblastoma Zebrafish Xenografts. *Pharmaceuticals* **13**, 345 (2020).

227. Gamble, J. T., Elson, D. J., Greenwood, J. A., Tanguay, R. L. & Kolluri, S. K. The Zebrafish Xenograft Models for Investigating Cancer and Cancer Therapeutics. *Biology* **10**, 252 (2021).

228. Gupta, M., Lee, H. J., Barden, C. J. & Weaver, D. F. The Blood–Brain Barrier (BBB) Score. *J. Med. Chem.* **62**, 9824–9836 (2019).

229. Pearson, A. Dj. *et al.* Bromodomain and extra-terminal inhibitors—A consensus prioritisation after the Paediatric Strategy Forum for medicinal product development of epigenetic modifiers in children—ACCELERATE. *European Journal of Cancer* **146**, 115–124 (2021).

230. Vieito, M. *et al.* Trotabresib (CC-90010) in combination with adjuvant temozolomide or concomitant temozolomide plus radiotherapy in patients with newly diagnosed glioblastoma. *Neuro-Oncology Advances* **4**, vdac146 (2022).

231. Noon, A. & Galban, S. Therapeutic avenues for targeting treatment challenges of diffuse midline gliomas. *Neoplasia* **40**, 100899 (2023).

232. Tosi, U. & Souweidane, M. Diffuse Midline Gliomas: Challenges and New Strategies in a Changing Clinical Landscape. *Cancers* **16**, 219 (2024).

233. Jovanovich, N. *et al.* Pediatric diffuse midline glioma: Understanding the mechanisms and assessing the next generation of personalized therapeutics. *Neuro-Oncology Advances* **5**, vdad040 (2023).

234. Piunti, A. *et al.* Therapeutic targeting of polycomb and BET bromodomain proteins in diffuse intrinsic pontine gliomas. *Nat Med* **23**, 493–500 (2017).

235. Haag, D. *et al.* H3.3-K27M drives neural stem cell-specific gliomagenesis in a human iPSC-derived model. *Cancer Cell* **39**, 407-422.e13 (2021).

236. Zheng, L. *et al.* Diffuse Midline Gliomas With Histone H3 K27M Mutation in Adults and Children: A Retrospective Series of 164 Cases. *American Journal of Surgical Pathology* **46**, 863–871 (2022).

237. Zhang, S. *et al.* BET inhibitors reduce cell size and induce reversible cell cycle arrest in AML. *J of Cellular Biochemistry* **120**, 7309–7322 (2019).

238. Uitdehaag, J. C. M. *et al.* Cell Panel Profiling Reveals Conserved Therapeutic Clusters and Differentiates the Mechanism of Action of Different PI3K/mTOR, Aurora Kinase and EZH2 Inhibitors. *Molecular Cancer Therapeutics* **15**, 3097–3109 (2016).

239. Khamisipour, G., Jadidi-Niaragh, F., Jahromi, A. S., Zandi, K. & Hojjat-Farsangi, M. Mechanisms of tumor cell resistance to the current targeted-therapy agents. *Tumor Biol.* **37**, 10021–10039 (2016).

240. Shi, Z.-D. *et al.* Tumor cell plasticity in targeted therapy-induced resistance: mechanisms and new strategies. *Sig Transduct Target Ther* **8**, 113 (2023).

241. Toure, M. A. & Koehler, A. N. Addressing Transcriptional Dysregulation in Cancer through CDK9 Inhibition. *Biochemistry* **62**, 1114–1123 (2023).

242. Sun, Y. *et al.* Safety and Efficacy of Bromodomain and Extra-Terminal Inhibitors for the Treatment of Hematological Malignancies and Solid Tumors: A Systematic Study of Clinical Trials. *Front. Pharmacol.* **11**, 621093 (2021).

243. Rabab'h, O., Gharaibeh, A., Al-Ramadan, A., Ismail, M. & Shah, J. Pharmacological Approaches in Neurofibromatosis Type 1-Associated Nervous System Tumors. *Cancers* **13**, 3880 (2021).

244. Terry L Riss *et al.* Cell Viability Assays. in *Cell Viability Assays* (Bethesda (MD): Eli Lilly & Company and the National Center for Advancing Translational Sciences, 2004).

245. Park, W. *et al.* Diversity and complexity of cell death: a historical review. *Exp Mol Med* **55**, 1573–1594 (2023).

246. Lowe, S. W. & Lin, A. W. Apoptosis in cancer. *Carcinogenesis* **21**, 485–495 (2000).

247. Huang, Z., Wang, T., Wang, C. & Fan, Y. CDK9 inhibitors in cancer research. *RSC Med. Chem.* **13**, 688–710 (2022).

248. Hogg, S. J. *et al.* BET Inhibition Induces Apoptosis in Aggressive B-Cell Lymphoma via Epigenetic Regulation of BCL-2 Family Members. *Molecular Cancer Therapeutics* **15**, 2030–2041 (2016).

249. Deng, W. *et al.* The role of PPM1D in cancer and advances in studies of its inhibitors. *Biomedicine & Pharmacotherapy* **125**, 109956 (2020).

250. Andrysik, Z., Sullivan, K. D., Kieft, J. S. & Espinosa, J. M. PPM1D suppresses p53-dependent transactivation and cell death by inhibiting the Integrated Stress Response. *Nat Commun* **13**, 7400 (2022).

251. Zhou, X., Hao, Q. & Lu, H. Mutant p53 in cancer therapy—the barrier or the path. *Journal of Molecular Cell Biology* **11**, 293–305 (2019).

252. Hernández Borrero, L. J. & El-Deiry, W. S. Tumor suppressor p53: Biology, signaling pathways, and therapeutic targeting. *Biochimica et Biophysica Acta (BBA) - Reviews on Cancer* **1876**, 188556 (2021).

253. Wang, H., Guo, M., Wei, H. & Chen, Y. Targeting p53 pathways: mechanisms, structures, and advances in therapy. *Sig Transduct Target Ther* **8**, 92 (2023).

254. Yoon, M.-K., Ha, J.-H., Lee, M.-S. & Chi, S.-W. Structure and apoptotic function of p73. *BMB Reports* **48**, 81–90 (2015).

255. Awais, R., Spiller, D. G., White, M. R. H. & Paraoan, L. p63 is required beside p53 for PERP-mediated apoptosis in uveal melanoma. *Br J Cancer* **115**, 983–992 (2016).

256. Shi, J. & Vakoc, C. R. The Mechanisms behind the Therapeutic Activity of BET Bromodomain Inhibition. *Molecular Cell* **54**, 728–736 (2014).

257. Xu, Y. & Vakoc, C. R. Targeting Cancer Cells with BET Bromodomain Inhibitors. *Cold Spring Harb Perspect Med* **7**, a026674 (2017).

258. Hayden, E. *et al.* Therapeutic Targets in Diffuse Midline Gliomas—An Emerging Landscape. *Cancers* **13**, 6251 (2021).

259. Lovén, J. *et al.* Selective Inhibition of Tumor Oncogenes by Disruption of Super-Enhancers. *Cell* **153**, 320–334 (2013).

260. Nagaraja, S. *et al.* Transcriptional Dependencies in Diffuse Intrinsic Pontine Glioma. *Cancer Cell* **31**, 635-652.e6 (2017).

261. Peterson, E. R. *et al.* Adaptive rewiring of purine metabolism promotes treatment resistance in H3K27M-mutant diffuse midline glioma. Preprint at https://doi.org/10.21203/rs.3.rs-3317816/v1 (2023).

262. Liu, Y. *et al.* Coordination of Steps in Single-nucleotide Base Excision Repair Mediated by Apurinic/Apyrimidinic Endonuclease 1 and DNA Polymerase β. *Journal of Biological Chemistry* **282**, 13532–13541 (2007).

263. The Gene Ontology Consortium *et al.* The Gene Ontology knowledgebase in 2023. *GENETICS* **224**, iyad031 (2023).

264. Ning, K., Fermin, D. & Nesvizhskii, A. I. Comparative Analysis of Different Label-Free Mass Spectrometry Based Protein Abundance Estimates and Their Correlation with RNA-Seq Gene Expression Data. *J. Proteome Res.* **11**, 2261–2271 (2012).

265. Magnusson, R. *et al.* RNA-sequencing and mass-spectrometry proteomic time-series analysis of T-cell differentiation identified multiple splice variants models that predicted validated protein biomarkers in inflammatory diseases. *Front. Mol. Biosci.* **9**, 916128 (2022).

266. Nagaraja, S. *et al.* Histone Variant and Cell Context Determine H3K27M Reprogramming of the Enhancer Landscape and Oncogenic State. *Molecular Cell* **76**, 965-980.e12 (2019).

267. Harutyunyan, A. S. *et al.* H3K27M in Gliomas Causes a One-Step Decrease in H3K27 Methylation and Reduced Spreading within the Constraints of H3K36 Methylation. *Cell Reports* **33**, 108390 (2020).

268. Mandal, R., Becker, S. & Strebhardt, K. Targeting CDK9 for Anti-Cancer Therapeutics. *Cancers* **13**, 2181 (2021).

269. Nepomuceno, T. C. *et al.* BRCA1 recruitment to damaged DNA sites is dependent on CDK9. *Cell Cycle* **16**, 665–672 (2017).

270. Stinson, B. M. & Loparo, J. J. Repair of DNA Double-Strand Breaks by the Nonhomologous End Joining Pathway. *Annu. Rev. Biochem.* **90**, 137–164 (2021).

271. Prakash, R., Zhang, Y., Feng, W. & Jasin, M. Homologous Recombination and Human Health: The Roles of BRCA1, BRCA2, and Associated Proteins. *Cold Spring Harb Perspect Biol* **7**, a016600 (2015).

272. Sengupta, S., Biarnes, M. C. & Jordan, V. C. Cyclin dependent kinase-9 mediated transcriptional de-regulation of cMYC as a critical determinant of endocrine-therapy resistance in breast cancers. *Breast Cancer Res Treat* **143**, 113–124 (2014).

273. Lee, D. J. & Zeidner, J. F. Cyclin-dependent kinase (CDK) 9 and 4/6 inhibitors in acute myeloid leukemia (AML): a promising therapeutic approach. *Expert Opinion on Investigational Drugs* **28**, 989–1001 (2019).

274. Ma, H., Seebacher, N. A., Hornicek, F. J. & Duan, Z. Cyclin-dependent kinase 9 (CDK9) is a novel prognostic marker and therapeutic target in osteosarcoma. *EBioMedicine* **39**, 182–193 (2019).

275. Dahl, N. A. *et al.* Super Elongation Complex as a Targetable Dependency in Diffuse Midline Glioma. *Cell Reports* **31**, 107485 (2020).

276. Rowland, B. D. & Bernards, R. Re-Evaluating Cell-Cycle Regulation by E2Fs. *Cell* **127**, 871–874 (2006).

277. García-Gutiérrez, L., Delgado, M. D. & León, J. MYC Oncogene Contributions to Release of Cell Cycle Brakes. *Genes* **10**, 244 (2019).

278. Ahmadi, S. E., Rahimi, S., Zarandi, B., Chegeni, R. & Safa, M. MYC: a multipurpose oncogene with prognostic and therapeutic implications in blood malignancies. *J Hematol Oncol* **14**, 121 (2021).

279. Zhang, L., Hsu, J. I. & Goodell, M. A. PPM1D in Solid and Hematologic Malignancies: Friend *and* Foe? *Molecular Cancer Research* **20**, 1365–1378 (2022).

280. El Hage, A., French, S. L., Beyer, A. L. & Tollervey, D. Loss of Topoisomerase I leads to R-loop-mediated transcriptional blocks during ribosomal RNA synthesis. *Genes Dev.* **24**, 1546–1558 (2010).

281. Gaillard, H. & Aguilera, A. Transcription as a Threat to Genome Integrity. *Annu. Rev. Biochem.* **85**, 291–317 (2016).

282. Aguilera, A. & Gómez-González, B. DNA–RNA hybrids: the risks of DNA breakage during transcription. *Nat Struct Mol Biol* **24**, 439–443 (2017).

283. Gan, W. *et al.* R-loop-mediated genomic instability is caused by impairment of replication fork progression. *Genes Dev.* **25**, 2041–2056 (2011).

284. Matos, D. A. *et al.* ATR Protects the Genome against R Loops through a MUS81-Triggered Feedback Loop. *Molecular Cell* **77**, 514-527.e4 (2020).

285. Chen, L. *et al.* R-ChIP Using Inactive RNase H Reveals Dynamic Coupling of R-loops with Transcriptional Pausing at Gene Promoters. *Molecular Cell* **68**, 745-757.e5 (2017).

286. Shivji, M. K. K., Renaudin, X., Williams, Ç. H. & Venkitaraman, A. R. BRCA2 Regulates Transcription Elongation by RNA Polymerase II to Prevent R-Loop Accumulation. *Cell Reports* **22**, 1031–1039 (2018).

287. Bisgrove, D. A., Mahmoudi, T., Henklein, P. & Verdin, E. Conserved P-TEFb-interacting domain of BRD4 inhibits HIV transcription. *Proc. Natl. Acad. Sci. U.S.A.* **104**, 13690–13695 (2007).

288. Itzen, F., Greifenberg, A. K., Bösken, C. A. & Geyer, M. Brd4 activates P-TEFb for RNA polymerase II CTD phosphorylation. *Nucleic Acids Res* **42**, 7577–7590 (2014).

289. Chen, R., Yik, J. H. N., Lew, Q. J. & Chao, S.-H. Brd4 and HEXIM1: Multiple Roles in P-TEFb Regulation and Cancer. *BioMed Research International* **2014**, 1–11 (2014).

290. Winter, G. E. *et al.* BET Bromodomain Proteins Function as Master Transcription Elongation Factors Independent of CDK9 Recruitment. *Molecular Cell* **67**, 5-18.e19 (2017).

291. Shao, W. & Zeitlinger, J. Paused RNA polymerase II inhibits new transcriptional initiation. *Nat Genet* **49**, 1045–1051 (2017).

292. Skourti-Stathaki, K. Detection of R-Loop Structures by Immunofluorescence Using the S9.6 Monoclonal Antibody. in *R-Loops* (eds. Aguilera, A. & Ruzov, A.) vol. 2528 21–29 (Springer US, New York, NY, 2022).

293. Cerritelli, S. M., Sakhuja, K. & Crouch, R. J. RNase H1, the Gold Standard for R-Loop Detection. in *R-Loops* (eds. Aguilera, A. & Ruzov, A.) vol. 2528 91–114 (Springer US, New York, NY, 2022).

294. Vanoosthuyse, V. Strengths and Weaknesses of the Current Strategies to Map and Characterize R-Loops. *ncRNA* **4**, 9 (2018).

295. Chédin, F., Hartono, S. R., Sanz, L. A. & Vanoosthuyse, V. Best practices for the visualization, mapping, and manipulation of R-loops. *The EMBO Journal* **40**, e106394 (2021).

296. Piunti, A. & Shilatifard, A. Epigenetic balance of gene expression by Polycomb and COMPASS families. *Science* **352**, aad9780 (2016).

297. Tie, F. *et al.* CBP-mediated acetylation of histone H3 lysine 27 antagonizes *Drosophila* Polycomb silencing. *Development* **136**, 3131–3141 (2009).

298. Wojcik, J. B. *et al.* Epigenomic Reordering Induced by Polycomb Loss Drives Oncogenesis but Leads to Therapeutic Vulnerabilities in Malignant Peripheral Nerve Sheath Tumors. *Cancer Research* **79**, 3205–3219 (2019).

299. Mackay, A. *et al.* Integrated Molecular Meta-Analysis of 1,000 Pediatric High-Grade and Diffuse Intrinsic Pontine Glioma. *Cancer Cell* **32**, 520-537.e5 (2017).

300. Mc Gee, M. M. Targeting the Mitotic Catastrophe Signaling Pathway in Cancer. *Mediators of Inflammation* **2015**, 1–13 (2015).

301. Huertas, D. *et al.* Antitumor activity of a small-molecule inhibitor of the histone kinase Haspin. *Oncogene* **31**, 1408–1418 (2012).

302. Sazonova, E. V., Petrichuk, S. V., Kopeina, G. S. & Zhivotovsky, B. A link between mitotic defects and mitotic catastrophe: detection and cell fate. *Biol Direct* **16**, 25 (2021).

303. Sorokina, I. V. *et al.* Involvement of autophagy in the outcome of mitotic catastrophe. *Sci Rep* **7**, 14571 (2017).

304. Imreh, G., Norberg, H. V., Imreh, S. & Zhivotovsky, B. Chromosomal breaks during mitotic catastrophe trigger γH2AX–ATM–p53-mediated apoptosis. *Journal of Cell Science* **129**, 1950–1950 (2016).